Modes of Sulfate-Deposit-Induced Metallic Corrosion at Elevated Temperatures: Mechanisms and Mitigation Strategies

by

Emily Kistler

Bachelor of Science, Pennsylvania State University, 2015

Submitted to the Graduate Faculty of Swanson

School of Engineering in partial fulfillment of

the requirements for the degree of

Doctor of Philosophy

University of Pittsburgh

2020

UNIVERSITY OF PITTSBURGH

SWANSON SCHOOL OF ENGINEERING

This dissertation was presented

by

Emily Kistler

It was defended on

March 3, 2020

and approved by

Gerald H. Meier, PhD, Professor, Department of Mechanical Engineering and Materials Science

Guofeng Wang, PhD, Associate Professor, Department of Mechanical Engineering and Materials Science

Götz Veser, PhD, Professor, Department of Chemical and Petroleum Engineering

Dissertation Director: Brian Gleeson, PhD, Harry S. Tack Chair Professor, Department of Mechanical Engineering and Materials Science

Modes of Sulfate-Deposit-Induced Metallic Corrosion at Elevated Temperatures: Mechanisms and Mitigation Strategies

Emily Kistler, PhD

University of Pittsburgh, 2020

Hot-section components of aero- and marine-gas turbines can be at risk of hot corrosion, a form of accelerated attack resulting from the presence of sulfate-containing deposits. There are two documented forms of hot corrosion, referred to as Type II (below T_m of Na_2SO_4 ; 884°C) and Type I (above T_m of Na_2SO_4), both of which have been inferred to involve liquid formation and subsequent oxide-scale fluxing. Previous literature has focused on relatively high SO_2-content environments (~1000 ppm SO_2 and above). However, in actual engine applications, the SO_2 contents are much lower. This study assessed the effect of SO_2 content on the corrosion behavior of relevant Ni-based alloys in environments of dry air and O_2-(2.5, 10, and 100) ppm SO_2 from 550°C-1000°C. It was found in the Type II regime, as SO_2 content increased, corrosion rate increased. The opposite trend was found in the Type I regime, where the dry-air environment resulted in the most severe attack. The reasons for these trends were deduced. It was also found that hot corrosion can occur at temperatures as low as 550°C, where liquid formation is not thermodynamically possible. Additional experiments were conducted on pure nickel samples to more clearly elucidate the mechanism of this newly observed form of low-temperature hot corrosion. Based on the results, a solid-state corrosion mechanism was inferred. The mechanism relies on the formation of a previously unreported compound phase, identified using TEM analysis to be nanocrystalline with a stoichiometry of $Na_2Ni_2SO_5$. This phase was found to be a rapid diffusor of Ni^{2+} and Na^+.

To mitigate against Type II hot corrosion, a chromized coating is often used, but the application of a coating can result in varying Cr content across a part. The Cr level needed for protection was analyzed via exposure of comparable NiCrAl model alloys. Protection against the sulfate deposit was linked to the ability of the alloy to establish and maintain a Cr_2O_3 scale. The presence of a sodium sulfate deposit leads to chromium-sulfide formation, depleting the alloy of Cr needed to form a protective scale. The effect of Co, TaC, and AlN was also studied.

Table of Contents

Acknowledgements xxiv

1.0 Introduction 1

2.0 Background 4

2.1 Overview of Nickel-based Superalloys 4

2.2 Oxidation of Nickel-based Superalloys 9

2.3 Hot Corrosion 17

2.3.1 Environmental Factors Affecting Hot Corrosion 22

2.3.2 Low Temperature (Type II) Hot Corrosion 23

2.3.3 High Temperature (Type I) Hot Corrosion 41

2.4 Diffusion Coatings 52

2.4.1 Hot Corrosion of Chromized Coatings 55

3.0 Research Objectives 58

3.1 Deficiencies in the Current Body of Knowledge 58

3.2 Research Goals 60

4.0 Experimental Procedures 61

4.1 Materials Studied 61

4.1.1 Nickel-based Superalloys 61

4.1.1.1 PWA 1484 61

4.1.1.2 ME 16 62

4.1.2 Pure Metals 62
4.1.3 Model Alloys Based on Chromized Coating 63
4.1.4 Heat-treated PWA 1484 65
4.2 Hot Corrosion Exposures 65
4.2.1 Environments Studied 65
4.2.2 Experimental Set-up and Procedure 67
4.3 Analytical Methods 69
5.0 Results and Discussion 72
5.1 Solid-state Mode of Hot Corrosion Occurring at 700°C and Below 72
5.1.1 Nickel-based Superalloy Hot Corrosion Exposures from 550°C-650°C 75
5.1.1.1 PWA 1484 75
5.1.1.2 ME 16 79
5.1.2 Ternary Liquid Assessment 81
5.1.3 Nickel-Na_2SO_4 Diffusion Couples 85
5.1.4 Pure Nickel Hot Corrosion Exposures 87
5.1.5 TEM analysis 96
5.1.6 Discussion 99
5.1.6.1 Criteria for Low-Temperature Corrosion 99
5.1.6.2 Proposed Mechanism 108
5.2 Spatial Influence of Na_2SO_4 Deposit on Oxidation and Corrosion 112
5.2.1 PWA 1484 Experiments 112
5.2.2 Pure Nickel Experiments 114
5.2.3 TEM Results 120

5.2.4 Effect of Na and S on NiO Growth [117] 126
5.2.5 Discussion 128
5.3 Effect of SO_2 Content on Alloy Hot Corrosion Over the Temperature Range 550°C-1000°C 134
5.3.1 Low Temperature (≤ 650°C) 137
5.3.2 Intermediate Temperature (700°C-850°C) 140
5.3.2.1 Heat-treated Alloys 143
5.3.3 High-Temperature (≥ 900°C) 147
5.3.4 Discussion 163
5.3.4.1 Low Temperature (≤ 650°C) 164
5.3.4.2 Intermediate Temperature (700-850°C) 164
5.3.4.3 High Temperature (≥ 900°C) 173
5.4 Influence of Chromium Content on the Low-temperature Hot Corrosion Behavior of Model Ni-Cr-Al Based Alloys 184
5.4.1 Short-term Oxidation Behavior 185
5.4.1.1 Exposures Without a Deposit 185
5.4.1.2 Exposure with an Na_2SO_4 Deposit 189
5.4.2 Low-temperature Hot Corrosion Exposures 191
5.4.3 Influence of Cobalt 198
5.4.4 Influence of Carbides and Nitrides 199
5.4.5 Discussion 200
5.4.5.1 Corrosion Mechanism 200
5.4.5.2 Concept of “Critical Cr Content” Beneath a Deposit 201

5.4.5.3 Effect of Alloying Additions Present in PWA 70 206

6.0 Concluding Remarks 209

6.1 Solid-state Mode of Hot Corrosion Occurring at 700°C and Below 209

6.2 Spatial Influence of Na_2SO_4 Deposit on Oxidation and Corrosion 210

6.3 Effect of SO_2 Content on Alloy Hot Corrosion Over the Temperature Range 550-1000°C 211

6.4 Influence of Chromium Content on the Low-temperature Hot Corrosion Behavior of Model Ni-Cr-Al Based Alloys 212

Appendix A 213

Bibliography 217

List of Tables

Table 2-1. Salt composition removed from turbine blade surfaces [3]..... 18

Table 2-2. SO_2 Content and Deposit Composition in Los Angeles, Beijing, and Delhi [15]..... 23

Table 2-3. Melting points of important compounds in hot corrosion..... 24

Table 4-1. Nominal composition of PWA 1484 [98]. 62

Table 4-2. Nominal composition of ME 16 [99]. 62

Table 4-3. Model alloy compositions in atomic %. 64

Table 4-4. Fraction of carbides in heat treated alloys, measured from 200x magnification cross-sectional SEM image. 65

Table 4-5. Calculated equilibrium SO_3 pressure in O_2-SO_2 environments studied from 550°C-1000°C. 66

Table 5-1. Structural data for $Na_xNi_yS_zO_w$ phases [114–116]. 124

Table 5-2. Comparison of d-spacing (Å) of observed ring pattern of nanocrystalline phase to known phases containing Na-Ni-S-O. 124

Table 5-3. E_{GB} values after simulations of NiO with Na, S, and Na+S impurities..... 127

Table 5-4. ICP-OES results after exposure of PWA 1484 at 800°C for 1.5 h and 5 h with 2.5 mg/cm^2 Na_2SO_4. The concentration is in mmol*10^3/cm^2. 170

Table 5-5. EDS results of composition in center of dendued zone after exposure of PWA 1484 at 950°C for 5 h and 100 h with 2.5 mg/cm^2 Na_2SO_4..... 183

Table A-1. Data from measurements after exposure of PWA 1484 after 20 h with 2.5 mg/cm^2 214

Table A-2. EDS measurements of nanocrystalline phase. 215

List of Figures

Figure 2-1. Left: Isothermal (1000°C) Ni-Al-Cr section showing superalloy composition region [21]. Right: PWA 1484 microstructure showing γ-Ni and γ'-Ni_3Al phases. 5

Figure 2-2. Elements included in nickel-based superalloys. Horizontal lined are unfavorable elements, and cross-hatched lines are minor alloying elements [23]..... 7

Figure 2-3. a) Disk alloy microstructure schematic [25], and b) cross-sectional SEM image of ME 16 indicating grain size. 8

Figure 2-4. Turbine entry temperature (TET) vs. time schematic for a flight cycle [20]. 9

Figure 2-5. Parabolic rate constants of select oxides [28]. 11

Figure 2-6. Ellingham diagram highlighting Al_2O_3 and Cr_2O_3 [4]. 12

Figure 2-7. a) Alumina formation, with PWA 1484 and ME 16 compositions plotted [36], and b) oxide map showing change in alumina formation with chromium addition [37]. 15

Figure 2-8. PWA 1484 oxide formation, 700°C for 100 hours in dry air. 16

Figure 2-9. Hot corrosion schematic: corrosion rate vs. temperature. 17

Figure 2-10. Na-O-S stability diagram illustrating deposit chemistry changes toward acidic or basic conditions [4]. 20

Figure 2-11. a) Oxide solubility as a function of deposit basicity [50], and b) schematic illustrating dissolution and precipitation of the oxide through the deposit [52]. 21

Figure 2-12. Cross-sectional SEM images showing the effect of increasing Mo content: 700°C, dry air, 100 h exposures with an Na_2SO_4 deposit [59]. 26

Figure 2-13. $CoSO_4$-Na_2SO_4 and $NiSO_4$-Na_2SO_4 stability diagrams [14, 61]. 27

Figure 2-14. a) $NiSO_4$-Na_2SO_4 phase diagram, and b) $CoSO_4$-Na_2SO_4 phase diagram. 28

Figure 2-15. Cobalt Co^{2+}/Co^{3+} exchange reaction mechanism, showing initial $CoSO_4$ formation and reaction products in intermediate and high SO_2 environments [14]. 30

Figure 2-16. Weight gain vs. time at 660°C and 700°C for pure nickel with and without a Na_2SO_4 deposit in O_2 + 4% SO_2 [61]. 34

Figure 2-17. Cross-sectional SEM images of pure nickel exposed to air and O_2+1000ppm SO_2 with and without an Na_2SO_4 deposit after 20 h exposure [7]. 35

Figure 2-18. Ni-O-S stability diagram shows reaction paths for pure nickel in O_2+SO_2 with and without an Na_2SO_4 deposit, and in air with an Na_2SO_4 deposit [7]. 37

Figure 2-19. Cross sectional SEM images after 20 h exposures at 700°C with an $MgSO_4$-Na_2SO_4 deposit, a) NiAl, b) NiAlCr [6]. 38

Figure 2-20. Weight gain vs. time in O_2-SO_2 containing enviornments for hot corrosion expsoure of Udiment-700 with 0.7 mg/cm^2 Na_2SO_4 at 950°C [74]. 43

Figure 2-21. a) Oxidation kinetics of alloy B-1900 with and without an Na_2SO_4 deposit, and b) oxidation kinetics of B-1900 bare alloy and alloy sulfidized [80]..... 45

Figure 2-22. Ni-O-S stability diagram at 1000°C, ‘x’ indicates the composition of the Na_2SO_4 deposit and the arrows show changing composition of the deposit due to reaction with nickel. The dashed lines correspond to sulfur isobars [12]. 46

Figure 2-23. Schematic of the mechanism of basic fluxing [12]. 48

Figure 2-24. Ni-O-S stability diagram, with measurements of P_{O2} and a_{Na2O}, after testing 99% pure pre-oxidized Ni at 1173K with an Na_2SO_4 deposit [82]. 49

Figure 2-25. Reactions occurring during pack cementation to enrich steel with chromium [87] 53

Figure 2-26. Partial pressure of species during pack cementation at 1100°C [88]..... 54

Figure 2-27. Coating selection based on oxidation and corrosion resistance [28] 56

Figure 2-28. Attack rate vs. chromium content in the alloy [94]..... 57

Figure 4-1. Ni-Cr-Al isothermal section at 1000°C, adapted from [21] with four model alloy compositions indicated..... 64

Figure 4-2. Schematic of furnace set-up. 67

Figure 5-1. Stability diagram of the CoO-Co_3O_4-$CoSO_4$-Na_2SO_4, adapted from Luthra [11] and NiO-$NiSO_4$-Na_2SO_4, adapted from Misra et al. [102], with pSO_3 in O_2-(2.5, 10, and 100) ppm SO_2 superimposed. Above the respective curves for CoO, Co_3O_4, and NiO indicates eutectic stability. The end point at the low temperature for the curves is at the eutectic temperature; 565°C for $CoSO_4$-Na_2SO_4 and 671°C for $NiSO_4$-Na_2SO_4..... 73

Figure 5-2. Weight change vs. temperature plots after 20 h exposures of PWA 1484 in O_2-(2.5 10, and 100) ppm SO_2 and dry air, with a 2.5 mg/cm^2 Na_2SO_4 deposit. Sample spallation occurred in the O_2-100ppm SO_2 environment at 750°C and 800°C, so no data points are shown. Three data points are shown for each O_2- 100 ppm SO_2 to illustrate the reproducibility. Open symbols indicate localized attack. 74

Figure 5-3. (a) Cross-sectional SEM images of the corrosion products formed on PWA 1484 after 20 h hot-corrosion exposure in air and O_2-(2.5, 10, and 100) ppm SO_2 and with 2.5 mg/cm^2 Na_2SO_4 deposit. (b) Phase identification for 600°C in O_2-2.5 ppm SO_2 based on EDS analysis 76

Figure 5-4. Cross-sectional SEM images of interal corrosion product on PWA 1484 after 20 hr exposure at 650°C in O_2-10 ppm SO_2 and with 2.5 mg/cm^2 Na_2SO_4 deposit, along with EDS results where the numbers in the image correspond to the numbers in the accompanying table..... 77

Figure 5-5. Cross-sectional SEM images after a time study completed on PWA 1484 at 650°C in O_2-10 ppm SO_2 and with 2.5 mg/cm^2 Na_2SO_4 deposit. 78

Figure 5-6. Cross-sectional SEM image after 6 h exposure of PWA 1484 at 550°C in O_2-10 ppm SO_2 and with 2.5 mg/cm^2 Na_2SO_4 deposit. 78

Figure 5-7. Weight change vs. time after exposure at 550°C and 650°C of ME 16 with 2.5 mg/cm^2 Na_2SO_4 in O_2-10 ppm SO_2. 80

Figure 5-8. Cross-sectional SEM images after 300 h exposure of ME 16 at 550°C and 650°C in O_2-10 ppm SO_2 and with 2.5 mg/cm^2 Na_2SO_4. 80

Figure 5-9. Ternary Na_2SO_4-$CoSO_4$-$NiSO_4$ digram with mixtures tested for liquid formation at 650°C in O_2-10 ppm SO_2 for 2 h. 82

Figure 5-10. Cross-sectional SEM images of sulfate mixtures after exposure at 650°C in O_2-10 ppm SO_2 for 2 h. The test numbers correspond to the numbers in Fig. 5-9. 82

Figure 5-11. NiSO-Na_2SO_4 and $CoSO_4$-Na_2SO_4 phase diagrams calculated from Pandat^{TM} [106]. DSC measurements are superimposed on the diagrams. 83

Figure 5-12. Sections of a ternary phase diagram of $CoSO_4$-$NiSO_4$-Na_2SO_4 for constant $CoSO_4$-$NiSO_4$ ratios of a) 3:1, b) 1:1, and c) 1:3 calculated using Pandat^{TM} [106]. The red circle data points are from the work of Bol'shakov and Feorov [107], and the blue data points are from DSC experiments [105]. 85

Figure 5-13. Plot of measured nickel content vs. distance into sulfate (from the nickel/sulfate interface) after exposure of nickel/Na_2SO_4 diffusion couples in O_2-10 ppm SO_2 and dry air for 4 h at 650°C. 86

Figure 5-14. Cross-sectional SEM images of nickel samples after 20 hr exposure in O_2-10 ppm SO_2 and with 2.5 mg/cm^2 of Na_2SO_4 deposit. 88

Figure 5-15. Cross-sectional SEM images of nickel samples preoxidized at 700°C for 24 h and 1000°C for 0.5 h followed by 20 h exposure in O_2-10 ppm SO_2 and with 2.5 mg/cm^2 of Na_2SO_4 deposit..... 89

Figure 5-16. EDS map of area shown in SEM cross-sectional image on the left of preoxidized Ni at 700°C for 24 h followed by 20 hr exposure in O_2-10 ppm SO_2 at 650°C with 2.5 mg/cm^2 Na_2SO_4 deposit. EDS map was taken of porous NiO that formed at the gas/sulfate interface [109]..... 89

Figure 5-17. Surface images of NiO scale after preoxidation exposure at the indicated temperature. 91

Figure 5-18. Cross-sectional SEM images after 20 h expsoure of nickel in O_2-10 ppm SO_2 with crystals of Na_2SO_4 on an initially bare (i.e., unnoxidized) nickel surface..... 92

Figure 5-19. Cross-sectional SEM image after 20 h exposure of nickel in dry air at 650°C with crystals of Na_2SO_4 on an initially bare (i.e., unoxidized nickel surface)..... 93

Figure 5-20. SEM surface images after 8 h exposure at 650°C of nickel in O_2-10 ppm SO_2 with crystals of Na_2SO_4 on the surface. 95

Figure 5-21. Cross-sectional SEM image after 20 h exposure at 650°C of nickel in O_2-10 ppm SO_2 with crystals of K_2SO_4 on the surface. 96

Figure 5-22.Image of TEM sample along with TEM images from the NiO+Na_2SO_4 region in the product formed on pure nickel after exposure at 650°C for 5.5 h with Na_2SO_4 grains..... 98

Figure 5-23. (a) Cross-sectional SEM image of PWA 1484 after 1.5 h exposure at 550°C in O_2-10 ppm SO_2 and with 2.5 mg/cm^2 of Na_2SO_4 deposit. (b) Corresponding TEM image showing identification of the nanoycrystalline phase next to a NiO filament..... 99

Figure 5-24. a) Ni-O-S stability diagram at 650°C. The PSO3 values in O_2-(10,100, and 1000)ppm SO_2 are plotted on the diagram. The red highlighted area corresponds to the section of the diagrams shown in 14b), c) shows the same region at 550°C. The region of stability for the metastable $Na_2Ni_2SO_5$ is shown in b) and c). 100

Figure 5-25. Cross-sectional SEM image of Na_2SO_4 applied to an alumina cruicible before and after thermal exposure at 650°C in O_2-10 ppm SO_2 for 2 h. Grains that sintered after the exposure are identified. 102

Figure 5-26. Weight change vs. time for nickel TGA data after oxidation at 700°C for 24 h followed by oxidation at 650°C for 20 h in dry air. 104

Figure 5-27. Free energy diagrams for hot-corrosion exposures of a) nickel, which was preoxidized in air at 700°C and b) nickel, which was not preoxidized. All exposures were at 650°C in O_2-10 ppm SO_2 for 20 h with 2.5 mg/cm^2 Na_2SO_4 deposit. 106

Figure 5-28. SEM cross-sectional image following exposure of a nickel sample at 650°C for 20 h in O_2-10 ppm SO_2 with 2.5 mg/cm^2 Na_2SO_4 deposit. The nickel sample was initially hot corrooded at 650°C for 20 h in O_2-10 ppm SO_2 with 2.5 mg/cm^2 Na_2SO_4 deposit to produce the result shown in Figure 5-15, then the deposit was removed, leaving an NiO scale that had formed beneath the Na_2SO_4 deposit. The speciman was then subjected to the same testing condition of 650°C for 20 h in O_2-10 ppm SO_2 with 2.5 mg/cm^2 Na_2SO_4 deposit. 107

Figure 5-29. Proposed mechanism for the observed low-temperature, Na_2SO_4-deposit-induced corrosion. 110

Figure 5-30. SEM cross-sectional images after hot corrosion exposure of pure nickel and cobalt at 500°C for 20 h in O_2-10 ppm SO_2 with 2.5 mg/cm^2 Na_2SO_4 deposit. 111

Figure 5-31. Schematic of test procedure, where one half of a PWA 1484 coupon was coated with 2.5 mg/cm^2 Na_2SO_4 deposit, along with cross-sectional SEM images after hot corrosion exposure at 550°C for 20 h in O_2-10 ppm SO_2. 113

Figure 5-32. Schematic of test procedure, where a PWA 1484 coupon was cut in half and one half was coated with 2.5 mg/cm^2 Na_2SO_4, along with cross-sectional SEM image of the unocated side after exposure at 550°C for 20 h in O_2-10 ppm SO_2. 113

Figure 5-33. Surface SEM image of pure nickel after exposure with single Na_2SO_4 grain at 650°C for 20 h, along with EDS results..... 115

Figure 5-34. Cross-sectional SEM images of a) affected area and b) unaffected area of pure nickel after exposure with single Na_2SO_4 grain at 650°C for 20 h. 115

Figure 5-35. Cross-sectional SEM images of nickel sample after exposure at 650°C in O_2-10 ppm SO_2 for 20 h with isolated Na_2SO_4 grain. 116

Figure 5-36. Cross-sectional SEM images of two locations, a) and b), on nickel sample after exposure at 625°C in O_2-10 ppm SO_2 for 20 h with isolated Na_2SO_4 grains. 118

Figure 5-37. Cross-sectional SEM images of nickel sample after exposure at 625°C in O_2-10 ppm SO_2 for 20 h with isolated Na_2SO_4 grains, along with EDS results in area unaffected by the presence of the suflate deposit, and two areas affected by the deposit. 119

Figure 5-38. Cross-sectional SEM images of nickel sample after exposure at 625°C in O_2-10 ppm SO_2 for 20 h with isolated K_2SO_4 grain. 120

Figure 5-39. SEM image of first TEM sample from expousre of Ni at 625°C for 20 h with isolated grains of Na_2SO_4, along with TEM images inidcating nanocrystalline phase formation and diffraction patterns from an area of NiO and an area with the nanocrystalline Na-Ni-S-O phase..... 121

Figure 5-40. SEM images of second TEM sample from expousre of Ni at 625°C for 20 h with isolated grains of Na_2SO_4, along with TEM images inidcating nanocrystalline phase formation and corresponding diffraction pattern. 123

Figure 5-41. NiO structures used in computer simulations with S doping, Na doping, and Na and S co-doping. 127

Figure 5-42. Schematic of proposed mechanism, with diffusion of Na along the surface included. 129

Figure 5-43. Calculated oxide thickness for grain sizes from 40-1000 nm after a 20 h exposure of nickel at 625°C..... 132

Figure 5-44. Average attack vs. tempearture after 20 h hot corrosion exposure of PWA 1484 in dry air and O_2-(2.5, 10, and 100) ppm SO_2 with 2.5 mg/cm^2 Na_2SO_4 deposit. 135

Figure 5-45. Weight change vs. tempearture after 20 h hot corrosion exposure of PWA 1484 in dry air and O_2-(2.5, 10, and 100) ppm SO_2 with 2.5 mg/cm^2 Na_2SO_4 deposit. 136

Figure 5-46. Cross-sectional SEM images after 1.5 h and 20 h exposure of PWA 1484 in dry air and O-(2.5, 10, and 100) ppm SO_2 with 2.5 mg/cm^2 Na_2SO_4..... 139

Figure 5-47. ICP-OES results showing concentration of Ni and Co in mmol/cm^2*10^3 after a 1.5 h exposure of PWA 1484 in dry air and O_2-(2.5, 10, and 100) ppm SO_2 with 2.5 mg/cm^2 Na_2SO_4 139

Figure 5-48. Cross-sectional SEM images of PWA 1484 after 20 h exposure at 700°C, 750°C, 800°C, and 850°C in dry air and O_2-(2.5, 10, and 100) ppm SO_2 with 2.5 mg/cm^2 Na_2SO_4. 141

Figure 5-49. Cross-sectional SEM images of PWA 1484 after a 2 h exposure at 850°C in O_2-10 ppm SO_2, along with WDS elemental maps of the highlighted area. 142

Figure 5-50. a) SEM cross-sectional image of PWA 1484 after a 20 h exposure at 850°C in O_2-10 ppm SO_2 with 2.5 mg/cm^2 Na_2SO_4 deposit with pit size marked, along with b) surface optical image of bare PWA 1484 indicating dendritic structure and size of interdendritic region is similar to the size of pits after a hot corrosion exposure. 144

Figure 5-51. SEM images of cross-section and surface of heat-treated PWA 1484 alloys. 144

Figure 5-52. Cross-sectional SEM image of heat-treated PWA 1484 alloys, along with EDS results of Al, Cr, Ni, and Co composition..... 145

Figure 5-53. Graph of the fraction of corrosion pits along the surface, measured from cross-sectional SEM images of PWA 1484 alloys that were heat-treated for a short, medium, and long times and exposured to 850°C for 20 h in O_2-10 ppm SO_2 with 2.5 mg/cm^2 Na_2SO_4 deposit. 146

Figure 5-54. Cross-sectional SEM images of PWA 1484 after 20 h exposure at 900°C, 950°C, and 1000°C in dry air and O_2-(2.5, 10 ,and 100) ppm SO_2 with 2.5 mg/cm^2 Na_2SO_4. 149

Figure 5-55. Cross-sectional SEM images after exposure of PWA 1484 at 950°C for 20 h in O_2-100 ppm SO_2, along with EDS analysis..... 150

Figure 5-56. Weight change vs. time after exposure of PWA 1484 at 900°C in dry air and O_2-10 ppm SO_2 with 2.5 mg/cm^2 Na_2SO_4. The resulting cross-sectional SEM image after the 100 h exposure is shown. 151

Figure 5-57. Weight change vs. time of PWA 1484 after exposure at 950°C in dry air and O_2-(2.5, 10, and 100) ppm SO_2 with 2.5 mg/cm^2 Na_2SO_4. 152

Figure 5-58. Cross-sectional SEM images of PWA 1484 after exposure at 950°C for 1.5, 5, 20, and 100 h in dry air and O_2-(2.5, 10, and 100) ppm SO_2 and with 2.5 mg/cm^2 Na_2SO_4. ... 154

Figure 5-59. Cross-sectional SEM image of PWA 1484 after exposure at 950°C in O_2-10 ppm SO_2 for 20 h with 2.5 mg/cm^2 Na_2SO_4, along with WDS elemental maps. 156

Figure 5-60. Cross-sectional SEM image of PWA 1484 after exposure at 950°C for 20 h in dry air with 2.5 mg/cm^2 Na_2SO_4, along with WDS elemental maps. 157

Figure 5-61. ICP-OES analysis after exposure of PWA 1484 at 950°C in dry air and O_2-(2.5, 10, and 100) ppm SO_2 with 2.5 mg/cm^2 Na_2SO_4. 158

Figure 5-62. Cross-sectional SEM images of mixed oxide product formed on PWA 1484 after exposure at 950°C for 100 h with 2.5 mg/cm^2 Na_2SO_4, along with EDS analysis. 160

Figure 5-63. XRD pattern of PWA 1484 after exposure at 950°C for 100 h in O_2-10 ppm SO_2 and dry air with 2.5 mg/cm^2 Na_2SO_4. The product spalled in dry air. XRD patterns were obtained from the top and bottom of the spalled product. 162

Figure 5-64. Cross-sectional SEM images after 20 h exposure of PWA 1484 at 950°C in dry air and O_2-10 ppm SO_2 with 5 mg/cm^2 Na_2SO_4..... 163

Figure 5-65. Heating profile of the time to reach 850°C. 165

Figure 5-66. Surface SEM images of PWA 1484 and three heat treated (HT) PWA 1484 alloys after a 5 min. oxidation exposure at 850°C in air. A high magnifcation and low magnification image is shown. 167

Figure 5-67. Cross-sectional SEM image of the short heat-treated PWA 1484 alloy after exposure at 850°C in O_2-10 ppm SO_2 for 20 h with 2.5 mg/cm^2 Na_2SO_4. The images show pit formation initiation at dendritie and interdendritic regions. 167

Figure 5-68. Cross-sectional SEM images after oxidation of PWA 1484 at 850°Cin dry air and O_2-10 ppm SO_2 for 100 h..... 168

Figure 5-69. Cross-sectioanl SEM image of Ni-5Cr-9Al after exposure at 750°C and 800°C for 20 h in O_2-10 ppm SO_2 with 2.5 mg/cm^2 Na_2SO_4 170

Figure 5-70. Cross-sectional SEM image of PWA 1484 after exposure at 750°C for 20 h in O_2-2.5 ppm SO_2, along with EDS analysis of oxide formed in area unreacted with deposit... 171

Figure 5-71. Free energy of formation per mole of S_2, data obtained from [130]. Dashed lines indicate the data was extrapolated to higher temperatures. 172

Figure 5-72. EDS elemental maps with corresponding cross-sectional SEM image after 100 h exposure of PWA 1484 in dry air and O_2-100 ppm SO_2 with 2.5 mg/cm^2 Na_2SO_4. 175

Figure 5-73. Na-Cr-O-S stability diagram at 950°C, with P_{SO_3} in O_2-(2.5, 10, and 100) ppm SO_2 envrionments indicated. Data for diagram was taken from [130]. 177

Figure 5-74. Schematic of solubility of Cr_2O_3 in Na_2SO_4 as a function of melt basicity, with hypothetical location for a dry air and O_2-100 ppm SO_2 enviornment. 178

Figure 5-75. Cross-sectional SEM image of PWA 1484 after 65 h exposure in dry air with 2.5 mg/cm^2 Na_2SO_4, along with WDS elemental maps. 180

Figure 5-76. a) Schematic of P_{SO_3} gradient that can develop for alloy-induced acdic fluxing in dry air and O-100 ppm SO_2, along with solubility diagrams for each environment. 181

Figure 5-77. Cross-sectional SEM image of PWA 70. 185

Figure 5-78. Raman spectrum from surface of Ni-16Cr-4Al after 2 h oxidation exposure in O_2-10 ppm SO_2 at 600°C-700°C. 186

Figure 5-79. Raman spectrum from surface of Ni-19Cr-4Al after 2 h oxidation exposure in O_2-10 ppm SO_2 at 600°C-700°C. 187

Figure 5-80. Raman spectrum from surface of Ni-23Cr-4Al after 2 h oxidation exposure in O_2-10 ppm SO_2 at 600°C-700°C. 188

Figure 5-81. Raman spectrum from surface of Ni-26Cr-4Al after 2 h oxidation in O_2-10 ppm SO_2 at 600°C-700°C. 189

Figure 5-82. Surface SEM images of NiCrAl alloys following removal of Na_2SO_4 deposit after exposure at 650°C in O_2-10 ppm SO_2 for 2 h with 2.5 mg/cm^2 Na_2SO_4 deposit. Numbers in surface SEM images correspond to number Raman spectrum below the images. 190

Figure 5-83. Weight change vs. tempertature of Ni-(16, 19, 23, and 26) Cr-4Al alloys after 100 h exposure at 600°C-700°C in O_2-10 ppm SO_2 with 2.5 mg/cm^2 Na_2SO_4 deposit..... 191

Figure 5-84. Cross-sectional SEM images of Ni-(16, 19, 23, and 26)Cr-4Al after 100 h exposure in O_2-10 ppm SO_2 with 2.5 mg/cm^2 Na_2SO_4 deposit. 192

Figure 5-85. Weight change vs. time graphs after hot corrosion exposure of Ni-(16, 19, 23, and 26)Cr-4Al at 600°C, 650°C, and 700°C in O_2-10 ppm SO_2 with 2.5 mg/cm^2 Na_2SO_4 deposit. 194

Figure 5-86. Cross-sectional SEM images of Ni-(16, 19, 23, and 26)Cr-4Al after 20 h exposure at 600°C in O_2-10 ppm SO_2 with 2.5 mg/cm^2 Na_2SO_4 deposit..... 194

Figure 5-87. Cross-sectional SEM image of Ni-(16 and 19)Cr-4Al after 20 h exposure at 650°C in O_2-10 ppm SO_2 with 2.5 mg/cm^2 Na_2SO_4. 195

Figure 5-88. Cross-sectional SEM images of NiCrAl alloys after 20 h exposure at 650°C in O2-10 ppm SO_2 with 2.5 mg/cm2 Na_2SO_4, along with EDS analysis of the Cr-rich scale and denuded zone. 196

Figure 5-89. Cross-sectional SEM image of Ni-(16 and 19)Cr-4Al after 20 h exposure at 700°C in O_2-10 ppm SO_2 with 2.5 mg/cm^2 Na_2SO_4. 197

Figure 5-90. Cross-sectional SEM image of Ni-26Cr-10Co-4Al after 100 h exposure at 600°C and 650°C in O_2-10 ppm SO_2 with 2.5 mg/cm^2 Na_2SO_4 deposit..... 198

Figure 5-91. Cross-sectional SEM images of Ni-26Cr-4Al,with additions of aluminum nitrides and tantalum carbides, after exposure at 650°C for 100 h in O_2-10 ppm SO_2 with 2.5 mg/cm^2 Na_2SO_4 deposit. 199

Figure 5-92. Cross-sectional SEM image of Ni-16Cr-4Al pre-oxidized at 900°C for 6 h in air with no deposit followed by exposure at 650°C in O_2-10 ppm SO_2 with 2.5 mg/cm^2 Na_2SO_4 202

Figure 5-93. Schematic of initial stages of deposit/alloy interaction..... 203

Figure 5-94. Schematic of NiCrAl exposures for 20 and 100 h in O_2-10 ppm SO_2 with 2.5 mg/cm^2 Na_2SO_4, illustrating protective vs. non-protective alloys. 204

Figure 5-95. Plot of measured concentration of Al, Ni, and Cr from ICP-OES analysis after exposure at 600°C for 2 h in O_2-10 ppm SO_2 with 2.5 mg/cm^2 Na_2SO_4 deposit. 205

Figure 5-96. Plot of measured concentration of Al, Ni, and Cr from ICP-OES analysis after exposure at 650°C for 4 h in O_2-10 ppm SO_2 with 2.5 mg/cm^2 Na_2SO_4 deposit. 207

Figure A-1. Example of average attack measurement on cross-sectional SEM image of PWA 1484 after exposure at 650°C in O_2-10 ppm SO_2 after 20 h with 2.5 mg/cm^2 Na_2SO_4. 214

Acknowledgements

I would first like to sincerely thank my advisor, Prof. Brian Gleeson, for his mentorship throughout my PhD. Having an advisor that is incredibly knowledgeable, patient, and encouraging made the process an enjoyable experience and made me a much better researcher. Also, thank you to Prof. Gerald Meier for his helpful discussions, and thank you to my committee members, Prof. Guofeng Wang and Prof. Götz Veser for their input it was much appreciated. Thank you also to Dr. Michael Task and Dr. Xuan Liu at Pratt & Whitney for their support in the project and for their discussions.

Thank you to the National Defense Science and Engineering Graduate (NDSEG) Fellowship Program, sponsored by the Air Force Research Laboratory (AFRL), the Office of Naval Research (ONR) and the Army Research Office (ARO), for financial support.

I would also like to thank all the lab members I have worked with throughout the years for assistance, helpful discussions, preparations for conferences, and for all the wonderful memories.

Lastly, I would like to thank my family for their love and support, especially to my husband for always encouraging and supporting me during the PhD process. Your work ethic in your own career always motivated me and I look forward to our next chapter in life.

1.0 Introduction

Hot-section components of aero-and marine-gas turbines are often composed of a nickel-based superalloy, which was developed to provide excellent high-temperature mechanical properties [1]. While these components may mechanically perform well, corrosion is a growing issue due to advances that increase the operating temperature of engines.

Deposit-induced attack by a sulfate, generally termed “hot corrosion” is one such form of corrosion that results in severe degradation of components and hence reduced part life. The deposit involved in hot corrosion is sulfate-containing, often Na_2SO_4 rich, and reaction of the alloy with the deposit, both above and below the deposit melting point, can result in severe corrosion. The deposit can originate from intake air (sea salt and particulate matter) or from fuel impurities that react with the environment [2, 3]. For instance, Bornstein and Allen [3] studied deposits removed from internal and external surfaces of turbine blades from the first and second stage of land-based turbine engines and found a similar composition in all cases, which suggests that particle impaction stemming from atmospheric condensates is the more likely scenario. Regardless, once the deposit is in contact with the components, hot corrosion can result.

There are two documented forms of hot corrosion, referred to as Type II (below T_m of Na_2SO_4) and Type I (above T_m of Na_2SO_4), both of which have been inferred to involve liquid formation. Type II hot corrosion is believed to occur if liquid formation is stabilized; in the case of a nickel-based superalloy possible eutectics are Na_2SO_4-$CoSO_4$ (T_m=565°C) or Na_2SO_4-$NiSO_4$ (T_m=671°C). The severity of attack is dependent on several factors, including: deposit mass; temperature; alloy composition; alloy microstructure; and gas composition. SO_2 in the

environment, specifically the reaction of SO_2 with O_2 to produce SO_3, is known to play an important role in hot corrosion due to the stabilization of sulfate compounds [4]. Previous and recent hot-corrosion research focused on relatively high SO_2 (~1000 ppm SO_2)-containing environments [5–14]. However, in real applications the SO_2 content will usually be much lower [15]. In addition, based on preliminary experiments, hot corrosion was found to occur on a nickel-based superalloy down to 550°C and at SO_2 pressures not sufficient for transition-metal sulfate stability. In engine applications, there are a number of component areas that operate at these lower temperatures. For instance, some areas of the internal cooling channels of turbine blades operate at temperatures of 700°C and below [16]. These passages are not always coated, making the base metal susceptible to Type II hot corrosion attack. In addition, turbine disks are uncoated components reaching temperatures from around 400°C to 800°C at the outer rim [17]. There is a paucity of information on the mechanism(s) of corrosion at temperatures below what is prototypical of Type II (i.e., below 700°C). The first part of this PhD thesis will focus on understanding the exact mechanism of hot corrosion occurring at 650°C and below, which will then aid in developing mitigation methods to prevent low-temperature attack.

The next part of this thesis will focus on understanding the effects of SO_2 content in the atmosphere on hot corrosion as a function of temperature. In particular, there is a need to better understand hot corrosion behavior at SO_2 contents closer to engine environments. A single-crystal nickel-based superalloy that is directly relevant to current engine application will be studied and the environments will be dry air and O_2-(2.5, 10, and 100) ppm SO_2. The temperature range studied will be 550-1000°C. The effect of SO_2 content on the corrosion rate and the mechanism in the low-,intermediate-, and high-temperature regimes will be analyzed. The results will aid in better

understanding the corrosion mechanism at more realistic SO_2 contents and, based on the SO_2 variation around the world, to better predict component susceptibility to hot-corrosion attack.

The deposition of an Al-rich or Cr-rich coating onto a component is a current technique used to inhibit hot corrosion. Diffusion coatings involve enriching the surface of a component with a protective element of interest [4]. A chromized coating is a surface layer that is enriched with a relatively high chromium content [18]. However, as discussed with our industrial collaborator, Pratt & Whitney, the process of chromizing components results in coatings with varying chromium content across the surface, which can lead to localized hot-corrosion attack if the chromium level is not sufficient in a certain area. The last part of this PhD thesis will focus on mitigation methods to hot corrosion attack, with the first method looking at chromized coating compositions, based on PWA 70 (Pratt & Whitney's chromized coating). The goal is to determine what level of chromium provides the best resistance to Type II hot-corrosion attack. Another mitigation method stems from preliminary results, which show in Type I hot corrosion that pitting occurs similar in distribution to the dendrite spacing of the nickel-based superalloy. Heat-treated alloys will be tested to determine the extent of improved corrosion resistance provided by alloy homogenization. These mitigation methods will aid in enhancing current protection techniques against hot corrosion.

2.0 Background

Hot corrosion of nickel-based superalloys is the focus of this thesis. This chapter will provide background information on the application of nickel-based superalloys, current understanding of hot corrosion, and relevant protection strategies against hot-corrosion attack. Deficiencies in current understanding will be highlighted throughout the various sections of this chapter.

2.1 Overview of Nickel-based Superalloys

The development of superalloys was driven by the creation of the gas-turbine engine. There was a need for a material that could endure the high-temperature and mechanical requirements that exist in engine operation. Superalloys refer to a class of materials with excellent high-temperature properties capable of operating up to 90% of their absolute melting temperature [19]. There exist nickel, iron-nickel, and cobalt-based superalloys. Of the three classes of superalloys, nickel-based superalloys provide the best combination of high-temperature properties, making them widely used in engine components [20]. In a gas-turbine engine, 40-50% of the weight is due to the nickel-based components [19]. The focus of this thesis is hot corrosion, which occurs on hot-section components of the turbine engine. The present study was driven by corrosion seen in service on turbine blades and disks, both of which are comprised of a nickel-based superalloy. Therefore, the following overview will only consider nickel-based superalloys.

Since the development of nickel-based superalloys, there have been major advances that resulted in refined compositions and processing methods. Current superalloys may contain over ten alloying elements, each serving a specific purpose [19]. The microstructure of nickel-based superalloys consists of an austenitic γ-Ni matrix with discrete γ'-Ni_3Al precipitates, as well as secondary carbide phases and perhaps even undesirable topologically closed packed (TCP) phases [19, 20]. The γ matrix is a solid solution of Ni, and FCC in structure [19]. The γ' phase is based on the ordered $L1_2$ Ni_3Al, which tends to be coherent with the matrix [1]. The γ' phase provides the precipitation hardening that results in excellent high-temperature mechanical properties. Figure 2-1 shows an isothermal section of the Ni-Al-Cr phase diagram and the region that is relevant to nickel-based superalloys. On the right of this figure is a secondary electron microscope image of a commercial nickel-based superalloy (PWA 1484).

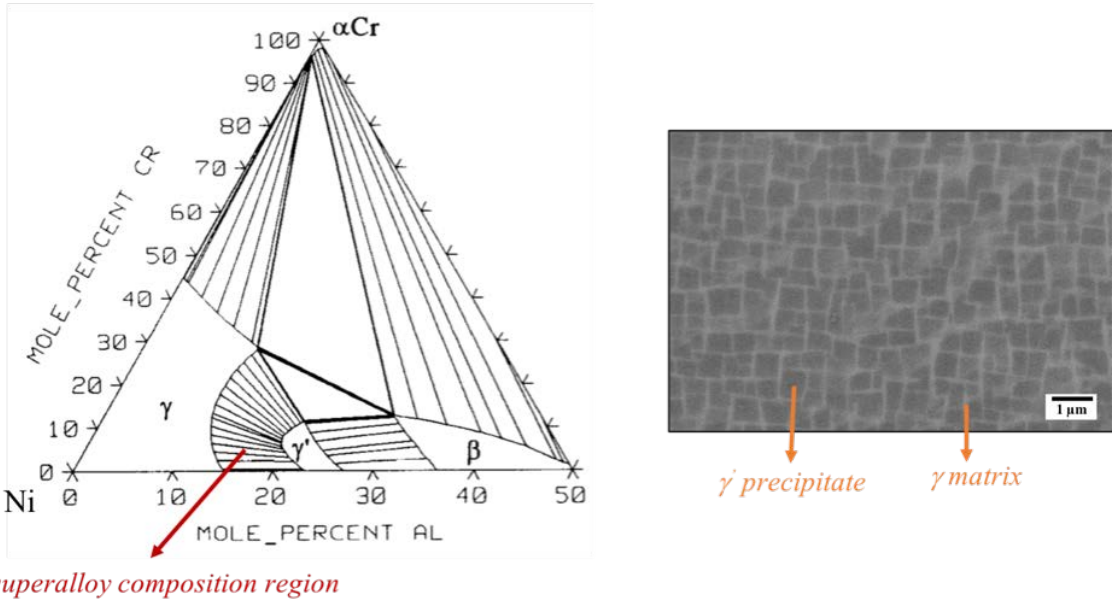

Figure 2-1. Left: Isothermal (1000°C) Ni-Al-Cr section showing superalloy composition region [21]. Right: PWA 1484 microstructure showing γ-Ni and γ'-Ni_3Al phases.

Alloying elements are added to serve the purpose of either benefitting oxidation and corrosion resistance or improving mechanical properties. Mechanical properties are impacted by the fraction of γ' precipitates that are able to form in the γ matrix and maintain throughout operation. Ti, Ta, and Nb may be added to strengthen the γ' phase [19]. Elements that aid in strengthening the γ phase are Cr, Mo, W, and Re. The main role of Co in the nickel-based superalloy is to decrease the solubility of elements in the γ phase, resulting in an increased volume fraction of the strengthening γ' phase [22]. In addition, at lower temperatures cobalt provides increased creep strength [1]. Al and Cr in the alloy also provide oxidation resistance. Figure 2-2 shows an overview of the role of alloying elements in a nickel-based superalloy. The elements marked by horizontal lines may be detrimental; minor amounts can segregate to grain boundaries impacting mechanical properties [23]. The elements marked by cross-hatched lines are minor and may be beneficial or detrimental, depending on the amount present. The height of a given element is proportional to the amount added in a nickel-based superalloy [23]. The exact composition of a given alloy will be dependent on the properties required, which are often dictated by the stress the component will endure during engine operation.

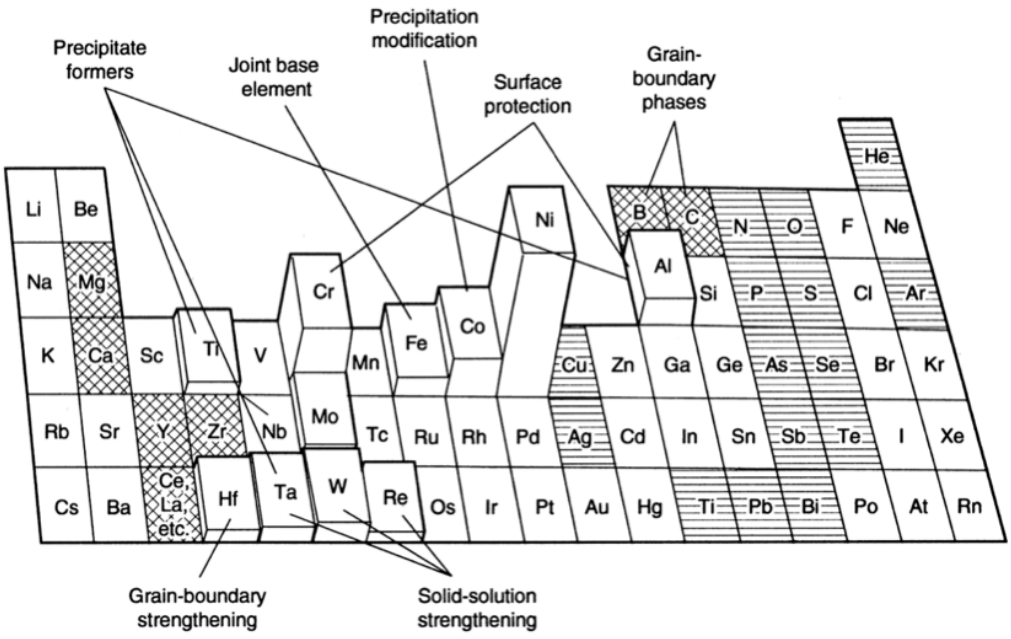

Figure 2-2. Elements included in nickel-based superalloys. Horizontal lined are unfavorable elements, and cross-hatched lines are minor alloying elements [23].

In this PhD thesis, a single-crystal nickel-based superalloy (PWA 1484), used to produce turbine blades, and a polycrystalline nickel-based superalloy (ME 16/ Rene 104/ ME 3), used as a disk alloy, will be studied. The purpose of a turbine disk is to secure the turbine blades [20]. This role imposes higher stresses than those experienced by turbine blades, but at lower temperatures of up to 800°C [20, 24]. The processing of ME 16 is via powder metallurgy, which results in reduced elemental segregation and finer grain size [20]. The control of grain size and phase distribution results in a material with high yield strength, fracture toughness, and fatigue life [20]. Figure 2-3 a) shows a schematic of the microstructure of a disk alloy [23], and b) shows a cross-sectional SEM image of ME 16 indicating the grain size. In comparison to Figure 2-1, showing the microstructure of PWA 1484, the disk alloy structure is less uniform in γ' size and distribution.

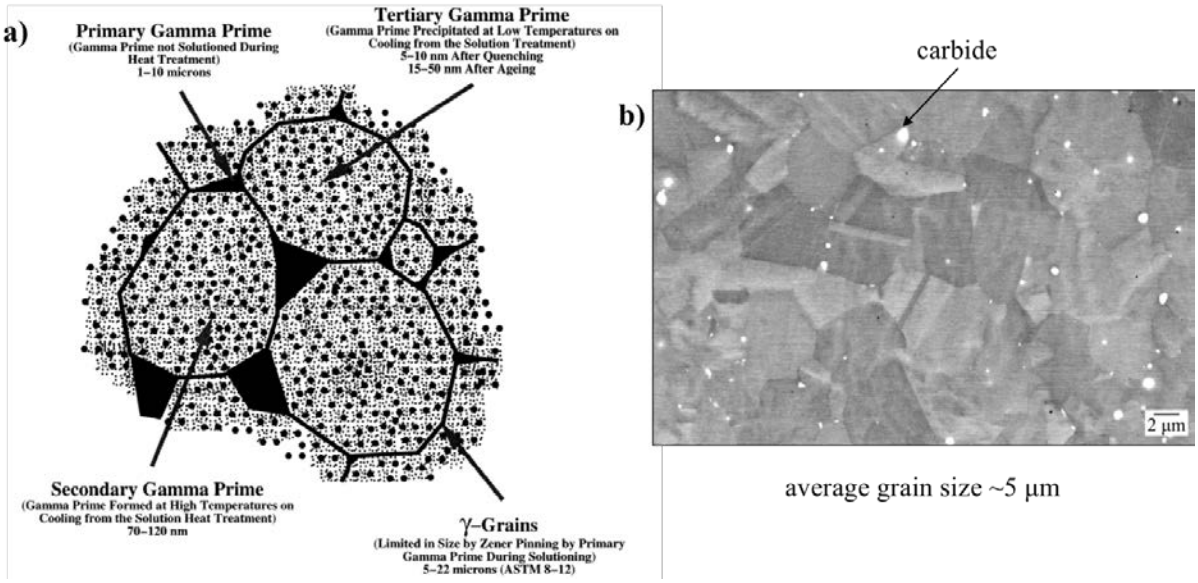

Figure 2-3. a) Disk alloy microstructure schematic [25], and b) cross-sectional SEM image of ME 16 indicating grain size.

The purpose of turbine blades is to extract work from the combustor portion of the turbine engine, and this work provides mechanical energy [20]. Turbine blades must exhibit good creep resistance as well as high-temperature properties, since blades are subjected to temperatures that may exceed 900°C [1, 26]. The property requirements led to advanced processing techniques. Currently, turbine blades are produced using investment casting, which allows for single-crystal production and intricate cooling channels in the internals of turbine blades [1]. Throughout a flight cycle, the turbine blades will experience a range of temperatures. Figure 2-4 shows a graph that illustrates the temperature changes during a cycle, where TET stands for “turbine entry temperature” (i.e., the temperature of the gas exiting the combustor). Component temperature is an important variable that will impact the occurrence of hot corrosion, as will be discussed in following sections. Protection against the environment at high temperatures will rely on the

formation of a stable, slow-growing oxide [20]. An overview of the oxidation of nickel-based superalloys will be provided in the next section.

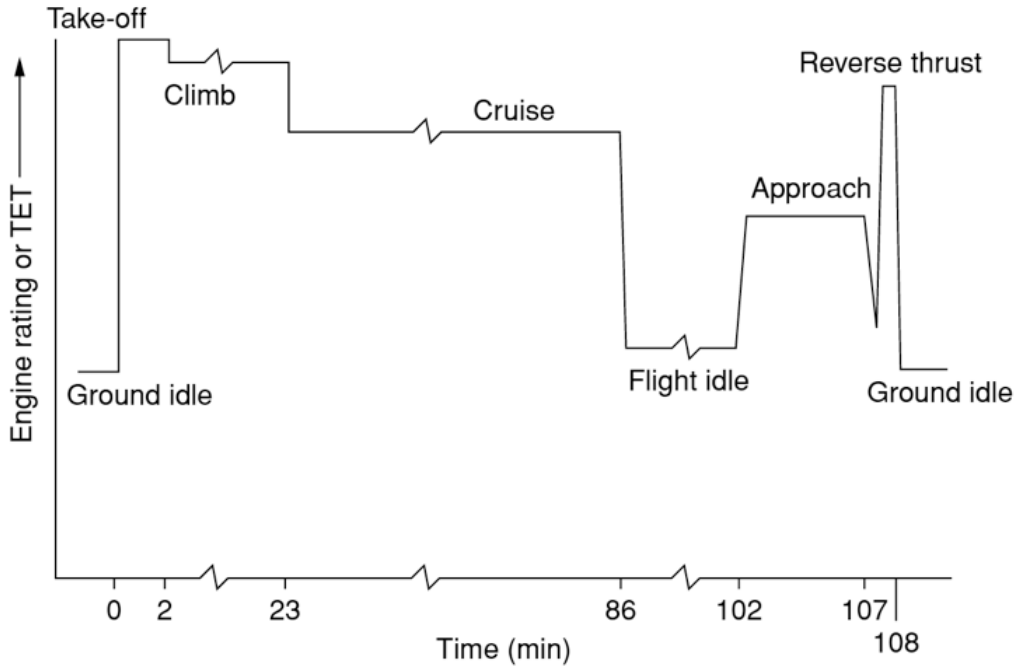

Figure 2-4. Turbine entry temperature (TET) vs. time schematic for a flight cycle [20].

2.2 Oxidation of Nickel-based Superalloys

Nickel-based superalloys rely on a stable, slow-growing oxide scale for protection during engine operation. Al_2O_3, Cr_2O_3, and SiO_2 are all potential oxides that can provide protection; however, SiO_2 and Cr_2O_3 have limitations to their use due to the formation of gaseous hydrides in the presence of steam. Moreover, increasing silicon content would decrease the melting point of the superalloy [27]. Further, Cr_2O_3 oxidizes to form gaseous CrO_3 at high temperature (above ~1000°C) and high oxygen partial pressure [4]. Therefore, nickel-based superalloys should ideally

rely on Al_2O_3-scale formation. Even so, there are coatings used at lower temperatures that are designed to form a chromia scale. Such coatings will be discussed in the context of protection against hot corrosion.

Starting with the basics of oxidation, at the initial stage, kinetics control oxide formation. Elements with faster growth kinetics (eg. Ni, Co) form transient oxides on the alloy that can predominate [4]. Growth kinetics are measured using a rate constant, k_p, generally reported in units of cm^2/sec or g^2/cm^4*sec [4]. The parabolic rate constant corresponds to the growth of the oxide under diffusion-controlled conditions. The equation relating scale thickness, rate constant, and time is shown in Eq. 2-1.

$$x^2 = k_p t \qquad (2-1)$$

Figure 2-5 shows the rate constant of various oxides. The important aspect of this figure is that Al_2O_3 is slow growing and the base metal oxide (NiO) grows about three orders in magnitude faster.

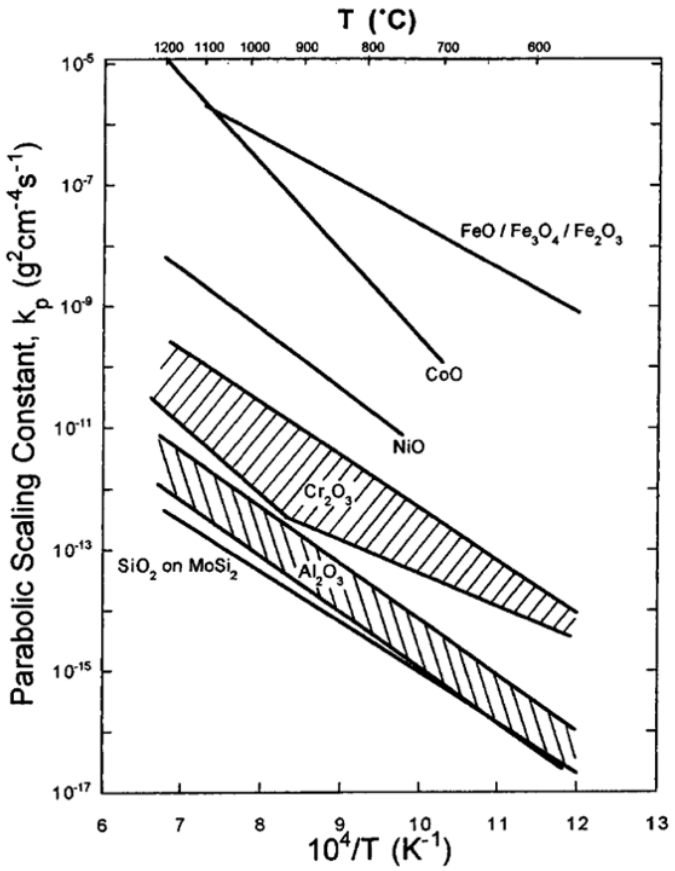

Figure 2-5. Parabolic rate constants of select oxides [28].

In the initial stages of superalloy oxidation, slower-growing oxides form as well, but due to kinetics are not able to quickly establish a continuous scale. Spinels may form in the oxidation process as a result of reaction between oxides growing alongside each other [4]. An example of a reaction to form a spinel is $NiO + Cr_2O_3 = NiCr_2O_4$. Eventually, slower-growing oxides with high stability form a continuous scale, resulting in steady-state oxidation behavior. Thermodynamics ultimately dictate the assemblage of oxides; more stable oxides exist closet to the alloy interface. The stability of an oxide is determined by the free energy of formation ($\Delta G°$), where a more negative value corresponds to higher stability [29]. Ellingham diagrams display $\Delta G°$ value for

specific oxides as a function of temperature. The Ellingham diagram in Fig. 2-6 shows that Al_2O_3 and Cr_2O_3 are very stable (i.e., relatively large and negative $\Delta G°$ at a given temperature). This means the dissociation pressures (minimum P_{O_2} to stabilize oxide formation) for these oxides are very low. Once a scale is established only oxides with a lower $\Delta G°$ can form below that scale.

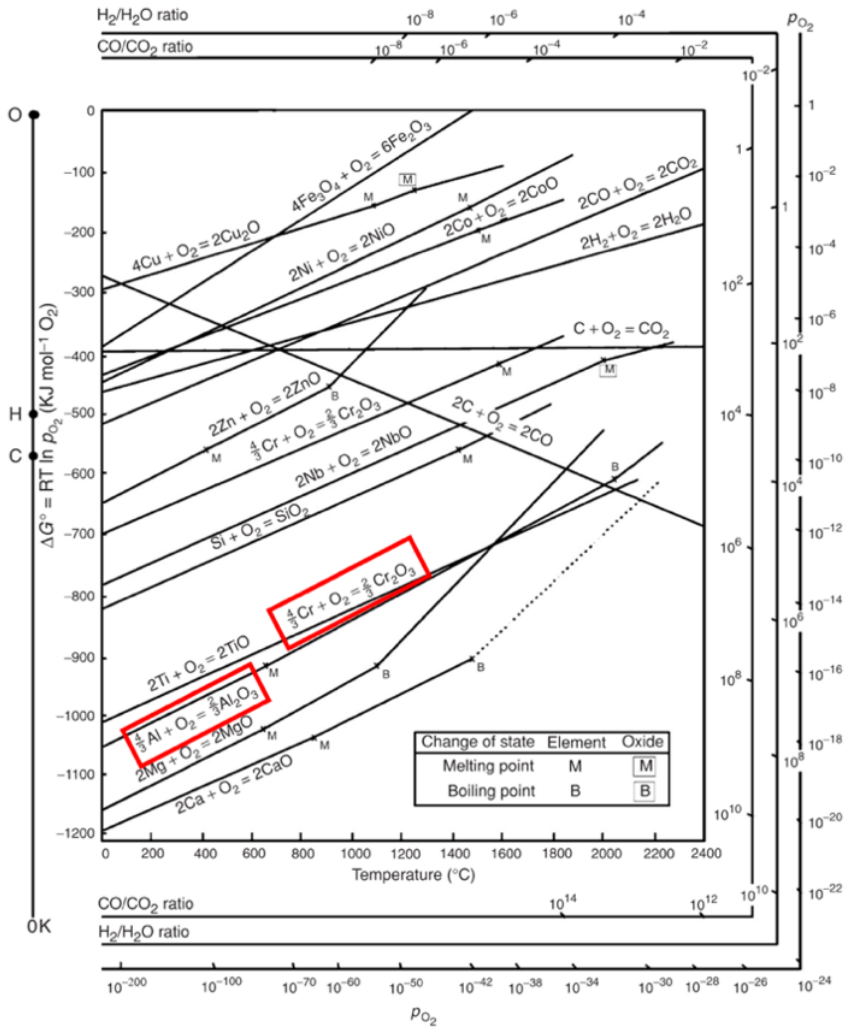

Figure 2-6. Ellingham diagram highlighting Al_2O_3 and Cr_2O_3 [4].

Oxide stability along with slow growth are important for protection of the alloy against the environment, however, in order for a continuous external scale to form two conditions must be met. Specifically, there must be a sufficient amount of the element to (1) form a continuous scale and to (2) maintain the growth of that scale [4]. Equations 2-2 and 2-3 stem from simplified models to determine if these conditions are met; specifically Eq. 2-2 calculates the amount of solute, B, to form the scale ($N_B^{(o)}(t)$), and Eqn. 2-3 determines the amount needed to maintain the scale ($N_B^{(o)}(s)$) [4, 30, 31]. In these equations, $N_B^{(o)}$is the concentration of solute B in the alloy, g^* is the critical volume fraction of internal oxide, $N_o^{(s)}$ is the oxygen solubility in the base metal, which, in turn, is dependent on P_{O_2}, D_o is the diffusivity of oxygen in the base metal, V_m is the molar volume of the alloy, D_B is the diffusivity of solute B in the alloy, V_{ox} is the molar volume of the oxide, ν is stoichiometric factor for the oxide AO_y, and k_p is the rate constant of the oxide [4].

$$N_B^{(o)}(t) > \left[\frac{\pi g^*}{2\nu} N_o^{(s)} \frac{D_o V_m}{D_B V_{ox}}\right]^{\frac{1}{2}} \qquad (2-2)$$

$$N_B^{(o)}(s) = \frac{V_m}{32\nu}\left(\frac{\pi k_p}{D_B}\right)^{\frac{1}{2}} \qquad (2-3)$$

Depending on the environment during oxidation, the terms in Eq. 2-2 and 2-3 will change. For example, SO_2 in the environment will serve to decrease the availability of oxygen at the surface for reaction, which will result in a decreased concentration of solute needed to form a continuous scale [32]. When water vapor is in the environment, the critical volume fraction of oxide is increased, which has the effect of increasing the concentration of solute needed for scale formation

[33]. Both these species are present in engine operation, and in turn will impact the oxide formation.

There are four allotropes of Al_2O_3 that can form: θ-Al_2O_3, γ-Al_2O_3, δ-Al_2O_3, and α-Al_2O_3 [34]. α-Al_2O_3 is the most stable structure that forms a slow growing and protective scale. During oxidation, the less stable γ-Al_2O_3, δ-Al_2O_3 and/or θ-Al_2O_3 may initially form, but over time will transform to α-Al_2O_3. It would be more beneficial to avoid metastable alumina formation altogether and to decrease the time to form a continuous α-Al_2O_3 scale. The addition of chromium aides in the establishment of an α-Al_2O_3 scale, since Cr_2O_3 is isostructural with α-Al_2O_3 (i.e., hexagonal) [34]. However, the mechanism by which Cr promotes Al_2O_3-scale establishment is still not fully resolved. One mechanism is that Cr acts as an oxygen getter; Cr_2O_3 formation restricts oxygen solubility and allows for only oxides of higher stability to form below the Cr_2O_3 scale [35].

As indicated above, the addition of chromium significantly reduces the concentration of aluminum needed to sustain external alumina scale formation. Figure 2-7 a) shows Al_2O_3-scale formation for the Ni-Al system, with the percent of aluminum in PWA 1484 and ME 16 plotted on the diagram. It is seen that plotting just the Al concentration, both alloys are unable to establish an external Al_2O_3 scale. Figure 2-7 b) is an oxide map for the Ni-Al-Cr system, at 1000°C, with the composition for PWA 1484 and ME 16 plotted, showing that with the chromium addition these alloys now lie in the external alumina scale formation region. Note the composition of the alloys were plotted by taking the absolute value of Ni, Al, and/or Cr. Other elements in the alloy will impact the exact location on the diagram.

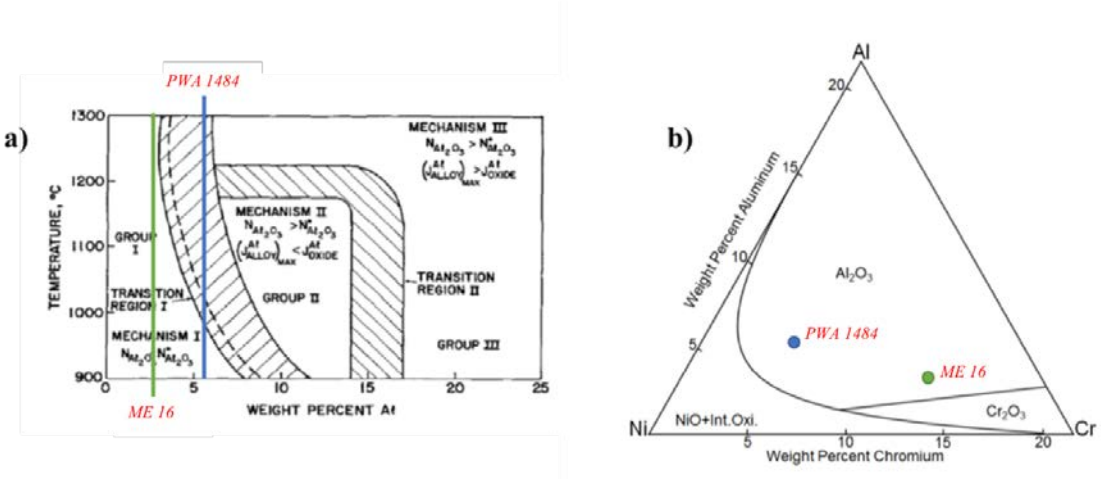

Figure 2-7. a) Alumina formation, with PWA 1484 and ME 16 compositions plotted [36], and **b)** oxide map showing change in alumina formation with chromium addition [37].

While Fig. 2-7 b) shows PWA 1484 and ME 16 in the alumina-scale-formation region at 1000°C, as temperature decreases, the establishment of an alumina scale is more difficult at the same concentration level due to kinetic displacement of the very slow-growing Al_2O_3 by faster growing base-metal oxides. Figure 2-8 shows the oxide formed on PWA 1484 at 700°C in dry air is no longer a continuous alumina scale. Rather, the scale consists of areas of spinel formation and areas of (Ni, Co) O above an Al-rich mixed oxide. Thus, the oxidation product shown in Figure 2-8 is not protective to the alloy, especially in the presence of a sulfate deposit. As will be discussed in Section 2.4, there are coating methods to protect the alloy at temperatures where continuous scale formation is not possible at the current composition.

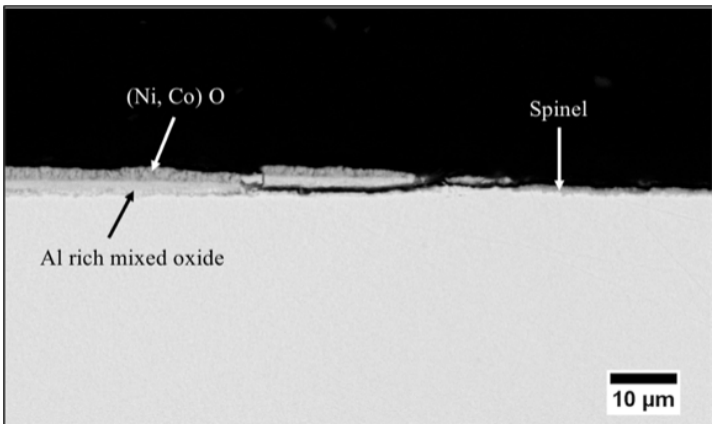

Figure 2-8. PWA 1484 oxide formation, 700°C for 100 hours in dry air.

The purpose of providing background for oxide-scale formation is to understand that nickel-based superalloys rely on the establishment of a continuous, stable oxide to provide a protective barrier between the alloy and the environment. When an alumina scale is unable to establish or is broken down, the oxide products that may form (NiO, CoO) have more rapid growth and are not good diffusion barriers, which leads to further component degradation. As will be discussed in the next section, these oxides are especially susceptible to reaction with sulfate compounds. Understanding the mechanism of hot corrosion at all temperatures will help to develop methods to protect the component against attack, such as increasing the chromium or aluminum content to aid in establishing and maintaining a protective scale.

2.3 Hot Corrosion

Hot corrosion is an accelerated form of attack due to the presence of a sulfate-containing deposit [4]. Hot corrosion has similarities to aqueous corrosion, since both involve electrochemical reactions and hot corrosion is believed to involve a liquid [38]. As mentioned in the Introduction, there are two forms of hot corrosion: Type II (below T_m of Na_2SO_4) and Type I (above T_m of Na_2SO_4). Figure 2-9 shows a schematic of corrosion rate vs. temperature where two different maximum exist in the Type II and Type I regions. When the temperature exceeds the dew point of the salt, accelerated oxidation takes over. The origin of representing corrosion rate vs. temperature with two maxima is believed to be industry discussion, with M. Gell from Pratt & Whitney initially cited [39]. The alloy system and environmental conditions used to generate the graph are unknown. Regardless, this graph has become the accepted way to illustrate the temperature dependence of hot corrosion.

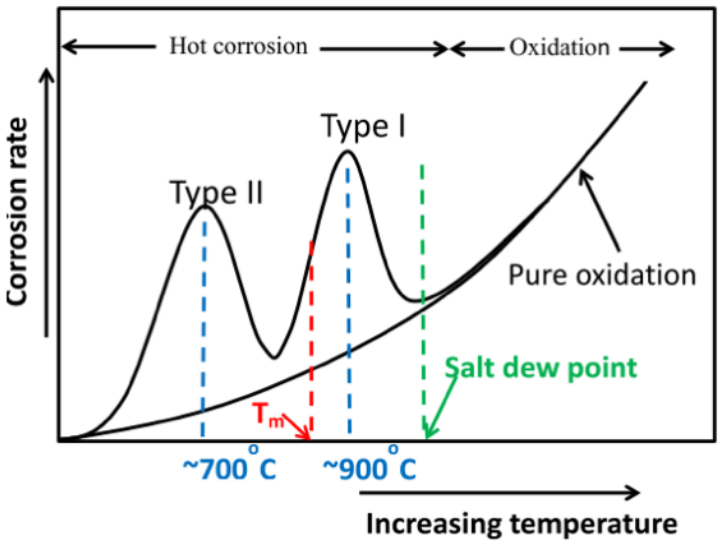

Figure 2-9. Hot corrosion schematic: corrosion rate vs. temperature.

Current understanding of the mechanism of each form of hot corrosion will be detailed in the following sections. Sulfate compounds are formed through constituents in the air and fuel and condense onto components, or are introduced through the environment since sulfates are in sea salt [3, 40]. Bornstein et al. [3] studied deposits removed from internal and external surfaces of land-based turbine blades. The inferred constituents of the sulfate deposits are given in Table 2-1, which shows four different sulfates are present. A eutectic exists between the four sulfates at a temperature of 695-698°C, which can initiate more rapid hot corrosion than a pure Na_2SO_4 deposit [15].

Table 2-1. Salt composition removed from turbine blade surfaces [3].

Airfoil Surface	Salt Constituent	First Stage Deposit Chemistry (mole%)	Second Stage Deposit Chemistry (mole%)
External (gas path)			
	Na_2SO_4	40	28
	K_2SO_4	4	3
	$CaSO_4$	40	59
	$MgSO_4$	13	8
Internal (cooling passages)			
	Na_2SO_4	45	37
	K_2SO_4	3.2	4.4
	$CaSO_4$	41	46
	$MgSO_4$	9.5	11.5

In some cases, deposits may also contain chloride or vanadium compounds. Chloride presence, in the form of NaCl, can form a low-melting eutectic with Na_2SO_4 further accelerating corrosion [41]. In addition, chloride can cause volatile compounds to form, which results in porous oxide formation, exposing the base alloy to the environment [4]. Vanadium is present in certain

fuels as an impurity. Vanadium oxide is acidic with a low melting point (T_m = 691°C), which can destroy the protective oxide(s) present [4]. In all deposit cases, the hot corrosion that results is detrimental and understanding the mechanism is vital to designing mitigation methods.

In both Type II and Type I hot corrosion, the mechanism involves an initiation and propagation stage. In the initiation stage, the deposit present is changing chemistry toward conditions that will cause rapid attack of the alloy, while the alloy itself is oxidizing, at least in the very early stages [4]. In the initiation stage, there is some interaction with the deposit and the alloy/oxide, such as elements in the alloy entering the deposit or sulfur from the deposit entering the alloy [4]. Considering an Na_2SO_4 deposit, there is an equilibrium between the basic (Na_2O) and acidic (SO_3) components, as shown in Eq. 2-4 [42].

$$Na_2SO_4 = Na_2O + SO_3 \qquad (2-4)$$

Interaction of the deposit with the alloy/oxide will shift the composition toward more basic (increase in Na_2O) or acidic (increase in SO_3) conditions, as shown in Fig. 2-10. The duration of the initiation period will depend on several factors, including: alloy composition; amount of deposit; gas composition; and temperature. Propagation follows the initiation period and is characterized by rapid degradation of the alloy [4]. The mechanism of hot corrosion is dependent on temperature, alloy composition, and the environment, as will be discussed in the following Type II and Type I hot corrosion sections.

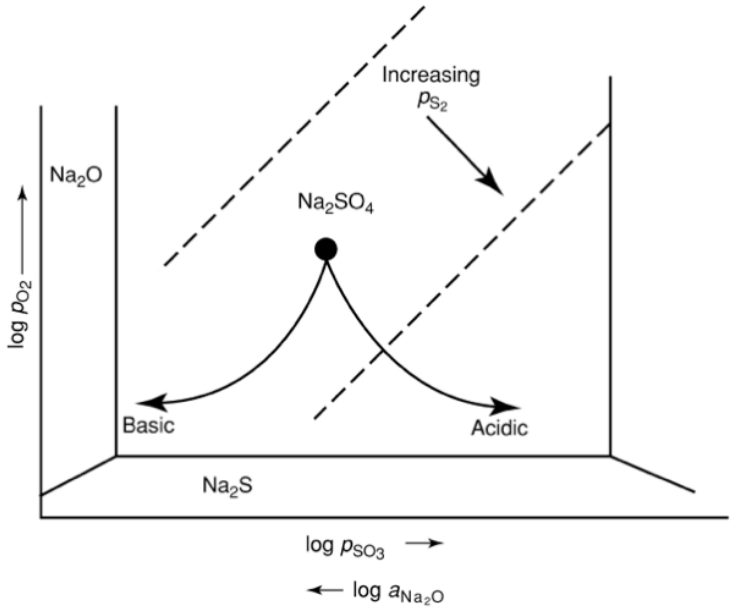

Figure 2-10. Na-O-S stability diagram illustrating deposit chemistry changes toward acidic or basic conditions [4].

Fluxing of species due to a negative solubility gradient is common to both Type II and Type I hot corrosion mechanisms. The solubility of NiO and Co_3O_4 [42, 43], Fe_2O_3 [45], CeO_2 [46], Cr_2O_3 [47], Al_2O_3 [48], and SiO_2 [49] in Na_2SO_4 as a function of the basicity of the melt was experimentally determined. Rapp summarized the results, shown in Fig. 2-11 a). The shape of the curves is due to the reaction process being predominately basic (negative slope) or acidic (positive slope) [50]. Common reactions for each process will be shown in the next section. Typical hot corrosion reaction products show oxide precipitation as discontinuous particles at the sulfate/gas interface. Determination of the solubility plots led to deductions on how hot corrosion proceeds under Type I conditions. Rapp and Goto proposed a mechanism that relies on a negative solubility gradient, known as the Rapp-Goto criterion [51]. As shown in Fig. 2-11 b), oxide dissolution will occur at the oxide/sulfate interface. If the solubility gradient is negative, at the deposit/gas

interface, where oxide solubility is decreased, precipitation of the oxide will occur [52]. If the reverse occurred (a positive solubility gradient), the deposit would become saturated with oxide at the oxide/sulfate interface until the solubility limit is reached, upon which no further reaction occurs [52]. In a following section, specific examples of this aspect of the mechanism of hot corrosion will be discussed in the context of both Type II and Type I cases.

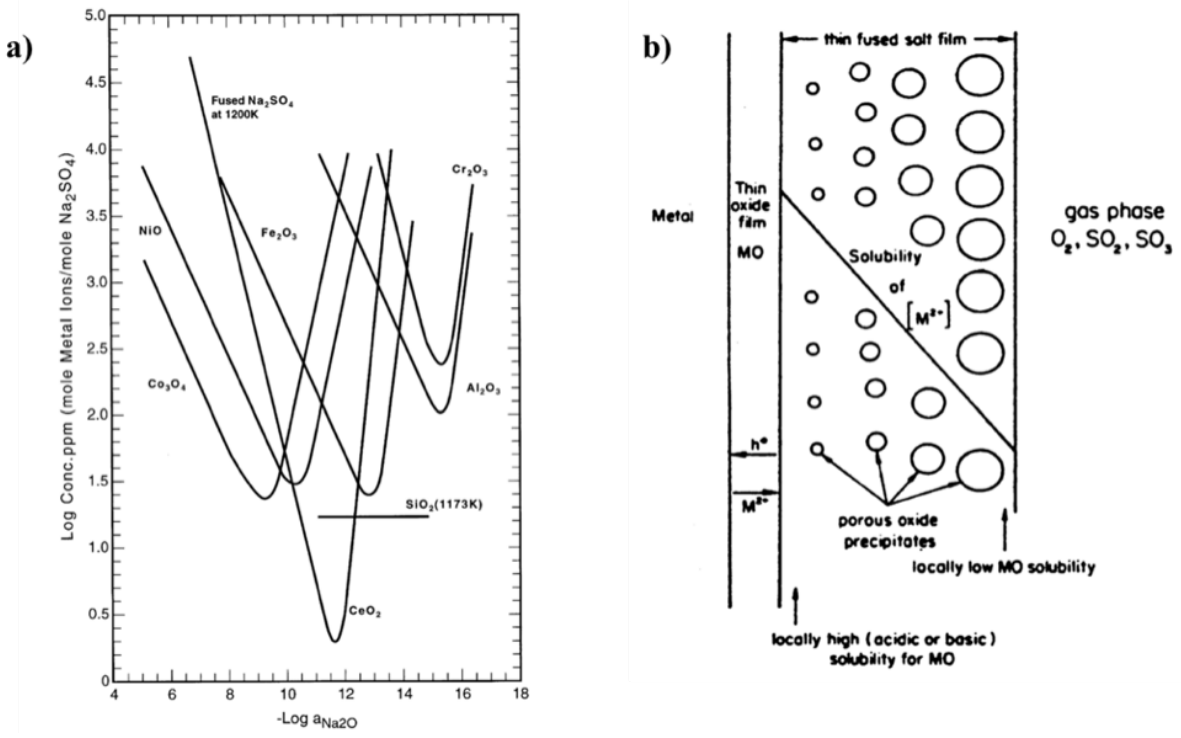

Figure 2-11. a) Oxide solubility as a function of deposit basicity [50], and b) schematic illustrating dissolution and precipitation of the oxide through the deposit [52].

2.3.1 Environmental Factors Affecting Hot Corrosion

As was discussed in the previous section, when deposits form on components, hot corrosion can occur, and the sulfate species present in the deposit are a mix of Na_2SO_4. K_2SO_4, $MgSO_4$, and $CaSO_4$ [53]. The ratio of species and the amount of deposit has a regional dependence [15]. While the research in this thesis focuses solely on sodium sulfate deposits, it is still important to recognize that deposit composition and concentration are variables encountered in engine application.

Another variable to consider is the SO_2 content in the environment. Sources of SO_2 include: volcanoes; power plants; smelters; and emission from the oil and gas industry [54]. As will be discussed in the following sections, both types of hot corrosion are affected by the presence of SO_2. Table 2-2 shows the variation in deposit composition, concentration, and SO_2 content in three regions [15]. Taking into account the pressure in an engine (~30 atm), the SO_2 content components will be exposed to ranges from 0.06 ppm in LA to 1.65 ppm in Beijing. The content of SO_2 also has a seasonal dependence and is constantly changing, so the values listed Table 2-2 may now differ. For instance, due to regulations on emissions in the United States, SO_2 content declined 91% from 1980 to 2018 [55]. The current maximum level translates to ~1 ppm SO_2 in an engine environment. In China, the SO_2 content has also been consistently declining, albeit from a relatively high value [56]. However, in India the opposite trend holds. The installation of the largest coal-fired power plant resulted in a 50% increase in SO_2 content since 2007 [56]. The large variation globally of SO_2 needs to be considered when addressing hot corrosion issues because as mentioned previously, SO_2 content in the atmosphere directly impacts the extent of attack. Indeed, it is important to understand variation in realistic environments. As will be discussed in the

following sections, previous literature has focused on high SO_2 contents (~1000 ppm and above) that are no longer representative of engine environments.

Table 2-2. SO_2 Content and Deposit Composition in Los Angeles, Beijing, and Delhi [15].

		Los Angeles	Beijing	Delhi
SO_2, ppm		0.002	0.055	0.007
Sulfate Salts	Concentration, μ mol./m^3	0.006-0.02	0.12-0.41	0.38-0.64
	Na_2SO_4, mol.%	48-52%	12-21%	32-56%
	K_2SO_4, mol.%	7-11%	9-28%	10-16%
	$MgSO_4$, mol.%	17%	10-12%	10-17%
	$CaSO_4$, mol.%	24%	41-67%	18-42%

2.3.2 Low Temperature (Type II) Hot Corrosion

Type II hot corrosion refers to deposit-induced attack occurring below the melting point of Na_2SO_4. As mentioned previously, it is generally believed that liquid formation is required for hot corrosion to occur. Liquid formation occurs through the formation of low-melting eutectics of nickel or cobalt sulfate with sodium sulfate, or in the case of high molybdenum or tungsten alloys a low melting compound can form [57]. Table 2-3 lists relevant invariant temperatures together with the melting point of pure Na_2SO_4. Typical reported microstructures of Type II hot corrosion

have no depletion region and a sulfur-enriched region at the alloy/scale interface but no distinct sulfide phase in the base metal, but there are exceptions to this [6, 57].

Table 2-3. Melting points of important compounds in hot corrosion.

	Melting Point (℃)
Na_2SO_4	884
Na_2SO_4 – 38% $NiSO_4$	671
Na_2SO_4 – 50% $CoSO_4$	565
Na_2MoO_4	687
Na_2WoO_4	689

The mechanism of Type II hot corrosion attack is believed to be either gas-phase induced acidic fluxing or alloy-induced acidic fluxing [4]. Acidic fluxing refers to oxides dissolving in the deposit by donating an oxide ion, as shown in Eqn. 2-5 for nickel. Eqn. 2-6 shows an equivalent way of writing the reaction. Additional equivalent reactions can be found in refence [4].

$$NiO + Na_2SO_4 = NiSO_4 + Na_2O \qquad (2-5)$$

$$NiO = Ni^{2+} + O^{2-} \qquad (2-6)$$

Alloy-induced acidic fluxing refers to elements in the alloy (Mo, W, or V), which form acidic oxides, shifting the chemistry of the deposit to allow for acidic fluxing to occur [4]. This latter mechanism is active in the Type I region, where the deposit is already liquid, but was found to also

occur in Type II conditions in the case of molybdenum-containing alloys [56, 58]. Liquid formation was reported to be due to Na_2MoO_4 formation, which melts at 687°C. The relevant reaction is shown in Eq. 2-7, where transient MoO_3 reacts with the deposit, creating the liquid compound and releasing SO_3 [59]. The result is an acidic liquid deposit of Na_2SO_4-Na_2MoO_4-MoO_3.

$$MoO_3(s) + Na_2SO_4(s) = Na_2MoO_4(l) + SO_3(g) \qquad (2-7)$$

The acidic deposit is able to dissolve oxides that form on the alloy. Precipitation occurs at the sulfate/gas interface due to the evaporation of MoO_3, which decreases the acidity of the melt, satisfying the negative solubility gradient criteria. With increased Mo content, the effect is more pronounced [59]. Figure 2-12 shows typical microstructures of alloy-induced acidic fluxing showing the effect of increasing Mo content [59]. In Type I conditions, alloy-induced acidic fluxing was shown to also occur with W [60]. It is reasonable to suggest a similar reaction as Eq. 2-7 can be written for W. In contrast to gas-phase induced acidic fluxing, which will be discussed next, alloy-induced acidic fluxing can occur in oxidizing environments without SO_2.

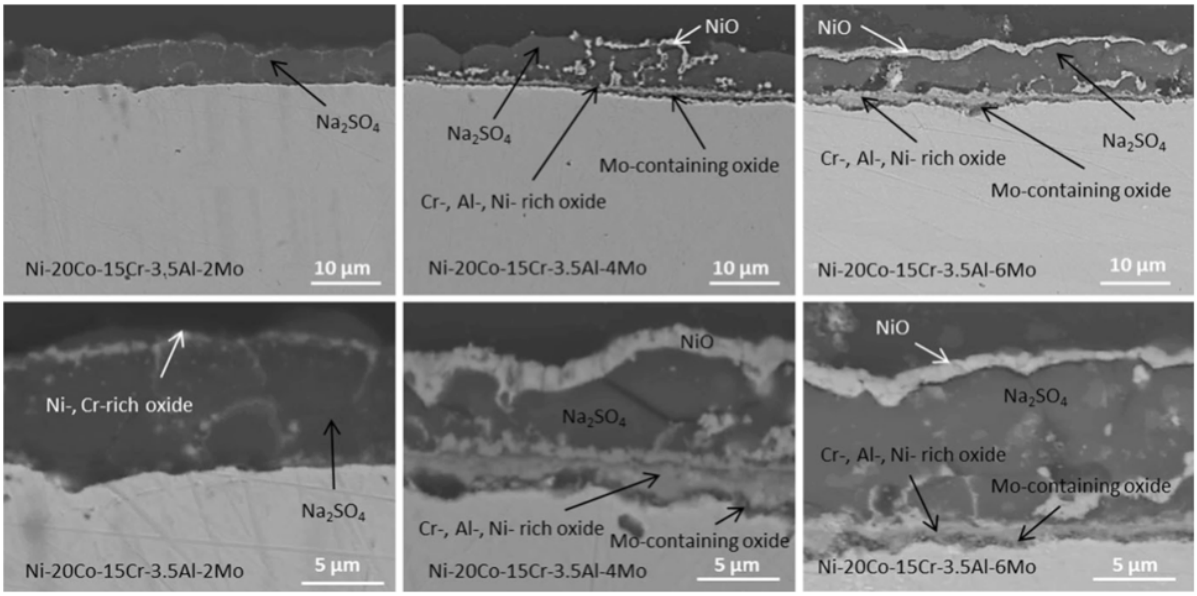

Figure 2-12. Cross-sectional SEM images showing the effect of increasing Mo content: 700°C, dry air, 100 h exposures with an Na_2SO_4 deposit [59].

Gas-phase induced acidic fluxing refers to the gas, specifically the SO_3 in the atmosphere, creating the acidic environment. SO_3 is formed from the reaction in Eq. 2-8. The SO_3 in the equation is a constituent in the atmosphere as well as an impurity in the fuel [15]. The SO_3 is essential for Type II hot corrosion via gas-phase induced acidic fluxing in stabilizing liquid formation. For both nickel and cobalt, there is a pressure of SO_3 needed for liquid formation, as shown in Fig. 2-13 for both the $CoSO_4$-Na_2SO_4 and $NiSO_4$-Na_2SO_4 systems. Note, the $NiSO_4$-Na_2SO_4 requires significantly higher SO_3 pressure for melt formation than the $CoSO_4$-Na_2SO_4.

$$SO_2 + \frac{1}{2}O_2 = SO_3 \qquad (2-8)$$

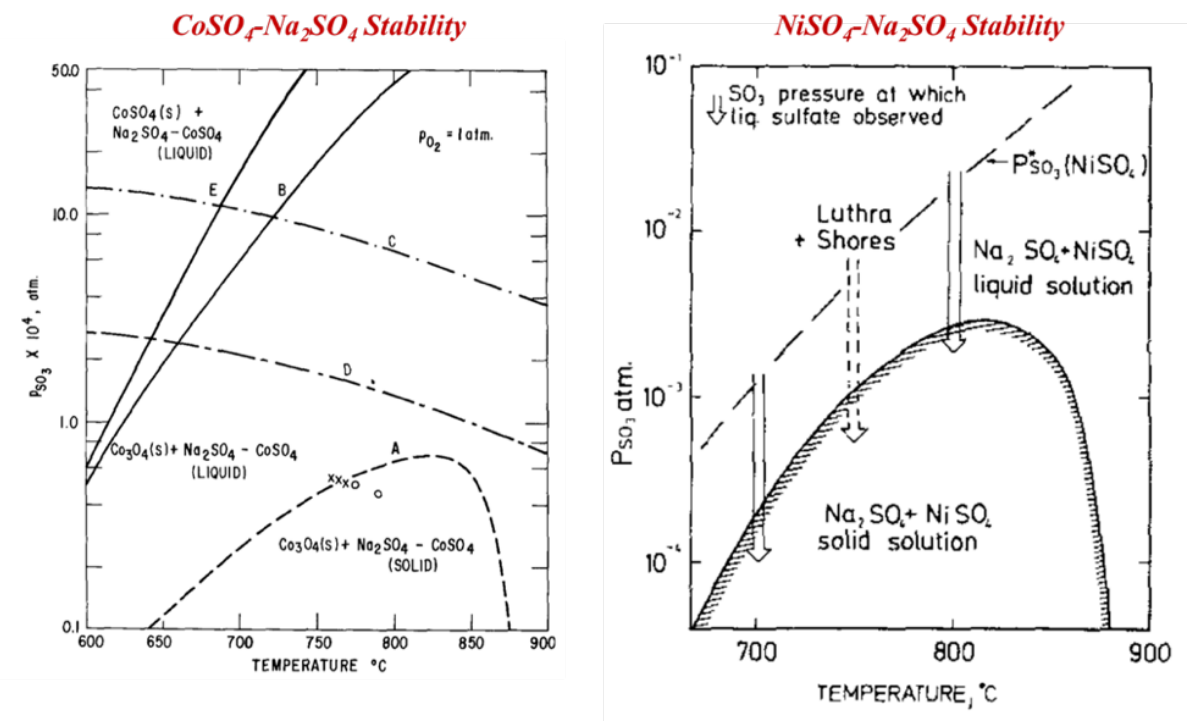

Figure 2-13. $CoSO_4$-Na_2SO_4 and $NiSO_4$-Na_2SO_4 stability diagrams [14, 61].

In the initiation stage of gas-phase induced acidic fluxing, the sulfates of cobalt and/or nickel begin to form by sulfidation of the oxide according to Eqn. 2-9, 2-10, and 2-11 below, where the underline indicates the sulfate forms in solution with Na_2SO_4 at an activity less than one [11]. The solid or liquid after the sulfates refers to the sulfate initially forming in the solid state; each sulfate has solubility in Na_2SO_4, as shown by the phase diagrams in Fig. 2-14. Once the activity of the $NiSO_4$ or $CoSO_4$ reaches a certain value, the liquid phase forms. Once the liquid phase forms, the propagation stage begins, where the oxides continuously dissolve as M^{x+} ions followed by precipitation at the sulfate/gas interface.

$$NiO\ (s) + SO_3\ (g) = \underline{NiSO_4\ (s,l)} \qquad (2-9)$$

$$CoO\ (s) + SO_3\ (g) = \underline{CoSO_4\ (s,l)} \qquad (2-10)$$

$$\frac{1}{3}Co_3O_4\ (s) + SO_3\ (g) = \underline{CoSO_4\ (s,l)} + \frac{1}{6}O_2\ (g) \qquad (2-11)$$

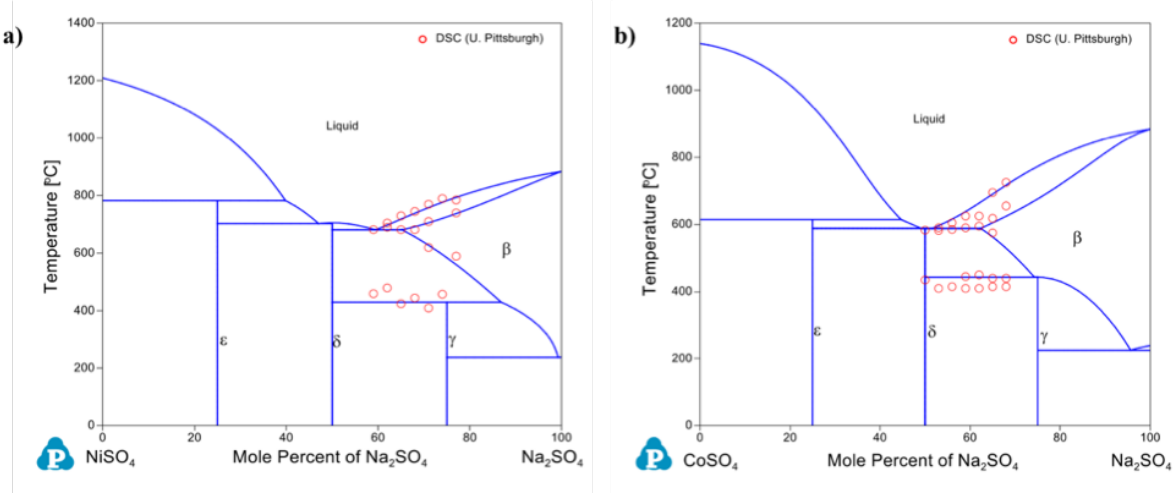

Figure 2-14. a) $NiSO_4$-Na_2SO_4 phase diagram, and b) $CoSO_4$-Na_2SO_4 phase diagram.

Before liquid formation, the solid sulfate deposit consists of grains, so the gas phase has the ability to contact the alloy. After the liquid forms or the deposit sinters, there is a barrier to the alloy, so the species in the gas (SO_3, O_2, SO_2) will dissociate and diffuse to the alloy surface. Luthra conducted calculations on the transport of possible ionic species through Na_2SO_4 ($S_2O_7^{2-}$, SO_3^{2-}, and O^{2-}) to determine which predominates in the reactions [14]. He found the ionic and gaseous forms of O_2 and SO_2 have very low solubility in the deposit, so are unlikely to play a role in the reaction. SO_3 in the ionic form $S_2O_7^{2-}$ is stable in the liquid deposit, and the flux of this ion

is able to explain the corrosion rates. Therefore, $S_2O_7^{2-}$ is the main ionic species, and diffuses by an exchange mechanism with SO_4^{2-}. Shores and Fang [62] and Rapp and Fang [63] completed electrochemical measurements that confirm the main oxidizing species as well as the exchange mechanism.

Nickel and cobalt oxides are often found at the sulfate/gas interface in Type II hot corrosion. As mentioned previously, there is a negative solubility gradient criterion to allow for dissolution followed by precipitation at the sulfate/gas interface. In the case of acidic environments, the P_{SO_3} is greater at the sulfate/gas interface than at the sulfate/alloy interface. This results in a positive solubility gradient, so according to the Rapp-Goto criterion discussed in the previous section, rapid attack should not occur. However, a few mechanisms were proposed for cobalt-based alloys to explain the Type II hot corrosion. Nickel-based alloys will be discussed later. After liquid formation, the first proposed mechanism relies on a Co^{2+}/Co^{3+} exchange reaction to account for cobalt diffusion through the melt followed by precipitation at the sulfate/gas interface [14]. Equation 2-12 shows the reaction used to explain the mechanism.

$$2CoSO_4(l) + SO_3 + \frac{1}{2}O_2 = Co_2(SO_4)_3(l) \qquad (2-12)$$

The Co^{2+}/Co^{3+} ratio will be higher at the scale/sulfate interface than at the sulfate/gas interface, so Co^{2+} ions diffuse through the melt to the sulfate/gas interface where, depending on the pressure of SO_2, Co_3O_4 or solid $CoSO_4$ (high p_{SO_2} case) is precipitated out. Figure 2-15 shows a schematic of the reaction sequences depending on SO_2 level. In both SO_2 cases there is a layer of sulfur enrichment at the oxide/alloy interface.

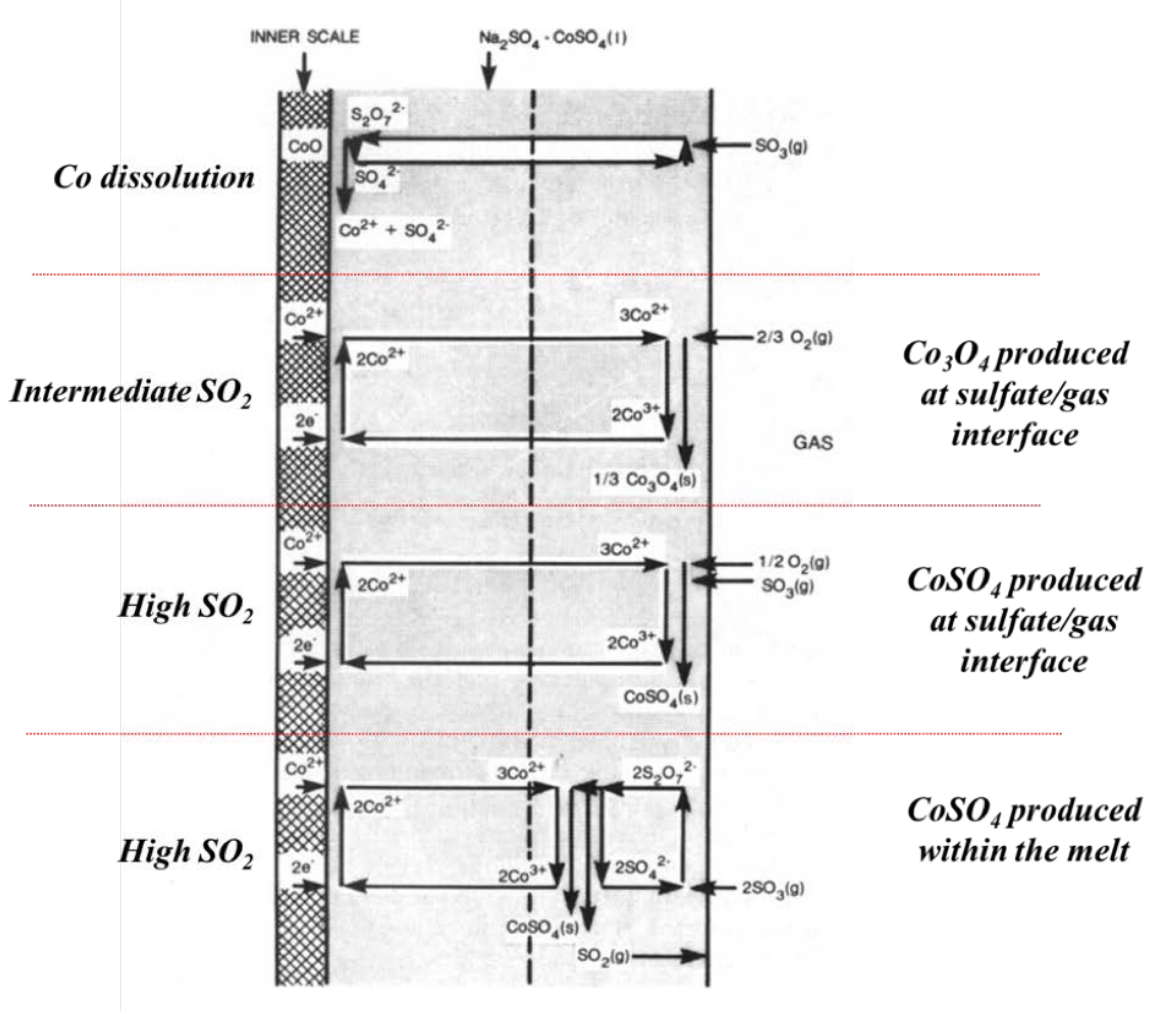

Figure 2-15. Cobalt Co^{2+}/Co^{3+} exchange reaction mechanism, showing initial $CoSO_4$ formation and reaction products in intermediate and high SO_2 environments [14].

Luthra proposed the Co^{2+}/Co^{3+} exchange mechanism completing experiments on Co-Cr, Co-Al, and Co-Cr-Al alloys using O_2-(30 ppm-10%) SO_2 [9], [14]. These SO_2 levels are all in liquid stable regions for Na_2SO_4-$CoSO_4$. Co-Cr and Co-Al alloys exhibited corrosion products with similar morphologies, the difference was in the severity of the attack; Co-Cr alloys had attack that was localized whereas Co-Al alloys had uniform attack. If the mechanism is correct, attack

should occur on pure Co. Luthra also studied pure cobalt samples pre-oxidized to form CoO, in a temperature range from 600-900°C in 0.02-2% SO_2 [64]. The reaction product was very similar to the alloy results. Therefore, the proposed mechanism was inferred to be validated. However, Chiang et al. [58] completed studies on pure cobalt samples with and without a deposit in pure O_2 and O_2-1000 ppm SO_2 and found conflicting results; no acceleration occurred with SO_2 and a deposit. These authors proposed a different mechanism that will be discussed in the following.

Chiang et al. [58] studied pure Ni, pure Co, Co-Cr, Co-Cr-Al, Ni-Cr, and Ni-Cr-Al alloys at 700 and 750°C in pure O_2, O_2-1000 ppm SO_2 and O_2-1% SO_2 environments. Based on results for pure Co, where SO_2 and a deposit did not accelerate corrosion, they postulated that Co dissolution and precipitation is not the cause of the accelerated attack. The morphology of the corrosion products they found contained pits rich in Cr/Al, O, and S at the base. In aluminum-containing alloys, the Al-rich β phase was preferentially attacked. Based on these findings, these authors proposed the accelerated attack, and the inability to form a protective oxide, was due to Al and Cr sulfidation. The formation of Cr_2O_3 and/or Al_2O_3 decreases the oxygen pressure, which locally results in increased sulfur pressure. This increased pressure locally causes sulfidation of the oxides which may form either sulfides in the alloy or sulfates, leading to acidic fluxing where the oxide precipitates at higher oxygen pressures above the deposit. The cobalt will also dissolve in the deposit and form an oxide at the sulfate/gas interface. In either mechanism, the initial stage relies on the pressure of SO_2 in the environment high enough to stabilize a liquid. To protect against hot corrosion, a protective oxide scale would need to establish. In the case of binary Co-Al and Co-Cr alloys, increasing Al or Cr would help establish a protective oxide, decreasing corrosion

[8]. The addition of a small amount of Al to the Co-Cr binary alloy results in accelerated attack; caused by hindering the ability of the alloy to form protective chromia and spinel.

Relating the two mechanisms above to Type II hot corrosion occurring on nickel-based alloys is challenging. Compared to the $CoSO_4$-Na_2SO_4 eutectic, the $NiSO_4$-Na_2SO_4 eutectic forms at a higher temperature and requires higher SO_3 pressure to stabilize a liquid [65]. There also is no stable Ni^{3+} compound, so the mechanism proposed by Luthra to explain the negative solubility gradient is not expected for nickel-based alloys [14]. As will be shown in the preliminary results, accelerated hot corrosion attack does occur on nickel-based alloys at temperatures below the eutectic, and in SO_2 atmospheres well below the required pressure for liquid stability. No current mechanism can explain the preliminary results. Despite those results, it is important to understand past knowledge on hot corrosion of nickel-based alloys.

Lillerud and Kofstad [61] studied the hot corrosion of pure nickel from 660-900°C in O_2+4% SO_2, with and without a Na_2SO_4 deposit. In the Type II regime, they found at 660°C, a temperature below the eutectic temperature, the sample without a deposit experienced more accelerated corrosion. The reverse was true for 700°C. Figure 2-16 shows the weight gain vs. time graphs for each temperature illustrating this finding. The corrosion occurring at 660°C was determined to be due to NiO + Ni_3S_2 scale formation. Diffusion through a sulfide is much faster than through an oxide [61], so due to the Ni_3S_2 formation, there is fast outward diffusion of nickel. When a deposit is applied, it can act as a diffusion barrier, since liquid formation is not stable at this temperature, and consequently lowers the reaction rate. At 700°C, liquid formation can occur. The reaction does not obey the negative solubility gradient criterion (Rapp-Goto criterion), and instead a different mechanism was proposed. The initial reaction is the formation of the $NiSO_4$-

Na_2SO_4 melt which initiates the attack. The reaction product consists of $(Ni\text{-}S)_{liquid}$ closest to the alloy, above this is a $NiO\text{-}Ni_3S_2$ mixed product, followed by an intermixed region of $NiO\text{-}(NiSO_4\text{-}Na_2SO_4)_{liquid}$ [61]. The sulfide formation, which allows for rapid nickel diffusion, is an important aspect in the mechanism proposed. The role of the melt is to maintain a sulfur activity below the deposit that is sufficient for sulfide formation. Nickel will diffuse outward and react with $SO_3/NiSO_4$ to produce NiO and Ni_3S_2. The high diffusivity through the sulfide phase leading to rapid corrosion rates is consistent with findings on pure nickel samples at 603°C in $SO_2\text{-}O_2\text{-}SO_3$ environments, which were high in SO_2 and/or SO_3 pressure [66]. The difference in reaction rate and scale thickness as temperature increases may be due to changes in the SO_2 pressure as well as transport rates [61]. After a certain time at 700°C, the reaction rate decreases significantly, as shown in Fig. 2-16 for the sample with a deposit, and the outer layer is composed of $NiO+NiSO_4$. There was no mention in the paper as to why the melt is no longer present.

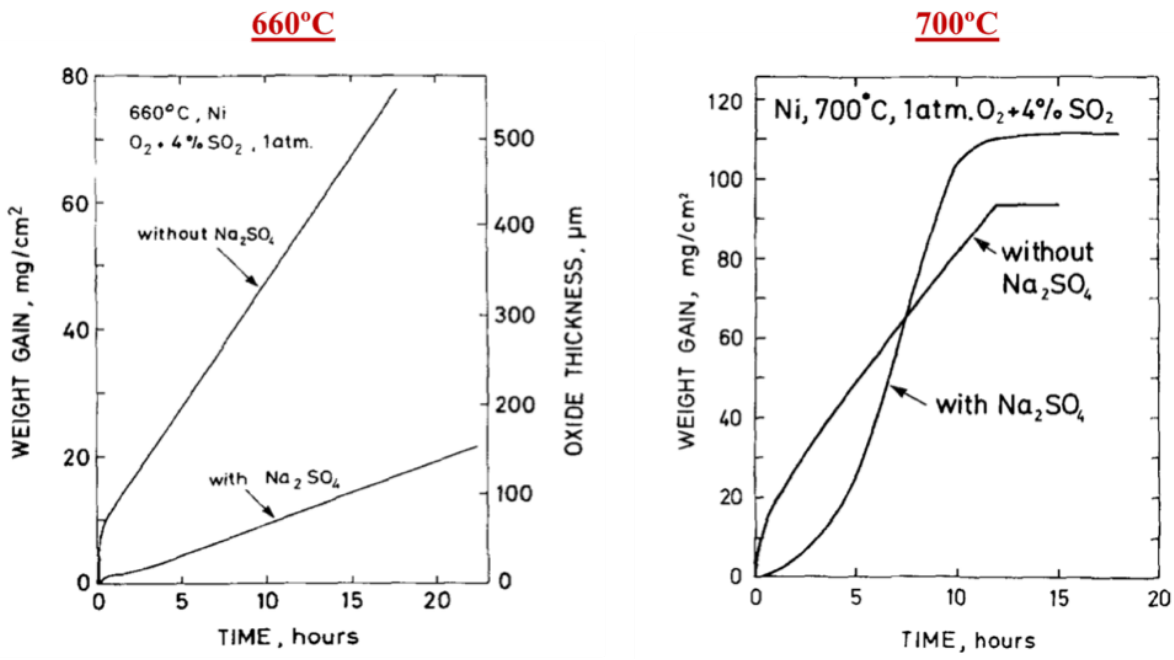

Figure 2-16. Weight gain vs. time at 660°C and 700°C for pure nickel with and without a Na_2SO_4 deposit in O_2 + 4% SO_2 [61].

The mechanism described above relies on high SO_2 pressure able to form the melt as well as sulfide formation. Mixed oxide/sulfide scales formed under Na_2SO_4 deposits have been found in other studies [7, 65, 67]. Gheno and Gleeson [7] studied pure nickel in O_2-1000ppm SO_2 and air environments with and without a deposit. This atmosphere contains much less SO_2 than the previous study; oxidizing, and not sulfidizing to nickel. Figure 2-17 shows the SEM cross-sectional images of the two environments with and without a deposit. Note the different scale bars used. The thickness of the NiO increases by either the addition of SO_2 to the environment, or applying a deposit on the surface.

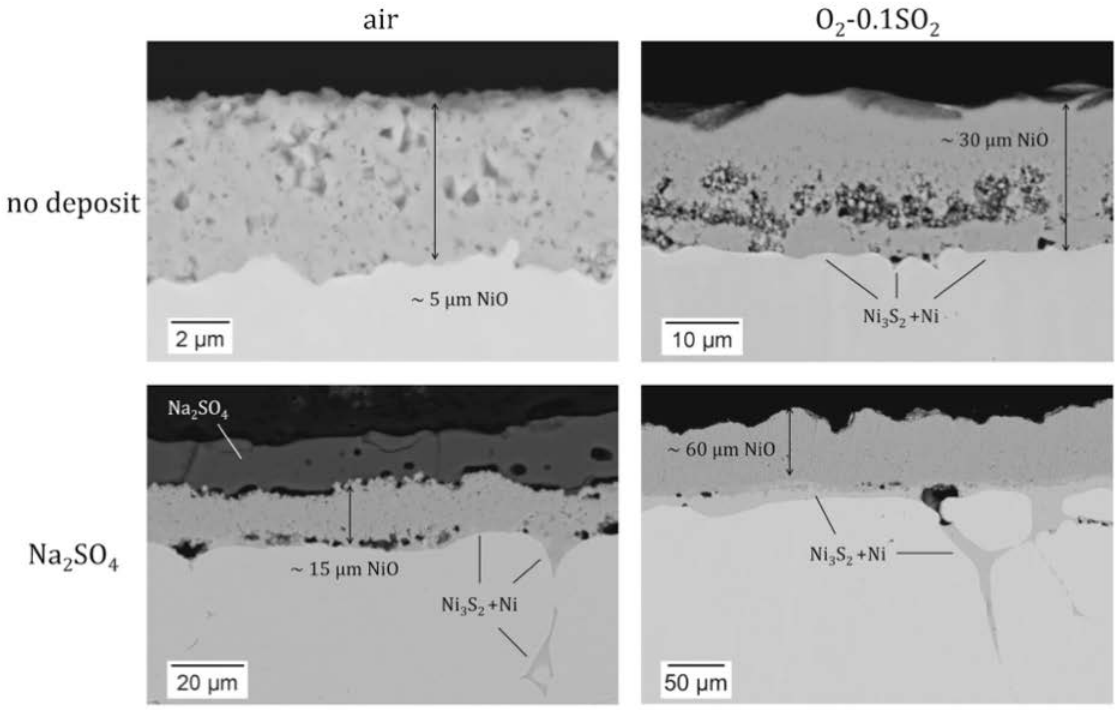

Figure 2-17. Cross-sectional SEM images of pure nickel exposed to air and O_2+1000ppm SO_2 with and without an Na_2SO_4 deposit after 20 h exposure [7].

In the case of pure nickel in air with a deposit, even though Ni_3S_2 is not stable according to the gas composition, the decomposition of the deposit causes sulfide formation which then wets the grain boundaries of the metal. The deposit remains solid, and no interaction occurs between the porous NiO that forms and the Na_2SO_4 besides minimal diffusion of nickel into the deposit. The addition of SO_2 into the environment leads to more extensive sulfide formation and consumption of the deposit to produce a very thick NiO scale. The mechanism wa postulated to be due to the NiO interacting with the deposit as well as oxidation-sulfidation. Initially, NiO interacts with the deposit to form $NiSO_4$. When a certain concentration is reached, the $NiSO_4$-Na_2SO_4 melt forms. The melt then penetrates the NiO until reaching a level where the SO_2 is no longer high

enough to stabilize liquid $NiSO_4$-Na_2SO_4. A positive solubility gradient exists in the deposit due to the SO_3 maintaining the highest concentration at the sulfate/gas interface, so the criteria proposed by Rapp does not exist. As mentioned previously, if a positive solubility gradient exists, this will result in saturation of the deposit with Ni until NiO is precipitated out. This does occur, while simultaneously occurring is the sulfidation-oxidation of nickel below the deposit. The deposit lowers the P_{O_2} leading to sulfidation. The sulfides initially form as connected networks in the oxide, and as in the previous study, provide rapid transport paths for nickel [7, 61]. The process continues until the melt is spread out due to NiO precipitation, no longer sealing the surface, which destabilizes the sulfide network. Figure 2-18 shows a stability diagram of the Ni-O-S system, with reaction paths for each case studied. These diagrams are useful in determining which products are stable in an environment. An important point to mention is that in these experiments, the oxide never forms above the deposit; the melt is confined to the outer portion of the reaction product. This study is seen to have similarities to previous studies, where the sulfide formation is important in providing fast transport paths and the SO_2 pressure must be high enough to stabilize the $NiSO_4$-Na_2SO_4 liquid formation.

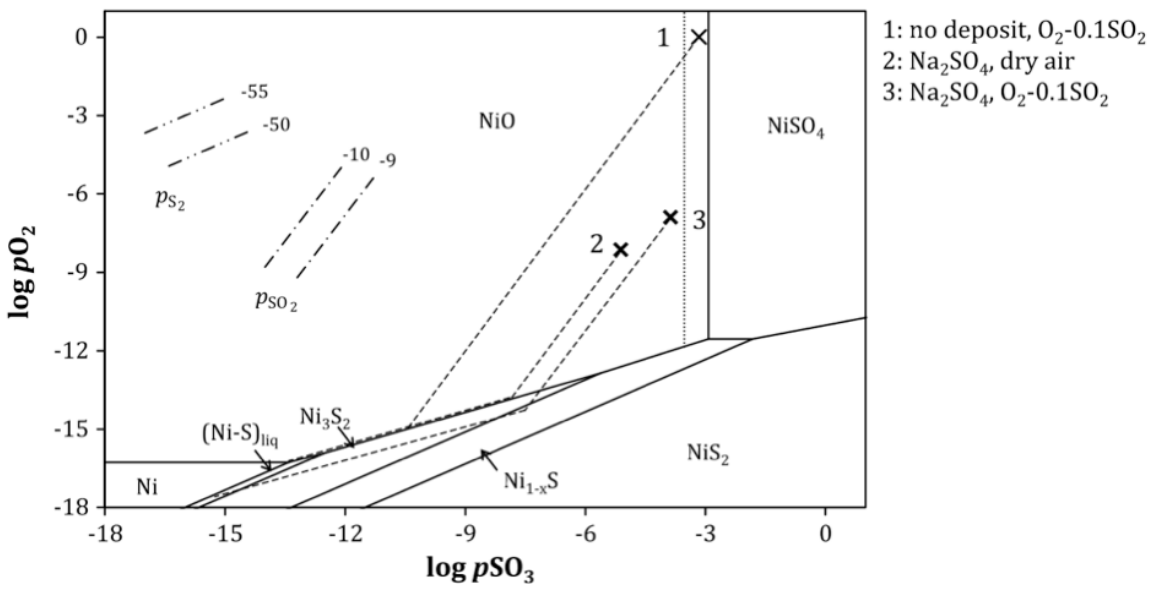

Figure 2-18. Ni-O-S stability diagram shows reaction paths for pure nickel in O_2+SO_2 with and without an Na_2SO_4 deposit, and in air with an Na_2SO_4 deposit [7].

One further mechanism exists to explain corrosion products formed on nickel-based alloys. This mechanism relies on synergistic fluxing of a basic and acidic oxide [6]. Gheno et al. [6] studied NiAl and NiAlCr alloys at 700°C in O_2-1000ppm SO_2 with a Na_2SO_4 deposit and an $MgSO_4$-Na_2SO_4 deposit, which is liquid at this temperature. In the case of the NiAl alloys, an alumina scale established initially, but some regions had nodules of internal oxide formation that was proposed to be due to sulfur at the oxide/metal interface. After longer periods of time, the internal oxidation was present uniformly across the sample. The addition of Cr caused uniform corrosion from the initial stages. This is a similar finding to studies done on Co-Cr and Co-Cr-Al alloys mentioned previously [8]. The morphology of the product is more typical of a hot corrosion product where the oxide forms above the deposit. Figure 2-19 shows the cross-sectional SEM images of the two alloys after exposure at 700°C with the already liquid $MgSO_4$-Na_2SO_4.

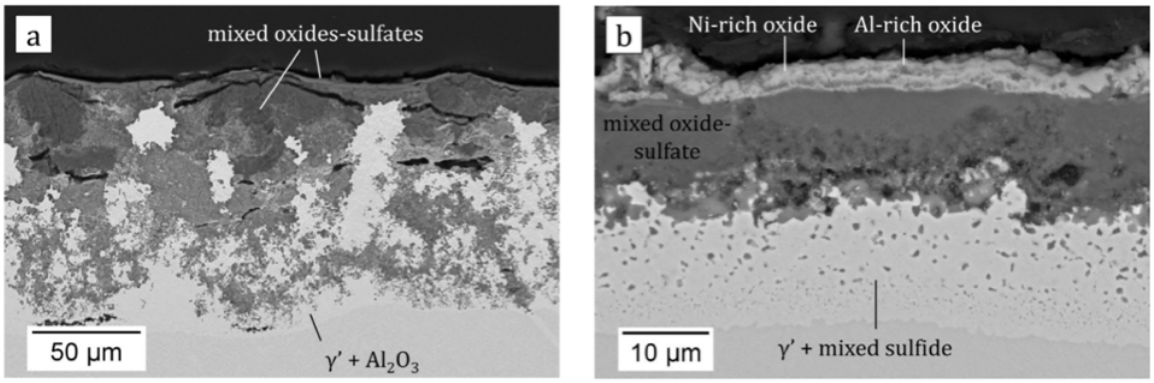

Figure 2-19. Cross sectional SEM images after 20 h exposures at 700°C with an $MgSO_4$-Na_2SO_4 deposit, a) NiAl, b) NiAlCr [6].

The mechanism of the NiAlCr alloy hot corrosion was proposed to be due to the synergistic effect of the basic fluxing of Cr_2O_3 (Eq. 2-13) providing SO_3 for the acidic fluxing of NiO (Eq. 2-14). The reactions shown in Eq. 2-13 and 2-14 are rapid and continue through the sulfate. This process also causes the basic dissolution of Al_2O_3 shown by Eq. 2-15. An important indication of this mechanism is the presence of Al, Cr, and Ni in the sulfate and oxide at the sulfate/gas interface, and as in the other mechanisms, the deposit must produce a liquid for fast transport. The next question is: Have there been studies at SO_2 pressures not sufficient for liquid formation? This will be discussed in the following.

$$Cr_2O_3 + 2SO_4^{2-} = 2CrO_2^- + S_2O_7^{2-} \qquad (2-13)$$

$$NiO + S_2O_7^{2-} = Ni^{2+} + 2SO_4^{2-} \qquad (2-14)$$

$$Al_2O_3 + 2SO_4^{2-} = 2AlO_2^- + S_2O_7^{2-} \qquad (2-15)$$

Jones and Gadomski [67] studied Nickel 200, Rene 80, and CoCrAlY alloys in 400-5000 ppm SO_2 + air environments with 50%NiO-50%Na_2SO_4 deposits. They found at SO_2 pressures unable to stabilize a liquid (400 ppm and 1000 ppm), very little corrosion occurred. This is consistent with previous studies, indicating liquid formation is necessary for corrosion [61]. At high enough SO_2 pressure, in the case of Nickel 200, liquid $NiSO_4$-Na_2SO_4 causes Ni-Ni_3S_2 liquid nodules to form leading to rapid oxidation-sulfidation [67]. In the Rene 80 (nickel-based superalloy) case, there was no sulfide formation, and the morphology was more consistent with typical Type II corrosion; NiO formation above the melt, and mixed oxide formation with no internal sulfide below the melt. There was no proposed explanation for the difference between these two samples as well as the Rene 80 mechanism.

Recent experiments have shown similar morphologies for nickel-based alloys at SO_2 pressures sufficient for liquid formation. Lortrakul et al. [13] studied CMSX-4 at 700°C with an Na_2SO_4 deposit and found the same morphology of the corrosion product, but did not provide an explanation as to how the NiO forms above the deposit, since the solubility gradient is positive. Sumner et al. [68] also studied CMSX-4 as well as IN738LC at 700°C with mixed sulfate and sulfate/chloride deposits and produced a similar structure, but as in the previous studies the SO_2 pressure was very high. Although the experiments by Sumner et al. provided insight into the rate of propagation, no mechanism was established. There have been previous experiments completed at temperatures of 550°C and 650°C, which are temperatures to be extensively studied for this thesis. However, the experiments were completed in air environments and the mechanism relies on either NaCl or $NaVO_3$ for the initiation of corrosion [69, 70].

The mechanisms presented all rely on liquid formation for Type II hot corrosion. Smeggil [71] reported hot corrosion occurring at temperatures down to 550°C for alloys PWA 1484 and In792+Hf having mixed deposits, with and without chloride additions. The tests were completed in an air environment, and he reported hot corrosion well below the melting point of the deposits tested. His limited explanation of how the corrosion occurs relied on the presence of $MgSO_4$ that decomposes and the released SO_3 causing the attack. The microstructures shown are very similar to preliminary results in this thesis, tested in SO_3-containing environments with pure Na_2SO_4 deposits. As indicated above, the mechanism presented by Smeggil was not detailed; there was no explanation as to how the nickel fluxes across the solid deposit. Indeed, the current literature on Type II hot corrosion does not aid in explaining this phenomenon.

A very recent article published by Zhang and Sharghi-Moshtahin [72] proposes low temperature hot corrosion is due to primarily oxidation/sulfidation. TEM samples were taken from field components. No Na, Mg, K, or Ca were identified. In the internal corrosion product Ta/Al/W-sulfides were present at the reaction front and Co/Cr-sulfides closer to the alloy interface. While the mechanism proposed is plausible, in the experiments in this thesis samples were simplified to pure nickel and very little sulfides were identified in the reaction product. The sulfides were also limited to the oxide/metal interface. Significant interaction occurred between the metal and deposit. Therefore, the mechanism to be discussed in Chapter 5.1 relies on sulfate/alloy interaction and cannot be explained by the recent article by Zhang and Sharghi-Moshtahin [72].

2.3.3 High Temperature (Type I) Hot Corrosion

Type I hot corrosion refers to deposit-induced attack occurring above the melting point of Na_2SO_4. The mechanisms of Type I hot corrosion are better understood than those of Type II hot corrosion. The attack occurs via alloy-induced acidic fluxing, basic fluxing, and/or sulfidation [4]. The alloy-induced acidic fluxing mechanism is very similar to that found in Type II conditions. Equation 2-7 applies in Type I conditions as well. A number of authors have studied alloy-induced acidic fluxing [73–78]. As in the Type II case, this mechanism does not rely on SO_2/SO_3 in the environment. Transient acidic oxides of Mo, W, and/or V decrease the oxide ion activity via consumption, as shown by Eq. 2-16 for the Mo case [58, 73].

$$MoO_3 + O^{2-} = MoO_4^{2-} \qquad (2-16)$$

A decrease in oxide ion activity equates to a more acidic melt, which allows for enhanced acidic fluxing of the oxide scale. The reaction for the acidic fluxing of alumina is shown in Eq. 2-17. Equivalent reactions exist for other oxides forming on superalloys (see Eq. 2-5 and 2-6 for nickel example).

$$Al_2O_3 = 2Al^{3+} + 3O^{2-} \qquad (2-17)$$

Al_2O_3 is consumed via this mechanism and precipitated at the sulfate/gas interface due to evaporation of the acidic oxide, such as MoO_3 (g) that forms in the case of Mo, satisfying the negative solubility gradient criteria. The precipitated oxide is porous and non-protective. A study

on NiCrAlMo alloys by Peters, Whittle, and Stringer [77] suggested greater than 3 wt. % Mo is needed for catastrophic corrosion to occur via alloy-induced acidic fluxing.

Fryburg et al. [76, 78] and Misra [75] conducted chemical analysis of water-soluble species after a given hot corrosion exposure. Nickel-based superalloys containing Mo were studied with a Na_2SO_4 deposit in O_2 environments. Fryburg et at. [76, 78] studied IN-738 at 975°C and B-1900 and NASA-TRW VIA at 900°C; while Misra [75] studied B-1900 and U-700 with different Mo contents at 950°C. Both authors found accelerated corrosion correlated to an increase in molybdenum content, due to Na_2MoO_4 formation. Misra [75] also studied deposits of Na_2MoO_4 and Na_2MoO_4 + MoO_3 and found that when MoO_3 was present a short induction period and extensive accelerated attack resulted. Evaporation of the MoO_3 at the gas interface, as mentioned previously, establishes conditions for the negative solubility gradient as described by Rapp-Goto. However, Misra [75] determined the evaporation rate for $xMoO_3$-yNa_2MoO_4 deposits and found as the concentration of MoO_3 in the melt increases, the evaporation rate decreases. They then speculated the role of MoO_3 is for electronic conduction in the melt as Mo can exist in a +4 and +6 state. The transport was hypothesized to be similar to the cobalt-based Type II mechanism proposed by Luthra [9], [14].

Complementary studies were done by Misra in O_2-(0.0105, 0.108, 0.24, 1, and 2)% SO_2 to determine the effect of SO_2 on hot corrosion. As in type II hot corrosion, the SO_2 in the environment was much higher than engine application. Figure 2-20 shows the resulting graph of weight gain vs. time in each environment. Increasing SO_2 content was determined to decrease the conversion of Na_2SO_4 to Na_2MoO_4 + MoO_3 and thus decreased the corrosion rate. Chemical analysis of water soluble species in products formed from exposures to 1% and 2% SO_2 detected

no Mo. The cross-sectional images revealed oxidation/sulfidation was the likely corrosion mechanism in the 1% and 2% SO_2 environments.

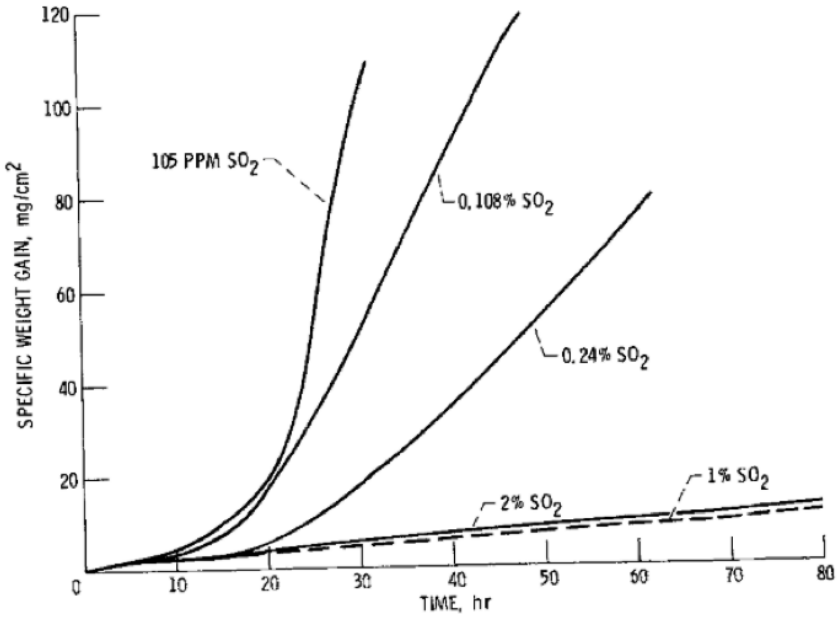

Figure 2-20. Weight gain vs. time in O_2-SO_2 containing enviornments for hot corrosion expsoure of Udiment-700 with 0.7 mg/cm^2 Na_2SO_4 at 950°C [74].

When the concentration of acidic oxides is not sufficient for alloy-induced acidic fluxing, the mechanism of Type I hot corrosion is via basic fluxing and/or sulfidation. Unlike Type II hot corrosion, SO_3 is not needed in the atmosphere for attack to occur, but may impact the extent of corrosion as will be discussed in a following paragraph. Typical Type I microstructures have internal oxide and sulfide formation, with sulfides present at the reaction front [4]. In earlier studied, it was suspected that the sulfide formation was responsible for the accelerated attack. Simons et al. [40] proposed that Na_2SO_4 supplied sulfur for liquid metal-metal sulfide formation

and it was the oxidation of the sulfides that was responsible for the accelerated kinetics. Seybolt [79] inferred that the depletion of chromium, a beneficial element for oxidation resistance, due to sulfide formation led to poor oxidation resistance. The result was accelerated attack.

Experiments completed by Bornstein and DeCrescente [80] disproved the postulation that sulfides were responsible for accelerated attack. These authors studied oxidation and hot corrosion of nickel-based alloys B-1900, U-700, and Waspaloy in an air environment. Figure 2-21 a) shows a graph of weight gain vs time for alloy B-1900, comparing the oxidation kinetics of the bare alloy and the alloy coated with an Na_2SO_4 deposit. The graph illustrates the significant increase in the extent of reaction when a deposit is present on the surface. They then compared the oxidation rates of bare alloy and alloy that was pre-sulfidized, to determine if the presence of sulfides would result in accelerated attack. The result was that the pre-sulfidized alloy had comparable kinetics to the as cast B-1900 alloy. Figure 2-21 b) shows a graph of weight gain vs. time illustrating this finding. That led to the question, if the sulfides are not responsible for accelerated attack what constituent is? To answer this, they repeated the hot corrosion experiments with an $NaNO_3$ deposit and compared the result to the experiment with an Na_2SO_4 deposit. The $NaNO_3$ deposit forms sodium and nitrogen oxides, so the similarity to the Na_2SO_4 deposit is the Na_2O. The results showed similar kinetics to the Na_2SO_4 deposit case. The microstructure was also very similar in appearance, with the formation of a non-protective oxide and a depletion region below the oxide. The depletion zone did not contain sulfides in the case of the $NaNO_3$ deposit on bare alloy. The conclusion was the interaction of the alloy with the Na_2O component in the deposit is responsible for the accelerated attack.

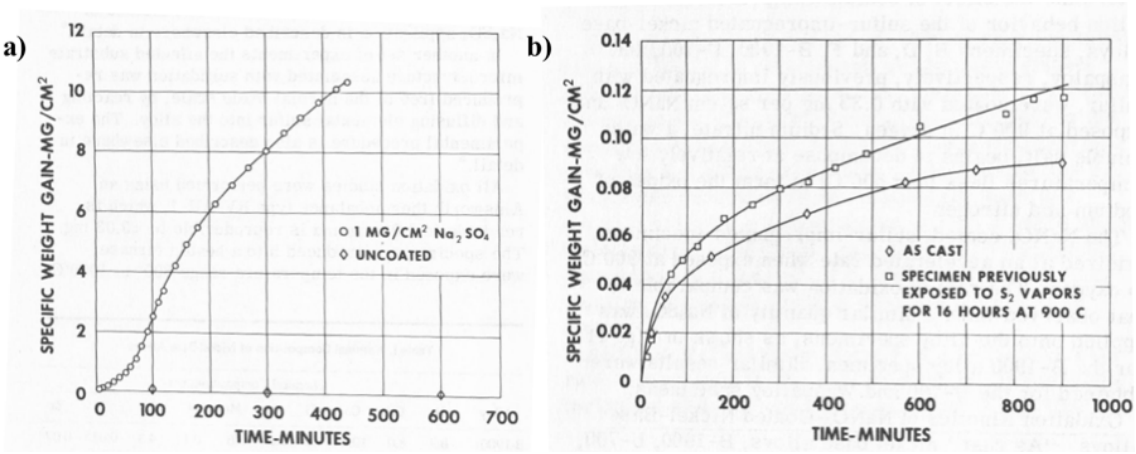

Figure 2-21. a) Oxidation kinetics of alloy B-1900 with and without an Na_2SO_4 deposit, and b) oxidation kinetics of B-1900 bare alloy and alloy sulfidized [80].

Goebel and Pettit [12] developed a mechanism for basic fluxing based on results completed on pure nickel specimens. These authors theorized hot corrosion relies on a condensed deposit. Experiments completed in Na_2SO_4 vapor did not result in accelerated attack; a composition gradient established across the deposit was determined to be essential for attack to occur. However, recent literature seems to contradicts this finding [81], but the mechanism proposed by Goebel and Pettit is still relevant because in both cases a melt is present on the surface. Goebel and Pettit created an Ni-O-S stability diagram to determine the stable phase of nickel and changes that can occur as the nickel interacts with the deposit. Figure 2-22 shows the diagram at 1000°C, where the **x** is the starting composition of the Na_2SO_4 deposit and the arrows indicate local changes of the deposit during reaction with nickel.

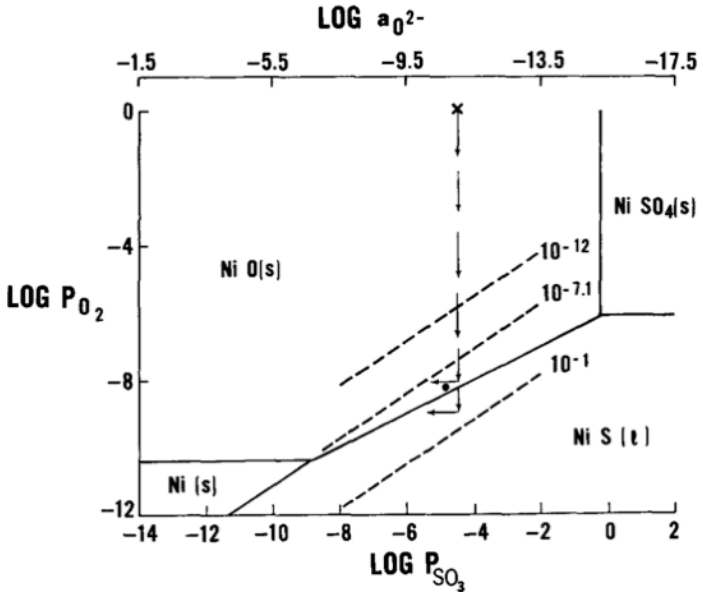

Figure 2-22. Ni-O-S stability diagram at 1000°C, 'x' indicates the composition of the Na_2SO_4 deposit and the arrows show changing composition of the deposit due to reaction with nickel. The dashed lines correspond to sulfur isobars [12].

The mechanism of basic fluxing of pure nickel, as presented by Goebel and Pettit, is as follows. According to Fig. 2-22, NiO is stable in the starting composition of Na_2SO_4. Oxygen supply for NiO formation comes from the deposit. The result of oxygen removal is an increase in the sulfur activity (shown by the arrows). The sulfur enrichment then leads to nickel-sulfide formation at the oxide/metal interface. The onset of sulfide formation corresponds to the start of the propagation stage of hot corrosion. This is because a decrease in sulfur leads to an increase in the oxide ion activity; relevant reactions are shown in Eq. 2-18. Assuming an equilibrium constant, if S_2 is removed to form sulfide, the oxide ion activity will increase, with the reverse true as well.

$$SO_4^{2-} = O^{2-} + SO_3 = O^{2-} + \frac{1}{2}S_2 + \frac{3}{2}O_2 \qquad (2-18)$$

The increase in oxide ion activity allows for dissolution of nickel into the melt according to Eq. 2-19 and 2-20.

$$NiO + O^{2-} = NiO_2^{2-} \qquad (2-19)$$

$$2NiO + O^{2-} + \frac{1}{2}O_2 = 2NiO_2^{-} \qquad (2-20)$$

The nickelate ions diffuse toward the sulfate/gas interface and due to the negative solubility gradient, precipitate out as NiO. The resulting NiO that forms in the deposit is porous and non-protective. Figure 2-23 shows a schematic of the mechanism at different stages. An important point of the mechanism is that the increased oxide ion activity causes the dissolution of NiO leading to accelerated attack; the sulfide formation serves the role of increasing the oxide ion activity.

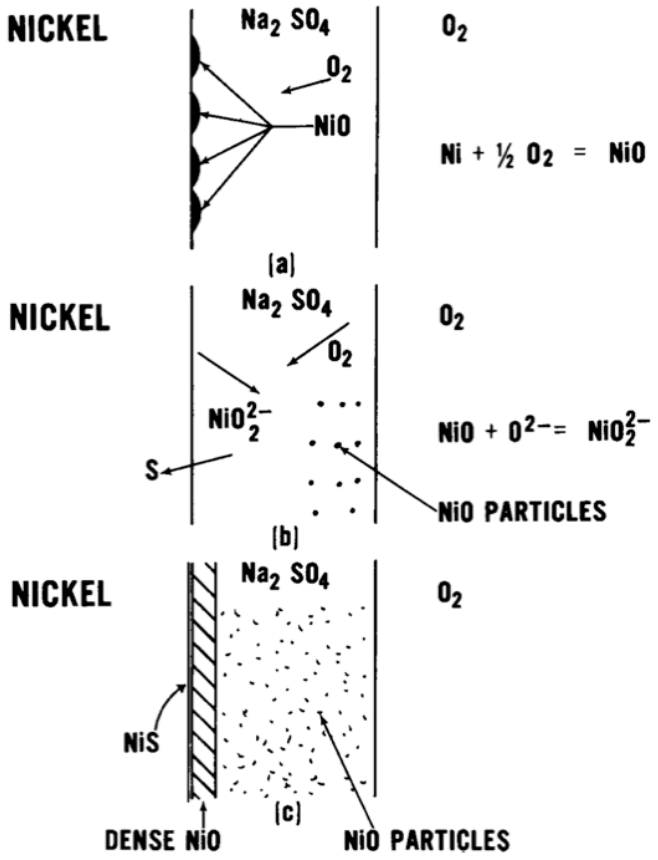

Figure 2-23. Schematic of the mechanism of basic fluxing [12].

The mechanism of basic fluxing and alloy-induced acidic fluxing can occur at different stages of reaction, as shown by Fryburg et al [78]. They studied nickel-based alloys B-1900 and NASA-TRW VIA in air environments at 900°C with an Na_2SO_4 deposit applied. Through chemical analysis and analytical methods, they found in the initial stages the mechanism is basic fluxing of alumina. The condition for basic fluxing is established due to sulfide formation in the alloy. After ~9-10 hours, the mechanism switches to alloy-induced acidic fluxing, due to the formation of an Na_2MoO_4/MoO_3 melt.

Otsuka and Rapp [82] addressed the question of the influence of SO_2 content on the basic fluxing mechanism. They studied pre-oxidized nickel of 99 and 99.99% purity in an O_2-1%SO_2 environment. An Na_2SO_4 deposit was applied and they were able to electrochemically measure the P_{O_2} and a_{Na_2O} through the use of electrodes. It was shown that, even though the environment was acidic, the reaction was dominated at the sulfate/oxide interface. Figure 2-24 shows the Ni-O-S stability diagram, with the measurements of the activity during reaction of the 99% pure pre-oxidized Ni with Na_2SO_4 plotted on the diagram. The measurements show that initially the sample is in the acidic region, but after a short period of time the chemistry of the deposit shifts and basic fluxing of NiO proceeds.

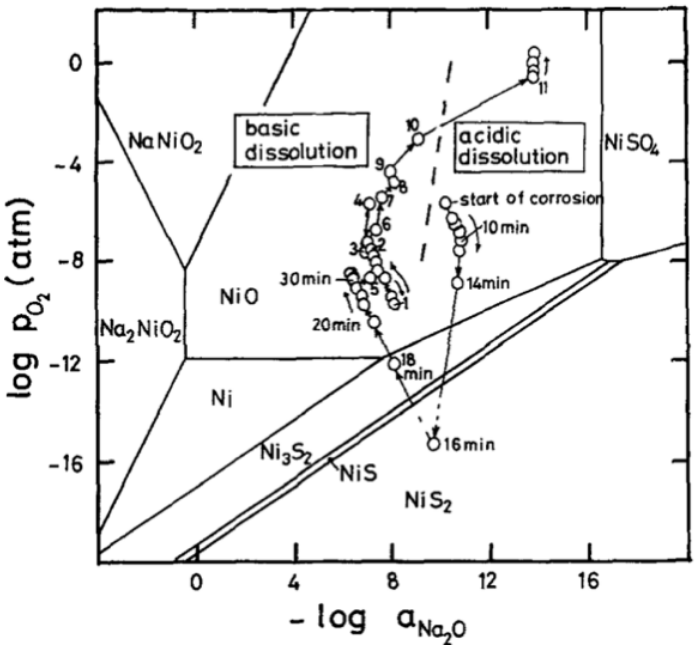

Figure 2-24. Ni-O-S stability diagram, with measurements of P_{O2} and a_{Na2O}, after testing 99% pure pre-oxidized Ni at 1173K with an Na_2SO_4 deposit [82].

Experiments conducted by Otsuka and Rapp [83] on 99.99% pure Ni revealed the effect of oxide formation on hot corrosion. The same experimental conditions as Fig. 2-24 using 99.99% pure Ni did not result in corrosion. This was attributed to the preformed oxide containing less defects. When the experiment was repeated, with the addition of Na_2O_2 to the deposit to create an initial condition of high oxygen ion activity, hot corrosion did occur. However, sulfides were absent from the oxide/alloy interface. This further proves that the mechanism is driven by the oxide-ion concentration in the deposit and its gradient.

Although the experiments using 99% pure Ni in an acidic environment showed the reaction is actually basic fluxing (Fig. 2-24), if the SO_3 content reaches a high enough value the mechanism will no longer be basic fluxing but instead may proceed due to sulfidation or acidic fluxing [4]. As the SO_2/SO_3 content increases, the impact on the corrosion rate will be system dependent. Misra and Whittle [65] found in the case of pure Ni, at 923°C the corrosion rate in four different environments varied as follows: Air < Air + 1.1% SO_2 < Air + 0.104% SO_2 < Air + 10% SO_2. In all previous experiments with SO_2 mentioned, the atmosphere was catalyzed to produce SO_3. Liu [32] studied the hot corrosion of PWA 1484 at 900°C and the effect of an uncatalyzed vs catalyzed environment containing O_2 + SO_2 mixtures; SO_2 varied from 10-1000 ppm. She found a greater corrosion rate in uncatalzyed atmospheres and as the SO_2 content increased, the extent of corrosion increased. The experiments mentioned all found a corrosion rate change with SO_2, however, Pettit studied an NiAl alloy in air and an O_2-SO_2 environment and found similar attack in either case. Therefore, the effect of SO_2/SO_3 on Type I hot corrosion depends on the alloy substrate composition.

Thus, as with Type II hot corrosion, the extent of attack is dependent upon alloy composition. Two beneficial alloying elements to Type I hot corrosion are Cr and Ta. Cr solubility in Na_2SO_4 is dictated by the P_{O_2} [84]. Near the salt/alloy interface where the P_{O_2} is lower, $NaCrO_2$ is stable; whereas near the salt/gas interface at higher P_{O_2}, Na_2CrO_4 is stable. The two components have different solubility in Na_2SO_4 and that solubility depends on P_{O_2}; $NaCrO_2$ is much more soluble than Na_2CrO_4 and as the P_{O2} increases, the solubility decreases. According to Rapp and Otsuka [84], conditions established by the environment and alloy/deposit interactions lead to a P_{O_2} gradient across the deposit corresponding to a positive solubility gradient for Cr. The positive solubility gradient is beneficial in Type I hot corrosion. Chromium will saturate the deposit and precipitate oxide at the sulfate/alloy interface instead of consuming the deposit. In addition, the reaction of Cr with Na_2SO_4 in the initial stages decreases the oxide ion activity to levels where other elements are unable to undergo basic fluxing [73]. Tantalum is beneficial because of the formation of Na_2TaO_3, a high-melting-point compound [78, 85]. This increases melt acidity, preventing basic dissolution of elements. Moreover, for alloys containing Mo, W, and/or V this prevents the formation of the highly acidic low melting species that lead to alloy-induced acidic fluxing.

Compared to Type II hot corrosion, the mechanisms of Type I are better established and agreed upon. In both Types of hot corrosion, there are variables that impact the corrosion rate (gas composition, alloy composition, deposit chemistry, etc.) and understanding the variability will better aid in predicting hot corrosion behavior.

2.4 Diffusion Coatings

Coatings are used to protect against hot corrosion, since base-alloy compositions typically do not prevent attack. Three different coatings exist: diffusion coatings, overlay coatings, and thermal barrier coatings. Diffusion coatings refer to diffusionally enriching the surface of the base alloy with an element of interest [4]. In engine applications, chromizing and aluminizing are employed. In the proposed research for this thesis, chromized coatings will be studied. Many methods can be used to introduce the element into the alloy, including: pack cementation, an above-the-pack method, chemical vapor deposition (CVD), and a slurry method [86]. All are based on surface enrichment, typically of one element. Pack cementation is inexpensive compared to other coating methods. The process consists of inserting the component in a mixture containing a source (either pure material or an alloy), a halide activator, and an inert filler [28]. Since the activator is a halide, volatilization will occur when the pack is heated and these species will react with the source creating gaseous products of the element of interest [4]. The gaseous species then react at the surface of the component. Figure 2-25 shows a schematic of reactions occurring during a pack cementation process for chromizing steel. Similar reactions apply to other alloys and elements.

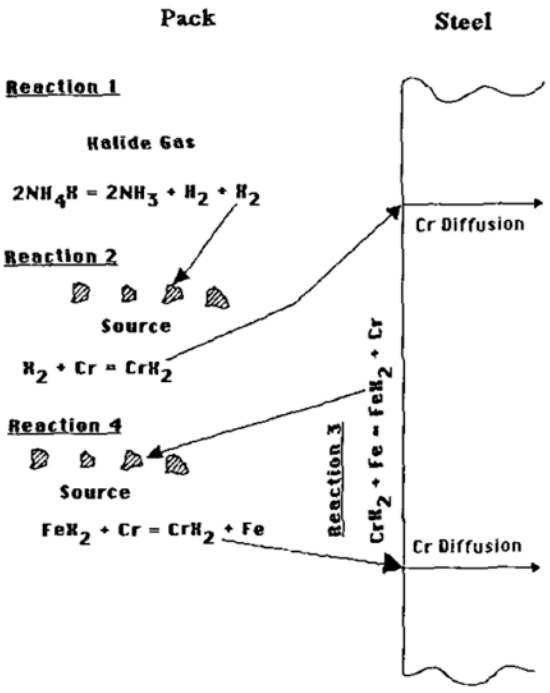

Figure 2-25. Reactions occurring during pack cementation to enrich steel with chromium [87].

The final concentration of the enriched element will depend on the activity at the surface of the sample, which is a function of the activator used, temperature, and the activity of the element in the source material. Figure 2-26 illustrates how the partial pressure of species change based on the source and activator used. In the most commonly used diffusion coatings, only one element of interest is targeted, but codeposition is possible if the partial pressures of the species are similar [88].

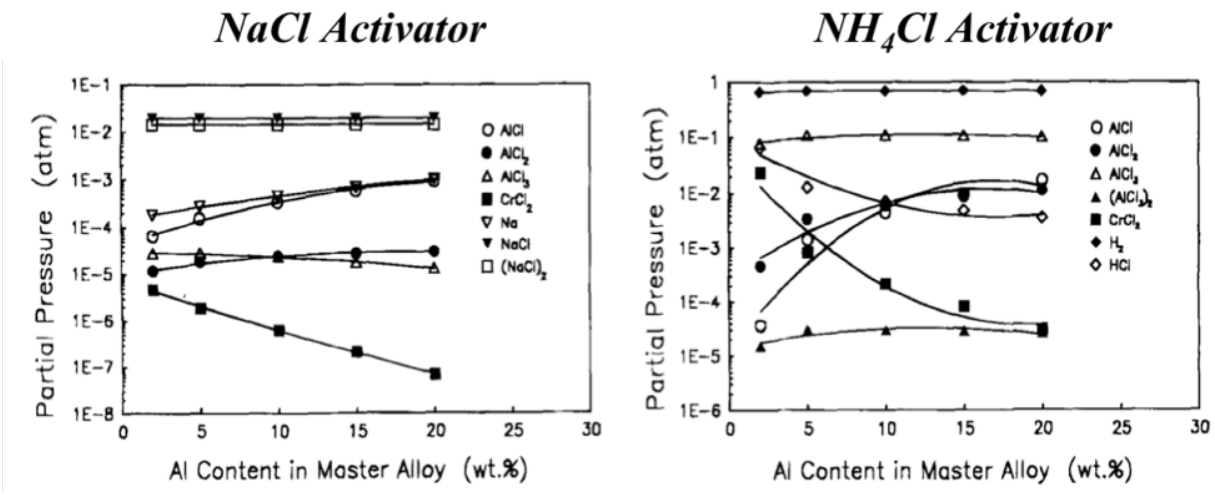

Figure 2-26. Partial pressure of species during pack cementation at 1100°C [88].

In the above-the-pack method, the components are placed above the pack mixture and the gases generated migrate to the components [4]. The advantage is the mixture of source, activator, and filler will not be incorporated in the coatings, which occurs in the pack-cementation process. In the CVD method, the gases are produced externally and fed into a furnace containing the component to be deposited. In the slurry method, a slurry containing the active element is applied to the component. The application of heat causes diffusion of the element of interest inward, but leaves behind residue that needs to be removed [89]. There are advantages and disadvantages to each process but the end result is the same; an enriched layer of a certain element.

The aluminide coating used is usually NiAl with or without modification by Pt. The Pt is electroplated to the part prior to the diffusion aluminizing process. Platinum in the NiAl provides a number of benefits, including the preclusion of void formation at the alumina scale interface [4, 90]. The resulting microstructure is based on β-NiAl with Pt in solution [4]. Depending on the thickness of the Pt layer, a $PtAl_2$ phase may also form. The microstructure of a chromized coating

on a Ni-based alloy is chromium in γ-Ni solution. As mentioned in the oxidation section, at high temperatures chomia becomes volatile, so there is a temperature limit to the use of chromized coatings. Based on discussion with Pratt & Whitney, one challenge of the chromizing process is producing a coating of uniform composition. Resulting coatings can have large variations in chromium content across a surface.

2.4.1 Hot Corrosion of Chromized Coatings

Coating selection will depend on the environment and temperature the components will be exposed to. Figure 2-27 shows a graph of oxidation resistance vs. corrosion resistance, showing that in terms of Type I corrosion resistance, high chromium coatings provide the best protection [28]. In Type II conditions, Luthra *et al.* [91] showed coatings of Co-Cr on Rene 80, with Cr level above 37.5 wt. %, were protective against a Na_2SO_4 deposit. The samples were tested in an aggressive condition of O_2-0.15% SO_2. In discussion with Pratt & Whitney, in engine application chromized coatings are often used to protect against the harsh environments.

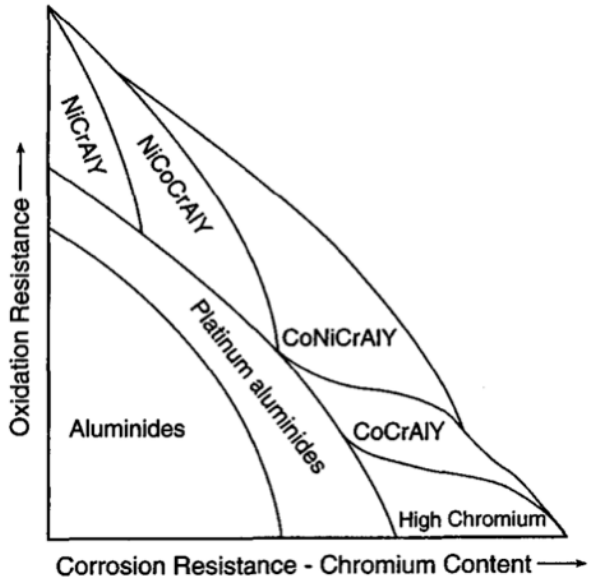

Figure 2-27. Coating selection based on oxidation and corrosion resistance [28].

It is well known that scale establishment is important in protecting against hot corrosion. Task et al. [92] showed the addition of Pt or Cr to a Ni-36Al alloy extended the incubation stage due to the rapid establishment of an Al_2O_3 scale. In a different study, Task et al. [93] demonstrated pre-oxidation reduced Type II hot corrosion. These studies show the importance of the establishment of a protective oxide scale to mitigate against Type II hot corrosion. Considering a chromized coating, Figure 2-28 shows there is an increasing trend of decreased attack vs. increased chromium content. The trend is related to the formation and sustained growth of a protective Cr_2O_3 scale. The environment of the study contained a sulfur content much higher than in engine application. In the research presented in this thesis, a systematic study will be conducted to determine the Cr content needed for low-temperature hot corrosion protection in more realistic engine environments. The analysis will be linked back to the establishment of a protective oxide.

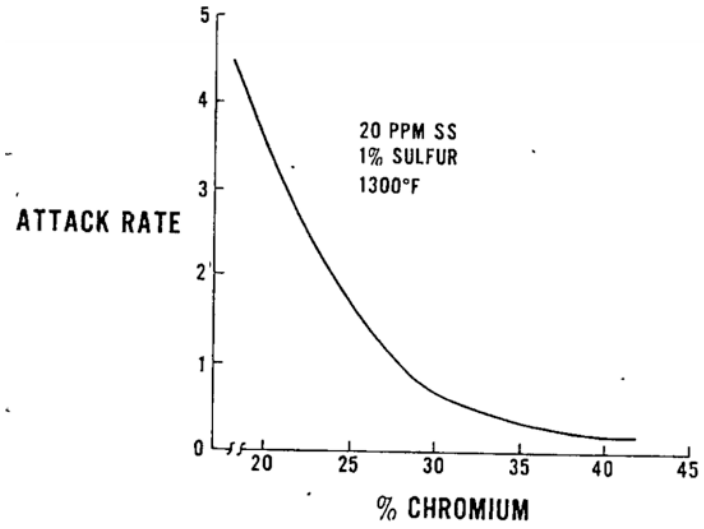

Figure 2-28. Attack rate vs. chromium content in the alloy [94].

3.0 Research Objectives

3.1 Deficiencies in the Current Body of Knowledge

Nickel-based superalloys are vital for components in gas-turbine applications, such as turbine blades and disks. In the previous Chapter, an overview of superalloys and the importance of the establishment of a continuous, stable scale was given. Maintaining this scale during operation is critical for protection against a harsh environment. However, sulfate-containing deposits along with the presence of SO_2 either prevent the alloy from forming a protective scale or can cause breakdown of the scale present. To protect against this form of deposit-induced attack, it is important to understand the mechanisms operating and how environmental factors impact the extent of attack.

One deficiency in the current literature is that the test environments tend to be very aggressive conditions. In Type II hot corrosion conditions, previous experiments, as outlined in the previous chapter, have focused on high SO_2 environments (e.g. [7, 9, 13, 58, 61, 67, 95, 96]) that are able to stabilize a liquid deposit. If SO_2 is not present in the testing environment, the mechanism relies on chlorides or vanadates to cause corrosion (e.g. [70, 97]). However, preliminary results with a pure Na_2SO_4 deposit show extensive corrosion at temperatures and SO_2 pressures where liquid formation is not predicted. In real applications, Pratt & Whitney has communicated similar findings. It is therefore necessary to further characterize and understand the mechanism of this low-temperature attack, since bare alloys are utilized for certain components in aero engines that operate in the Type II regime and lower.

The mechanism of Type I hot corrosion is better understood, but past literature has the same deficiencies as Type II hot corrosion in that the testing environment is either air or has an extremely high SO_2 content. In actual service environments, the SO_2 content varies across different regions of the world, but never approaches values used by in past studies (e.g. 4% SO_2 [61]). A more realistic SO_2 level in an aero engine is around 10 ppm or lower. It is therefore of interest to study Type I and Type II hot corrosion in relatively low SO_2 environments and to determine how the corrosion rate and behavior change with SO_2 content at low levels. This will provide both a better understanding and the ability to predict corrosion behavior based on the geographic region of engine operation.

Currently, base-alloy compositions are generally not protective against hot corrosion attack. Therefore, various coatings exist to provide resistance to hot corrosion. As discussed in the previous Chapter, in Type II hot corrosion conditions, high chromium-coatings can protect against attack, with a trend of increasing chromium content resulting in decreased attack. However, applying a chromized coating to a component can prove challenging as uniform composition is often not obtainable, resulting in varying chromium content across a surface. Past experiments on the effects of chromium-content level were completed in high-SO_2-containing environments and were limited to 700°C and above (eg. [91, 94]). To better guide the commercial application of chromized coatings, it is important to understand what content of Cr is needed for protection in environments more representative of real application. The results will aid in establishing limits to the range of Cr enrichment across the surface that is acceptable for providing protection.

3.2 Research Goals

Based on the above discussion, the main research goals of this thesis are to:

1. Determine the mode and mechanism of low-temperature hot corrosion, occurring at temperatures of 650°C and below. The main focus will be a single crystal nickel-based superalloy, however, a few experiments will be conducted using a disk alloy. Both of these materials are exposed in service to low temperatures in an uncoated state.
2. Better understand the role of SO_2-content in the atmosphere on the hot-corrosion behavior of a single crystal nickel-based superalloy. The temperature range will be 550°C-1000°C, encompassing both Type II and Type I regions. Environments studied will be dry air and O_2-(2.5, 10, and 100) ppm SO_2. The SO_2 contents chosen are more representative of engine application. The goal is to determine how the mechanisms changes based on temperature and SO_2 content.
3. Test potential mitigation methods to hot corrosion. The main aim is to prevent low-temperature attack. Chromized coating compositions with systematically varying chromium content will be studied to determine the most beneficial chromium content to prevent low temperature attack. Exposures will be done from 600°C-700°C in O_2-10 ppm SO_2.

4.0 Experimental Procedures

4.1 Materials Studied

4.1.1 Nickel-based Superalloys

The nickel-based superalloys to be studied in this thesis are PWA 1484 and ME 16. Model alloys were also studied to represent a chromized coating on PWA 1484. Various heat-treated alloys of PWA 1484 were prepared to determine if homogenization has an effect on hot corrosion.

4.1.1.1 PWA 1484

The majority of the experiments were conducted using PWA 1484 as the substrate. This is a single crystal nickel-based superalloy that was supplied by Pratt & Whitney. The nominal composition of PWA 1484 [98] is shown in Table 4-1, and a representative microstructure in shown in Fig. 2-1. The coupon samples used were semicircular with dimensions *ca.* 1.5cm^2 x 1.5mm-thick. The effect of SO_2 content on the corrosion rate from 550°C to 1000°C was studied using PWA 1484. Further extensive analysis was done from 700°C and below using this alloy to determine the low temperature mechanism of hot corrosion.

Table 4-1. Nominal composition of PWA 1484 [98].

Element	Ni	Cr	Mo	W	Re	Ta	Al	Co	Hf
Weight %	Bal.	5	2	6	3	8.7	5.6	10	0.1
Atomic %	Bal.	5.98	1.3	2.03	1	2.99	12.91	10.56	0.03

4.1.1.2 ME 16

A few experiments were conducted at 700°C and below on ME 16, a powder metallurgy disk superalloy provided by Pratt & Whitney. ME 16 is sometimes also referred to as ME 3 or Rene 104 [24]. The nominal composition of ME 16 [99] is shown in Table 4-2. Rectangular samples *ca.* 0.6cm x 1.3cm x 1.5mm-thick were tested.

Table 4-2. Nominal composition of ME 16 [99].

Element	Ni	Cr	Co	Mo	Ti	Ta	Al	Nb	Zr	C
Weight %	Bal.	13	20.6	3.8	3.7	2.4	3.4	0.9	0.05	0.05
Atomic %	Bal.	14.22	19.89	2.25	4.4	0.75	7.17	0.03	0.24	0.24

4.1.2 Pure Metals

To understand the mechanism of low-temperature hot corrosion, experiments were simplified to pure metals. 99.98% purity nickel and cobalt coupons, purchased from Goodfellow Corporation were used. Square samples *ca.* 1cm^2 x 1mm-thick were tested.

4.1.3 Model Alloys Based on Chromized Coating

As mentioned in the literature review, chromizing is a coating process that introduces chromium into the alloy that will aid in the formation of a protective oxide that resists against hot corrosion. From discussion with Pratt & Whitney, it is understood that producing a uniform chromized coating composition is challenging. The goal therefore was to understand in low-temperature hot corrosion what level of chromium is needed to provide protection. Four Ni-Cr-Al model alloys were prepared via Ar-arc melting pure forms of the constituents. The alloys were prepared in the form of 10-15 gram buttons via Ar-arc melting. For all preparations, the melting of 3 grams of 99.95% pure Zr was done prior to the alloy melting in order to getter oxygen from the arc-melting chamber. After Ar-arc melting the alloys were homogenized at 1200°C for 24 hours. The samples studied were *ca.* 1-1.3cm^2 x 1mm-thick. The alloys had controlled variation in Cr content based on the composition range of PWA 70 (i.e, commercial name of Pratt & Whitney's chromized coating). Figure 4-1 shows the four compositions plotted on a simplified Ni-Cr-Al isothermal section, illustrating that the alloy structure is γ-Ni. Additional model alloys were made that included cobalt and tantalum carbides. Cobalt is present in the conventional alloy. Carbides and nitrides are introduced via the chromizing process. Select alloys were also nitrided by exposure at 900°C in Argon + 2% NH_4 for 20 h. Table 4-3 lists all model alloys studied.

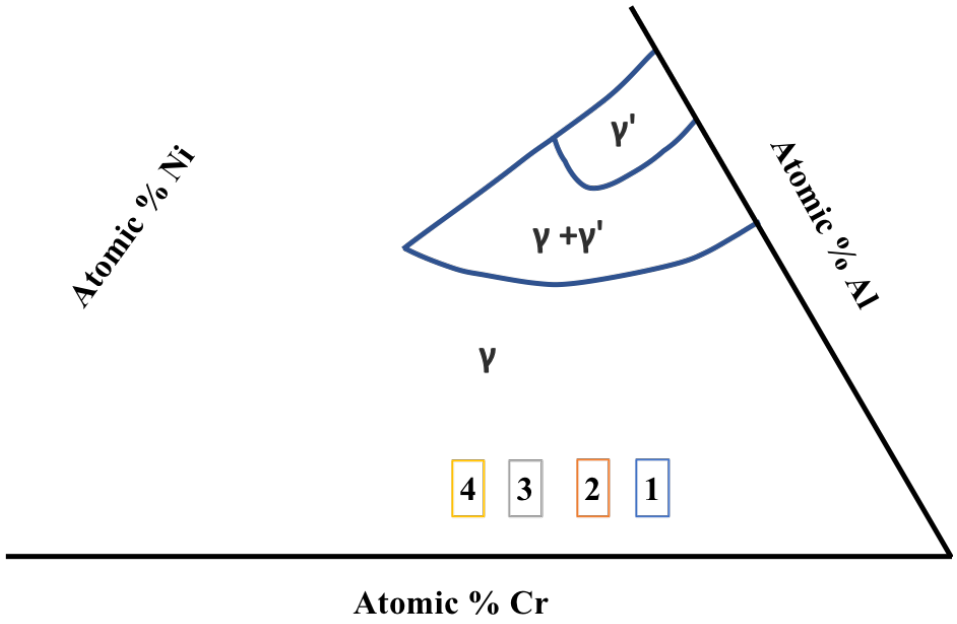

Figure 4-1. Ni-Cr-Al isothermal section at 1000°C, adapted from [21] with four model alloy compositions indicated.

Table 4-3. Model alloy compositions in atomic %.

	Ni	Al	Cr	Co	TaC
Alloy 1	80	4	16		
Alloy 2	76	4	19		
Alloy 3	73	4	23		
Alloy 4	70	4	26		
Alloy 5	60	4	26	10	
Alloy 6	56	4	26	10	4

4.1.4 Heat-treated PWA 1484

A few experiments were completed using heat-treated PWA 1484 alloys to determine the effect heat treatment has on hot corrosion. Three samples referred to as “short”, “medium”, and “long” heat treatment were tested. Heat treatment homogenizes the alloy and decreases the fraction of carbides. Table 4-4 lists the measured fraction of carbides present in each heat-treated alloy, determined using ImageJ analysis on a 200x magnification cross-sectional SEM image.

Table 4-4. Fraction of carbides in heat treated alloys, measured from 200x magnification cross-sectional SEM image.

	Heat Treatment		
	short time	**medium time**	**long time**
Fraction of carbides	0.40	0.27	0.13

4.2 Hot Corrosion Exposures

4.2.1 Environments Studied

Environments of dry air and O_2+(2.5, 10, and 100) ppm SO_2 were studied. In the SO_2-containing environments a platinum mesh was placed upstream at the edge of the hot zone to catalyze the reaction shown in equation 4-1.

$$SO_2 + \frac{1}{2}O_2 = SO_3 \qquad (4-1)$$

The gases were obtained premixed from Matheson Gas Products, Inc. Equilibrium SO_3 pressure at each temperature was determined using HSC Software [100]. The resulting values are shown in Table 4-5. As temperature increases for a given environment, the SO_3 pressure decreases.

Table 4-5. Calculated equilibrium SO_3 pressure in O_2-SO_2 environments studied from 550°C-1000°C.

	O_2-2.5 ppm SO_2	**O_2-10 ppm SO_2**	**O_2-100 ppm SO_2**
550°C	2.40×10^{-6}	9.58×10^{-6}	9.58×10^{-5}
600°C	2.27×10^{-6}	9.10×10^{-6}	9.10×10^{-5}
650°C	2.07×10^{-6}	8.29×10^{-6}	8.29×10^{-5}
700°C	1.79×10^{-6}	7.16×10^{-6}	7.16×10^{-5}
750°C	1.46×10^{-6}	5.83×10^{-6}	5.83×10^{-5}
800°C	1.13×10^{-6}	4.51×10^{-6}	4.51×10^{-5}
850°C	8.40×10^{-6}	3.36×10^{-6}	3.36×10^{-5}
900°C	6.14×10^{-6}	2.26×10^{-6}	2.46×10^{-5}
950°C	4.46×10^{-6}	1.78×10^{-6}	1.78×10^{-5}
1000°C	3.25×10^{-6}	1.30×10^{-6}	1.30×10^{-5}

4.2.2 Experimental Set-up and Procedure

A horizontal three-zone furnace (Mellen Corp.) was used for hot corrosion testing. A schematic of the set-up is shown in Figure 4-2. An argon and an O_2-xSO_2 gas cylinder are connected to the furnace. Argon was used for flushing the furnace after O_2-xSO_2 exposure. The outlet of the furnace was connected to a saturated solution of Na_2CO_3, for removal of SO_2 and SO_3 from the exiting gas.

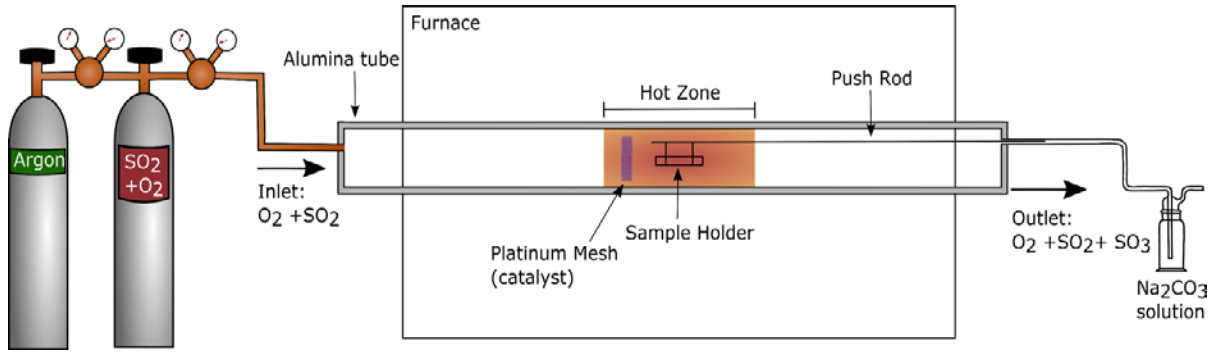

Figure 4-2. Schematic of furnace set-up.

The testing procedure was as follows:

1. The sample was ground to a 1200 grit surface finish and then ultrasonically cleaned in ethanol for at least 5 minutes.
2. The weight and surface area of the sample was recorded.
3. If an Na_2SO_4 deposit was applied, a saturated solution of DI water + Na_2SO_4 was used to spray 2.5 ± 0.5 mg/cm^2 of deposit onto one surface of the sample. This was achieved by heating the sample with a heat gun to ~200°C. The sample was held up to the spray gun using tweezers.

After 20 seconds, the saturated solution of DI water + Na_2SO_4 was sprayed onto the heated sample, which caused the water in the sprayed deposit to evaporate leaving behind Na_2SO_4 deposit. Continued heating and spraying followed until the desired deposit mass was achieved. Using this method, an adherent deposit forms uniformly on the surface.

4. Once a deposit was applied, the sample was then placed in an alumina boat at the entry of the work tube, which in turn was sealed. Pre-mixed xSO_2+O_2 was then flowed through the furnace, which was set at the desired temperature, at a rate of 50 mL/min for 2 hours.
5. After 2 hours of flushing, the sample was inserted into the hot zone of the furnace for the pre-determined test period.
6. After exposure, the sample was withdrawn from the furnace hot zone and argon flushed for 1 hour to ensure removal of the xSO_2+O_2 gas, then the sample was removed.
7. After removal from the furnace, the weight gain of the sample was recorded.
8. The sample was then characterized using various techniques that will be outlined in the following section.

4.3 Analytical Methods

Before cold-mounting the exposed samples in epoxy for metallographic preparation, surface characterization may have been done. After surface analysis, if done, the samples were cold mounted in an epoxy resin and then cross-sectionally polished to a 0.25 μm finish using an oil-based solution to preserve the water-soluble products. The following are the characterization techniques that were used in this study.

Scanning Electron Microscopy (SEM) and Energy Dispersive X-Ray Spectroscopy (EDS)

SEM was used to generate images of the corrosion products. Most images were taken using backscattered electrons. Cross-sections of samples as well as sample surfaces were analyzed using SEM. Standardless EDS was done on areas to obtain semi-quantitative information on the elements and amount present. Three SEMS were used in the study: a JEOL JSM 6610LV, a ZEISS Sigma 500 VP, and an FEI Apreo. The ZEISS and FEI SEMs are field-emission and so used when better resolution was needed. The JEOL is an environmental SEM. The ZEISS and JEOL were equipped with Oxford Aztec X-EDS. The FEI was equipped with EDAX TEAM for EDS. Surface SEM imaging and EDS analysis was done at 10 kV. Cross-sectional imaging and EDS analysis was done at 20 kV.

Electron Probe Microanalysis (EPMA)

EPMA was conducted on cross sections when better chemical resolution than EDS analysis was desired. The EPMA has wavelength dispersive spectroscopy (WDS) capability, which has better spectral resolution than EDS, allowing for more accurate compositional measurements. In addition, PWA 1484 and ME 16 contain molybdenum, which has a characteristic energy level emission very close to that of sulfur. In addition, EDS peaks for Ta and W are very close.

Analyzing the wavelength instead eliminates this problem. A JEOL JXA-8530F EPMA was used for the analysis. Elemental maps were created, which does not require the use of standards.

Transmission Electron Microscopy (TEM)

TEM analysis was conducted on select samples for high-resolution assessment. A length of 10µm x 10µm thin foil for TEM analysis was lifted from a given polished cross-sectional mount using a Scios™ Dual-Beam™ FIB/SEM. A JEOL 2100F transmission electron microscope (TEM) was used for sample analysis.

Raman Spectroscopy

Raman spectroscopy was conducted on the surface of select samples to identify the oxides that formed. A Reinshaw inVia Raman microscope was used for the analysis, operating with a 633 nm laser.

X-Ray Diffraction (XRD)

X-Ray diffraction was done to identify the phases present after a given exposure. XRD is a surface characterization technique. A Bruker D8 Discover X-ray Diffraction system with a Cu Kα source was used at 40 kV and 40 mA. A scan range of 10° to 90° with a step size of 0.02°/sec was used.

Inductively Coupled Plasma – Optical Emission Spectroscopy (ICP-OES)

ICP-OES enables determination of the concentration of water soluble species in a given product or deposit. Considering a sodium sulfate deposit in contact with an alloy/oxide, the products of the resulting interaction from dissolution or compound formation incorporating sulfur and oxygen tend to be soluble in water. Therefore, elemental concentration detected using ICP-OES analysis could be correlated to what elements are participating in the reaction and the extent

of attack. ICP was done after submerging a sample in 20 mL of hot DI water, then after 24 hours that water was tested in the ICP-OES. A Thermo Scientific iCAP 7000 Series was used for ICP-OES analysis. Elemental standards were obtained from SPEX CertiPrep.

Thermogravimetric Analysis (TGA)

TGA in air was done on a nickel sample. TGA analysis is used for determining reaction rate(s) by measuring weight gain vs. time. The TGA used was a Setaram TAG.

5.0 Results and Discussion

5.1 Solid-state Mode of Hot Corrosion Occurring at 700°C and Below

This chapter is modified from the published paper: E. Kistler, W. T. Chen, G. H. Meier, and B. Gleeson, "A new solid-state mode of hot corrosion at temperatures below 700°C," *Mater. Corros.*, vol. 70, 2019, pp. 1346–1359 [101].

Considering the mechanisms discussed in Chapter 2.3 for Type II hot corrosion, it is generally believed liquid formation is required either through Na_2MoO_4 (T_m=687°C) formation or the formation of relatively low-temperature eutectic melt of $NiSO_4$-Na_2SO_4 (T_e=671°C) or $CoSO_4$-Na_2SO_4 (T_e=565°C) from reaction of the alloy with the deposit. Formation of $NiSO_4$-Na_2SO_4 and $CoSO_4$-Na_2SO_4 requires a sufficient SO_3 pressure to stabilize liquid formation. Figure 5-1 shows a stability diagram of the CoO-Co_3O_4-$CoSO_4$-Na_2SO_4, adapted from Luthra [11] and NiO-$NiSO_4$-Na_2SO_4, adapted from Misra et al. [102]. This stability diagram defines the P_{SO_3} needed for liquid formation at a given temperature. The green line corresponds to NiO and the orange lines correspond to CoO and Co_3O_4. Above the respective lines, liquid formation is stable. Superimposed on this diagram are equilibrium P_{SO_3} contours for O_2-(2.5, 10, and 100) ppm SO_2 environments. From the diagram, it is seen that the critical P_{SO_3} for liquid stabilization is lower for cobalt. This is because $CoSO_4$ is thermodynamically more stable than $NiSO_4$. In all the environments to be studied here, liquid formation from reaction with nickel is not stable (Fig. 5-1).

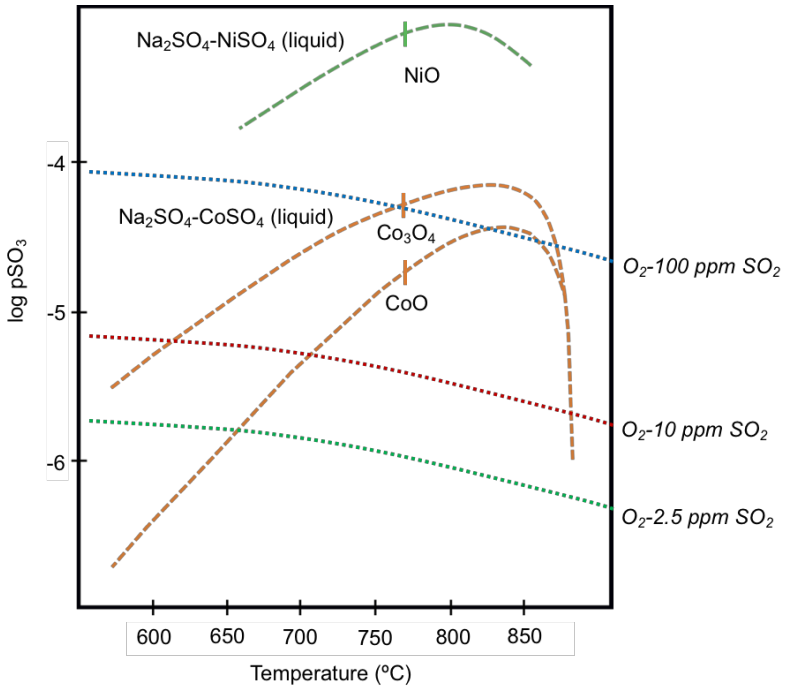

Figure 5-1. Stability diagram of the CoO-Co_3O_4-$CoSO_4$-Na_2SO_4, adapted from Luthra [11] and NiO-$NiSO_4$-Na_2SO_4, adapted from Misra et al. [102], with pSO_3 in O_2-(2.5, 10, and 100) ppm SO_2 superimposed. Above the respective curves for CoO, Co_3O_4, and NiO indicates eutectic stability. The end point at the low temperature for the curves is at the eutectic temperature; 565°C for $CoSO_4$-Na_2SO_4 and 671°C for $NiSO_4$-Na_2SO_4.

As an initial assessment of the effects of temperature and SO_2/SO_3 content on hot-corrosion behavior, 20 h exposures of PWA 1484 were conducted from 550°C-1000°C in dry air and O_2-(2.5, 10, and 100) ppm SO_2 with 2.5 mg/cm^2 Na_2SO_4. Figure 5-2 shows the resulting weight change vs. temperature plots with the region of interest for this section (550°C-650°C) highlighted. In the O_2-100 ppm SO_2 environment, spallation occurred at 750°C and 800°C so no data point is presented. In Chapter 5.3, average attack vs. temperature will be analyzed. In the region of interest for this section, at 650°C and below in the environments studied, the only possible liquid formation

under equilibrium conditions is through the formation of $CoSO_4$-Na_2SO_4 eutectic (based on Fig. 5-1). PWA 1484 is a nickel-based superalloy with relatively low cobalt content, so eutectic formation from cobalt is expected to be minimal. In addition, hot corrosion was apparently occurring at 550°C, a temperature below the $CoSO_4$-Na_2SO_4 eutectic. The research goal therefore is to understand the mechanism of low-temperature hot corrosion by an in-depth analysis of exposures with nickel-based superalloys and pure nickel.

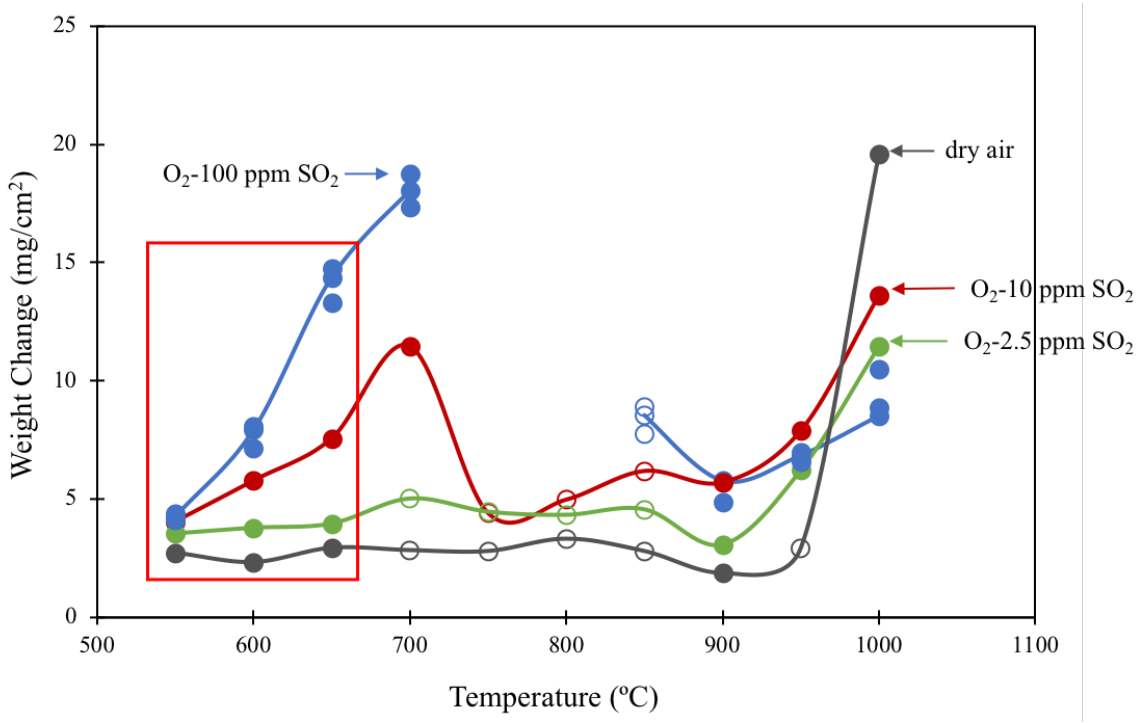

Figure 5-2. Weight change vs. temperature plots after 20 h exposures of PWA 1484 in O_2-(2.5 10, and 100) ppm SO_2 and dry air, with a 2.5 mg/cm^2 Na_2SO_4 deposit. Sample spallation occurred in the O_2-100ppm SO_2 environment at 750°C and 800°C, so no data points are shown. Three data points are shown for each O_2- 100 ppm SO_2 to illustrate the reproducibility. Open symbols indicate localized attack.

5.1.1 Nickel-based Superalloy Hot Corrosion Exposures from 550°C-650°C

5.1.1.1 PWA 1484

Cross-sectional SEM images of PWA 1484 after 20 h hot-corrosion exposure in O_2-(2.5-100) ppm SO_2 and dry air at three temperatures are shown in Fig. 5-3 The corrosion-product morphologies are seen to be similar; although, the extent of corrosion generally increases with increasing SO_2 content and temperature. The corrosion product in the SO_2-containing environments consisted of (Ni,Co)O at the sulfate/gas interface, with distinct sulfate particles in the oxide. The internal product consisted of a mixed oxide/sulfide, containing all elements of the base alloy, with Al content the highest. Figure 5-3 (b) identifies the corrosion products, as deduced from EDS analysis, in the scale formed after hot-corrosion exposure at 600ºC in O_2-2.5 ppm SO_2. Most noteworthy are the (Ni,Co)O channels which formed through the deposit thickness. By contrast, exposures in the SO_2-free air environment resulted in only slight oxide formation within the deposit. Moreover, the oxide did not reach to the sulfate/gas interface, indicating that the presence of SO_2/SO_3 is essential for the attack to propagate. Figure 5-4 shows a high magnification image of the internal product at 650°C after the 20 h exposure, along with associated EDS results. The sulfur content was highest at the alloy/mixed oxide/sulfide interface and preferential attack of the γ phase at this interface was observed. A remnant of the base-alloy γ/γ' microstructure is observed in the internal product and is inferred to be due to slow kinetics of element diffusion in the base alloy at this low reaction temperature. The phenomenon has been reported in previous studies [13, 103].

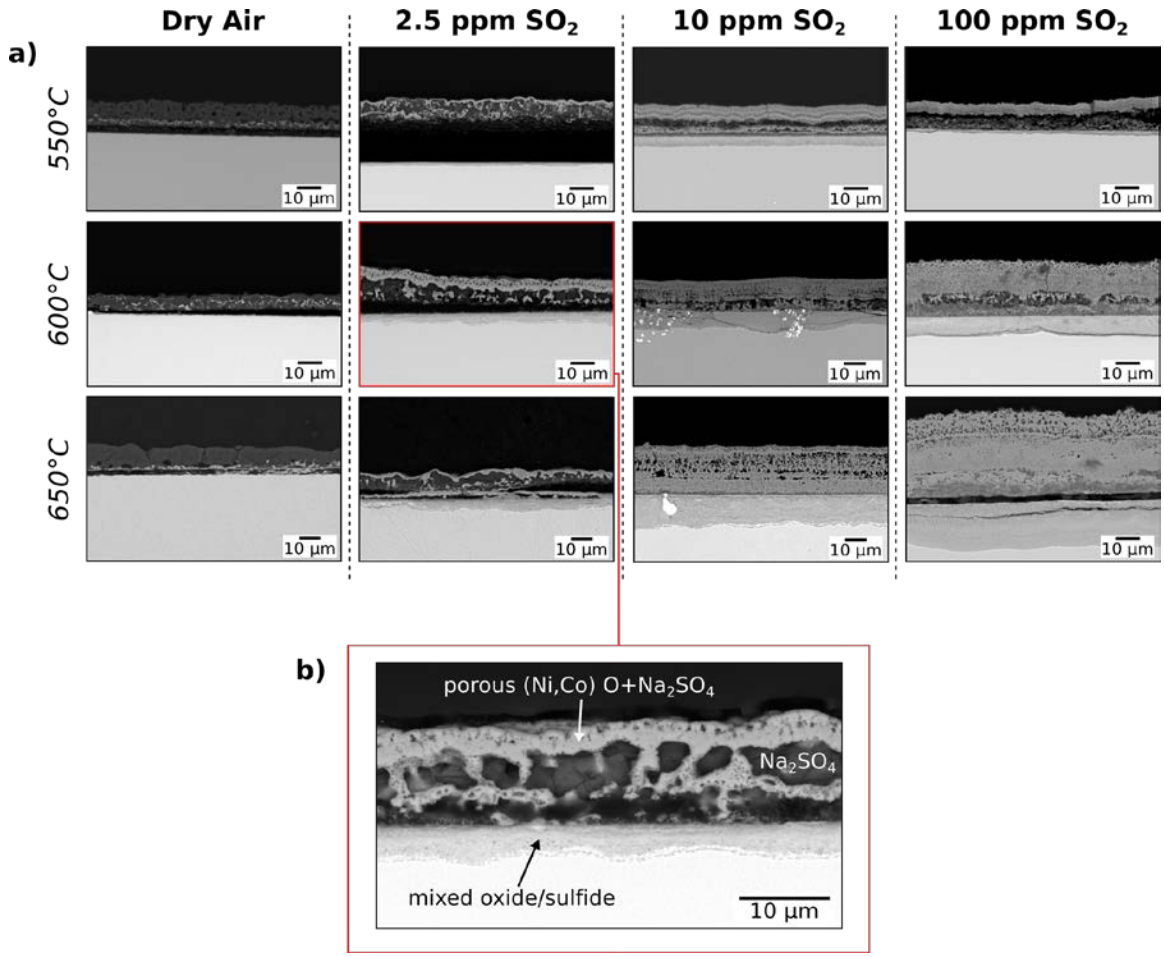

Figure 5-3. (a) Cross-sectional SEM images of the corrosion products formed on PWA 1484 after 20 h hot-corrosion exposure in air and O_2-(2.5, 10, and 100) ppm SO_2 and with 2.5 mg/cm^2 Na_2SO_4 deposit. (b) Phase identification for 600°C in O_2-2.5 ppm SO_2 based on EDS analysis.

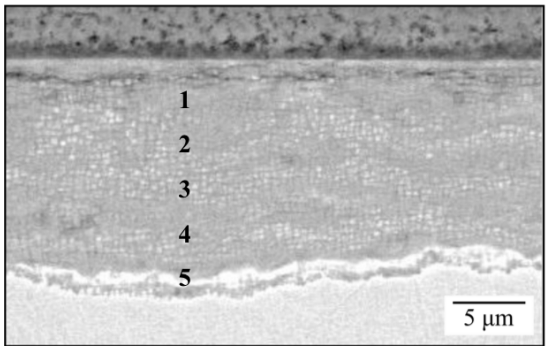

	O	Na	Al	S	Cr	Co	Ni	Ta + W + Re
1	66	2	11	3	6	0	7	5
2	64	0	12	4	7	0	8	6
3	62	2	13	3	7	0	7	6
4	61	2	12	4	7	0	8	6
5	48	0	14	16	6	0	4	12

Figure 5-4. Cross-sectional SEM images of interal corrosion product on PWA 1484 after 20 hr exposure at 650°C in O_2-10 ppm SO_2 and with 2.5 mg/cm^2 Na_2SO_4 deposit, along with EDS results where the numbers in the image correspond to the numbers in the accompanying table.

Time studies were conducted at 550°C and 650°C in the 10 ppm SO_2 environment to better understand the reaction progression. The scale development was similar at both temperatures. The 650°C results are presented in Fig. 5-5 for six different exposures times. For comparison, an image from the 6 h exposure at 550°C is shown in Fig. 5-6. As shown in Fig. 5-5, an oxide layer forms at the sulfate/alloy interface within 30 minutes exposure. Based on EDS analysis, nickel is the primary metal component in this oxide layer. After an hour of exposure, a thin layer of (Ni,Co)O is clearly present at the sulfate/gas interface. The cobalt content in this layer is less than 10 at.%. Localized regions of (Ni,Co)O are seen in Fig. 5-5 to also be distributed within the Na_2SO_4 deposit after the 1, 2 and 4 h exposures. As noted earlier, these regions often extended through the deposit in the form of channels. The magnified image of the outer (Ni,Co)O layer of the 4 h exposed specimen shows that it contains occluded sulfate, suggesting that this layer thickens by inward progression at the oxide/sulfate interface. The 15 h exposed specimen shows that the Na_2SO_4 deposit becomes consumed by the continued growth of the inner and outer (Ni,Co)O layers. After

20 h of exposure there is no evidence of the deposit layer, though regions of sulfate are distributed throughout the merged (Ni,Co)O scale. The overall thickness of the (Ni,Co)O scale is ~25µm after 20 h of exposure at 650ºC, whereas it was ~8µm after 20 h at 550°C.

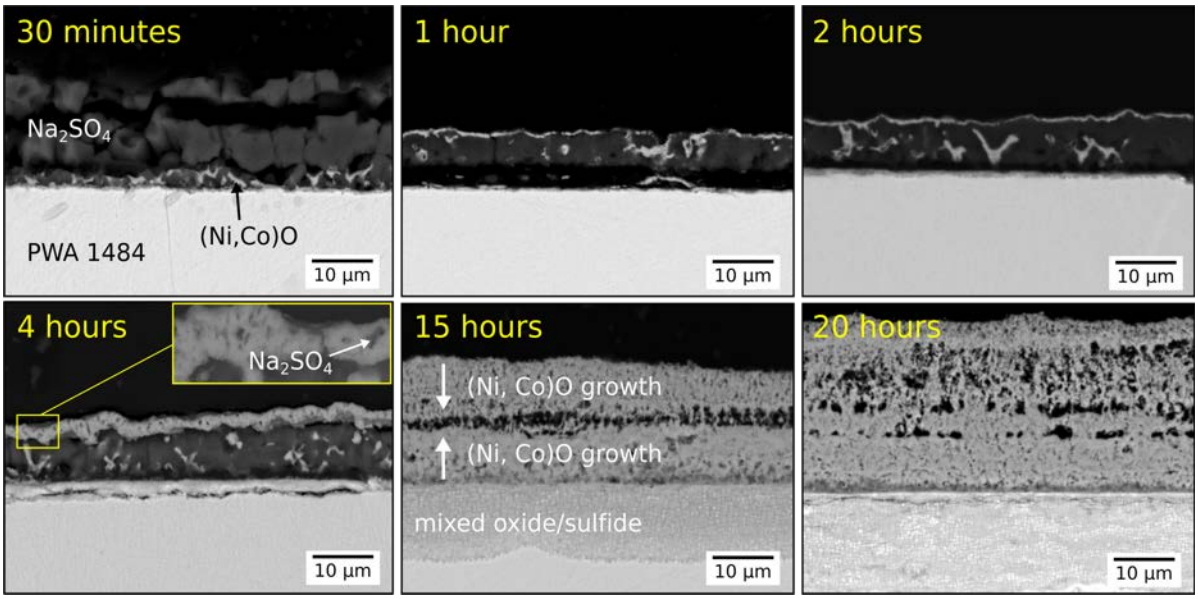

Figure 5-5. Cross-sectional SEM images after a time study completed on PWA 1484 at 650°C in O_2-10 ppm SO_2 and with 2.5 mg/cm^2 Na_2SO_4 deposit.

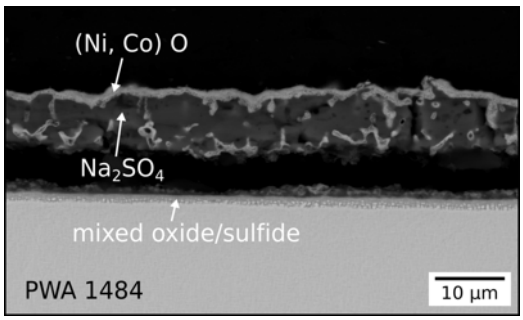

Figure 5-6. Cross-sectional SEM image after 6 h exposure of PWA 1484 at 550°C in O_2-10 ppm SO_2 and with 2.5 mg/cm^2 Na_2SO_4 deposit.

The cobalt content in the sulfate deposit after a given exposure was found by EDS analysis to be very low, while the nickel content exceeded the solubility given by the $NiSO_4$-Na_2SO_4 phase diagram [61]. For example, after a 6 h exposure in the O_2-10ppm SO_2 environment at 650°C the Na_2SO_4 deposit was found to contain an average of 9 at. % Ni (phase diagram indicates the Ni solubility in Na_2SO_4 to be ~5 at.% at 650ºC) and a maximum of 1 at.% Co. Often the Co content was not even measurable in the sulfate.

5.1.1.2 ME 16

A turbine disk operates at temperatures from ~400°C to a maximum of 800°C at the outer rim [17]. The low-temperature corrosion seen on PWA 1484 is therefore likely to affect disk components. Hot corrosion exposures of the disk alloy ME 16 were completed for up to 300 h at 550°C and 650°C in dry air and O_2-10 ppm SO_2. The resulting weight gain vs. time graph for the O_2-10 ppm SO_2 environment is shown in Fig. 5-7. Very minimal attack occurred in dry air. Cross-sectional SEM images after 300 h at each exposure temperature in O_2-10 ppm SO_2 are shown in Fig. 5-8. The morphology of the corrosion product looks very similar to PWA 1484, i.e., porous (Ni, Co)O with entrapped Na_2SO_4 and an internal mixed oxide/sulfide product. The mechanism of hot corrosion is expected to be similar for the two alloys since the product morphology is similar and both alloys are nickel-based with many of the same alloying elements. Comparing corrosion rate, PWA 1484 is much more severe after a 20 h exposure. The Cr content in ME 16 is ~14 at. %, while PWA 1484 is only ~6 at. %. The difference in corrosion extent is postulated to be related to scale formation, where an increase in Cr in the alloy allows for protective scale formation that delays the onset of accelerated hot corrosion.

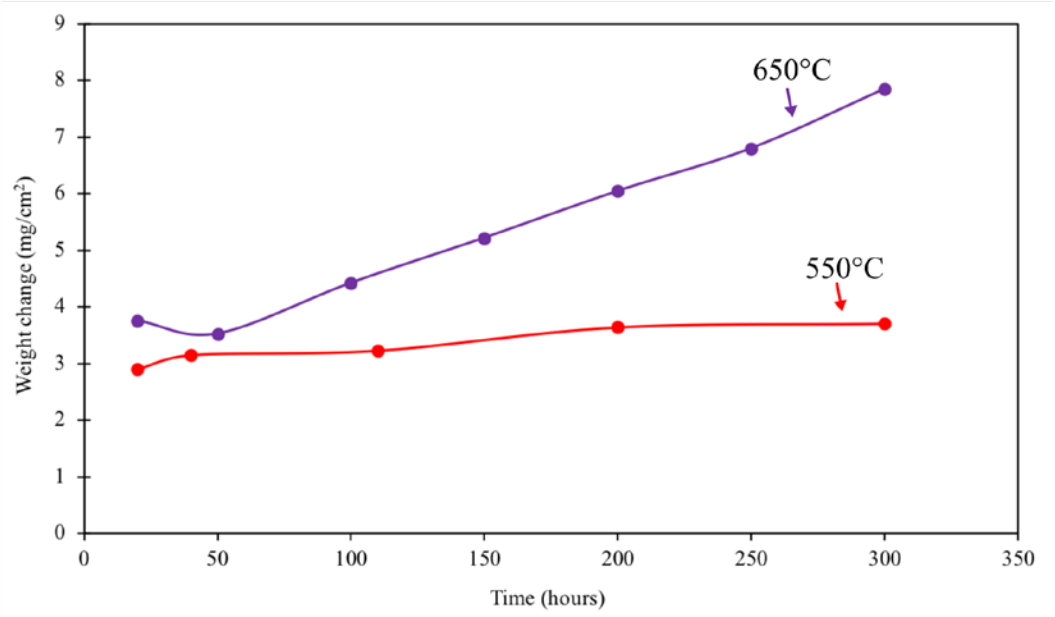

Figure 5-7. Weight change vs. time after exposure at 550°C and 650°C of ME 16 with 2.5 mg/cm^2 Na_2SO_4 in O_2-10 ppm SO_2.

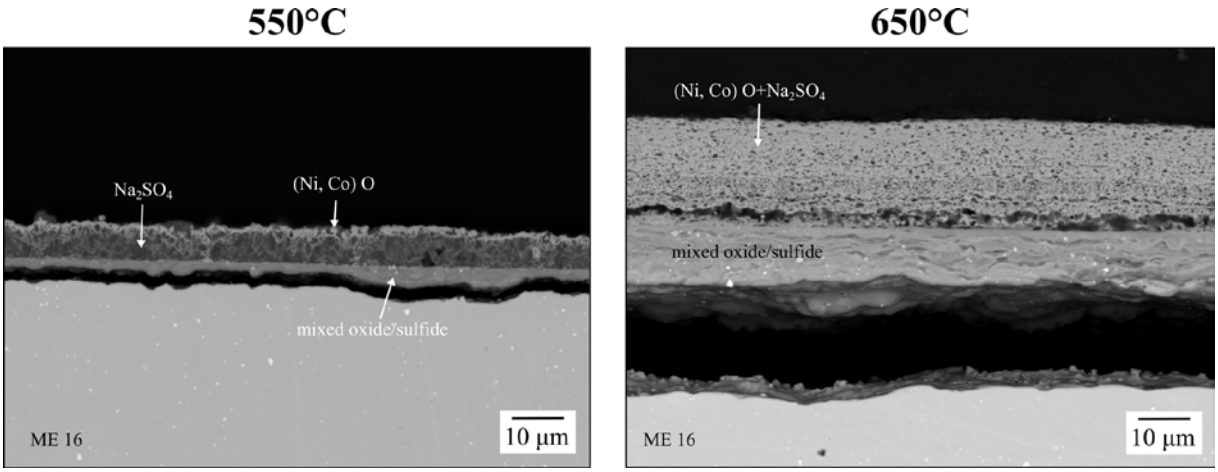

Figure 5-8. Cross-sectional SEM images after 300 h exposure of ME 16 at 550°C and 650°C in O_2-10 ppm SO_2 and with 2.5 mg/cm^2 Na_2SO_4.

5.1.2 Ternary Liquid Assessment

Hot corrosion was found to occur at 550°C, which is below the Na_2SO_4-$CoSO_4$ and Na_2SO_4-$NiSO_4$ eutectics, which are 565ºC and 671ºC, respectively. The possibility of an Na_2SO_4-$CoSO_4$-$NiSO_4$ ternary mixture that melts below 550°C was considered. As mentioned in an article by Jones and Gadomski [67], Co_3O_4-NiO-Na_2SO_4 in 3000 pm SO_2 at 750°C produced a ternary Co-Ni-Na mixed sulfate that was more reactive than just Ni or Co, but they did not conclude a ternary eutectic was forming. To test for a ternary eutectic with a T_e as low as 550°C, mixtures of xNa_2SO_4-$yCoSO_4$-$zNiSO_4$ were placed in an alumina boat and exposed for 2 h at 650°C in O_2-10 ppm SO_2. Figure 5-9 is a ternary section that shows Na_2SO_4-$CoSO_4$-$NiSO_4$ sulfate mixtures tested. Compositions that exhibited liquid formation are indicated in this diagram, as determined using visual analysis coupled with cross-sectional SEM images shown in Fig. 5-10. Attachment of the sulfate mixture to the alumina boat or fusing of the deposit indicates some fraction of liquid formation. Composition 6, which remained solid, was representative of a composition detected in remnant sulfate deposit after a hot corrosion exposure. Liquid formation only occurred 650°C if significant $CoSO_4$ content was present. Therefore, any possible liquid formation at an exposure temperature of 650°C would have to be to cobalt-rich liquid channels, which were undetected using EDS analysis.

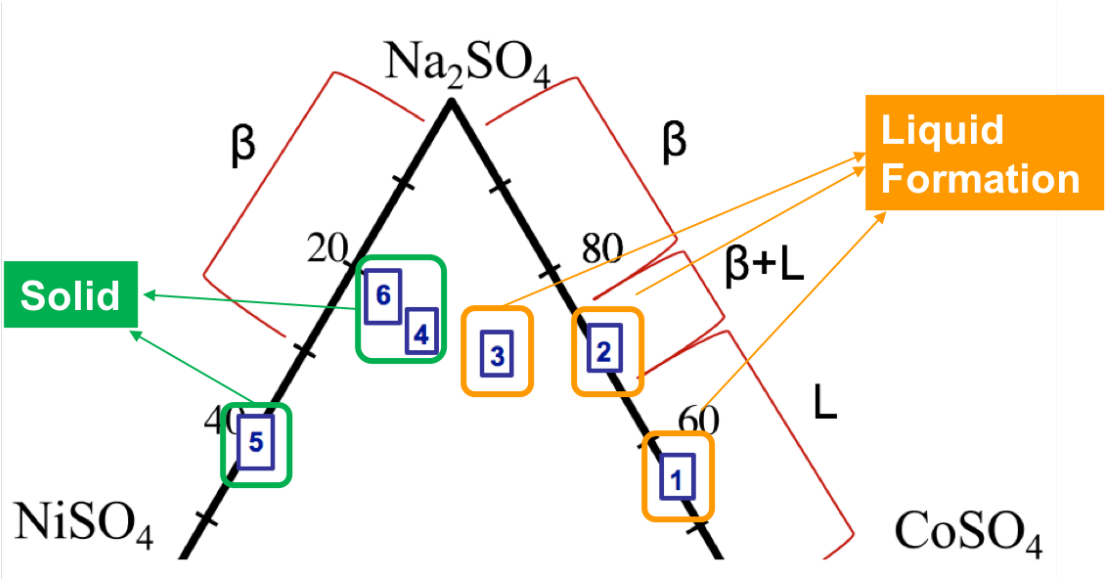

Figure 5-9. Ternary Na_2SO_4-$CoSO_4$-$NiSO_4$ digram with mixtures tested for liquid formation at 650°C in O_2-10 ppm SO_2 for 2 h.

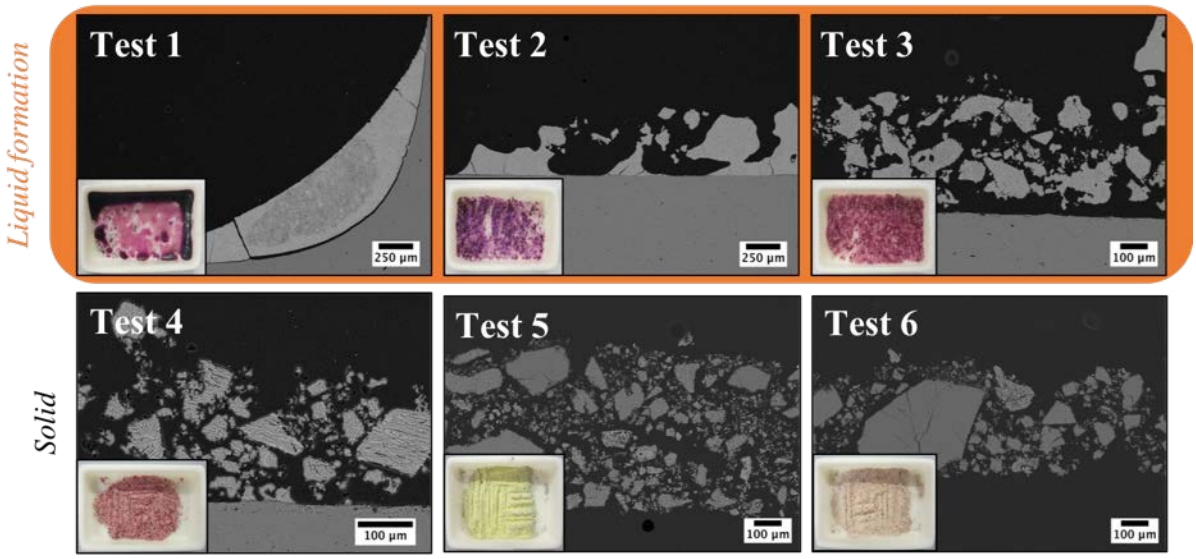

Figure 5-10. Cross-sectional SEM images of sulfate mixtures after exposure at 650°C in O_2-10 ppm SO_2 for 2 h. The test numbers correspond to the numbers in Fig. 5-9.

Additional experiments were completed using differential scanning calorimetry (DSC) to determine the accuracy of the previously-reported binary phase diagrams of Na_2SO_4-$CoSO_4$ and Na_2SO_4-$NiSO_4$ [104]. The experiments were done by a Matthew Kovalchuk in our group [105]. The environment used was dry air. The binary phase diagrams were then calculated using Pandat™ [106] for comparison between experimental and computational analyses. Figure 5-11 shows the results for both diagrams. The experimental and computational results agreed, and were also in agreement with previous experiments [104]. The Na_2SO_4-$NiSO_4$ eutectic is ~671°C and the Na_2SO_4-$CoSO_4$ eutectic is ~565°C.

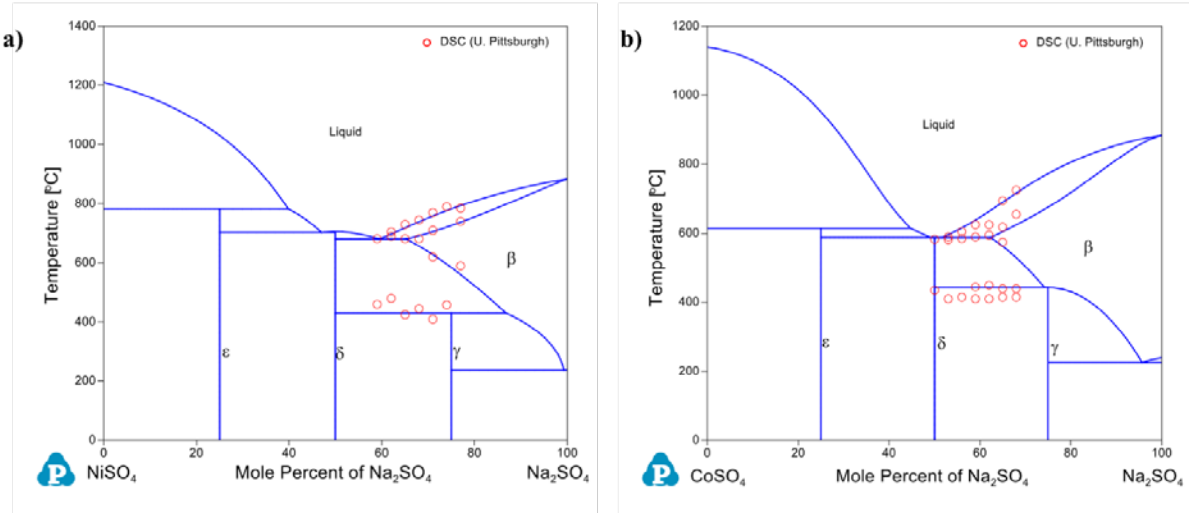

Figure 5-11. NiSO-Na_2SO_4 and $CoSO_4$-Na_2SO_4 phase diagrams calculated from Pandat™ [106]. DSC measurements are superimposed on the diagrams.

Additional DSC experiments were conducted in dry air using ternary Na_2SO_4-$NiSO_4$-$CoSO_4$ mixtures, modeled after the work by Bol'shakov and Feorov [107]. This was done to verify the visual examinations presented above using a more precise measurement method. The experiments were compared to diagrams calculated using Pandat^{TM} [106]. Figure 5-12 shows the results for both experiments, with a constant ratio of $CoSO_4$:$NiSO_4$ ratio of 3:1, 1:1, and 1:3. The red circle data points in the figures are from the work of Bol'shakov and Feorov [107], and the blue square data points are the DSC results. The results confirm that no ternary mixture melts as low as 550°C. Therefore, the operating low-temperature corrosion mechanism found in this study is inferred to be solid-state.

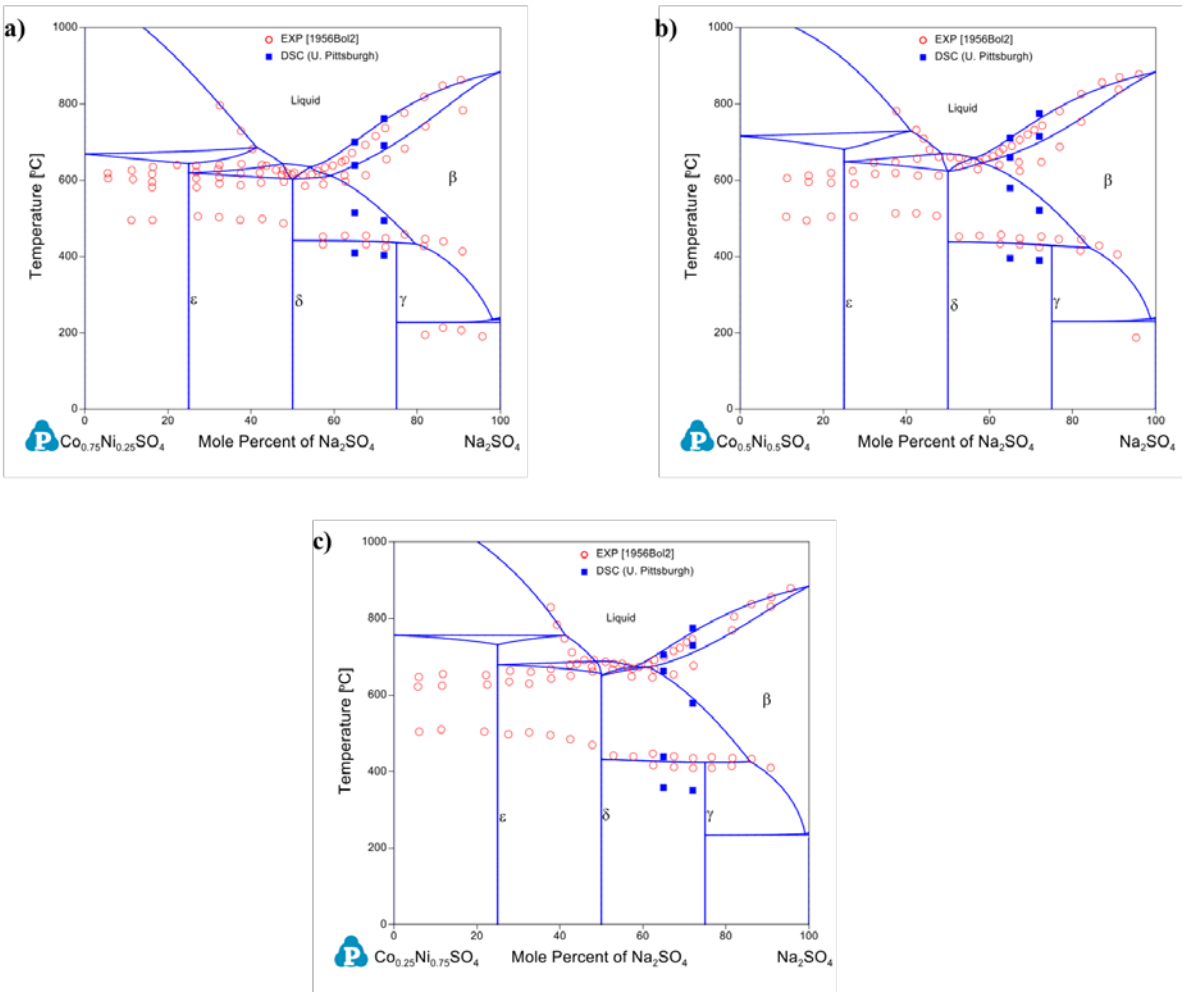

Figure 5-12. Sections of a ternary phase diagram of $CoSO_4$-$NiSO_4$-Na_2SO_4 for constant $CoSO_4$-$NiSO_4$ ratios of a) 3:1, b) 1:1, and c) 1:3 calculated using Pandat™ [106]. The red circle data points are from the work of Bol'shakov and Feorov [107], and the blue data points are from DSC experiments [105].

5.1.3 Nickel-Na_2SO_4 Diffusion Couples

To assess the solid-state lattice diffusion of nickel in sodium sulfate, pseudo Ni/Na_2SO_4 diffusion couples were prepared. This was done by submerging a nickel sample into fused Na_2SO_4 which was subsequently solidified. The sulfate was contained in an alumina crucible and melting

was done in an argon atmosphere. The time of contact between the liquid Na_2SO_4 and the nickel sample was less than 5 mins. The pseudo diffusion couples were then exposed at 650°C for 4 h in dry air and O_2-10 ppm SO_2 environments. Figure 5-13 shows the resulting measured plots of nickel content in the sulfate as a function of distance from the nickel/sulfate interface.

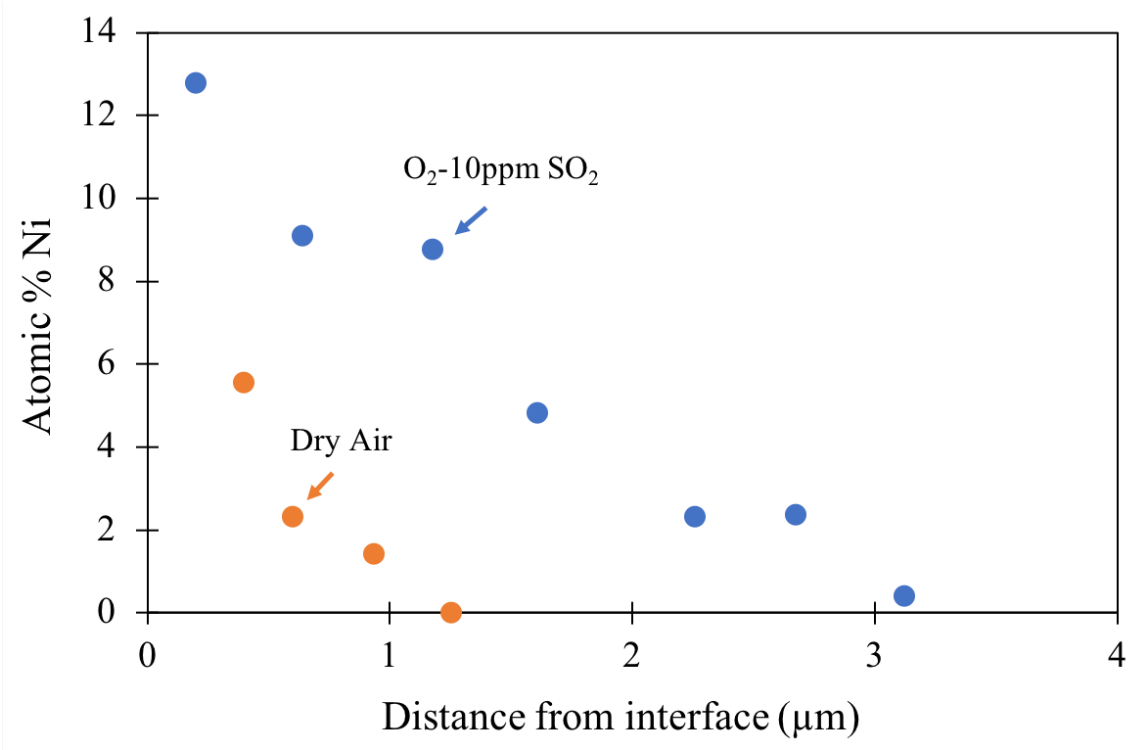

Figure 5-13. Plot of measured nickel content vs. distance into sulfate (from the nickel/sulfate interface) after exposure of nickel/Na_2SO_4 diffusion couples in O_2-10 ppm SO_2 and dry air for 4 h at 650°C.

Assuming semi-infinite diffusion [108] and a stationary Ni / Na_2SO_4 interface, the diffusion coefficient of nickel in Na_2SO_4 was calculated using Eq. 5-1. $C_{(x,t)}$ is the concentration at a specified distance and time, C_s is the surface concentration, C_o is the initial concentration, *x* is the distance,

D is the diffusion coefficient, and *t* is time. The diffusion coefficient was determined to be 1.3×10^{-12} cm^2/s for the SO_2-containing environment and 3.5×10^{-13} cm^2/s for the air environment.

$$\frac{C_{(x,t)} - C_s}{C_o - C_s} = \text{erf}\left(\frac{x}{2\sqrt{Dt}}\right) \qquad (5-1)$$

Using these diffusion coefficients, the times it would take to diffuse 10μm (~the thickness of the 2.5 mg/cm^2 Na_2SO_4 deposit) are approximated using Eq. 5-2 to be 218 h in the O_2-10ppm SO_2 environment and 798 h in the air environment.

$$x = \sqrt{Dt} \qquad (5-2)$$

Given that the results in Fig. 5-5 show extensive corrosion after only 20 h of exposure, it is clear, based on these diffusion calculations, that the necessary nickel transport for such corrosion cannot be ascribed to nickel diffusion through the sulfate lattice. Rather, some form of a "short-circuit" diffusion process must be responsible for the attack.

5.1.4 Pure Nickel Hot Corrosion Exposures

Specimens of pure nickel (99.98% purity) were also studied with the aim of better understanding the mechanism of the observed low-temperature corrosion. Corrosion exposures were conducted from 500°C to 650°C in O_2-10ppm SO_2 for 20 h and using about 2.5 mg/cm^2 Na_2SO_4 deposit. Thus, all exposure temperatures were below the Na_2SO_4-$NiSO_4$ eutectic.

Resulting cross-sectional SEM images are shown in Fig. 5-14. The morphology of the reaction products at 500°C and 550°C are very similar to the alloy exposures, further supporting the inference that the corrosion mechanism involves a solid-state process. At those temperatures the corrosion product consisted of porous NiO at the gas/sulfate interface and within the deposit. The porous NiO contained distinct regions of Na_2SO_4. Interestingly, no visible interaction occurred between the oxide and the deposit at 650°C and the deposit appeared completely sintered after the 20 h exposure.

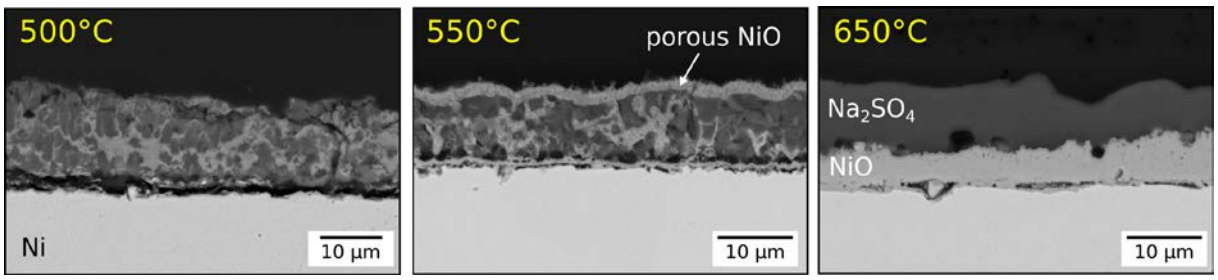

Figure 5-14. Cross-sectional SEM images of nickel samples after 20 hr exposure in O_2-10 ppm SO_2 and with 2.5 mg/cm^2 of Na_2SO_4 deposit.

To determine if pre-oxidation could affect subsequent corrosion, nickel specimens were pre-oxidized in air at two different temperatures (700°C and 1000°C) to obtain a ~5µm scale and then hot-corroded (*i.e.*, 2.5 mg/cm^2 Na_2SO_4 deposit) at 650°C in O_2-10ppm SO_2. The resulting cross-sectional SEM images after 20 h exposure are shown in Fig. 5-15. When the nickel specimen was pre-oxidized at a low temperature (700°C), an outermost ~10 µm porous NiO layer containing Na_2SO_4 formed. Figure 5-16 shows an EDS map taken from a TEM sample of the outer porous NiO and reveals the presence of the fine precipitates of Na_2SO_4 (identified based on EDS analysis).

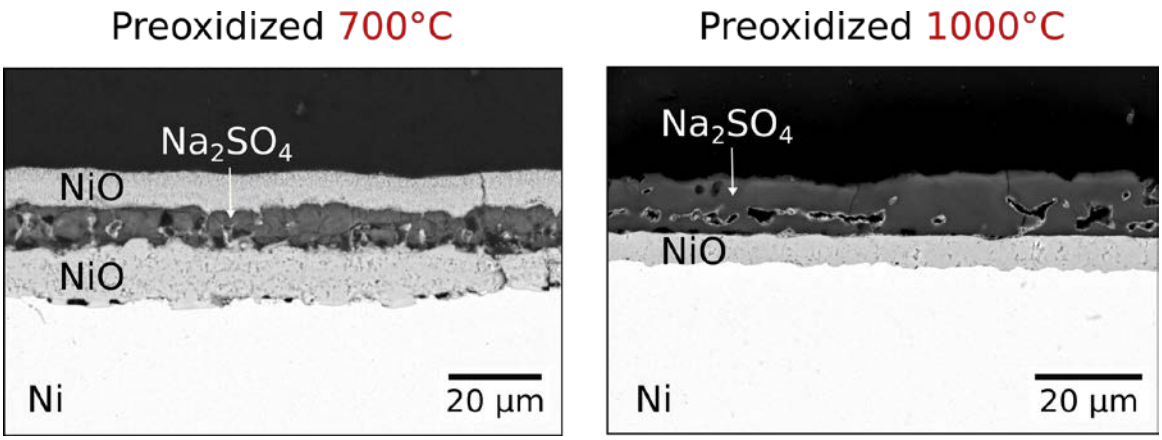

Figure 5-15. Cross-sectional SEM images of nickel samples preoxidized at 700°C for 24 h and 1000°C for 0.5 h followed by 20 h exposure in O_2-10 ppm SO_2 and with 2.5 mg/cm^2 of Na_2SO_4 deposit.

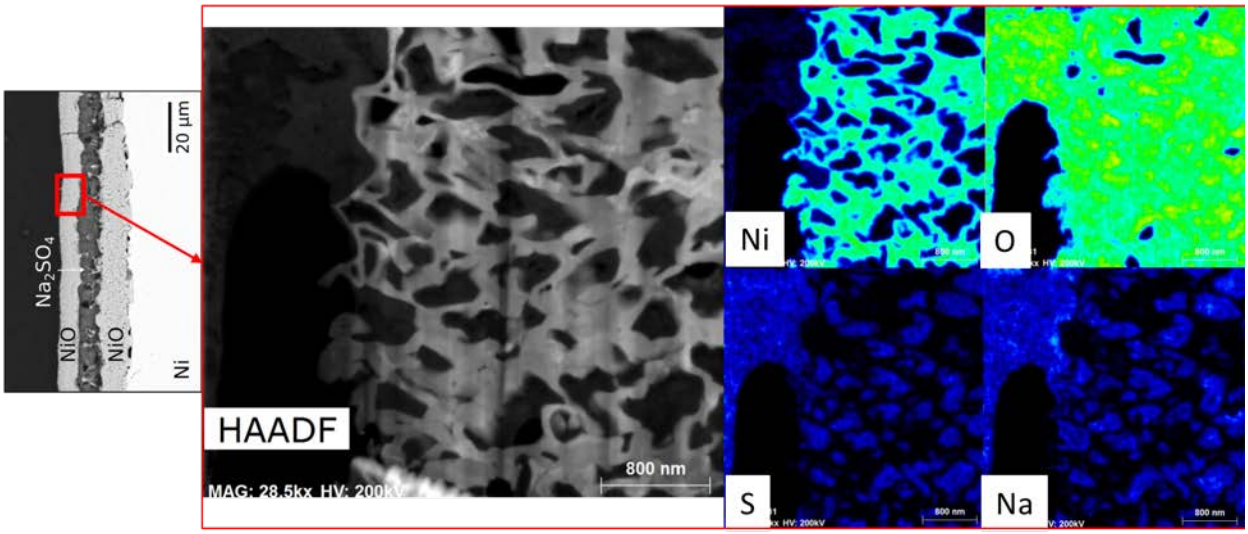

Figure 5-16. EDS map of area shown in SEM cross-sectional image on the left of preoxidized Ni at 700°C for 24 h followed by 20 hr exposure in O_2-10 ppm SO_2 at 650°C with 2.5 mg/cm^2 Na_2SO_4 deposit. EDS map was taken of porous NiO that formed at the gas/sulfate interface [109].

At the metal/oxide interface, sulfides were present and the enrichment of sulfur at that interface may have stabilized void formation [110]. A minimal amount of sulfur (max. ~2 at.%) was detected within the pre-formed oxide after the hot-corrosion exposure and no sulfide network was established throughout the scale. When pre-oxidized at a higher temperature (1000°C), little to no oxide-sulfate interaction was observed to occur and no sulfur was present in the NiO or at the oxide/metal interface. Therefore, the channel-formation mechanism and associated formation of an outermost NiO-rich layer must not have involved decomposition of the existing NiO, but rather relied on Ni^{2+} supplied via diffusion through this oxide scale. Peraldi *et al.*[109, 110] reported a detailed study on NiO-scale growth at 500-1200°C and showed that as temperature increases, the NiO grain size also increases. This is confirmed qualitatively in Fig. 5-17, which shows surface images of the NiO scale after pre-oxidation in air at the two different temperatures. Oxidation at 700°C resulted in a fine-grained, porous structure; while oxidation at a higher temperature of 1000°C resulted in a large-grained structure. At the low temperatures of hot-corrosion exposures, grain-boundary diffusion of nickel through the NiO scale would predominate [111, 112]. The fine-grained structure of the NiO formed during 700°C pre-oxidation would provide the highest nickel flux, which apparently facilitated the subsequent Na_2SO_4-induced oxidation.

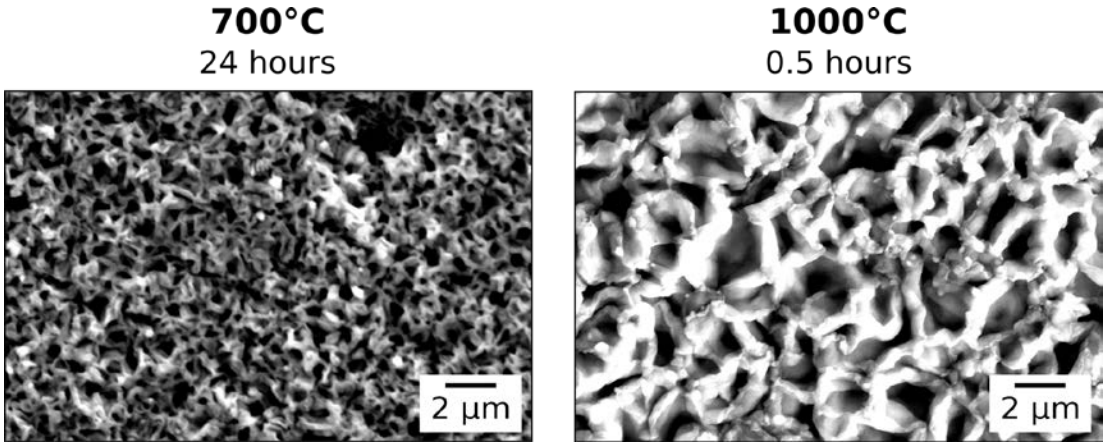

Figure 5-17. Surface images of NiO scale after preoxidation exposure at the indicated temperature.

To further assess the mechanism controlling the NiO formation above the sulfate deposit, the interaction of individual Na_2SO_4 crystals on pure nickel specimens was studied. Figure 5-18 shows SEM cross-sectional images after 20 h exposure at 650°C and 625°C in O_2-10 ppm SO_2 (*n.b.*, the magnification of the images are different). It is seen that an effective "wetting" of the Na_2SO_4 crystals by NiO occurred. At the lower exposure temperature NiO was only able to form over the entire surface of smaller crystals, due to decreased kinetics. Even so, and given that the test temperature is below the Ni-Ni_3S_2 eutectic of 645°C [29], the results further confirm that the corrosion process involves a solid-state mechanism.

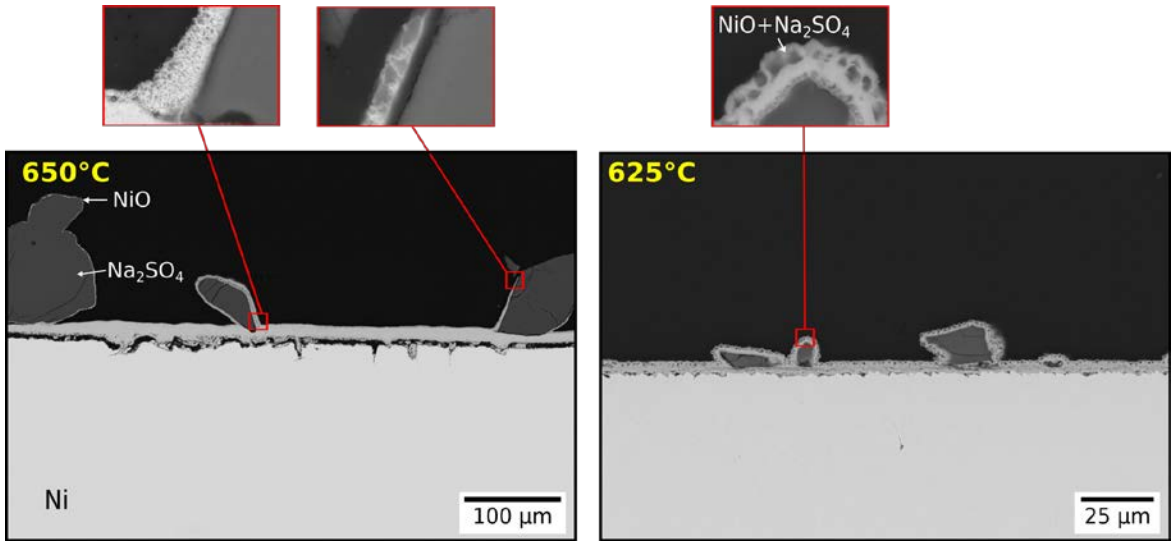

Figure 5-18. Cross-sectional SEM images after 20 h expsoure of nickel in O_2-10 ppm SO_2 with crystals of Na_2SO_4 on an initially bare (i.e., unnoxidized) nickel surface.

For the 650°C exposure, separation of the NiO scale at the oxide/metal interface occurred and localized nickel sulfide of an undetermined stoichiometry was detected at that interface, but no sulfide formation was found in the scale. In the case of the 625°C exposure, which is below the Ni-Ni_3S_2 eutectic, sulfide formation also occurred at the oxide/metal interface along with void formation, but scale spallation was not as severe. As with the 650°C exposure, no connected network of sulfides was detected within the NiO. At both exposure temperatures, the scale that formed in proximity to a given sulfate crystal was consistently much thicker than NiO scale formed in O_2-10 ppm SO_2 without a deposit applied (~2-3µm oxide). This interesting observation will be discussed in a following section, but it is relevant to note here that the proximal influence of the sulfate in accelerating the scale growth rate is inferred to be by a solid-state mechanism that is similar to what will be presented in the following.

A magnified image of the reaction products on the Na_2SO_4 crystal is shown in Fig. 5-18 for both exposure temperatures. A porous NiO formed along the surface and into the lattice of the sulfate. Discrete regions of Na_2SO_4 are contained within the NiO. The exposure of Ni with Na_2SO_4 crystals was repeated in a dry air environment, as shown in Fig. 5-19, at 650°C and no visible interaction was observed. Therefore, the results of the Na_2SO_4-crystal exposures indicate that SO_2/SO_3 is very important in the mechanism and that the "short circuit" diffusion of nickel occurs along the surfaces of the sulfate crystals. Different progressions of the reaction can be seen in the 650°C cross-sectional image in Fig. 5-18. Specifically, a thin NiO scale developed along much of the surface of the large Na_2SO_4 crystal in the left portion of this image, while a porous NiO scale enveloped the entire surface and progressed into the lattice of the smaller Na_2SO_4 crystal in the center portion of the image.

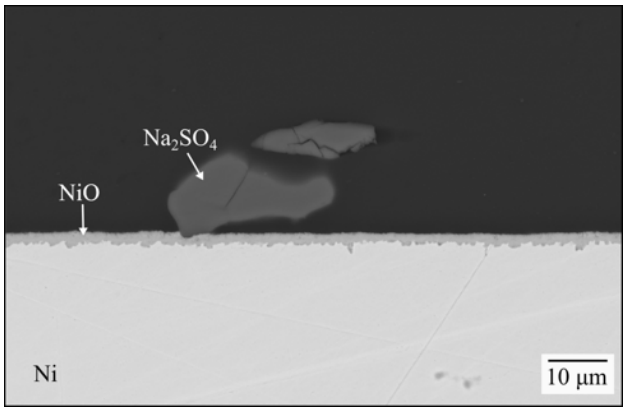

Figure 5-19. Cross-sectional SEM image after 20 h exposure of nickel in dry air at 650°C with crystals of Na_2SO_4 on an initially bare (i.e., unoxidized nickel surface).

The NiO formation progressed as high as ~150 μm along the sulfate surface after 20 h exposure at 650°C. Based on this progression distance, a diffusion coefficient of 1.6×10^{-9} cm^2/s is calculated. There was some variability in similar calculations, but the values were consistently orders of magnitude higher than the reported effective diffusion coefficient of nickel in NiO at 700°C [111], which takes into account the lattice diffusion, grain boundary diffusion, and NiO grain size.

Surface images were also collected after exposure of nickel with deposited Na_2SO_4 crystals. Figure 5-20 shows a surface image after an exposure of 8 h at 650°C; the products are identified in the image. The image shows a front of finger-like NiO formation along the surface of a sulfate crystal. A high-magnification image of this front is shown in Fig. 5-20. The lighter grey phase contains a significant amount of nickel. The identification of this phase will be discussed in the following section. An important aspect of the surface analysis is that it showed that the nickel-containing phase is mainly limited to the reaction front, with NiO and Na_2SO_4 being behind this front. As will be discussed, the nickel-containing phase at the reaction front is inferred to be metastable.

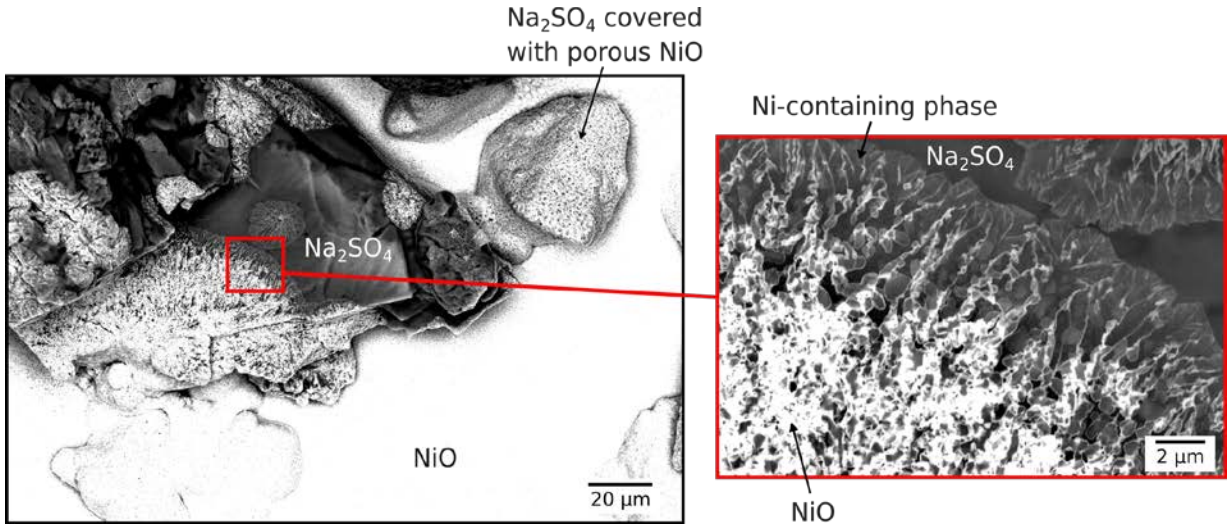

Figure 5-20. SEM surface images after 8 h exposure at 650°C of nickel in O_2-10 ppm SO_2 with crystals of Na_2SO_4 on the surface.

It is interesting to note that experiments were also conducted using grains of K_2SO_4 and a similar reaction product was identified, as shown in Fig. 5-21 for the 650°C exposure in O_2-10 ppm SO_2. Therefore, the solid-state mechanism occurring is also relevant to other sulfate deposits. For both Na_2SO_4 and K_2SO_4 grain exposures, NiO forms within the sulfate grain. The mechanism by which the NiO penetrates the sulfate is unclear.

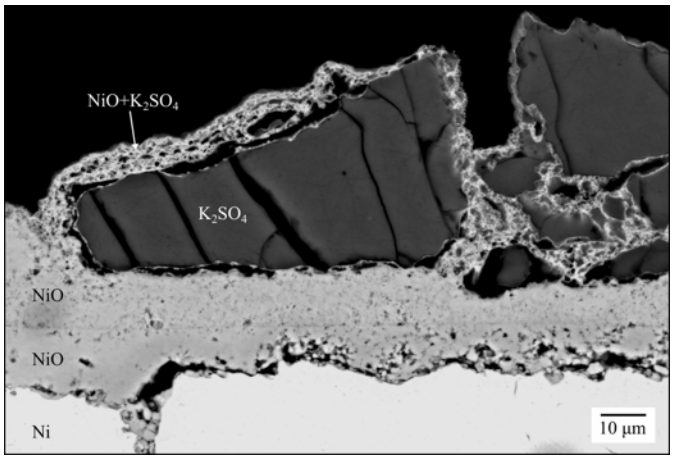

Figure 5-21. Cross-sectional SEM image after 20 h exposure at 650°C of nickel in O_2-10 ppm SO_2 with crystals of K_2SO_4 on the surface.

5.1.5 TEM analysis

The porous NiO product which forms on the Na_2SO_4 was assessed in greater detail using TEM analysis. Site-specific sections ~10 μm × 10 μm in size were lifted from polished cross-sections using a standard FIB sample preparation technique. Two cross-sections were analyzed: (1) pure nickel after 5.5 h exposure at 650°C in O_2-10ppm SO_2 and with Na_2SO_4 crystals deposited on the surface; and (2) PWA 1484 after 1.5 h exposure at 550°C in O_2-10ppm SO_2 and with ~2.5 mg/cm^2 Na_2SO_4 deposit. Representative TEM images from the exposed nickel specimen are shown in Fig. 5-22. The phases in each image are identified based on EDS analysis. The different shades of the NiO grains are indicative of different crystallographic orientations. The "vacuum" regions correspond to prior Na_2SO_4 which had evaporated under the electron beam of the TEM. It is seen that filaments of NiO penetrated into the Na_2SO_4. Moreover, these filaments were enveloped by what was deduced to be a nanocrystalline phase. Moreover, these filaments were enveloped by

what was deduced to be a nanocrystalline phase. From multiple EDS measurements, a composition in atomic percent was found to be (17±3)Na-(19±5)Ni-(7±3)S-(56±4)O (see Appendix A, composition varies so stoichiometry may not be exactly correct). Based on this composition spread, an approximated stoichiometry of $Na_2Ni_2SO_5$ is determined. As far as the authors are aware, the existence of an $Na_2Ni_2SO_5$ phase has not been previously reported. The thickness of the nanocrystalline phase in the image shown in Fig. 5-22 is ~10 nm; however, similar to the sulfate, the electron beam caused the nanocrystalline phase to evaporate, albeit at a comparatively slower rate. Further, the image was taken after EDS analysis. As stated above, the $Na_2Ni_2SO_5$ phase was also found in the product formed on the alloy. Figure 5-23a shows an SEM cross-sectional image of the corrosion product that formed on a 1484 alloy specimen and Fig. 5-23b shows a corresponding TEM image, identifying the nanocrystalline $Na_2Ni_2SO_5$ phase along an NiO filament. In this case the $Na_2Ni_2SO_5$, which was ~100 nm thick, contained a minor amount (*i.e.*, max of 3-5 at.%) of cobalt, as measured by EDS. It is conjectured that the rapid nickel transport needed for the observed solid-state corrosion process is attributable to the presence of the nanocrystalline $Na_2Ni_2SO_5$ phase. An attempt was made to synthesize the nanocrystalline phase by reacting 50 mol% $NiCl_2$ with 50 mol% Na_2SO_4 at 550°C in O_2-10 ppm SO_2 for 5 h. After the exposure a significant amount of Cl was still present and there was no semblance of the $Na_2Ni_2SO_5$ phase.

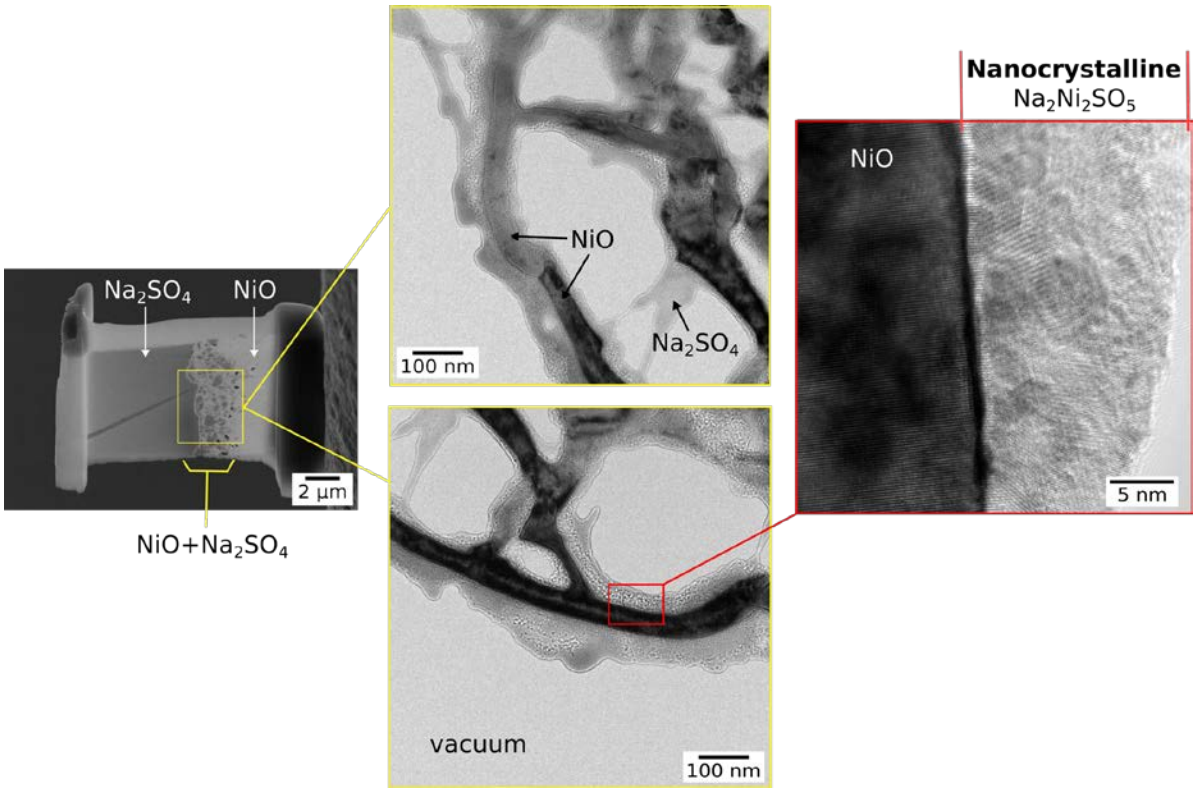

Figure 5-22. Image of TEM sample along with TEM images from the $NiO+Na_2SO_4$ region in the product formed on pure nickel after exposure at 650°C for 5.5 h with Na_2SO_4 grains.

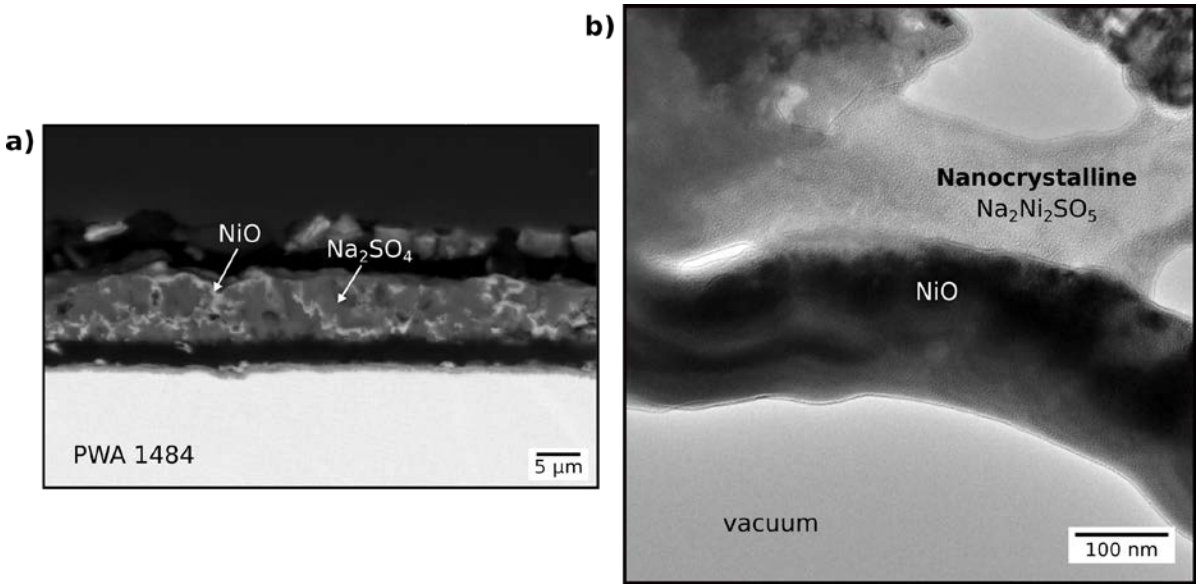

Figure 5-23. (a) Cross-sectional SEM image of PWA 1484 after 1.5 h exposure at 550°C in O_2-10 ppm SO_2 and with 2.5 mg/cm^2 of Na_2SO_4 deposit. (b) Corresponding TEM image showing identification of the nanoycrystalline phase next to a NiO filament.

5.1.6 Discussion

5.1.6.1 Criteria for Low-Temperature Corrosion

Prior to discussing the proposed mechanism, the inferred two criteria which are necessary for the observed low-temperature corrosion to occur will be discussed. The first criterion is formation of the nanocrystalline $Na_2Ni_2SO_5$ phase. The presence of this phase is essential for the requisite rapid nickel transport. The stability of the phase can be considered using P_{O_2} *vs*. P_{SO_3} stability diagrams for the Ni-O-S system, as shown in Fig. 5-24. These diagrams were determined using HSC software [100] with unit activity assumed for all condensed phases ($(Ni\text{-}S)_{liq.}$ Is excluded from the diagram). Shown in each diagram are the equilibrium P_{SO_3} values for the O_2-

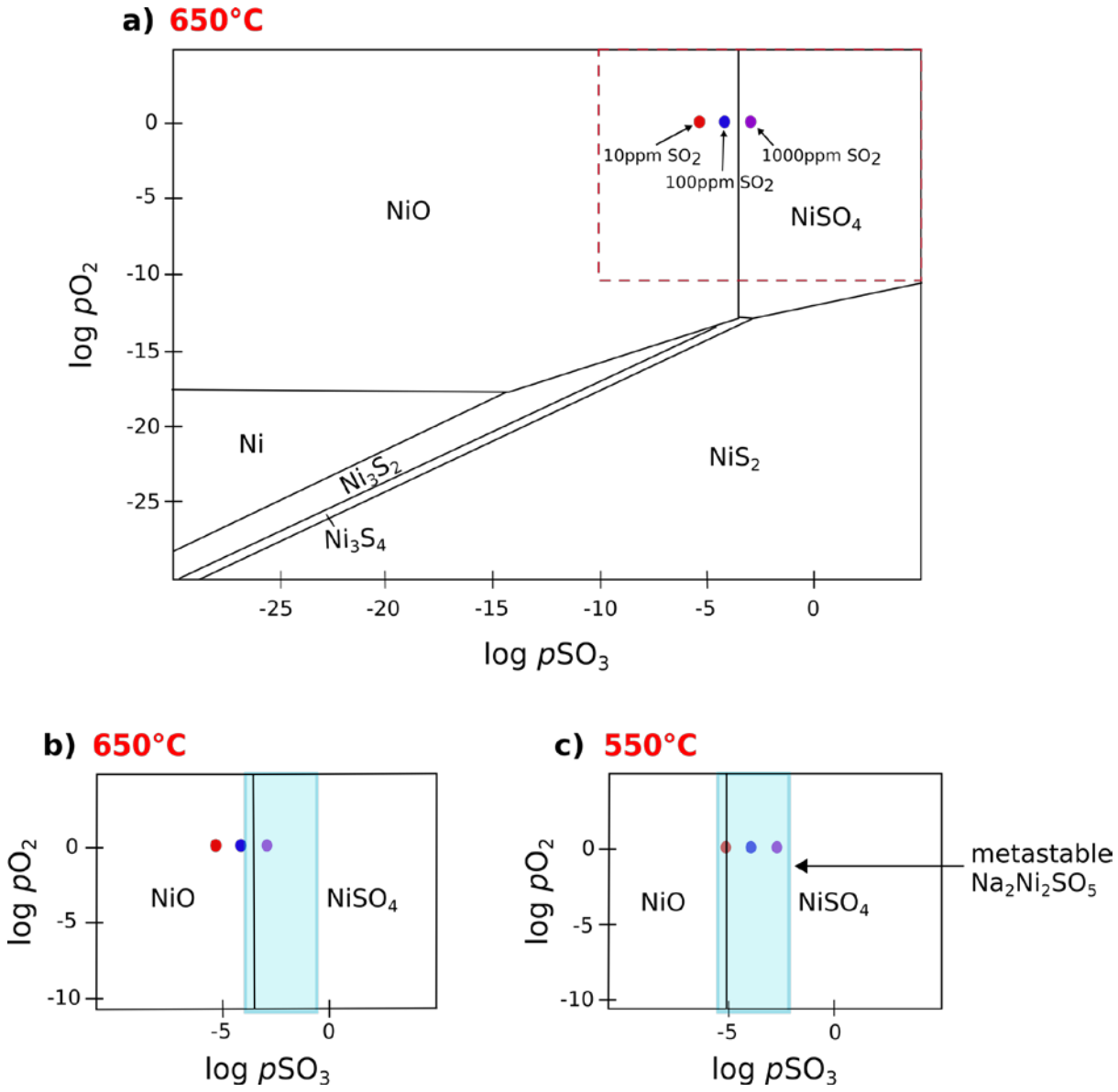

Figure 5-24. a) Ni-O-S stability diagram at 650°C. The P_{SO_3} values in O_2-(10,100, and 1000)ppm SO_2 are plotted on the diagram. The red highlighted area corresponds to the section of the diagrams shown in 14b), c) shows the same region at 550°C. The region of stability for the metastable $Na_2Ni_2SO_5$ is shown in b) and c).

(10,100, and 1000) ppm SO_2 atmospheres used in this study. Figure 5-24a shows the stability diagram for 650°C, with a more limited region of interest outlined in this figure and shown in Fig. 5-24b. Figure 5-24c shows the same limited P_{O_2} *vs*. P_{SO_3} region for the case of 550°C. The shaded regions in Figs. 5-24b and 5-24c indicate where the metastable $Na_2Ni_2SO_5$ phase is generally estimated to form. This phase must form before the deposit sinters, so that a dynamic interaction can occur between NiO, Na_2SO_4 and the environment (i.e., SO_3). The $Na_2Ni_2SO_5$ stability can be explained based on the corrosion exposures of pure nickel. At 650°C in the O_2-10 ppm SO_2 environment, no visible interaction occurred between the nickel and the Na_2SO_4 deposit (see Fig. 5-19). By contrast, if the SO_2 content is increased to 1000 ppm, there is significant Ni/Na_2SO_4 interaction and the resulting corrosion product consists of NiO + entrapped Na_2SO_4 at the sulfate/gas interface. As the temperature decreases, the P_{SO_3} in an O_2-*x*SO_2 environment increases and, as can be seen in the stability diagram at 550°C, the NiO/$NiSO_4$ boundary also shifts to a lower P_{SO_3} value. The P_{SO_3} O_2-(10, and 100) ppm SO_2 environments is now in a $NiSO_4$ stable region at the lower temperature of 550°C. The metastable phase forms in kinetic preference to $NiSO_4$, so at this temperature Ni/Na_2SO_4 interaction and resulting corrosion occur (Fig. 5-14).

The second criterion is that there must be a sufficient flux of nickel to sustain the $Na_2Ni_2SO_5$ phase formation. This criterion is inferred from the Ni pre-oxidation results (Fig. 5-15), which showed that a more defective NiO scale pre-formed at 700°C and below facilitated subsequent accelerated formation of porous NiO + entrapped sulfate at the deposit surface. It is known from studies by Peraldi *et al.* [109, 110],for instance, that NiO formed at 700°C and below is porous and fine-grained, and thus contains numerous short-circuit paths for the outward diffusion of Ni^{2+}. It is the supply of nickel via diffusion through the NiO scale – rather than via NiO

decomposition due to reaction with the Na_2SO_4 - which facilitates and sustains the $Na_2Ni_2SO_5$ formation. However, if the deposit sinters before substantial $Na_2Ni_2SO_5$ can form, accelerated interaction will not occur because it is the metastable phase along the sulfate surface that provides the fast diffusion path for the Ni^{2+}. Based on the results shown in Fig. 5-15, the sintering rate of the deposit is ostensibly greater than the flux of nickel through the NiO pre-formed oxide at 1000°C, as no interaction occurred. Evidence of deposit sintering can be surmised from a test in which Na_2SO_4 was deposited on an alumina coupon and exposed at 650°C for 2 h. Figure 5-25 shows representative cross-sectional SEM images taken before and after the thermal exposure. An example of a grain boundary that resulted from sintering is indicated in the post-exposure image. Further, it is inferred from Fig. 5-25 that sintering initiates at the deposit/substrate interface.

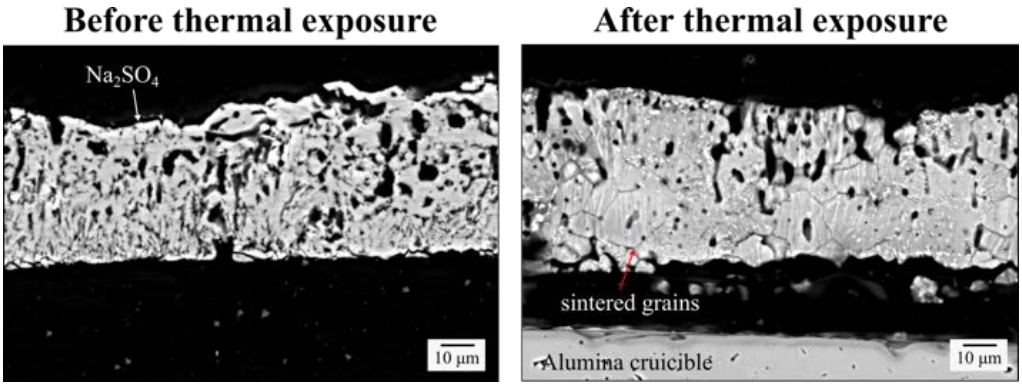

Figure 5-25. Cross-sectional SEM image of Na_2SO_4 applied to an alumina cruicible before and after thermal exposure at 650°C in O_2-10 ppm SO_2 for 2 h. Grains that sintered after the exposure are identified.

The flux of nickel required for the observed rapid corrosion was calculated using Fick's first law as an order-of-magnitude estimate, as shown in Eq. 5-3, where D is the diffusion coefficient, C is concentration, and x is the distance. A diffusion coefficient of 1.6×10^{-9} cm^2/s, as determined from the Na_2SO_4 crystal experiment at 650°C (Fig. 5-18) was used in the calculation. ∂x was set to 10 μm, roughly the thickness of a 2.5 mg/cm^2 Na_2SO_4 deposit, and the concentration of nickel at the NiO interface was set to 0.5 mol/cm^3, and at the deposit/gas interface was set to 0 mol/cm^3.

$$J = -D\frac{\partial C}{\partial x} \qquad (5-3)$$

The flux of nickel along the surface of the sulfate crystal equates to approximately 8×10^{-7} $mol/cm^2 \cdot s$ at a reaction time of 20 h. To determine if the flux of nickel through the NiO scale pre-formed at a low temperature can provide such a flux, TGA experiments were conducted. Nickel specimens were first oxidized at 700°C (24 h) followed by oxidation at 650°C for 20 h. The k_p from oxidation at 700°C was measured to be 4.7×10^{-6} $mg^2/cm^4 \cdot s$. Subsequent oxidation of that sample at 650°C for 20 h resulted in a decrease of the k_p to 5.6×10^{-8} $mg^2/cm^4 \cdot s$. The resulting graph of weight change vs. time is shown in Fig. 5-26, with the indicated temperature change and k_p values.

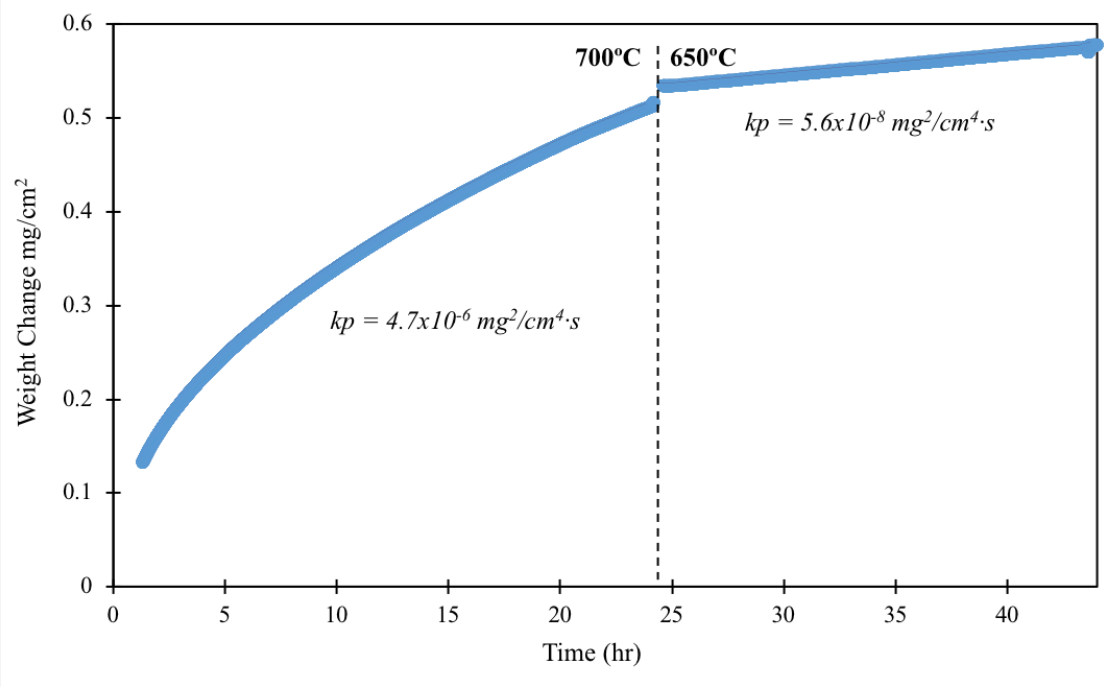

Figure 5-26. Weight change vs. time for nickel TGA data after oxidation at 700°C for 24 h followed by oxidation at 650°C for 20 h in dry air.

Using the k_p data, a Ni flux through the NiO is determined to be of 7.8×10^{-11} mol/cm^2·s after the 20 h exposure at 650°C. This value is four orders of magnitude lower than the flux of nickel along a sulfate surface. It may be that the SO_2/SO_3 in the atmosphere effected an increase in the nickel flux through the pre-formed NiO, as some nickel sulfide was detected at the oxide/metal interface, but the extent of sulfide formation is deemed to be insufficient to account for such a rapid nickel flux. TGA analysis was repeated in an O_2-10 ppm SO_2 environment. The mass gain at the end of the exposure (24 h at 700°C, then 20 h at 650°C) was ~1 mg/cm^2, which is about a factor or two higher than in the dry air environment after the same exposure conditions.

Thus, sulfur appears to increase nickel diffusion in NiO, but still the increase is much less compared to what was found with the Na_2SO_4 deposit.

Considering the first criterion in discussing the 700°C pre-oxidation result, a microclimate at the sulfate/oxide interface must have existed in which the locally P_{SO_3} increased to stabilize the $Na_2Ni_2SO_5$ formation. The P_{SO_3} increase may have resulted from further NiO formation at the expense of Na_2SO_4, which in turn would have increased the local sulfur potential, similar to what has been proposed for the Type I hot corrosion of nickel [12]. Indeed, it is known that the sulfur potential at the sulfate/oxide interface can be significantly different and varying from the environmental gas composition [83]. At the oxide/metal interface the sulfur pressure clearly increased to a level that allowed for discrete nickel-sulfide formation, with the sulfur being supplied from the gas or the deposit. However, there remains the apparent inconsistency that the NiO formed beneath the sulfate deposit on the nickel exposed at 650°C (i.e., there was no pre-oxidation) exhibited no visible interaction with the sulfate (Fig. 5-14). There were interactions for similar exposures at lower temperatures due, it is conjectured, to very slow sintering kinetics of the deposit in comparison to the rate of $Na_2Ni_2SO_5$ formation. To address the observation of no visible interaction at 650°C, it is necessary to consider the energetics of the reactions involved. Figure 5-27 shows hypothetical free-energy diagrams for two cases: (a) pre-oxidation of Ni at 700°C followed by Na_2SO_4 deposition and then 20 h exposure at 650°C in O_2-10ppm SO_2; and (b) Ni with no pre-formed oxide and Na_2SO_4 deposit exposed under the same conditions as case (a). When the pre-formed oxide is in contact with the deposit, the $Na_2Ni_2SO_5$ phase is able to form as an intermediate that is in metastable equilibrium with the pure oxide and sulfate, as indicated in Fig. 5-27a. In accordance with the second diagram in Fig. 5-27a, decomposition of the metastable

$Na_2Ni_2SO_5$ will occur after a certain period. The product of this decomposition is NiO + Na_2SO_4. Microstructurally, this is manifested as the porous NiO with the entrapped Na_2SO_4.

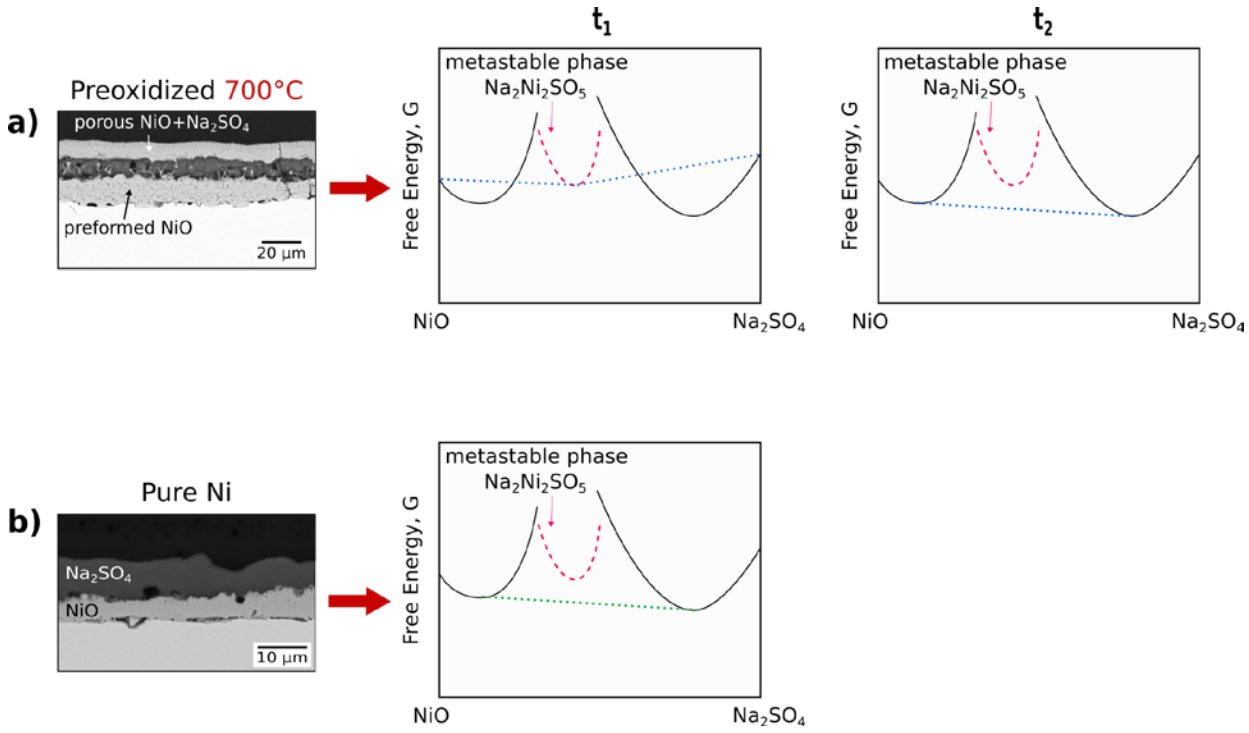

Figure 5-27. Free energy diagrams for hot-corrosion exposures of a) nickel, which was preoxidized in air at 700°C and b) nickel, which was not preoxidized. All exposures were at 650°C in O_2-10 ppm SO_2 for 20 h with 2.5 mg/cm^2 Na_2SO_4 deposit.

The situation is different when there is no pre-formed oxide, as indicated in Fig. 5-27b. At the exposure temperature, the NiO begins to form and a small amount of sodium and sulfur become incorporated into the oxide and nickel into the deposit, corresponding to their respective solubilities. As shown by the free-energy diagram in Fig. 5-27b, local NiO/Na_2SO_4 equilibrium would be maintained in such a situation, thus precluding the kinetically driven formation of the metastable $Na_2Ni_2SO_5$ phase. If this is correct, then it should be that the NiO formed in equilibrium

with the deposit should not show any interaction with a freshly applied Na_2SO_4 followed by exposure to the same conditions of 650°C and O_2-10ppm SO_2. In this case, the initially applied sulfate is removed such that the Ni specimen has the appearance of a pre-formed oxide. As shown in Fig. 5-28, conducting such an experiment resulted in no observable NiO/Na_2SO_4 interaction, thus giving validation to the above analysis.

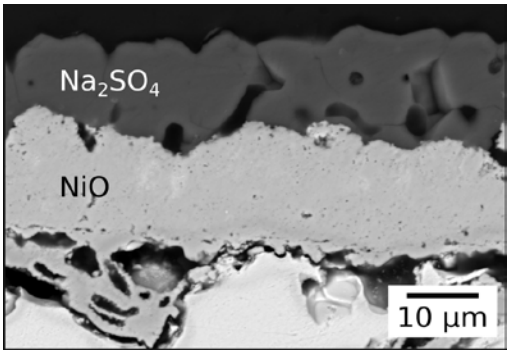

Figure 5-28. SEM cross-sectional image following exposure of a nickel sample at 650°C for 20 h in O_2-10 ppm SO_2 with 2.5 mg/cm^2 Na_2SO_4 deposit. The nickel sample was initially hot corrooded at 650°C for 20 h in O_2-10 ppm SO_2 with 2.5 mg/cm^2 Na_2SO_4 deposit to produce the result shown in Figure 5-15, then the deposit was removed, leaving an NiO scale that had formed beneath the Na_2SO_4 deposit. The speciman was then subjected to the same testing condition of 650°C for 20 h in O_2-10 ppm SO_2 with 2.5 mg/cm^2 Na_2SO_4 deposit.

5.1.6.2 Proposed Mechanism

Based on the analysis presented thus far, a mechanism is proposed for the observed low-temperature, deposit-induced corrosion. Figure 5-29 presents a schematic of the mechanism for the case of an Na_2SO_4 crystal on the surface of a nickel specimen; below is a schematic of a magnified region of the reaction front. Though only a single Na_2SO_4 crystal is considered in this figure for the sake of clarity, the proposed mechanism is also applicable to a deposited Na_2SO_4 layer. Further, it is relevant to note that we also found that K_2SO_4 as the deposit produces comparable results, as shown in Fig. 5-21. The first critical step in the proposed mechanism is formation of the $Na_2Ni_2SO_5$, a nanocrystalline, solid phase. The metastability of this phase was discussed in the previous section. Its formation is due to a relatively high Ni^{2+} flux that enriches the Na_2SO_4 in the presence of SO_3 in the atmosphere. The proposed reaction, which is surface mediated, is[1]:

$$2Ni^{2+} + 4e^{-} + Na_2SO_4(s) + SO_3(g) \longrightarrow Na_2Ni_2SO_5(s) + SO_2(g) \qquad (5-4)$$

It is recalled that the $Na_2Ni_2SO_5$ stoichiometry is approximated, as it is based solely on an average of multiple EDS measurements for both pure Ni and PWA 1484 exposed specimens. The nanocrystalline structure of the $Na_2Ni_2SO_5$ that forms is essential for providing a rapid Ni^{2+} flux along and also into the solid Na_2SO_4. As determined from the experiments conducted at 650°C,

[1] The speciation of the sulfur species is unknown, but for the sake of discussion it is assumed to be SO_3

the diffusion coefficient in the nanocrystalline $Na_2Ni_2SO_5$ must be about 10^{-9} cm^2/sec in magnitude. Interestingly, this is about an order of magnitude greater than the reported grain-boundary diffusion coefficient of nickel in NiO at 650°C [112].

Provided that the $Na_2Ni_2SO_5$ progresses along the Na_2SO_4 surface at a rate faster than the deposit's sintering rate, sustained attack may be established. In such a case, the second step of the mechanism is decomposition of the metastable $Na_2Ni_2SO_5$ phase. This decomposition results in $NiO + Na_2SO_4$, with NiO being the primary phase and the Na_2SO_4 present as coarse particles. The NiO that forms from the decomposition must contain some amount of Na and S. The resulting NiO is also highly defective with grain boundaries and porosity. It is postulated that all these factors contribute to providing a relatively high Ni^{2+} flux which is necessary for the continued rapid degradation and associated Na_2SO_4 consumption. A further contributing factor is that some $Na_2Ni_2SO_5$ was found to remain in contact with the NiO, thus providing high-diffusivity paths.

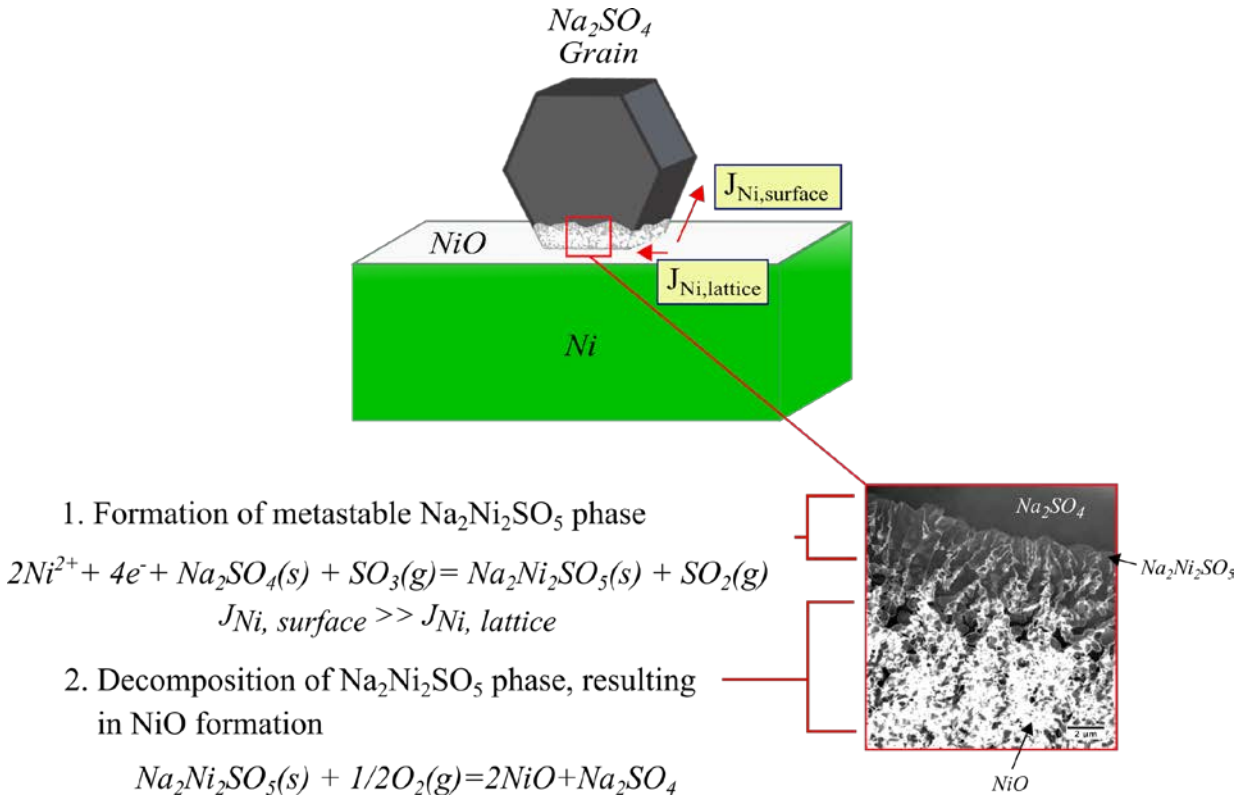

Figure 5-29. Proposed mechanism for the observed low-temperature, Na_2SO_4-deposit-induced corrosion.

The proposed mechanism is applicable to the nickel-based superalloy studied because nanocrystalline $Na_2Ni_2SO_5$ was also identified in the reaction product of PWA 1484 after a corrosion exposure. The superalloy contains many different alloying elements, one of which is cobalt. Cobalt is identified in the oxide which forms at the gas interface, so pure cobalt exposures were also conducted. Figure 5-30 compares the resulting cross-sections of pure nickel and pure cobalt after exposure at 500°C. The cobalt exposure is more accelerated, indicating that cobalt may produce a similar nanocrystalline $Na_2M_2SO_5$ phase (where M = metal like Ni or Co), and the presence of cobalt in the alloy may accelerate the deposit-induced attack. At a reaction temperature of 750°C, Chiang *et al.* [58] reported that the presence of 1000 ppm SO_2 and 1 mg/cm^2 Na_2SO_4

deposit did not produce accelerated attack of pure cobalt in comparison to the same test using O_2 only. This apparent variance with the current results may be due to a different mechanism operating at the higher exposure temperature. Further experiments would need to be completed to verify this.

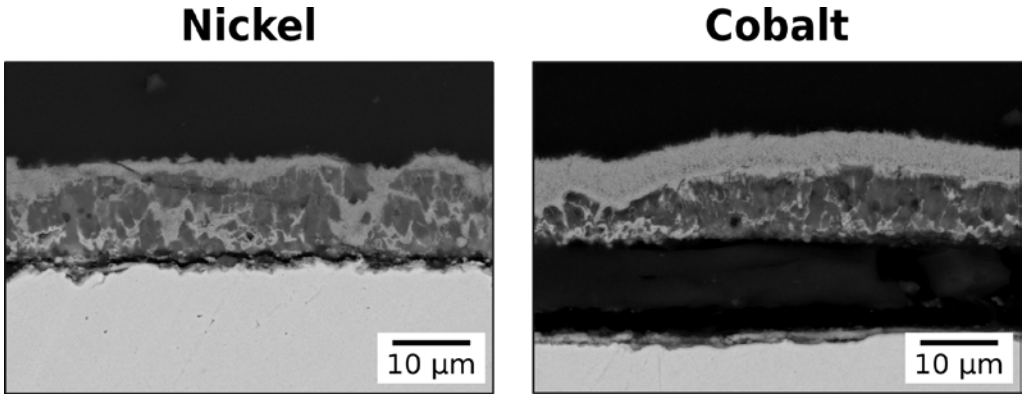

Figure 5-30. SEM cross-sectional images after hot corrosion exposure of pure nickel and cobalt at 500°C for 20 h in O_2-10 ppm SO_2 with 2.5 mg/cm^2 Na_2SO_4 deposit.

5.2 Spatial Influence of Na_2SO_4 Deposit on Oxidation and Corrosion

Experiments conducted using PWA 1484 and pure nickel substrates showed the nanocrystalline phase identified in the previous section has a spatial influence, which will be discussed in this section.

5.2.1 PWA 1484 Experiments

To assess the spatial influence of the nanocrystalline phase, a 2.5 mg/cm^2 Na_2SO_4 deposit was first applied to a PWA 1484 sample. Deposit was removed from half the sample surface using water on a cotton swab. SEM imaging was done before the exposure to confirm no deposit remained on that half of the sample surface. The sample was then tested at 550°C in O_2-10 ppm SO_2 for 20 h. Figure 5-31 shows a schematic of the test procedure along with cross-sectional SEM images of the coated side, of the uncoated/coated juncture, and of the uncoated side. The important finding was that Na was detected at the uncoated side. Therefore, the Na is either spreading laterally or transported via a vapor phase. An additional experiment was done to determine the mode of transport. In this case, a PWA 1484 coupon was cut in half, and only one of the halves was coated with 2.5 mg/cm^2 Na_2SO_4 deposit. The two half coupons were then tested, with a small gap between them, at 550°C for 20 h in O_2-10 ppm SO_2. The resulting SEM image of the uncoated side, along with a schematic of the test procedure are shown in Fig. 5-32. Oxidation of the uncoated side was unaffected, indicating the “throwing power” of the sulfate deposit is not due to vapor phase transport.

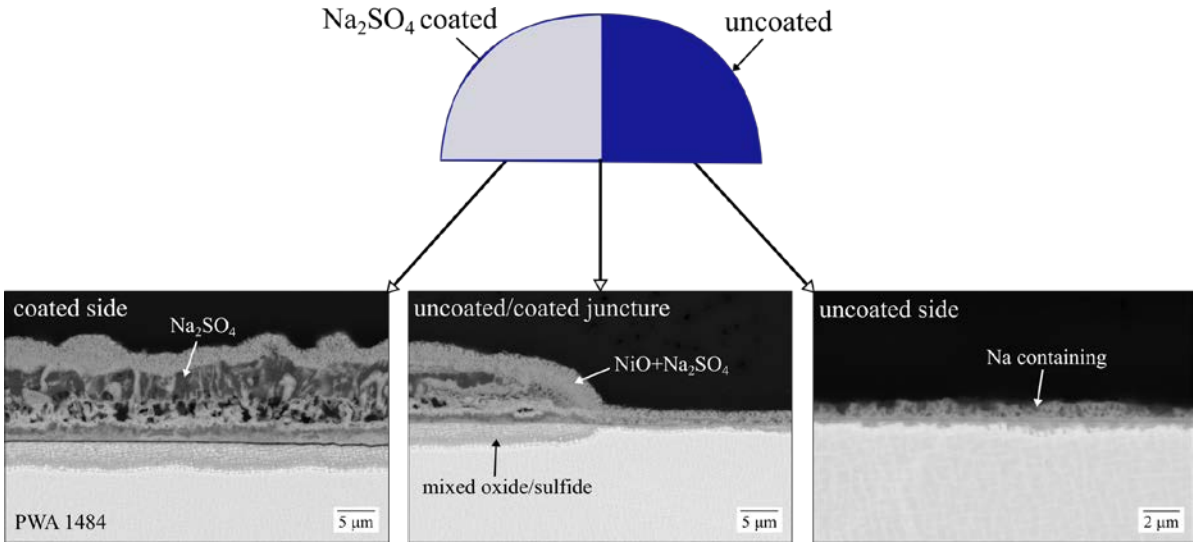

Figure 5-31. Schematic of test procedure, where one half of a PWA 1484 coupon was coated with 2.5 mg/cm^2 Na_2SO_4 deposit, along with cross-sectional SEM images after hot corrosion exposure at 550°C for 20 h in O_2-10 ppm SO_2.

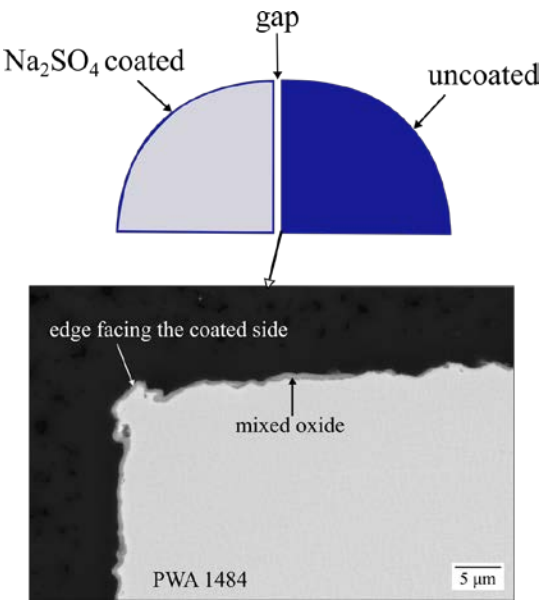

Figure 5-32. Schematic of test procedure, where a PWA 1484 coupon was cut in half and one half was coated with 2.5 mg/cm^2 Na_2SO_4, along with cross-sectional SEM image of the unocated side after exposure at 550°C for 20 h in O_2-10 ppm SO_2.

5.2.2 Pure Nickel Experiments

Pure nickel (99.99%) samples were studied to complement experiments in Section 5.1 to better understand the low-temperature mechanism. As in Section 5.1, exposures were done at 650°C and 625°C. The significance is that 625°C is below the Ni-Ni_3S_2 eutectic, thus ensuring no liquid contribution to the corrosion process at that temperature. Initially, a few grains of Na_2SO_4 were placed on the coupon surface. A drop of ethanol was added to the surface, which allowed the grains to better adhered to the sample. The sample was then tested at 650°C for 20 h in O_2-10 ppm SO_2. Figure 5-33 shows the resulting surface image of a single grain, along with EDS analysis, and Fig. 5-34 shows the resulting cross-sectional image. EDS analysis revealed Na to be ~250 μm away from where the sulfate grain was deposited. Based on this distance, a diffusion coefficient of $8.7x10^{-9}$ cm^2/s was calculated, which is slightly higher than the diffusion of nickel along the sulfate grain. Additionally, the cross-sectional images in Fig. 5-34 a) shows the morphology of the product adjacent to the sulfate grain to consist of an outer region of porous NiO intermixed with an Na/S-containing phase. The total thickness, denoted in the cross-sectional image, decreases further away from the sulfate crystal, indicating that the influence is caused by a diffusion process along the surface. Figure 5-34 b) shows the NiO formed in area unaffected by the presence of the deposit. The thickness is denoted in the image, which is much less than in the affected area.

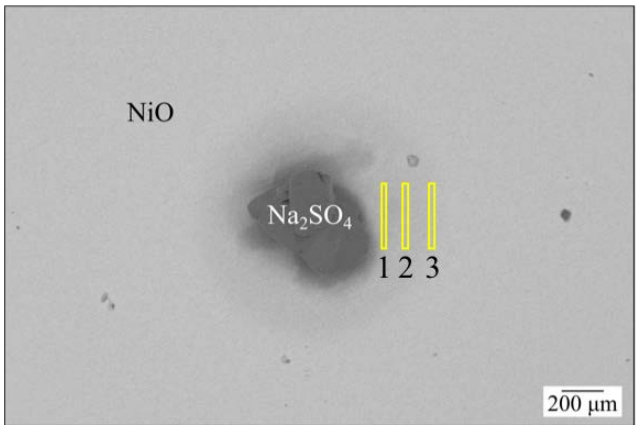

	O	Na	S	Ni
1	46	12	4	38
2	47	7	3	43
3	48		1	51

Figure 5-33. Surface SEM image of pure nickel after exposure with single Na_2SO_4 grain at 650°C for 20 h, along with EDS results.

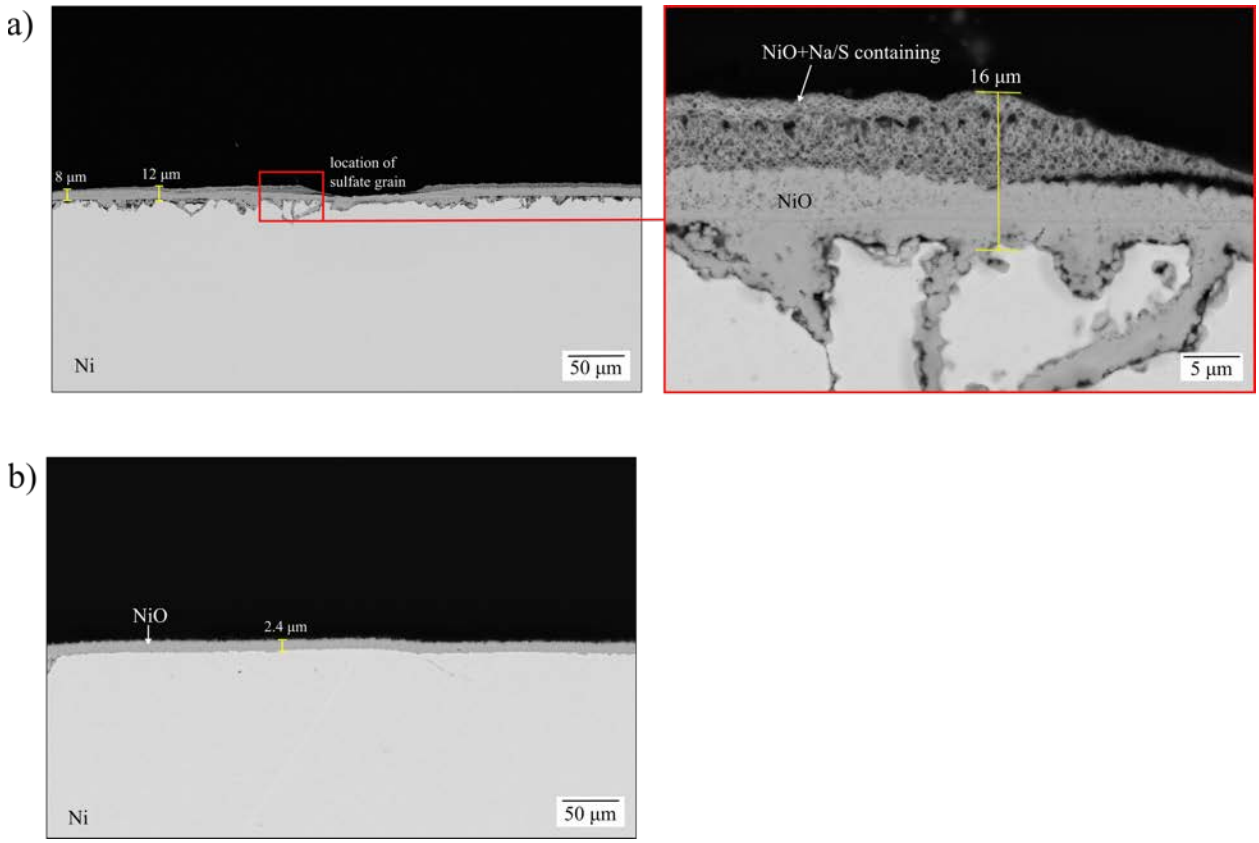

Figure 5-34. Cross-sectional SEM images of a) affected area and b) unaffected area of pure nickel after exposure with single Na_2SO_4 grain at 650°C for 20 h.

The previous results confirmed a spatial influence of the Na_2SO_4 deposit on a pure nickel sample. However, ethanol was used for better adherence of the grains to the surface. Without the ethanol it was challenging to complete the exposure because the grains would roll off the sample upon inserting. Contamination could have been an issue with the addition of ethanol and the use of multiple grains along the surface. Therefore, an additional experiment was designed in which a shallow indent was created on the surface of the nickel sample using a drill. A Na_2SO_4 grain or a few very small grains were placed in the hollow indent using tweezers. The result was the isolation of Na_2SO_4 and ethanol was not needed to contain the grains. The result of the experiment completed at 650°C for 20 h in O_2-10 ppm SO_2 is shown in Fig. 5-35. As in the previous experiment, Na was detected away from where the sulfate grain was deposited. The region where the oxidation is no longer affected by the presence of the sulfate deposit is indicated. That distance is ~750 μm away from the sulfate grain. Based on this distance, a diffusion coefficient of 7.8×10^{-8} cm^2/s, which is again higher than the diffusion of nickel along the sulfate grains (1.6×10^{-9} cm^2/s).

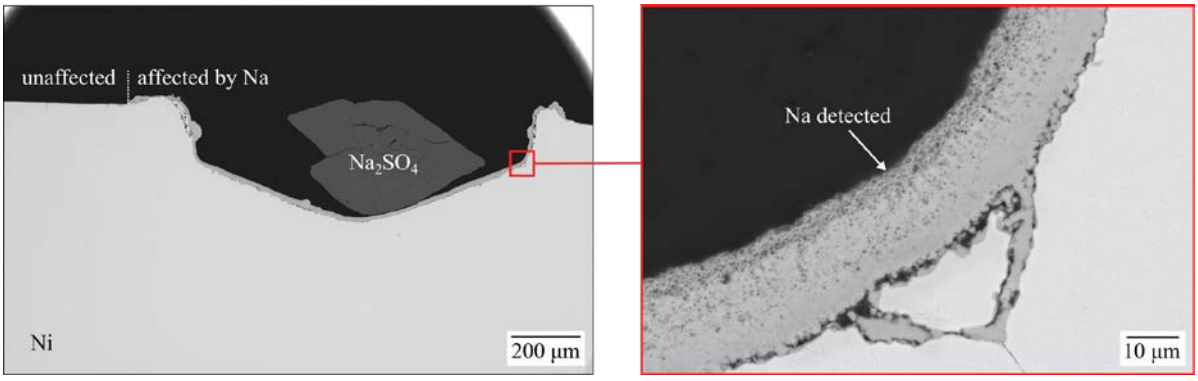

Figure 5-35. Cross-sectional SEM images of nickel sample after exposure at 650°C in O_2-10 ppm SO_2 for 20 h with isolated Na_2SO_4 grain.

A similar experiment was done on pure nickel at 625°C for 20 h in O_2-10 ppm SO_2. Instead of a single large grain, a few smaller grains of sulfate were deposited. Resulting cross-sectional SEM images from two areas are shown in Fig. 5-36. As in the 650°C exposure, oxidation was affected away from where the sulfate grains were deposited and Na was detected at the oxide surface. In Fig. 5-36 a), the affected area was observed up to ~500 μm away from the sulfate grains. Figure 5-36 b) shows the presence of Na at the reaction front. Also, note that the thickness of the oxide in the affected area is measured to be 18 $\pm$ 6 μm while the thickness of the oxide after "normal" oxidation in O_2-10 ppm SO_2 is only ~ 3 μm. In both areas, within the oxide scale a small amount (~1-2 atomic %) of S was detected. In the area affected by the presence of Na, a minor amount of nickel sulfide and void formation was detected below the oxide. EDS measurements confirming this are shown in Fig. 5-37. Two areas are shown for the affected NiO, with the S and Na detection included.

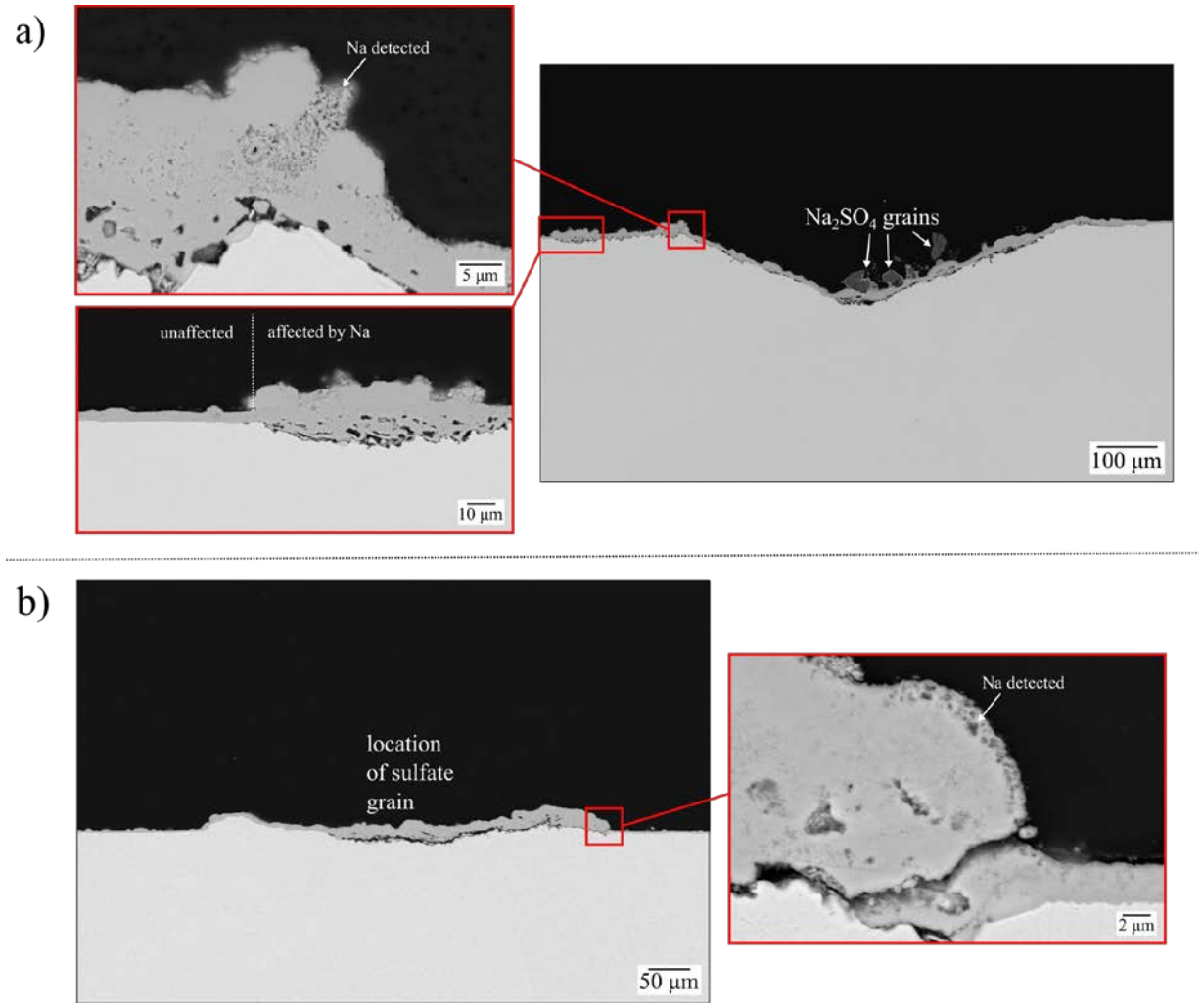

Figure 5-36. Cross-sectional SEM images of two locations, a) and b), on nickel sample after exposure at 625°C in O_2-10 ppm SO_2 for 20 h with isolated Na_2SO_4 grains.

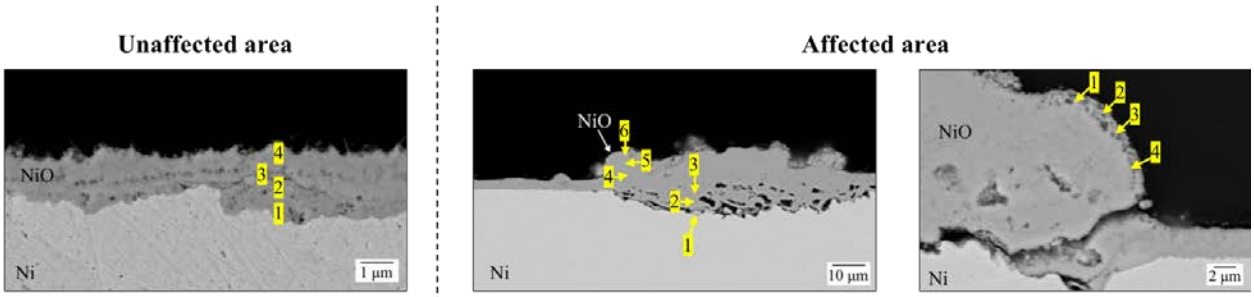

Spectrum	O	Ni	S
1	42	58	0
2	46	54	0
3	46	53	1
4	47	52	1

Spectrum	O	Ni	S
1		61	38
2	48	54	0
3	48	52	0
4	53	45	2
5	50	48	2
6	49	49	2

Spectrum	O	Ni	S	Na
1	55	42	2	3
2	44	50	3	3
3	50	48	2	0
4	55	42	2	

Figure 5-37. Cross-sectional SEM images of nickel sample after exposure at 625°C in O_2-10 ppm SO_2 for 20 h with isolated Na_2SO_4 grains, along with EDS results in area unaffected by the presence of the suflate deposit, and two areas affected by the deposit.

A complementary experiment of isolating K_2SO_4 grains was done at 625°C in O_2-10 ppm SO_2 for 20 h because the previously discussed solid-state mechanism was shown to apply to a K_2SO_4 deposit as well. The resulting cross-sectional SEM images are shown in Fig. 5-38. As with the Na_2SO_4 deposit, oxidation is affected away from where the deposit is located. The affected area is observed up to ~350 μm away from the K_2SO_4 deposit Additionally, K is identified at the oxide surface, as indicated in Fig. 5-38. The “throwing power” observed is therefore applicable to both sulfate deposits.

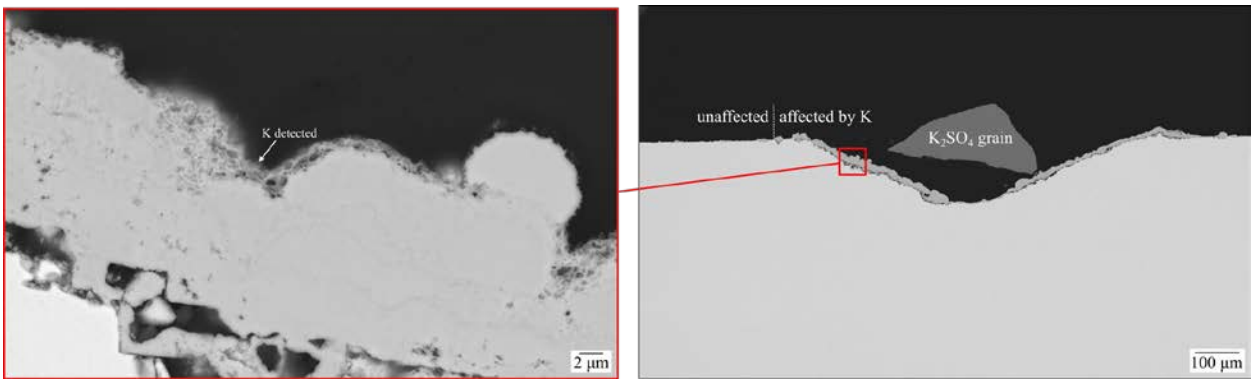

Figure 5-38. Cross-sectional SEM images of nickel sample after exposure at 625°C in O_2-10 ppm SO_2 for 20 h with isolated K_2SO_4 grain.

5.2.3 TEM Results

The pure nickel with isolated Na_2SO_4 grains and exposed at 625°C in O_2-10 ppm SO_2 for 20 h, shown in Fig. 5-36, was analyzed using TEM. Site-specific sections ~10 µm x 10 µm in size were lifted from the polished cross-sections using a standard FIB sample preparation technique. The two areas shown in Fig. 5-36 were assessed. Fig. 5-39 shows the TEM sample from the first area, together with corresponding TEM images and diffraction patterns. The nanocrystalline phase containing Na-Ni-O-S was identified and a selected area electron diffraction (SAED) pattern was obtained. More about this pattern will be discussed subsequently. A diffraction pattern was also obtained from the NiO region, confirming the NiO stoichiometry and structure. With regard to the nanocrystalline phase, EDS analysis generally corresponded to the stoichiometry $Na_2Ni_2SO_5$; however, there was an outlier measurement that corresponded to $Ni_3Na_7SO_{22}$. It is postulated that this outlier composition is non-representative of a single product and will therefore be ignored.

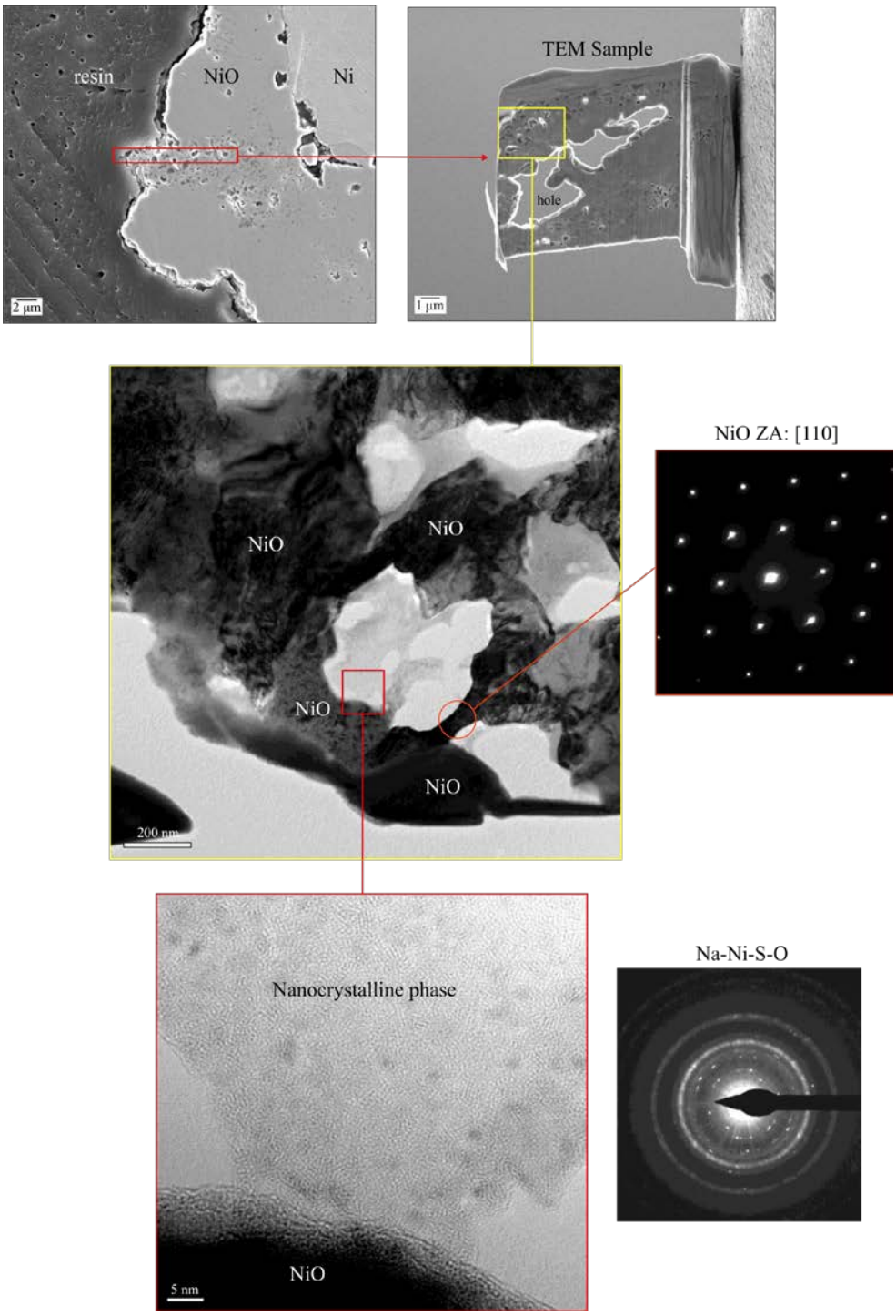

Figure 5-39. SEM image of first TEM sample from expousre of Ni at 625°C for 20 h with isolated grains of Na_2SO_4, along with TEM images inidcating nanocrystalline phase formation and diffraction patterns from an area of NiO and an area with the nanocrystalline Na-Ni-S-O phase.

The second TEM sample, along with analysis of a magnified image at the reaction front is shown in Fig. 5-40. The nanocrystalline $Na_2Ni_2SO_5$ phase was identified by EDS at the reaction front. EDS analysis from areas where the phase was identified are also shown in this figure. The measured composition range was small. As mentioned in the previous chapter, $Na_2Ni_2SO_5$ was determined after averaging multiple EDS measurements, so the stoichiometry may not be exact. Structural analysis would be needed to determine the stoichiometry. As in the first sample, a diffraction pattern was obtained in the nanocrystalline region. The same diffraction ring was observed, indicating the Na-Ni-S-O phase identified is the same in both samples. Simulated SAED patterns from other known Na-Ni-S-O structures and the known structures of Na_2SO_4 were compared to the diffraction pattern, but no match was found. Table 5-1 shows the structural data used for comparison. The orthorhombic (V) structure of Na_2SO_4 is stable up to 180°C and the hexagonal (I) structure is the high temperature phase, stable above 237°C [114]. Between 180°C and 237°C, orthorhombic structures (II and III) with slightly different lattice parameters are formed [114]. Table 5-2 shows a comparison of the d-spacings for the observed Na-Ni-S-O phase compared to the known structures. The number in bold corresponds to the 100% intensity ratio (I/I_{max}) for the given structure. The observed ring structure of the nanocrystalline phase does not match the known structures. To verify the stoichiometry, structural data would be needed, which was deemed beyond the scope of this study.

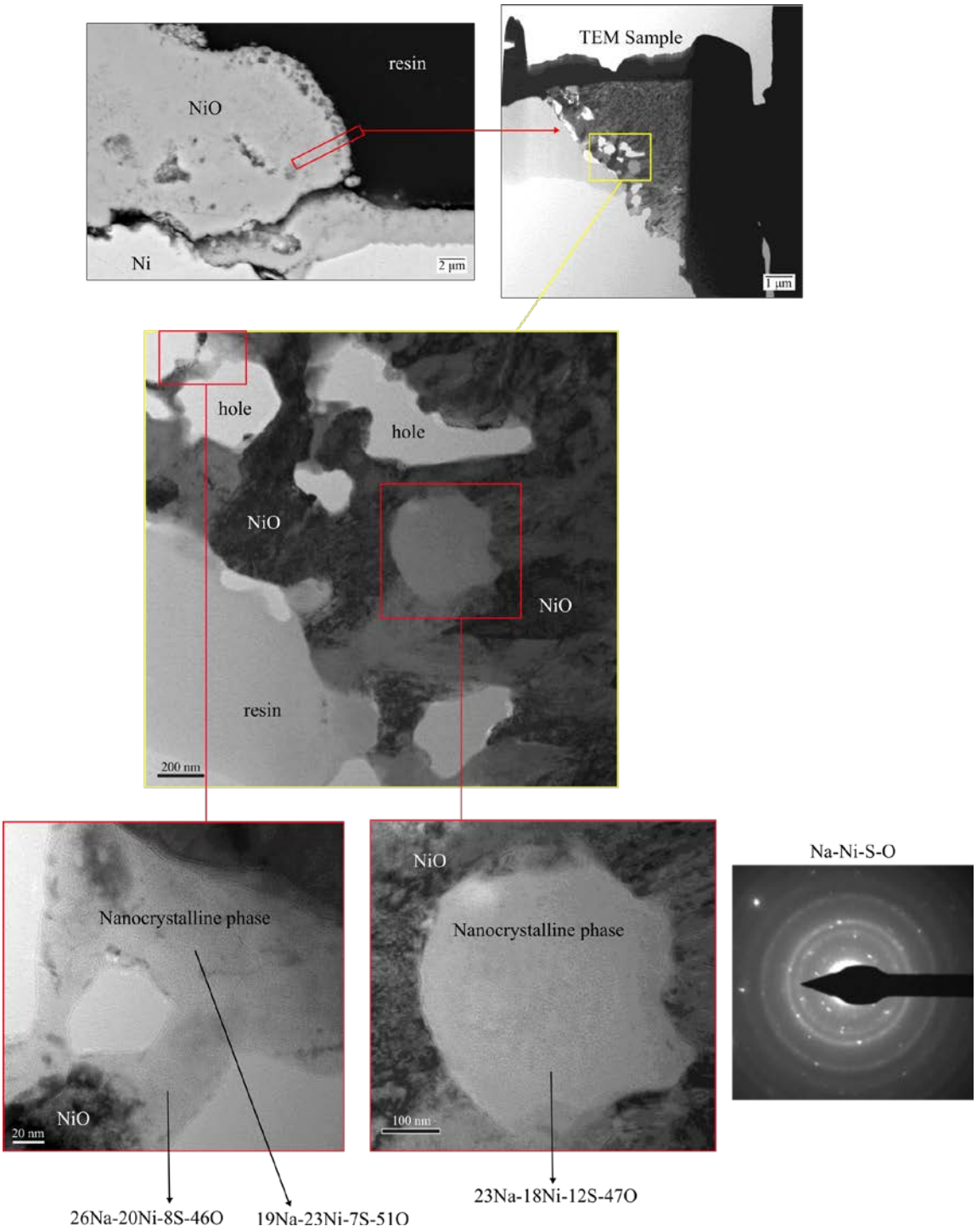

Figure 5-40. SEM images of second TEM sample from expousre of Ni at 625°C for 20 h with isolated grains of Na_2SO_4, along with TEM images inidcating nanocrystalline phase formation and corresponding diffraction pattern.

Table 5-1. Structural data for $Na_xNi_yS_zO_w$ phases [114–116].

	Na_2NiSO_2	$Na_2Ni(SO_6)_2$	$Na_2Ni(SO_4)_2$	Na_2SO_4 (V)	Na_2So_4 (I)
Structure	Tetragonal	Monoclinic	Monoclinic	Orthorhombic	Hexagonal
a	4.58	5.46	23.56	5.86	5.36
b	8.18	8.21	10.38	12.30	-
c	171.58	11.14	17.51	9.82	7.06
α	90.00	90.00	90.00	90.00	90
β	90.00	97.07	99.19	90.00	90
γ	90.00	90.00	90.00	90.00	120

Table 5-2. Comparison of d-spacing (Å) of observed ring pattern of nanocrystalline phase to known phases containing Na-Ni-S-O.

Rings	**Observed**	Na_2NiSO_2	$Na_2Ni(SO_6)_2$	$Na_2Ni(SO_4)_2$	Na_2SO_4 (V)	Na_2So_4 (I)
1	4.06	4.58	4.13	4.50	3.83	4.64
2	2.50	4.00	4.04	3.99	3.17	**3.87**
3	**2.14**	3.23	3.69	3.77	3.07	3.53
4	1.97	**2.54**	3.36	3.37	**2.78**	2.81
5	1.53	2.29	**3.27**	2.89	2.64	2.68
6	1.25	2.04	2.76	**2.59**	2.32	2.32
7	1.06	1.99	2.59	1.88	1.86	2.13

Another aspect analyzed in the second TEM sample was the NiO grain size. As noted in Fig. 5-36, a much thicker NiO formed in areas affected by the presence of the sulfate deposit then NiO formed in unaffected areas. At the temperatures studied, grain-boundary diffusion is much faster than lattice diffusion [112], so understanding the grain size should aid in the analysis. However, as discussed by Peraldi et al. [108, 109], determining grain size in NiO formed at this low temperature is challenging due to its complex microstructure, which can be duplex and contain pores. Moreover, the scale development has a significant dependence on metal orientation. The reported grain size is therefore a rough estimate based on TEM analysis. In the Na-affected area of the NiO scale formed at 625°C in O_2-10 ppm SO_2, the grain size at the bottom of the sample (~middle of the oxide that formed) was determined to be 60 $\pm$ 16 nm. A TEM sample was not made in the unaffected area for this exposure, but the NiO grain size can be estimated based on prior TEM analysis. From a TEM sample of nickel oxidized at 700°C in dry air for 20 h the grain size was measured to be 357$\pm$ 94 nm. Comparing to the literature, based on the analysis of Peraldi *et al.* [108, 109], at 700°C an NiO grain size of 500 nm for a scale up to 10 μm in thickness, such a grain size is similar to that measured by TEM in this study. While the present test temperature was 625°C, a 75°C difference should not have a huge effect on oxide grain size. Atkinson *et al.* [113] reported a grain size of 500 nm after oxidation at 700°C for 5 h and a grain size of 350 nm after oxidation at 600°C for 6 h. While there is a difference, the important point is the grain size is much larger than for the NiO affected by the presence of the Na.

5.2.4 Effect of Na and S on NiO Growth [117]

A small grain size was reported in the previous section for the NiO affected by the presence of the Na-Ni-S-O phase. Density functional theory (DFT) calculations were conducted by Zhenyu and Wang [117] to determine how the presence of Na, S, and co-doping of Na and S impacts the grain-boundary energy. The atoms added were substitutional with Ni and O, respectively. Note, substituting Na^{+} for Ni^{2+} results in a charge imbalance. Vacancies were not introduced but rather a small amount of Ni^{3+} or O^{-} exists in the simulated cell. Figure 5-41 shows the resulting 2D projections of the structures for each simulation. The impurity concentration was 1.25 atomic % total for all simulations. This value is realistic for the values detected in the oxide (Fig. 5-37). A Σ5 (3 1 0) grain boundary was created, which is a boundary often used for evaluating NiO [118], [119]. Table 5-3 shows the calculated grain-boundary energies. A given grain-boundary energy was calculated using Eq. 5-5, where E_{GB} is the energy of the grain boundary, $E_{boundary}$ is the energy of the simulated cell with the impurity at the grain boundary, E_{bulk} is the energy of the cell with the impurity in the bulk, and A is the contact area of the bi-crystal (~55.73 $Å^2$). The values in Table 5-3 indicate doping of Na, S, and Na+S all decrease the grain-boundary energy. Na and S together results in the largest decrease. This result is in agreement with Na+S doping having the effect of decreasing the NiO grain size. Further, Na doping done would not be expected to have much of an effect.

$$E_{GB} = \frac{\left(E_{boundary} - E_{bulk}\right)}{2A} \qquad (5-5)$$

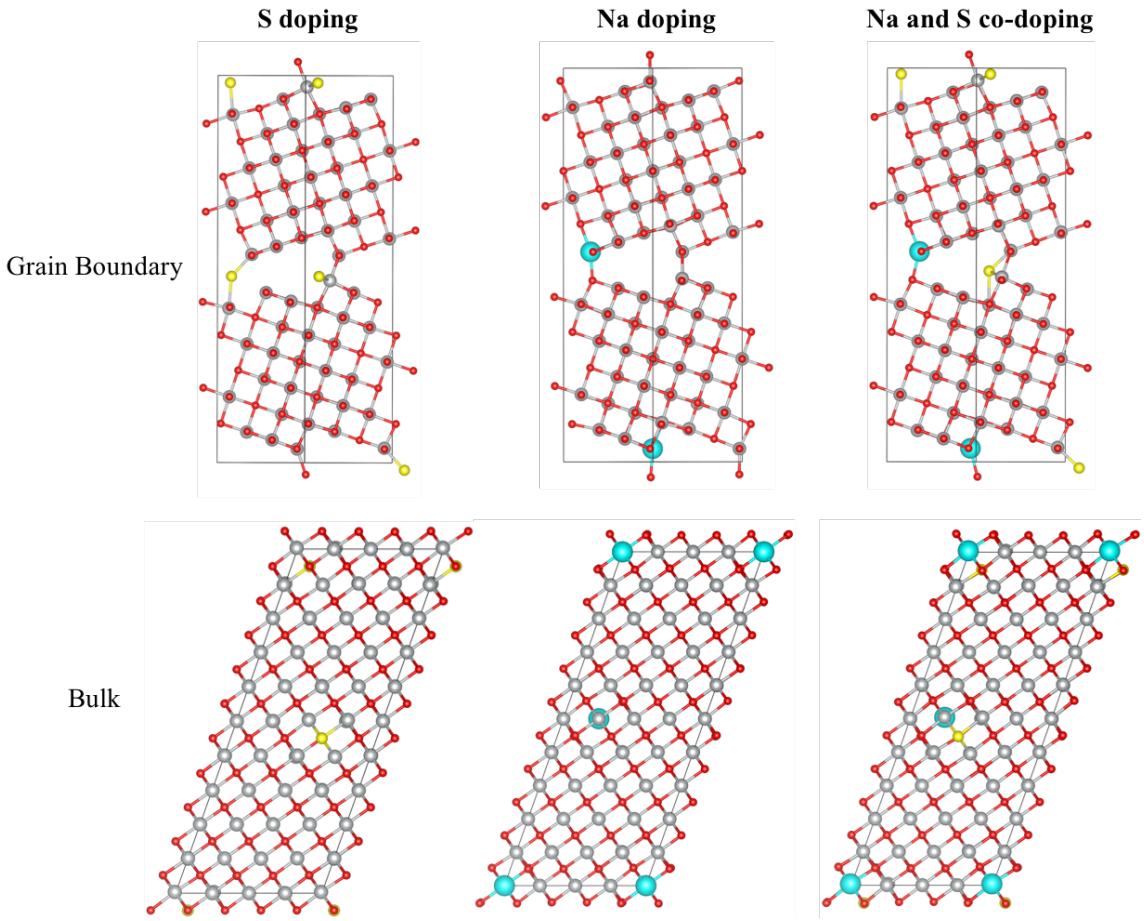

Figure 5-41. NiO structures used in computer simulations with S doping, Na doping, and Na and S co-doping.

Table 5-3. E_{GB} values after simulations of NiO with Na, S, and Na+S impurities.

	E_{GB} (J/m^2)
Without dopant	1.37
Doping S	1.07
Doping Na	1.26
Co-doping Na and S	0.91

5.2.5 Discussion

The solid-state mechanism proposed in the previous chapter was further assessed in this chapter. It was found that the Na_2SO_4 appears to have a spatial influence up to ~750 μm at 650°C and up to ~500 μm at 625°C. Note, those were the largest distances measured, each area showed variation so the kinetics of the surface diffusion is not accurately known. The important aspect is that the results showed convincing evidence that the nanocrystalline phase that forms is also rapidly diffusing Na^+, resulting in a spread of this phase parallel to the surface. The evidence for this is based on the experiments where Na_2SO_4 grains were isolated and resulting TEM analysis indicating $Na_2Ni_2SO_5$ formation at the reaction front. Figure 5-42 re-introduces the schematic of the mechanism with diffusion of Na included. The modified schematic is also applicable to K_2SO_4. An additional reaction is included, where Na^+ diffusing along the surface via the nanocrystalline phase and reacts with Ni^{2+} from the metal and sulfur from the atmosphere to form additional $Na_2Ni_2SO_5$. The reaction must be rapid allowing for an effective “spreading” of the nanocrystalline phase a large distance away from the deposited sulfate grain.

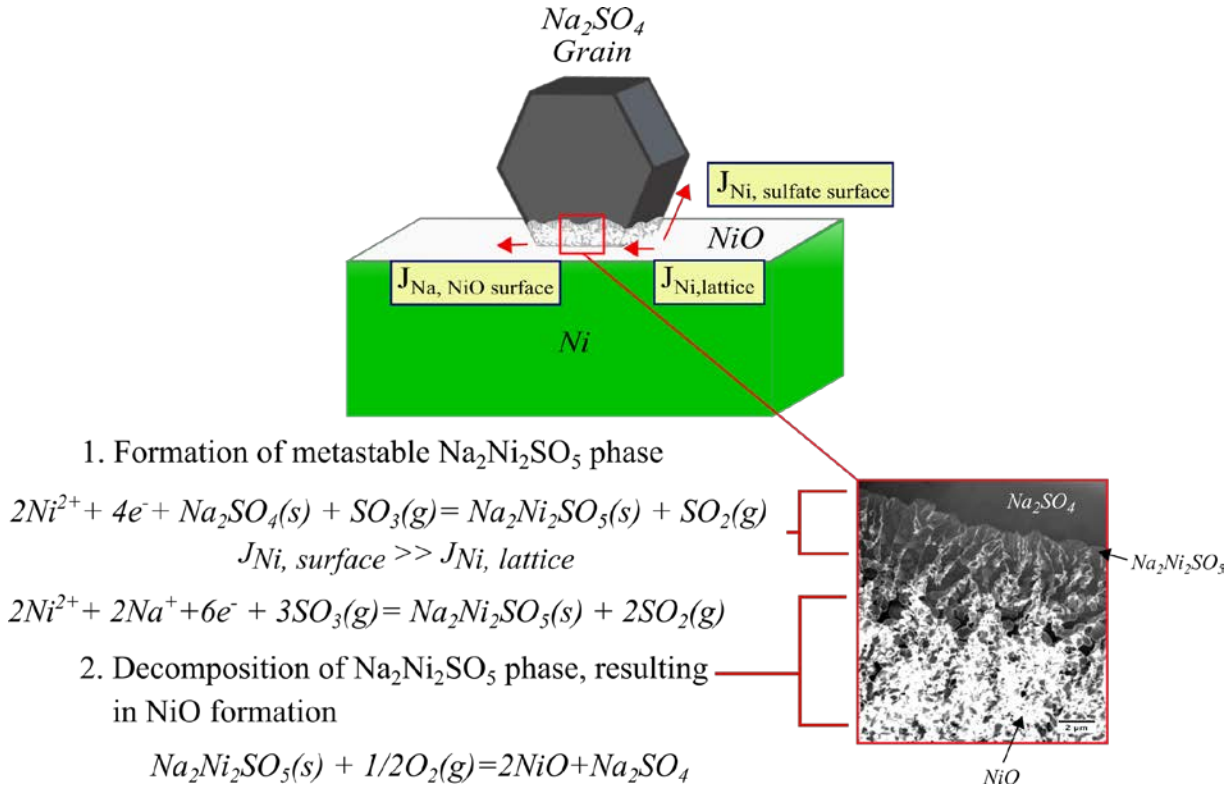

Figure 5-42. Schematic of proposed mechanism, with diffusion of Na along the surface included.

The TEM samples analyzed in this section, from areas away from the deposited sulfate, showed nanocrystalline phase formation near the oxide/gas interface. No Na_2SO_4 was observed, and the structure consisted of a fine-grained NiO below where the nanocrystalline phase existed. If the nanocrystalline phase decomposed, as observed in the previous section, Na_2SO_4 should have been observed. It is possible the TEM samples were taken from areas of early-stage reaction and that a sample closer to the sulfate deposit may show Na_2SO_4 particles from the decomposition of the metastable phase. Regardless, the thickness of the NiO in areas affected by the presence of the Na-Ni-S-O phase was 18 ± 6 μm at 625°C, whereas in unaffected areas the thickness was only ~3 μm, so the nanocrystalline phase is significantly influencing the nickel oxidation.

The DFT calculations on the effect of Na and/or S as a dopant on the grain-boundary energy revealed both Na and S decrease the energy. Co-doping Na and S resulted in the largest decrease in grain-boundary energy. As mentioned in the previous section, a minor amount of S was detected within the NiO in both areas unaffected and affected by the presence of Na. The DFT calculations assumed only 1.25 atomic % of S and/or Na. Those values are in agreement with the amount detected during EDS analysis. In accordance with the DFT calculations, the grain size of nickel without a deposit in O_2-10 ppm SO_2 may be expected to be smaller than in dry air due to the presence of S. However, the thickness was much less than the Na-affected NiO area. Therefore, sulfur alone cannot explain the thick NiO formed beneath the nanocrystalline phase. A combination of Na and S, resulting in the largest decrease in grain-boundary energy is apparently needed to form the fine grained structure. Therefore, the presence of both Na and S in the nanocrystalline phase is hypothesized to promote nucleation of new NiO rather than sustain growth of existing grains. This is corroborated by the extremely fine polycrystalline NiO structure in the presence of Na and S (note that NiO is columnar or larger grained when formed in only O_2).

The grain size previously discussed can be used to analyze the growth kinetics. The growth of NiO follows parabolic kinetics, discussed in Section 2.2. Therefore, the predicted oxide scale thickness can be calculated based on the grain size determined using TEM analysis. The rate constant can be related to grain boundary diffusion through Eq. 5-6, presented by Atkinson *et al.* [113], where k_p is the parabolic rate constant, D^* is the measured lattice diffusion, $(D'\delta)^*$ is the measured short-circuit diffusion, and g is the grain size. The values for D^* and $(D'\delta)^*$ were obtained from Atkinson *et al.* [113].

$$k_p\left(p_{O_2}=1\right)=6.4\left[D^*+\frac{2(D'\delta)^*}{g}\right] \qquad (5-6)$$

By using Eq. 5-6 to calculate a rate constant for a given grain size, the predicted scale thickness can then be calculated using Eq. 2-1 in Section 2.2. Figure 5-43 shows a plot of oxide-scale thickness after 20 h for grain sizes from 40–1000 nm. The measured grain size of NiO affected by the nanocrystalline phase was 60 $\pm$ 16 nm. Using Eq. 5-6, a calculated oxide thickness after exposure at 625°C for 20 h is ~9.4 μm . The measured thickness after the experiment shown in Fig. 5-36 was 18 $\pm$ 6 μm. A diffusion coefficient for Ni through NiO would have to be ~1.9x10^{-12} to form an oxide of that thickness. The difference in calculated vs. measured oxide thickness may be due to the presence of Na and S increasing the diffusion coefficient of Ni through the NiO grain boundaries. More analysis would be needed to confirm this hypothesis. In addition, some of the NiO measured may be due to decomposition of the nanocrystalline phase and Na_2SO_4 was just not identified in that sample. In the absence of the deposit the grain size is estimated to be 357$\pm$94 nm, based on discussion in the previous section. Using Eq. 5-6, a calculated oxide thickness after exposure at 625°C for 20 h is ~3.8 μm, which is only slightly higher than the actual measured thickness of ~3 μm.

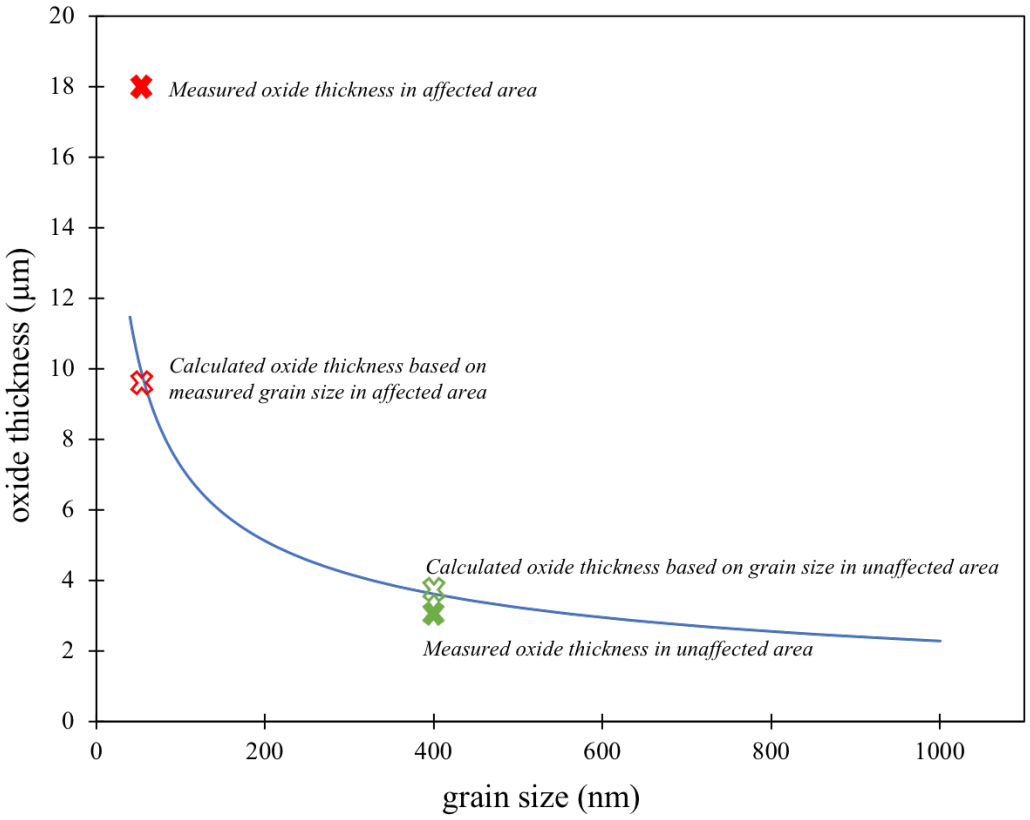

Figure 5-43. Calculated oxide thickness for grain sizes from 40-1000 nm after a 20 h exposure of nickel at 625°C.

The purpose of studying pure nickel was to enable better understanding of nickel-based superalloys in engine application. The experiment completed on PWA 1484, with Na_2SO_4 present on only half the sample, showed a "throwing power" of the sulfate deposit. The mechanism is predicted to be the same as discussed for pure nickel. The morphology of the corrosion product was an external intermixed product of an Na-containing phase intermixed with NiO and an internal mixed oxide/sulfide. A TEM sample would be needed to determine if the Na-containing phase was primarily $Na_2Ni_2SO_5$ or $NaSO_4$: a thick NiO was not observed on PWA 1484 as there was also Cr oxidation. However, the discussed mechanism should still be applicable. If the alloy is depleted

and begins to form NiO, the presence of the nanocrystalline phase can lead to a fine grained structure that begins to rapidly oxidize.

The observed “throwing power” is important in instances where a crack forms on a component. Brooking et al. [120] completed fatigue testing of a nickel-based superalloy at 550°C in air+300 vpm SO_2. An 80 Na_2SO_4/20 K_2SO_4 deposit was applied to the sample surface and, after exposure, sodium was detected in the crack tip. Based on the analysis in this section, it is postulated that the mechanism discussed applies. Thus, in engine application whenever a crack is present the spreading of the metastable phase can lead to corrosion within the crack, further accelerating attack. Further study of this is warranted.

5.3 Effect of SO_2 Content on Alloy Hot Corrosion Over the Temperature Range 550°C-1000°C

The previous chapters presented a new solid-state mode of hot corrosion applicable to nickel-based superalloys. To expand understanding of hot corrosion over a broader range of conditions, this chapter will focus on the modes and mechanisms of hot corrosion as a function of temperature and SO_2 content from 550°C-1000°C. As discussed in Section 2.3, in presenting corrosion rate vs. temperature a typical schematic with two maxima is often used [121]. The origin is traced back to M. Gell [39] from Pratt & Whitney, indicating industry discussion led to the representation. The actual graph of corrosion rate vs. temperature will be dependent on many variables such as alloy composition, environment, deposit, etc. A key aspect of this chapter is to understand the trend for a nickel-based superalloy in lower content SO_2-environments.

Preliminary results of weight change vs. temperature after a 20 h exposure, shown in Section 5.1, indicated spallation in O_2-100 ppm SO_2 at 750°C and 800°C. A graph of average attack vs. temperature was plotted to understand if both measurements could be used for analysis, and to predict the trend in O_2-100 ppm SO_2 where spallation occurred. Figure 5-44 shows the measured plots of average attack vs. temperature and Fig. 5-45 shows corresponding plots of weight change vs. temperature. Comparing the two sets of plots, the separation between data points varies, but the trend for each environment holds for both measured parameters, i.e. the maximum occurs at the same temperature. Therefore, either measure of attack can be used in analyzing data. In Fig.5-45 the dashed line indicates the predicted trend in O_2-100 ppm SO_2 where spallation occurred based on the trend in the average attack vs. temperature plot in Fig.5-44. Appendix A shows how the average attack measurements were calculated for each environment.

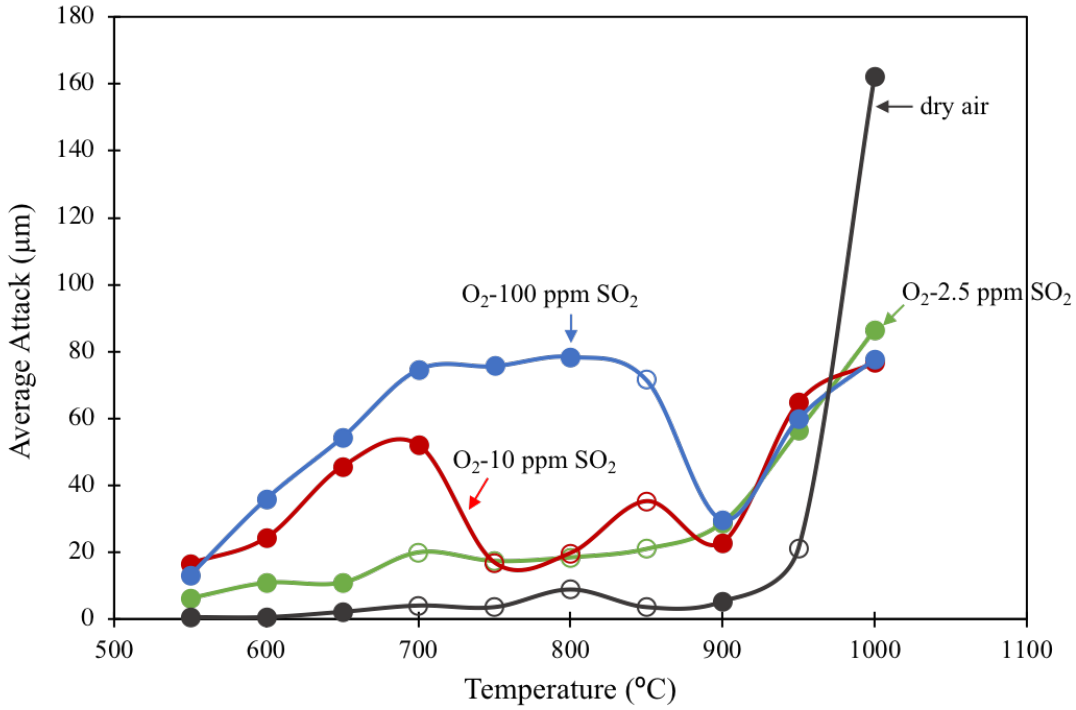

Figure 5-44. Average attack vs. tempearture after 20 h hot corrosion exposure of PWA 1484 in dry air and O_2-(2.5, 10, and 100) ppm SO_2 with 2.5 mg/cm^2 Na_2SO_4 deposit.

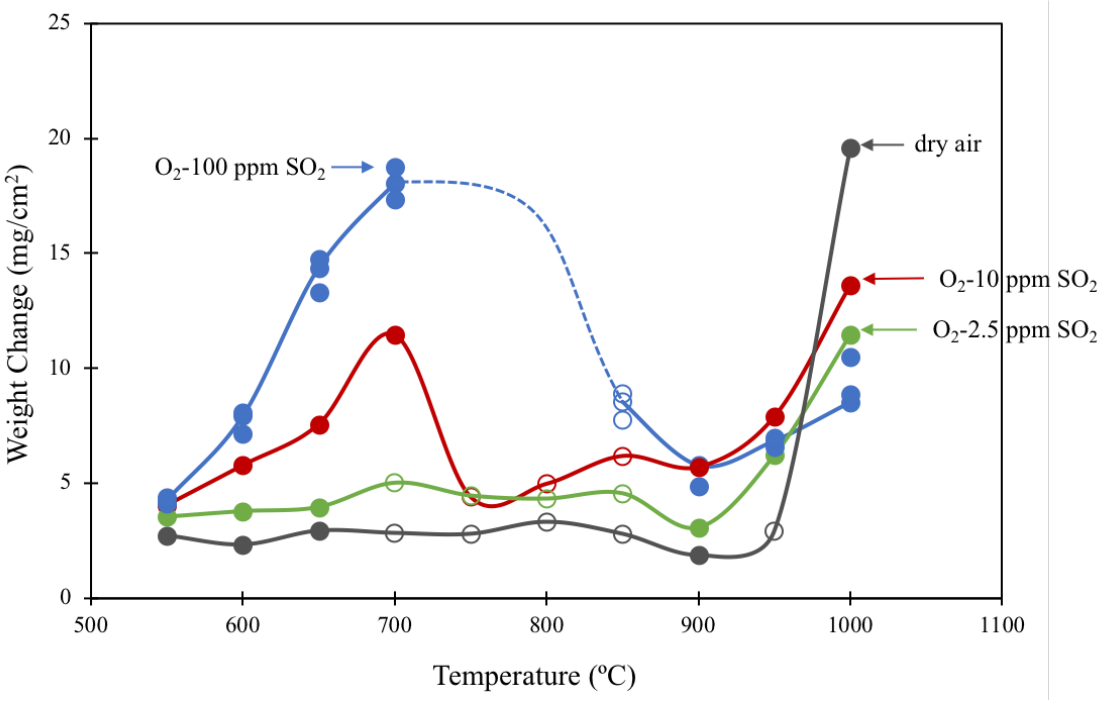

Figure 5-45. Weight change vs. tempearture after 20 h hot corrosion exposure of PWA 1484 in dry air and O_2-(2.5, 10, and 100) ppm SO_2 with 2.5 mg/cm^2 Na_2SO_4 deposit**.**

The plots can be compared to the schematic of corrosion rate vs. temperature, shown in Fig. 2-9. In dry air and O_2-2.5 ppm SO_2, minimal attack occurred at the low (550°C-650°C) and intermediate (700°C-850°C) temperatures, while at high temperatures, average attack started to increase. Exposure in O_2-10 ppm SO_2 resulted in the characteristic curve with two maxima as shown in Fig. 5-44 and 5-45. Increasing the SO_2 content to 100 ppm resulted in similar average attack across the intermediate-temperature regime and therefore the absence of the two distinct peaks. This result can be analyzed considering the $NiSO_4$-Na_2SO_4/CoSO4-Na_2SO_4 stability diagram, as shown in Fig. 5-2, indicating the P_{SO_3} need for liquid formation. Key points from this diagram are: the $NiSO_4$-Na_2SO_4 eutectic is not stable in any of the environments (dry air and O_2-

(2.5, 10, and 100) ppm SO_2) studied and the formation of the $CoSO_4$-Na_2SO_4 eutectic from CoO[2] is stable from the eutectic temperature (565°C) up to ~650°C in O_2-2.5 ppm SO_2, up to ~700°C in O_2-10 ppm SO_2, and up to ~800°C in O_2-100 ppm SO_2. At intermediate temperatures under conditions in which liquid formation is predicted, significant attack occurs at a rate that is apparently independent of temperature. What results is a graph without the characteristic two maxima, as shown in the O_2-100 ppm SO_2 environment. Analysis of the mechanism at the low, intermediate, and high temperature range will be discussed in the following sections.

5.3.1 Low Temperature (≤ 650°C)

For this study, low-temperature hot corrosion is classified as occurring at 650°C and below. This reasoning is based on the eutectic temperature of $NiSO_4$-Na_2SO_4 (671°C). Below that eutectic temperature, the only stable liquid for the system and conditions studied is $CoSO_4$-Na_2SO_4 (T_e=565°C). Therefore, liquid formation for the traditional mechanism of Type II hot corrosion, as proposed by Luthra [9, 11, 60], would have to involve cobalt. Subsequent dissolution and precipitation of alloying elements would follow. Low-temperature hot corrosion can also occur via the solid-state mechanism discussed in Section 5.1 and 5.2 (see also [101]). The resulting formation of a metastable $Na_2Ni_2SO_5$ phase is followed by decomposition to a porous NiO with

[2] Co_3O_4 is the stable oxide in the environments studied. Considering local environments that develop below the sulfate deposit, a decrease in P_{O_2} would stabilize CoO

Na_2SO_4 particles incorporated. Below the T_e of $CoSO_4$-Na_2SO_4, the only operating mechanism for interaction with Na_2SO_4 in the low SO_2 content environment is the solid-state process.

Regardless of the mechanism, SO_2/SO_3 is required and the extent of attack is impacted by the P_{SO_3}. Figure 5-46 shows cross-sectional SEM images at 650°C in dry air and O_2-(2.5, 10, and 100) ppm SO_2 after a 1.5 h and 20 h exposures with 2.5 mg/cm^2 of Na_2SO_4. In the dry air environment, very little interaction occurred and (Ni, Co)O formed at the deposit/alloy interface. In the SO_2-containing environments, porous (Ni, Co)O formed at the deposit/gas interface and the extent of attack increased as SO_2 content increased. ICP-OES was coupled with the cross-sectional SEM analysis to determine the extent of attack as a function of SO_2 content. For the ICP-OES analysis, the metastable $Na_2Ni_2SO_5$ phase is conjectured to be soluble in water. Figure 5-47 shows plots of the ICP-OES results of Co and Ni content after the 1.5 h exposure in each environment studied. All other alloying elements detected are not considered because they were present in very small amounts and were not impacted by increasing SO_2 content. The plots indicate a low content of cobalt that slightly increases as SO_2 content increases. Nickel content is much higher and it increases greatly with increasing SO_2 in the atmosphere. Considering that 650°C is below the Na_2SO_4-$NiSO_4$ eutectic, the majority of the corrosion at this temperature is occurring via the solid-state process. According to the reaction,

$$2Ni^{2+} + 4e^- + Na_2SO_4(s) + SO_3(g) = Na_2Ni_2SO_5(s) + SO_2(g) \qquad (5-7)$$

increasing the P_{SO_3} will increase the $Na_2Ni_2SO_5$ content, in agreement with the ICP-OES results. The formation of a $CoSO_4$-Na_2SO_4 eutectic is predicted to only have a minor role due to the very

low levels of Co found in the ICP-OES analysis. A similar trend is expected for the other low-temperature exposures. Representative cross-sectional SEM images from lower-temperature exposure can be found in Section 5.1.

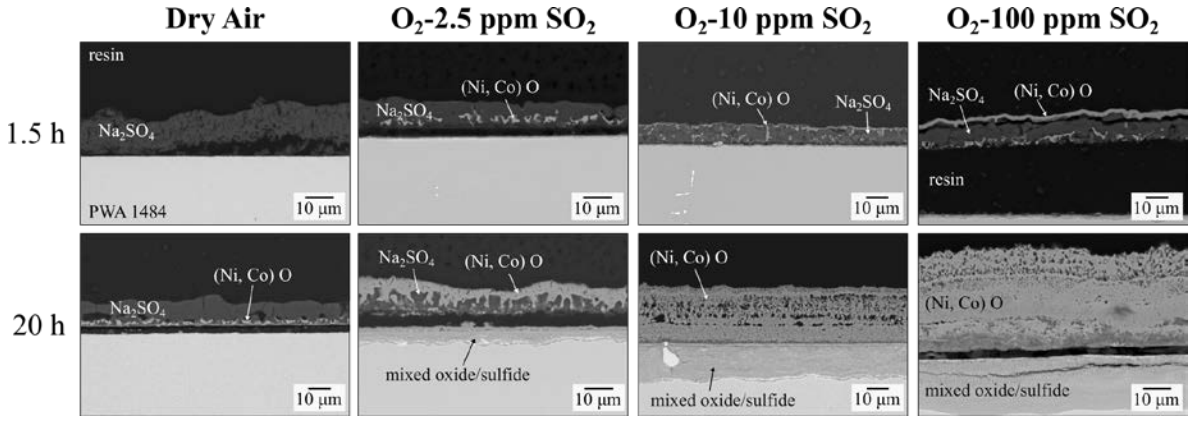

Figure 5-46. Cross-sectional SEM images after 1.5 h and 20 h exposure of PWA 1484 in dry air and O-(2.5, 10, and 100) ppm SO_2 with 2.5 mg/cm^2 Na_2SO_4.

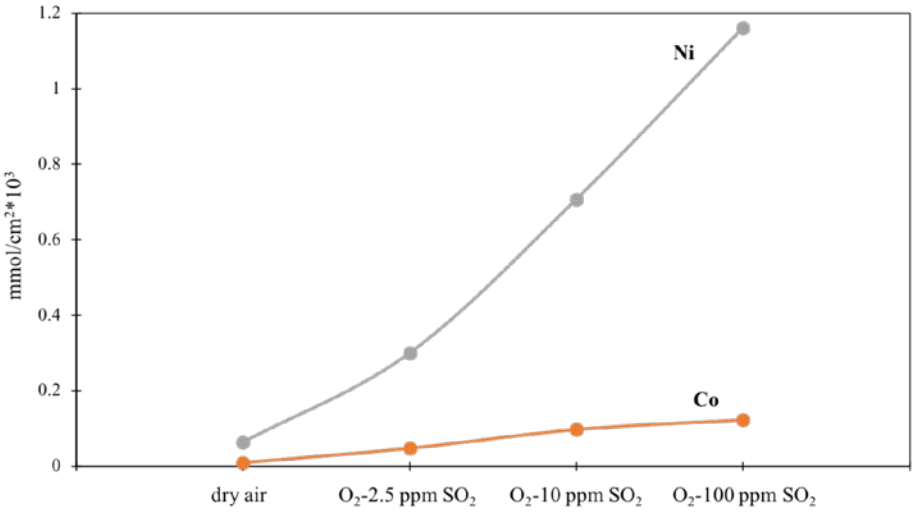

Figure 5-47. ICP-OES results showing concentration of Ni and Co in mmol/cm^2*10^3 after a 1.5 h exposure of PWA 1484 in dry air and O_2-(2.5, 10, and 100) ppm SO_2 with 2.5 mg/cm^2 Na_2SO_4.

5.3.2 Intermediate Temperature (700°C-850°C)

As temperature increases, the P_{SO_3} in each environment decreases, and considering a Ni-O-S phase diagram the NiO/$NiSO_4$ phase boundary shifts to a higher P_{SO_3} value. The proposed solid-state mechanism (Section 5.1 and 5.2) requires in the initial stage: (1) the gas can access the surface of the sulfate grains for reaction; and (2) a sufficient P_{SO_3} exists for metastable phase formation. As the temperature increases, for a given SO_2-containing environment the decrease in P_{SO_3} and increase in the sintering rate of the deposit makes formation of the metastable phase for the solid-state mechanism less likely. Therefore, intermediate temperature is defined as the region where liquid formation in the form of reaction with the sulfate deposit is the predicted initial mechanism. Based on previous studies, the mechanism is predicted to occur via Type II hot corrosion [11] and/or alloy-induced acidic fluxing [59].

Figure 5-48 shows cross-sectional SEM images of PWA 1484 after a 20 h exposure at 700°C, 750°C, 800°C, and 850°C in dry air and O_2-(2.5, 10, and 100) ppm SO_2 with 2.5 mg/cm^2 of Na_2SO_4. The structures at 700°C, 750°C, and 800°C consist of an external porous (Ni, Co) O with an internal mixed oxide/sulfide. Sulfur is enriched at the oxide/metal interface. Localized attack occurs at 700°C in dry air and O_2-2.5 ppm SO_2 and at 750°C and 800°C in dry air and O_2-(2.5 and 10) ppm. In O_2-100 ppm SO_2 for all temperatures and in O_2-10 ppm SO_2 at 700°C, Na_2SO_4-$CoSO_4$ eutectic is stable and uniform attack occurs.

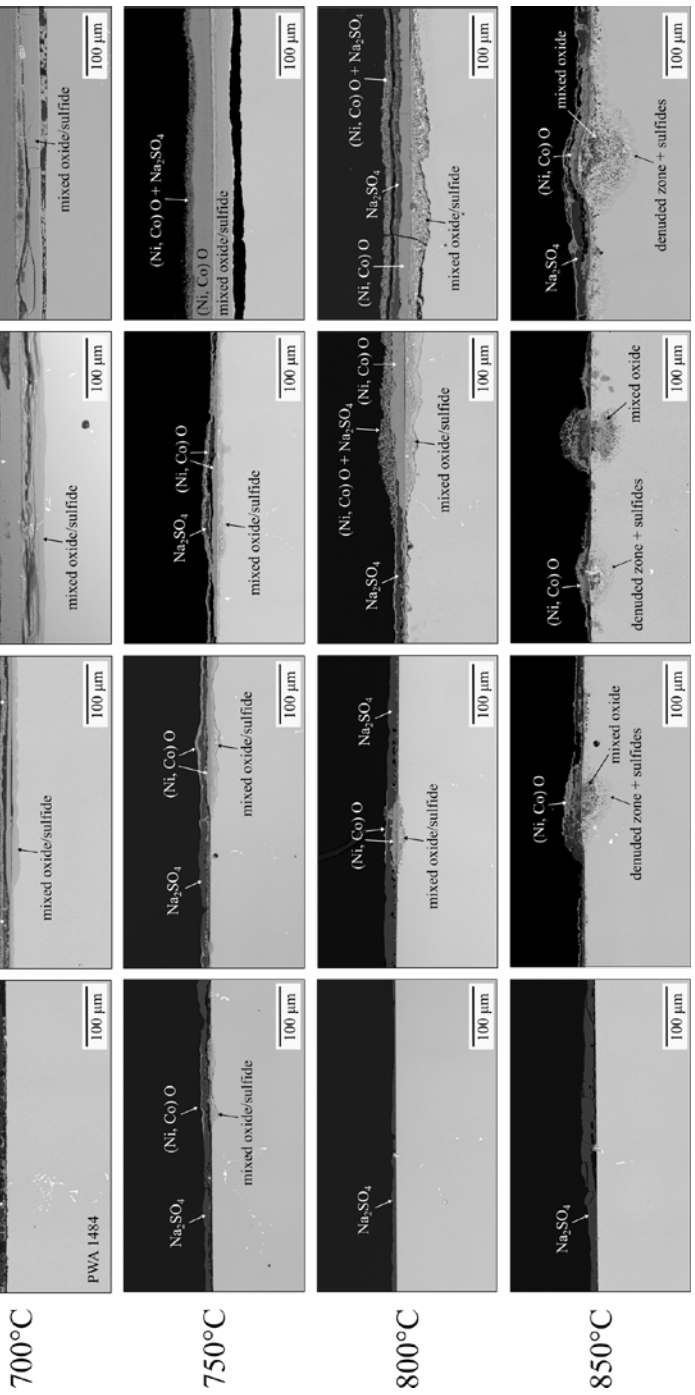

Figure 5-48. Cross-sectional SEM images of PWA 1484 after 20 h exposure at 700°C, 750°C, 800°C, and 850°C in dry air and O_2-(2.5, 10, and 100) ppm SO_2 with 2.5 mg/cm^2 Na_2SO_4.

At 850°C, pit formation occurs and the attack is localized in all environments. 850°C is also the first temperature where discrete sulfide particles form in the underlying alloy. More discussion will follow regarding this temperature due to the distinct morphology. Figure 5-49 shows a WDS map of a cross-section after exposure at 850°C in the O_2-10 ppm SO_2 environment for 2 h. Note that the depth of the pit is ~15 um after just 2 h of exposure. The map indicates an internal mixed oxide of Cr, Al, W, and Ta forms. In the denuded zone, the map indicates the formation of Cr_xS_y and $(Ta, W, Mo)_xS_y$, and Cr and Al depletion.

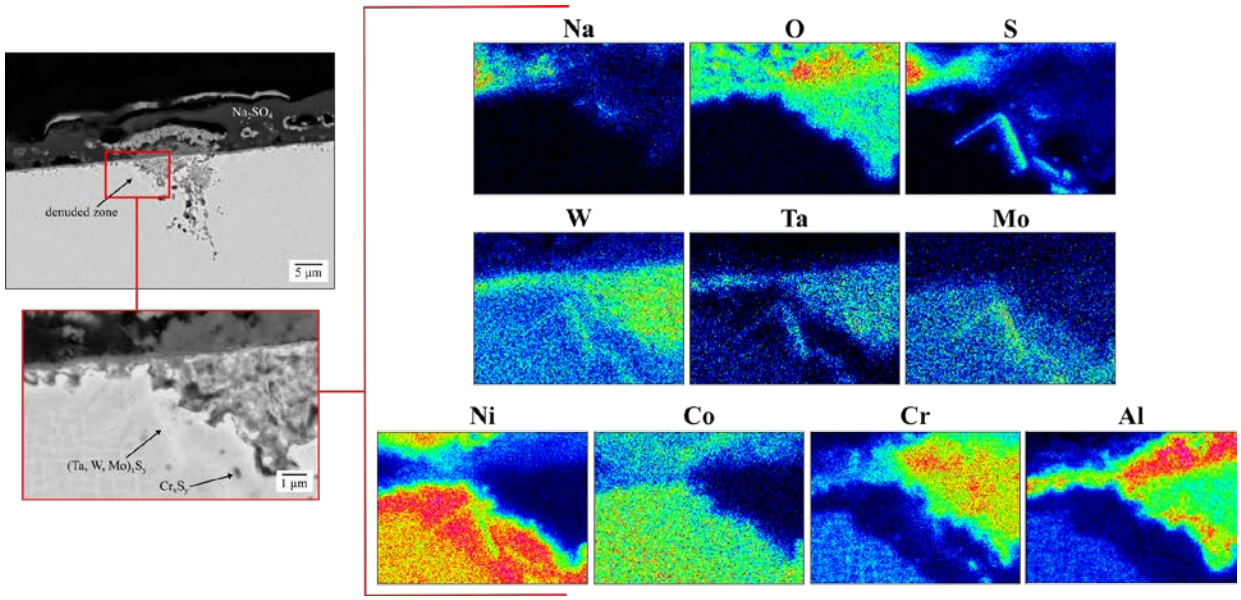

Figure 5-49. Cross-sectional SEM images of PWA 1484 after a 2 h exposure at 850°C in O_2-10 ppm SO_2, along with WDS elemental maps of the highlighted area.

5.3.2.1 Heat-treated Alloys

Considering the formation of pits at 850°C, it was found that the pit size is similar to the dendritic spacing of the alloy, as shown in Fig. 5-50, indicating initiation may occur due to the slightly different chemical composition in the dendritic vs. interdendritic regions (see Fig. 5-52). The pit size is observed to correlate to the spacing between dendrites; however, it is not directly evident where the exact initiation sites are. Pit formation was also found to occur where carbides were present. A similar observation was reported by Potter *et al.* [122]. Thus, two different causes are proposed to explain pit formation: (1) due to the dendritic structure; and (2) due to carbides present. To confirm that the dendritic structure affects pit formation, heat-treated model alloys were prepared. These were referred to as HT-short, HT-medium, and HT-long, referencing the heat-treatment duration. Heat treating the alloy further homogenizes the structure and decreases the fraction of carbides present, as was confirmed by optical and SEM analysis. Figure 5-51 shows surface and cross-sectional SEM images revealing the dendritic structure for the three heat-treated conditions. Figure 5-52 shows plots of Al Cr, Ni, and Co content as a function of position across dendritic and interdendritic regions. Refractory elements were excluded due to uncertainty in the values because of peak overlap in EDS. However, there have been past literature studies focused on element partitioning and found that Ni, Al, and Ta partition to the interdendritic region, while Cr, Co, W, Re, and Mo partition to the dendritic core [122, 124, 125]. The plots in Fig. 5-52 clearly show that as heat-treatment duration increases, the composition becomes more uniform. Also, note that the carbides are located in the interdendritic regions.

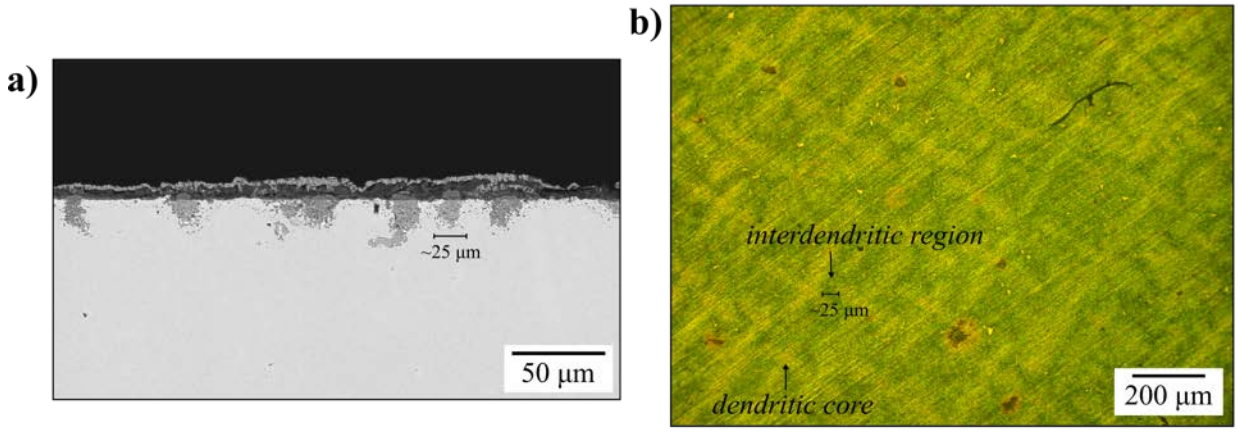

Figure 5-50. a) SEM cross-sectional image of PWA 1484 after a 20 h exposure at 850°C in O_2-10 ppm SO_2 with 2.5 mg/cm^2 Na_2SO_4 deposit with pit size marked, along with b) surface optical image of bare PWA 1484 indicating dendritic structure and size of interdendritic region is similar to the size of pits after a hot corrosion exposure.

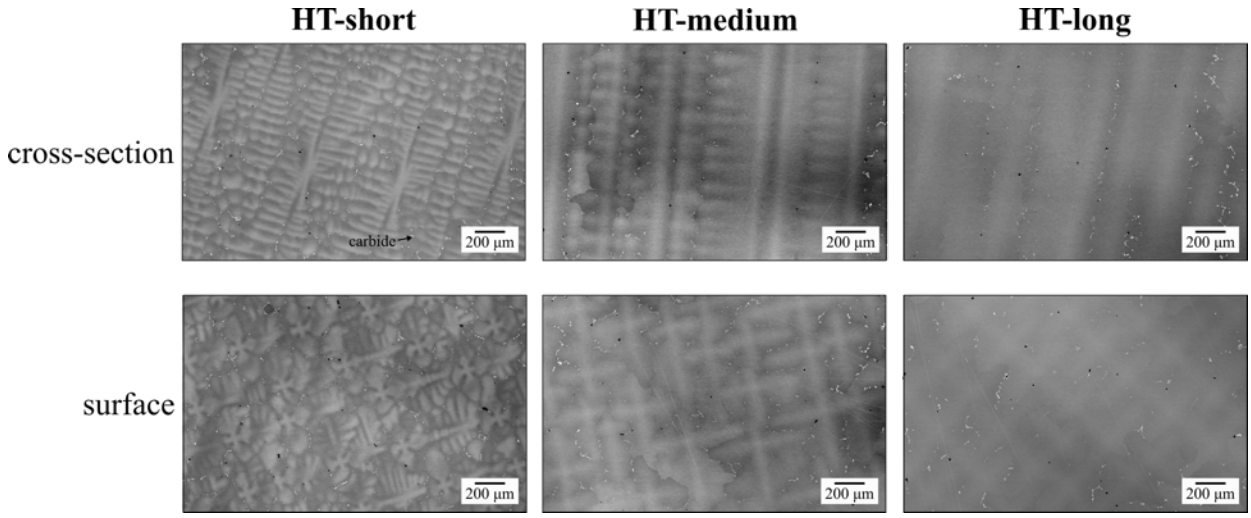

Figure 5-51. SEM images of cross-section and surface of heat-treated PWA 1484 alloys.

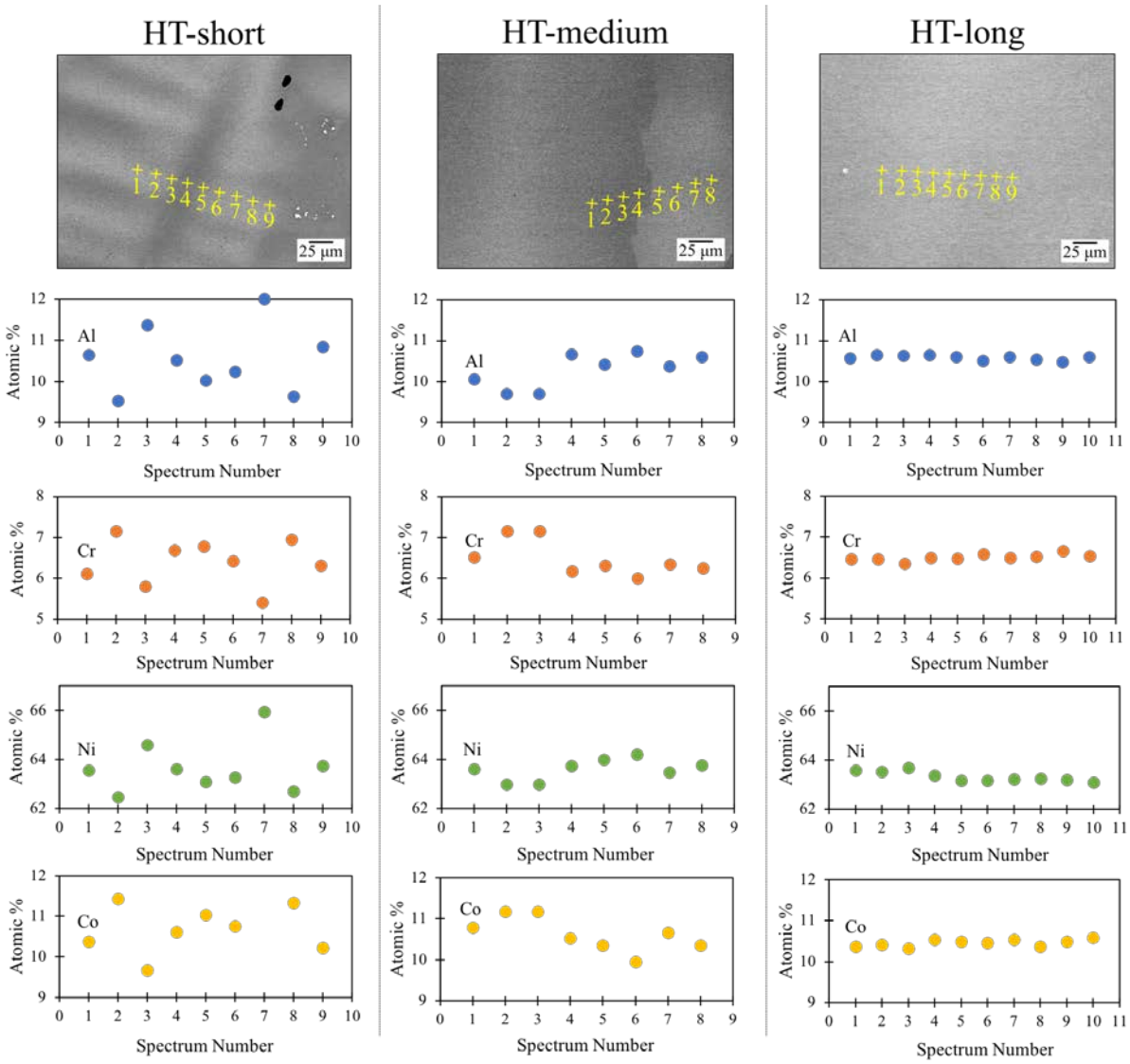

Figure 5-52. Cross-sectional SEM image of heat-treated PWA 1484 alloys, along with EDS results of Al, Cr, Ni, and Co composition.

The heat-treated alloys were hot-corrosion tested at 850°C for 20 h in O_2-10 ppm SO_2 with 2.5 mg/cm^2 Na_2SO_4. Figure 5-53 shows a graph of the fraction of pits across the surface of the sample, measured via cross-sectional SEM images. Heat-treating the sample greatly reduces the pit fraction, confirming the chemical segregation of the alloy led to pit formation. However, heat-

treatment did not completely eliminate pit formation. Pit formation on the sample with the longest heat-treatment was generally found to occur around a carbide. Therefore, heat-treatment homogenized the structure but did not completely eliminate the present carbides.

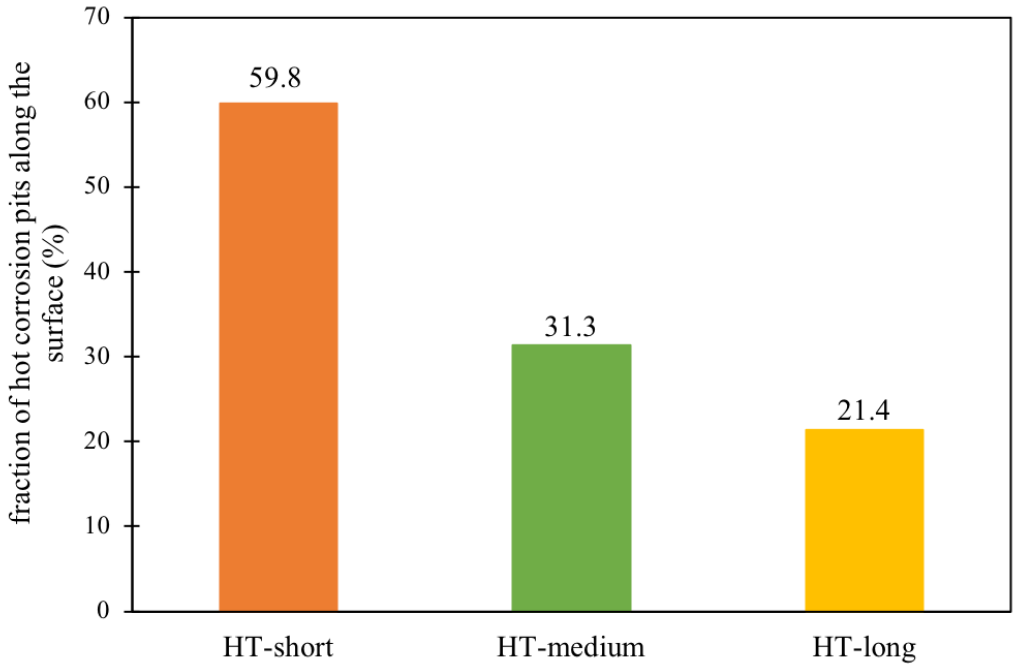

Figure 5-53. Graph of the fraction of corrosion pits along the surface, measured from cross-sectional SEM images of PWA 1484 alloys that were heat-treated for a short, medium, and long times and exposured to 850°C for 20 h in O_2-10 ppm SO_2 with 2.5 mg/cm^2 Na_2SO_4 deposit.

5.3.3 High-Temperature (≥ 900°C)

High-temperature is defined as being above the melting point of the Na_2SO_4 deposit. Known mechanisms operating in this regime are basic fluxing, alloy-induced acidic fluxing, and if the P_{SO_3} is high enough, acidic fluxing may occur [4]. Figure 5-54 shows the resulting cross-sectional SEM images of PWA 1484 after the 20 h exposure from 900°C-1000°C in dry air and O_2-(2.5, 10, and 100) ppm SO_2 and with 2.5 mg/cm^2 Na_2SO_4 deposit. At 900°C, minimal interaction occurs, with a mixed-oxide and chromium-sulfide particles identified. The dry-air environment shows very little interaction compared to the SO_2-containing environments. Exposure at 950°C and 1000°C to the SO_2-containing environments led to a mixed oxide being present at the gas interface and the formation of sulfide particles in the base alloy. The mixed oxide in the SO_2 environments primarily contains Cr and Al regions, and W and Ta regions. Al-rich oxide was found on the surfaces of the identified pores, as shown in the EDS of a magnified area of a cross-section of PWA 1484 after the 20 h exposure in O_2-100 ppm SO_2 in Fig. 5-55. In the dry air environment at 950°C, attack is localized with deep internal mixed oxide forming along with an external (Ni, Co) O product. As in the SO_2-containing environments, the mixed oxide in dry air at 950°C primarily contains Cr and Al regions, and W and Ta regions. More analysis of the oxide product will be presented in a later section. The difference between the environments is that the internal mixed oxide is uniformly penetrated into the alloy in the SO_2-containing environments. In the dry-air environment, the mixed oxide at 950°C has a morphology of internal precipitates intermixed with a γ-Ni matrix, formed due to depletion of Al and Cr. At 1000°C in the dry-air environment, the attack was significant (note the magnification difference). Compared to the SO_2-

containing environments, extensive reaction occurs with a porous mixed-oxide product. The mixed oxide contains regions rich in Al and Cr and also regions with high Ni content. The morphology is similar to corrosion products identified on NiCrAlMo alloys that underwent alloy-induced acidic fluxing [59].

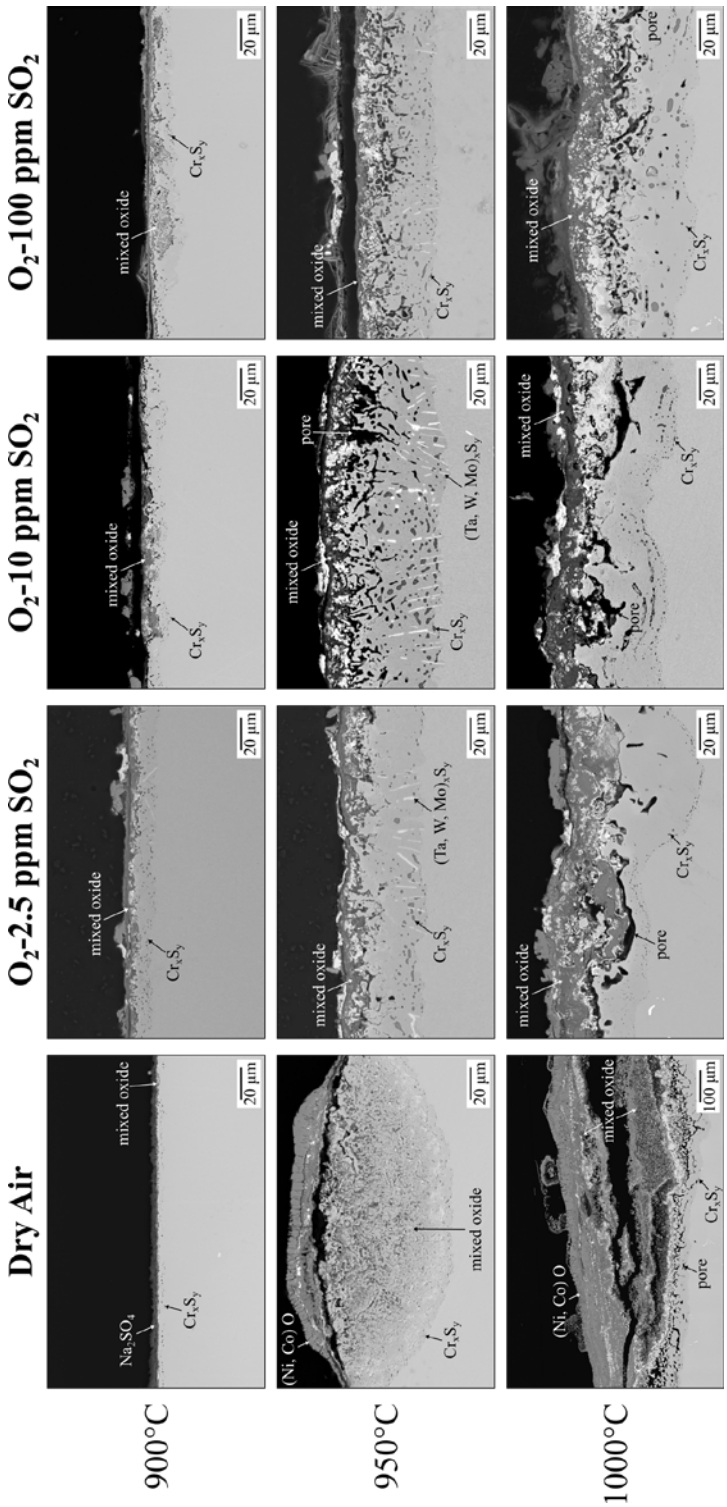

Figure 5-54. Cross-sectional SEM images of PWA 1484 after 20 h exposure at 900°C, 950°C, and 1000°C in dry air and O_2-(2.5, 10 ,and 100) ppm SO_2 with 2.5 mg/cm^2 Na_2SO_4.

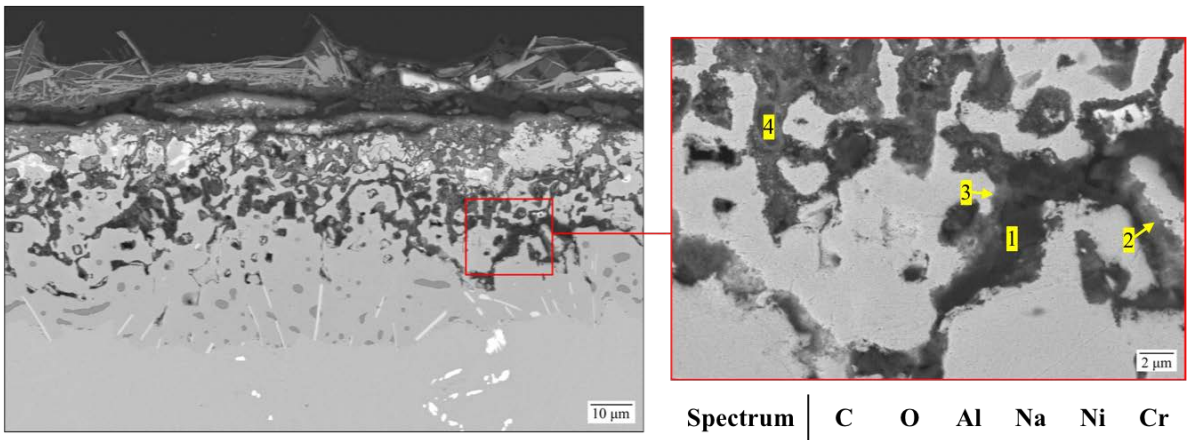

Spectrum	C	O	Al	Na	Ni	Cr
1	100	0	0	0	0	0
2	24	42	25	0	9	0
3	41	37	16	16	6	0
4	34	38	18	2	0	8

Figure 5-55. Cross-sectional SEM images after exposure of PWA 1484 at 950°C for 20 h in O_2-100 ppm SO_2, along with EDS analysis.

As discussed in Section 2.3, Type I hot corrosion involves initiation and propagation stages of attack. At 900°C, minimal attack occurs in all environments after the 20 h exposure. To determine if 20 h was still in the initiation stage, a 100 h exposure was carried out in dry air and O_2-10 ppm SO_2. The resulting weight change vs. time plots along with corresponding cross-sectional SEM images after the 100 h exposure are shown in Fig. 5-56. Note, the deposit was applied before the thermal exposure and the sample remained in the furnace during the duration of the experiment (i.e. there was no re-application of salt). Each data point represents a different sample. In the dry-air environment very little interaction occurred and compared to the 20 h exposure there was minimal additional weight gain. In the O_2-10 ppm SO_2 environment, the product continues to grow from 20 h to 100 h. The reaction product after the 20 h exposure was

~15 μm. After the 100 h exposure, the product is now ~50 μm. The morphology consists of mixed oxide with internal sulfide particles. While the growth was significant, the kinetics of the reaction are much slower than 950°C or 1000°C, where the product thickness formed in the O_2-10 ppm SO_2 was ~71 μm and ~ 80 μm, respectively. In addition, rapid weight change was not observed. Therefore, the alloy did not undergo breakaway corrosion.

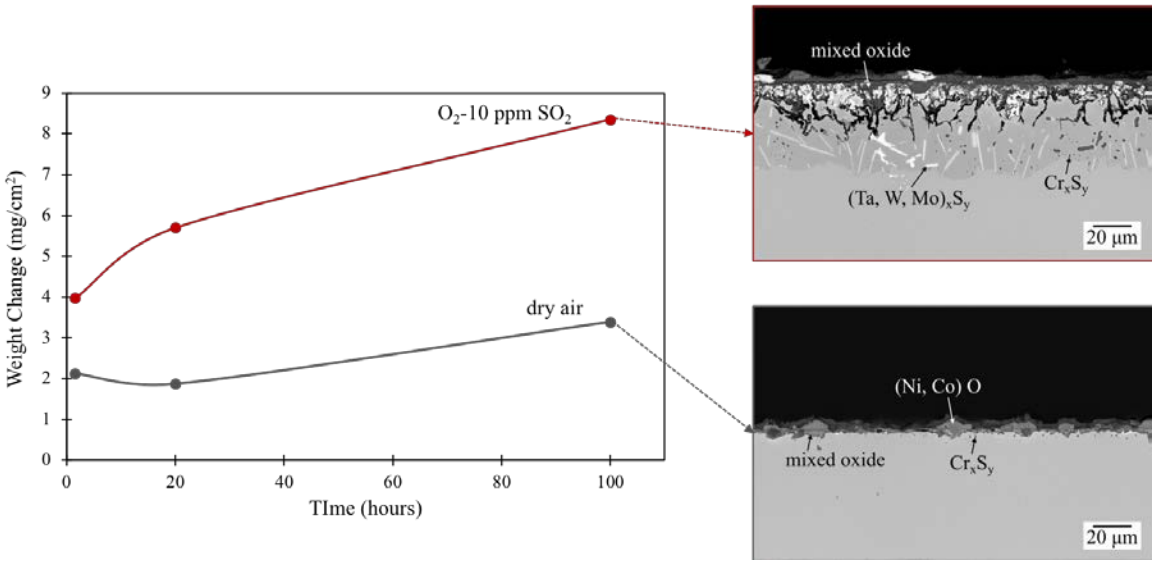

Figure 5-56. Weight change vs. time after exposure of PWA 1484 at 900°C in dry air and O_2-10 ppm SO_2 with 2.5 mg/cm^2 Na_2SO_4. The resulting cross-sectional SEM image after the 100 h exposure is shown.

At 950°C, the reaction product formed in dry air is distinctly different from the products formed in the SO_2-containing environments. A time study was completed to understand how the reaction progresses up to 100 h. Figure 5-57 shows the resulting plots of weight change vs. time for the four environments studied. In dry air and O_2-2.5 ppm SO_2, the weight change rapidly increases, indicting the reaction went through a propagation stage. Extending the exposure to 100 h was necessary for the propagation of the reaction to be realized. After the 100 h exposure, the

trend curiously shows that increasing the SO_2 content decreases the relative extent of attack. In the O_2-(10 and 100) ppm SO_2 environments, the weight change follows parabolic behavior, indicating a diffusion-controlled process. The trend observed is opposite to that in the low- and intermediate-temperature ranges. Additional analysis was done to determine the operating mechanism. Note that, while the O_2-(10 and 100) ppm SO_2 environments show much less weight gain than dry air and O_2-2.5 ppm SO_2, the attack is still much more extensive than pure oxidation.

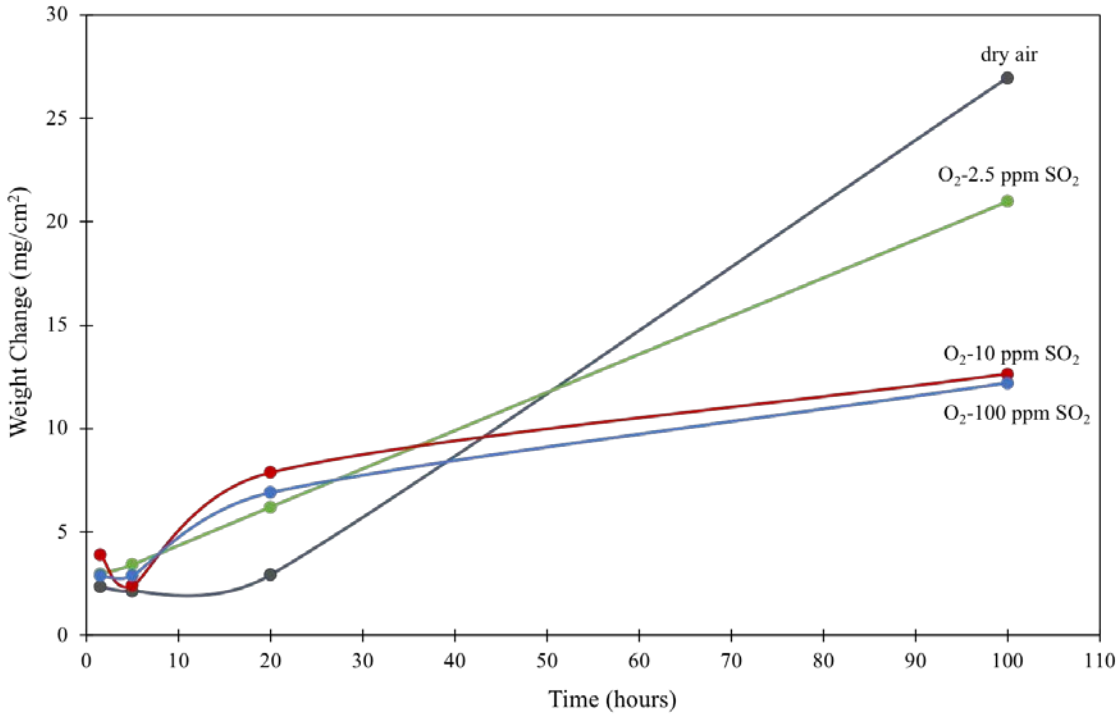

Figure 5-57. Weight change vs. time of PWA 1484 after exposure at 950°C in dry air and O_2-(2.5, 10, and 100) ppm SO_2 with 2.5 mg/cm^2 Na_2SO_4.

Cross-sectional SEM images after the time study at 950°C are shown in Fig. 5-58. The reaction products at each time will be discussed in the following. After the 1.5 h exposure in all environments a small amount of chromium sulfides formed in the base metal. Near the sulfate/alloy interface an Al-rich layer was identified.. After the 5 h exposure, sodium sulfate is still present on the samples. In the air environment minimal interaction occurs with still only a small amount of chromium sulfides. Much more sulfides are present in the SO_2-containing environments, indicating sulfur is supplied from the environment. In O_2-(2.5 and 10) ppm SO_2, a mixed-oxide product is identified at the deposit/alloy interface. In O_2-100 ppm SO_2, the corrosion product primarily consists of sulfide formation in the base alloy. No mixed-oxide product was identified. After 20 h exposure, localized internal oxidation begins to occur in the dry air environment. In the SO_2-containing environments, a uniform product forms consisting of mixed oxide and internal sulfide formation. After 100 h, in O_2-(10 and 100) ppm SO_2, the thickness of the mixed-oxide product increases and sulfides are identified deeper in the alloy, suggesting the parabolic behavior shown in Fig. 5-57 is due to oxidation-sulfidation. In dry air and O_2-2.5 ppm SO_2, the weight change plots in Fig. 5-57 indicate breakaway corrosion. Cross-sectional SEM images in Fig. 5-58 show internal oxidation with the formation of (Ni, Co) O at the alloy/gas interface. Note the scale bar in the dry-air exposure after 100 h. The product formed in dry air is much thicker than in O_2-2.5 ppm SO_2 and spallation is observed.

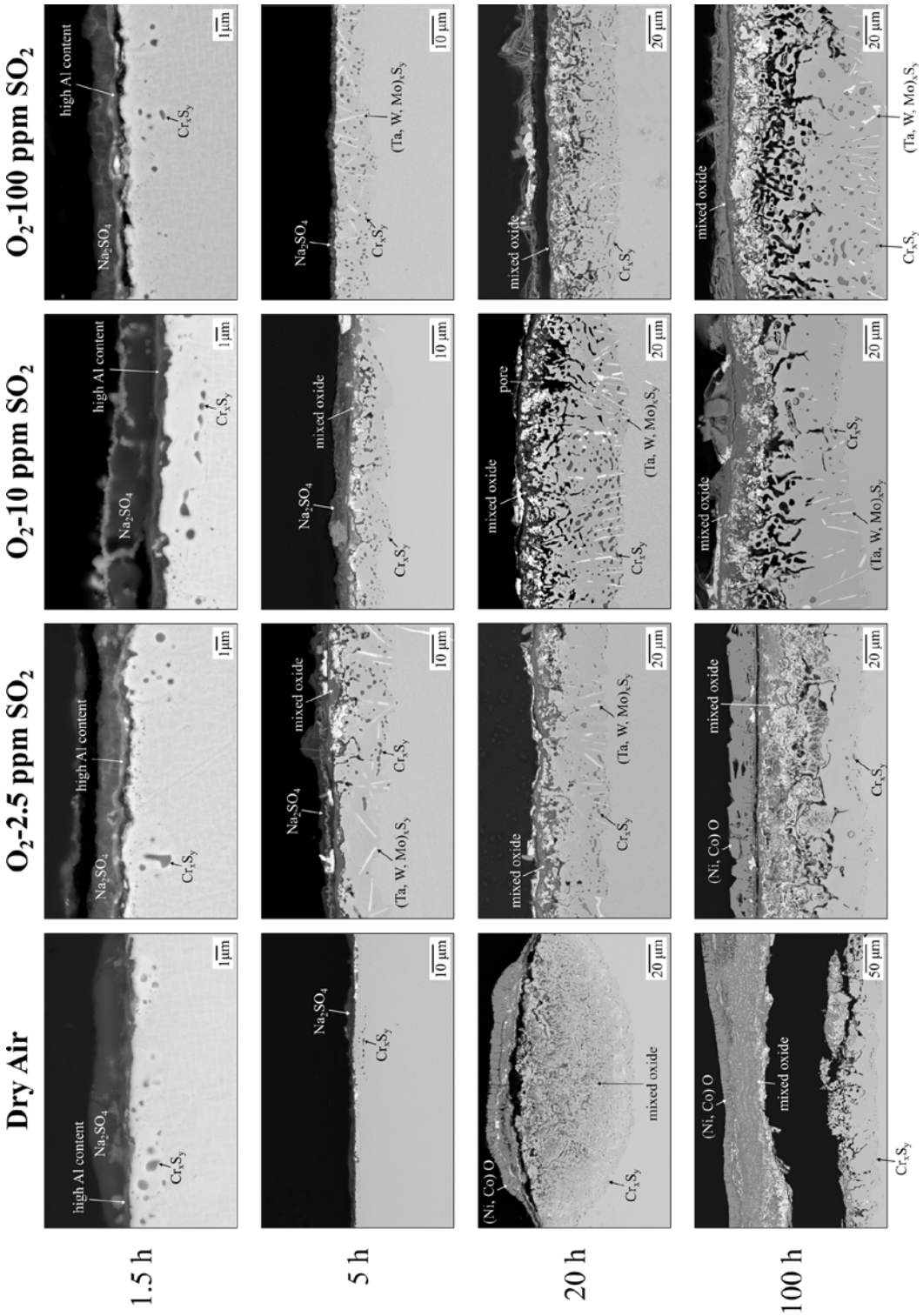

Figure 5-58. Cross-sectional SEM images of PWA 1484 after exposure at 950°C for 1.5, 5, 20, and 100 h in dry air and O_2-(2.5, 10, and 100) ppm SO_2 and with 2.5 mg/cm^2 Na_2SO_4.

Cross-sectional WDS elemental maps were collected from the alloy exposed for 20 h to the dry air and O_2-10 ppm SO_2 environments to assess the element distributions in the reaction products. Figure 5-59 shows the resulting maps after exposure in O_2-10 ppm SO_2 and Fig. 5-60 shows the resulting maps after exposure in dry air. In O_2-10 ppm SO_2, the mixed oxide product contains areas enriched in Cr and Al, and areas enriched in Ta and W. Sodium is also identified in the oxide, but it is unclear what product is formed. Molybdenum, an element known to induce alloy-induced acidic fluxing [74] is not identified in the mixed oxide. In the dry-air environment, the internal mixed oxide consists of Ta, Al, W, Cr, Ni, and Mo. Sodium is identified at the gas interface and appears to correlate well with the W map.

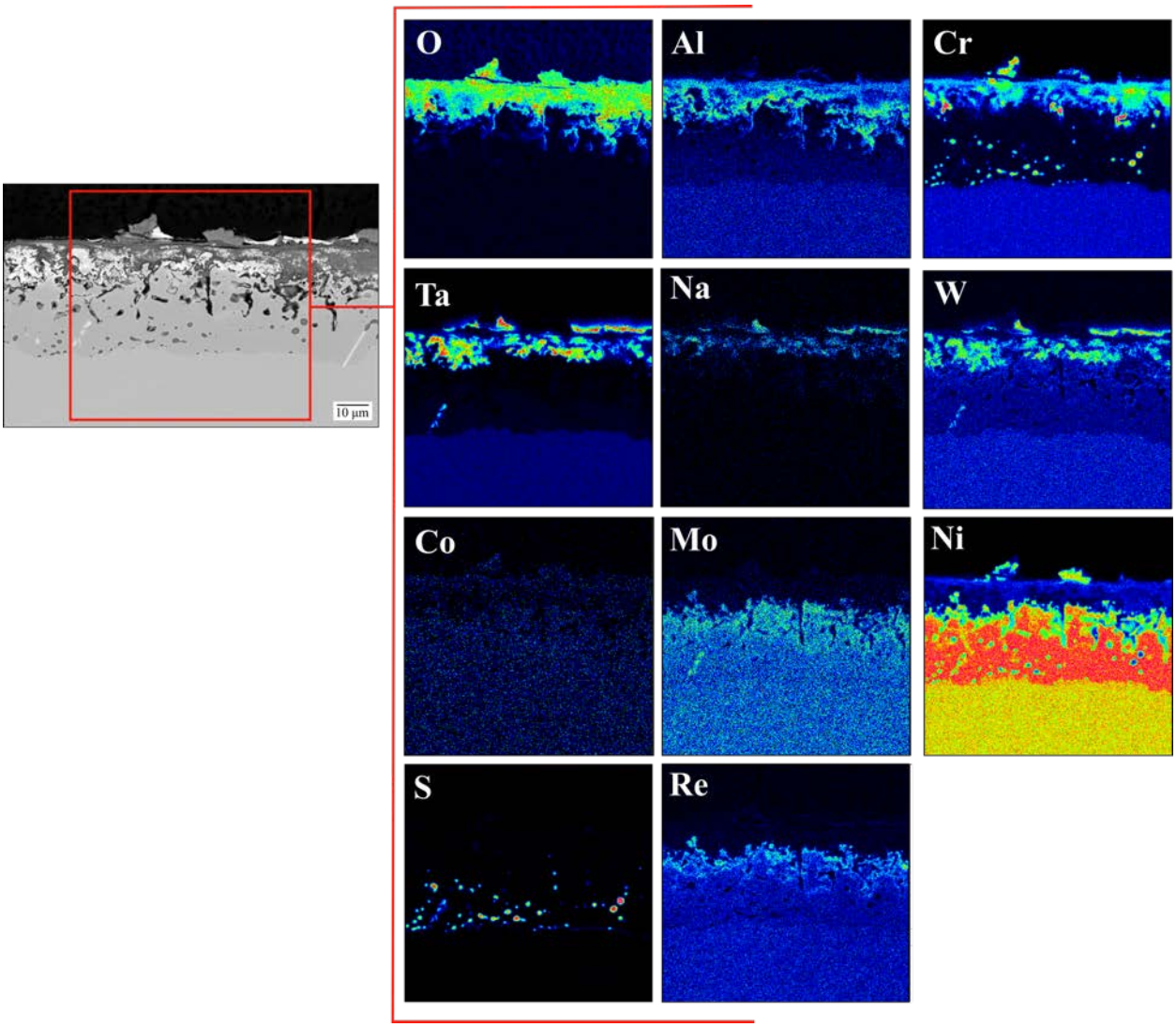

Figure 5-59. Cross-sectional SEM image of PWA 1484 after exposure at 950°C in O_2-10 ppm SO_2 for 20 h with 2.5 mg/cm^2 Na_2SO_4, along with WDS elemental maps.

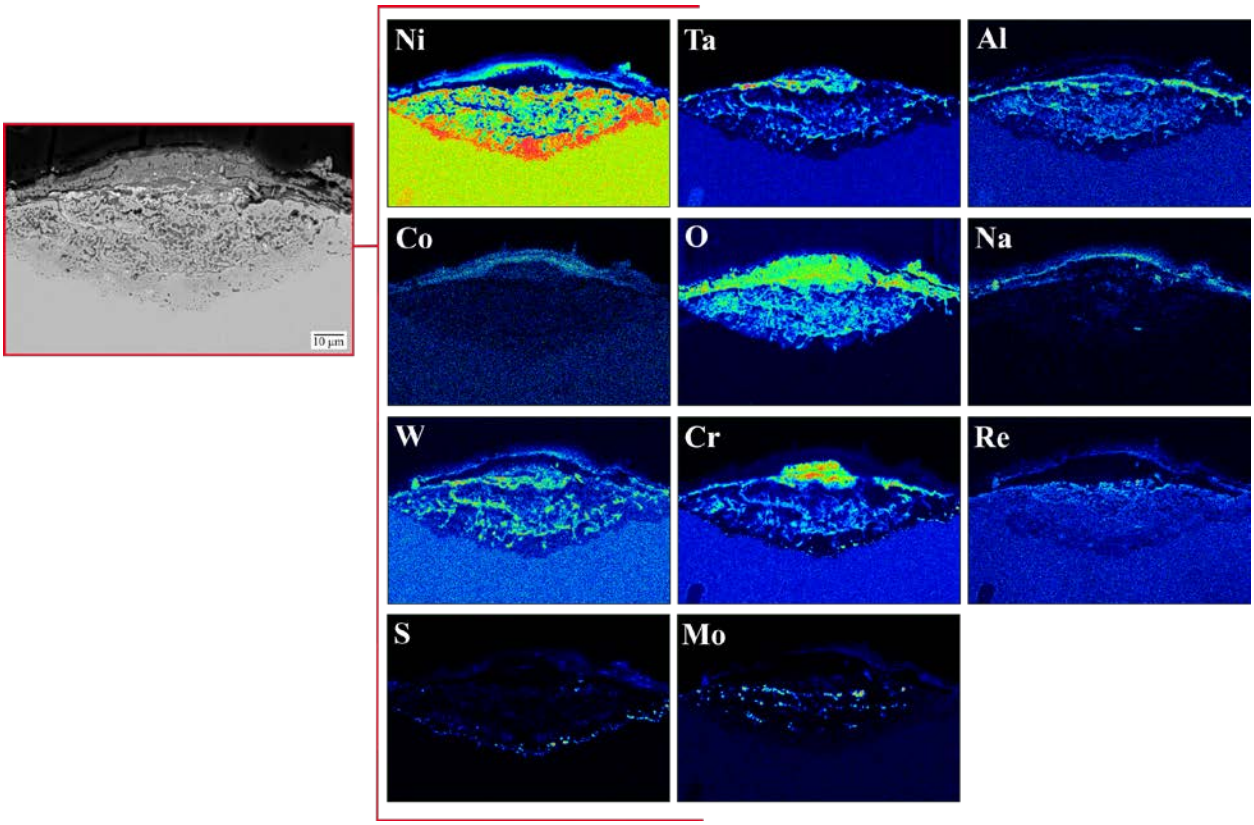

Figure 5-60. Cross-sectional SEM image of PWA 1484 after exposure at 950°C for 20 h in dry air with 2.5 mg/cm^2 Na_2SO_4, along with WDS elemental maps.

ICP-OES measurements were taken after a 1.5, 5, 20, and 100 h exposure at 950°C in all environments to compare to the time-study characterizations. Figure 5-61 shows the resulting graph of concentration (mmol*10^3/cm^2) vs. time. The results show that the majority species present is Cr. The water-soluble Cr species are Na_2CrO_4 and $NaCrO_2$. Comparing the SO_2-containing environments, as the SO_2 content increases, the concentration of Cr decreases. After 100 h of exposure, in dry air and O_2-2.5 ppm SO_2 significant Cr is still present, whereas for O_2-(10 and 100) ppm SO_2 the Cr content is minimal. The dry air and O_2-2.5 ppm SO_2 environments also show the highest W contents after the 100 h exposure. Also, note that Al is not present in the diagrams

because a negligible concentration was detected for all environments. While it is possible that the Al precipitated in the water prior to the ICP-OES analysis, it is still inferred that Al was not a factor in the overall corrosion process.

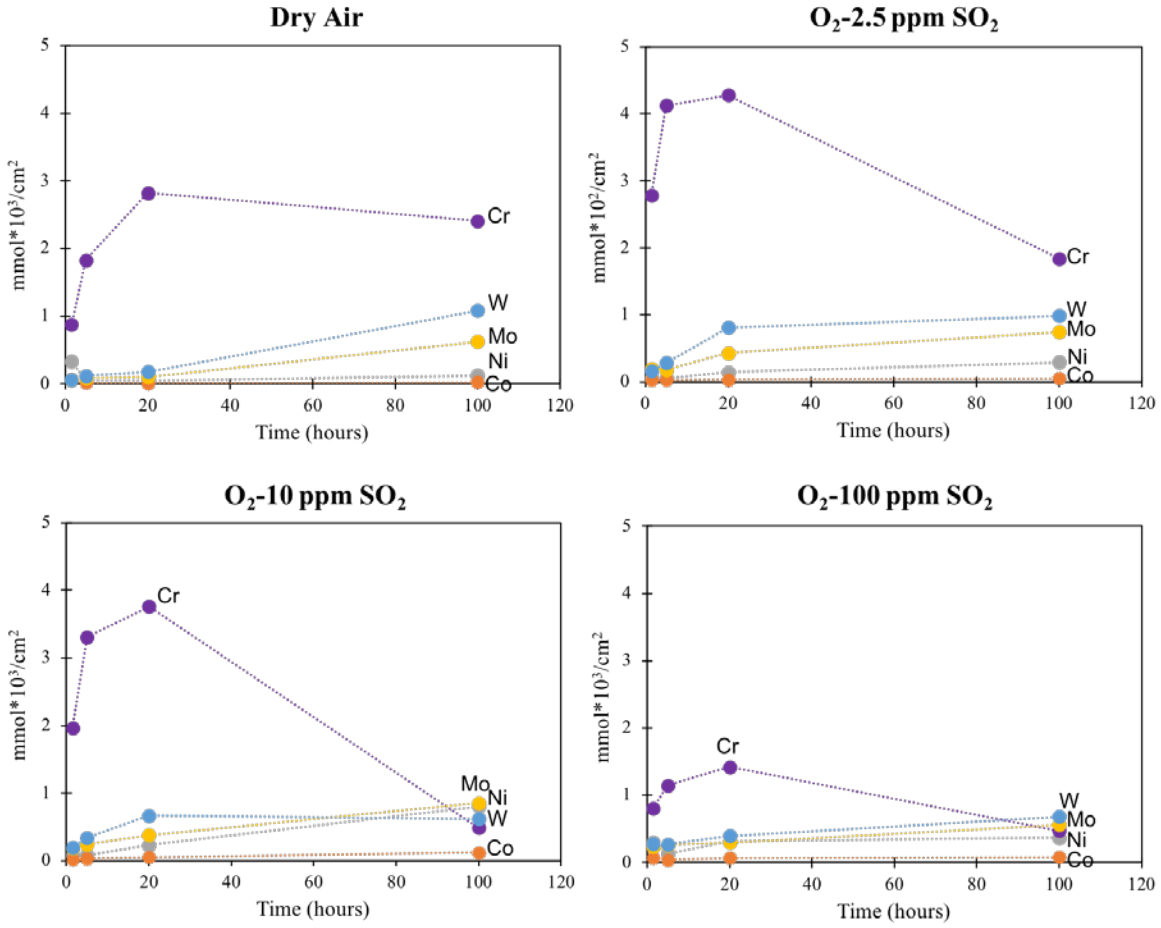

Figure 5-61. ICP-OES analysis after exposure of PWA 1484 at 950°C in dry air and O_2-(2.5, 10, and 100) ppm SO_2 with 2.5 mg/cm^2 Na_2SO_4.

EDS analysis was completed after the 100 h exposures to aide in identifying the mixed oxide products. Figure 5-62 shows a high magnification image in each environment along with the EDS results. In the dry air environment there are areas with high nickel content, indicating NiO formation, areas of increased Cr and Al content, and an area with Ta, Na, and O is identified indicating possible Na_2TaO_3 formation. The O_2-2.5 ppm SO_2 environment shows (Ni, Co)O at the gas interface. The O_2-(2.5, 10, and 100) ppm SO_2 environments all show an internal product of Al/Cr/Ni containing oxide, and tantalum rich oxide with stoichiometry indicating Ta_2O_5.

Dry Air

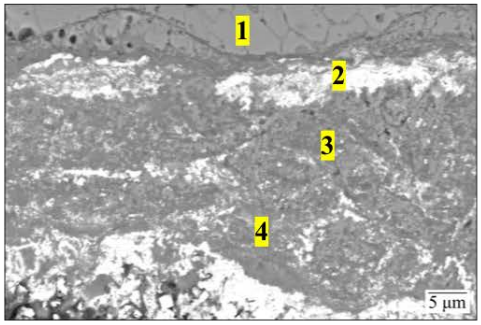

	O	Na	Al	Cr	Co	Ni	Ta
1	38	0	0	1	11	50	0
2	52	15	2	4	3	4	19
3	48	0	7	4	7	33	0
4	53	0	14	10	7	14	1

O_2-2.5 ppm SO_2

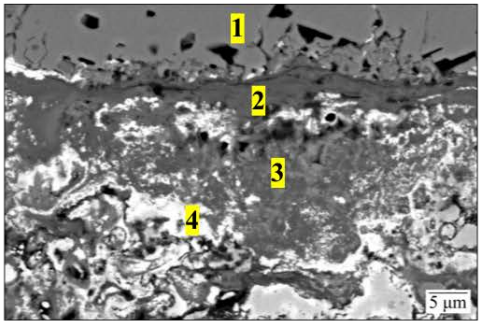

	O	Al	Cr	Co	Ni	Ta
1	39	0	0	19	42	0
2	50	16	16	6	10	1
3	48	14	12	6	19	1
4	63	0	13	1	5	18

O_2-10 ppm SO_2

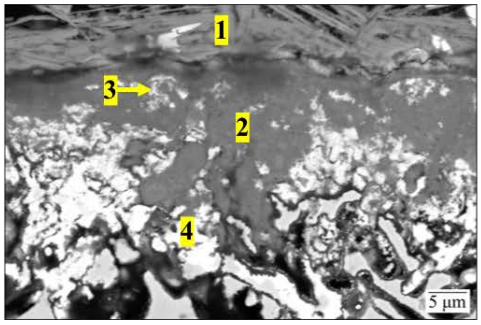

	O	Na	Al	Cr	Co	Ni	Ta
1	47	1	9	21	10	10	2
2	54	0	13	16	7	8	1
3	54	7	10	11	5	7	2
4	63	0	8	1	1	2	25

O_2-100 ppm SO_2

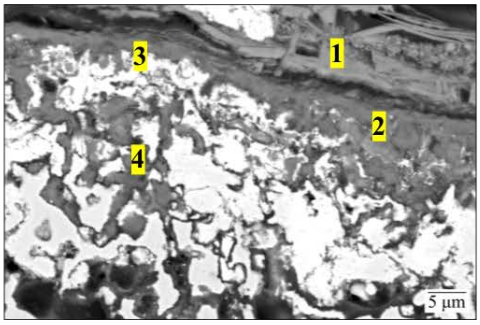

	O	Na	Al	Cr	Co	Ni	Ta
1	56	3	13	0	3	10	3
2	55	0	15	14	4	10	1
3	68	0	0	3	1	2	26
4	58	0	23	15	0	2	1

Figure 5-62. Cross-sectional SEM images of mixed oxide product formed on PWA 1484 after exposure at 950°C for 100 h with 2.5 mg/cm^2 Na_2SO_4, along with EDS analysis.

XRD analysis was then completed on the scale formed in dry air and O_2-10 ppm SO_2 to compliment EDS and WDS analysis in identifying phases that formed. The scale formed in dry air spalled (as shown in Fig. 5-58), so patterns were obtained from the top and bottom surface of the spalled product. The resulting XRD patterns are shown in Fig. 5-63. The XRD pattern obtained is on the surface of the sample, so texture may be present and products formed deeper in the alloy may not be identified. There were notable difference between the product in air vs. SO_2. However, since the reaction product is complex, identifying phases was challenging. Peaks that were identified are labeled in Fig. 5-63. Phases identified in the O_2-10 ppm SO_2 environment were $NaTaO_3$, $NiCr_2O_4$, NiO, and Co_3O_4. No Al-containing phases were identified in the reaction product, so additional XRD analysis would need to be completed. In the dry air environment, NiO, Co_3O_4, $NiWO_4$, Ni, $AlNiO_4$, Ta_2O_5, $NaTaO_3$ and $NiCr_2O_4$ were identified. The phase identification was consistent with elements present in the EDS and WDS analysis. However, ICP-OES analysis indicated Cr-soluble species formed, likely Na_2CrO_4 which were not identified in XRD analysis.

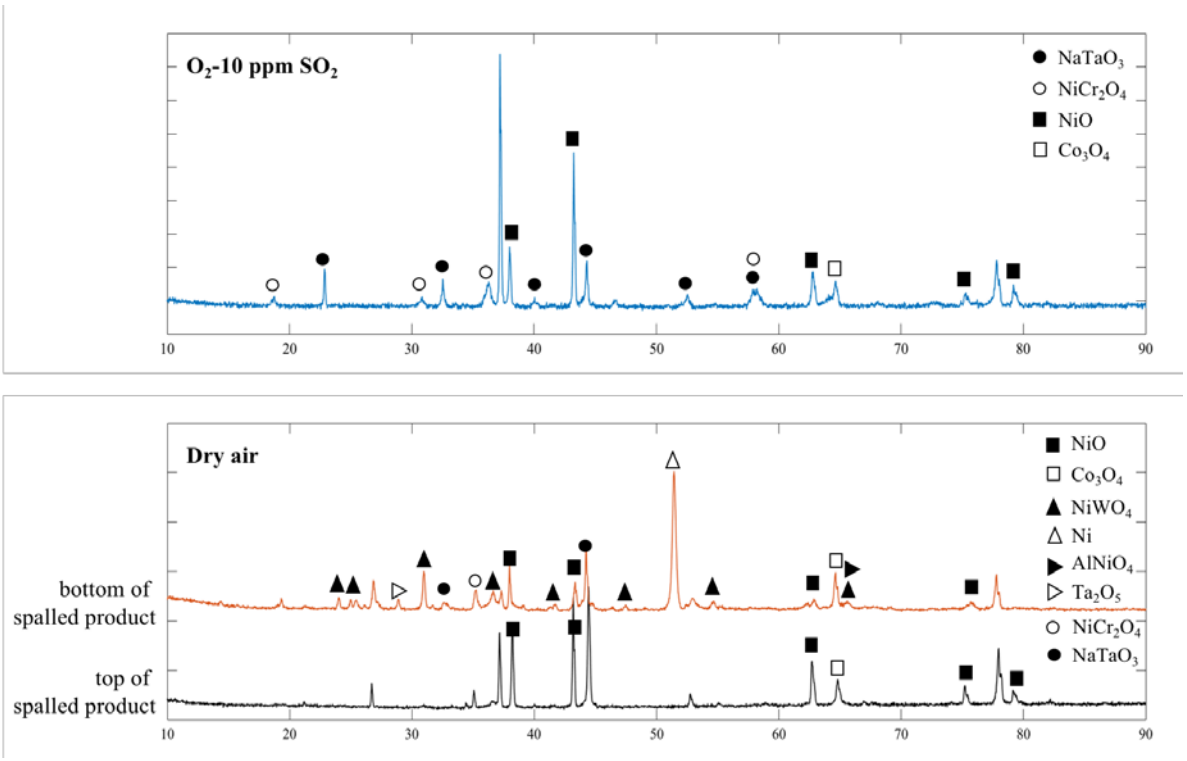

Figure 5-63. XRD pattern of PWA 1484 after exposure at 950°C for 100 h in O_2-10 ppm SO_2 and dry air with 2.5 mg/cm^2 Na_2SO_4. The product spalled in dry air. XRD patterns were obtained from the top and bottom of the spalled product.

To further understand the variation in corrosion morphology in the dry-air and SO_2-containing environments in the high-temperature regime, additional experiments were completed on the effect of deposit mass on corrosion rate. The 20 h exposure was repeated at 950°C in dry air and O_2-10 ppm SO_2 with 5 mg/cm^2 Na_2SO_4. The resulting cross-sectional SEM images are shown in Fig. 5-64. Doubling the deposit mass in dry-air significantly increased the corrosion rate, due to alloy/deposit interaction. In O_2-10 ppm SO_2 the corrosion rate was unaffected.

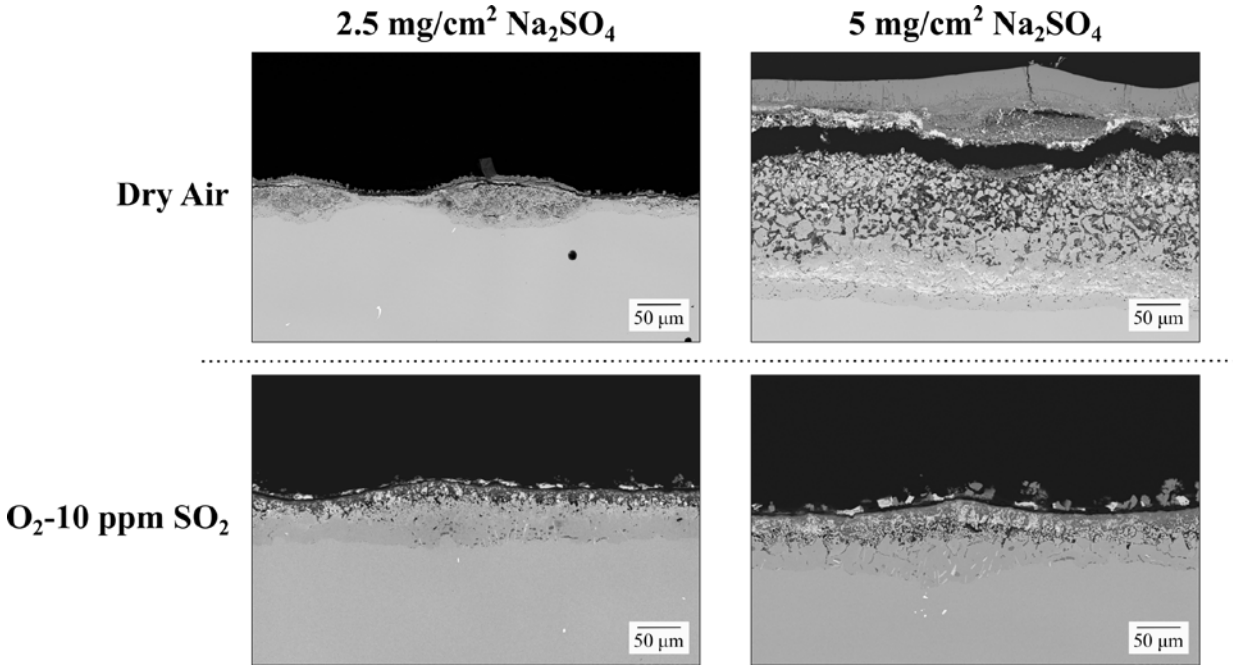

Figure 5-64. Cross-sectional SEM images after 20 h exposure of PWA 1484 at 950°C in dry air and O_2-10 ppm SO_2 with 5 mg/cm^2 Na_2SO_4.

5.3.4 Discussion

The corrosion rate of PWA 1484 was assessed from 550-1000°C in dry air and O_2-(2.5, 10, and 100) ppm SO_2. It was shown that both variables of weight change or average attack can be used when presenting corrosion rate results. At the low and intermediate temperatures, corrosion rate increased as SO_2 content increased. The opposite trend was observed in the high-temperature regime. In the following, the mechanism in each temperature regime will be discussed.

5.3.4.1 Low Temperature (≤ 650°C)

The low-temperature hot corrosion results behaved as expected, i.e., increasing SO_2 content increased the extent of attack. ICP-OES results showed an increase in SO_2 content resulted in an increased concentration of Ni. The Ni detected is predicted to be from the formation of the nanocrystalline, $Na_2Ni_2SO_5$ phase (Eq. 5-6). The ICP-OES results also showed minimal Co that only slightly increased as SO_2 content increased. In the environments studied, the Na_2SO_4-$NiSO_4$ eutectic is not stable. In the low temperature regime, Na_2SO_4-$CoSO_4$ eutectic is stable in O_2-(2.5, 10 and 100) ppm SO_2 at 650°C and 600°C. However, as the ICP-OES results showed only minor Co content, the liquid is not predicted to play a major role. Thus, it is the high rate of $Na_2Ni_2SO_5$ formation that is inferred to sustain the rapid attack occurring in the low-temperature regime.

5.3.4.2 Intermediate Temperature (700-850°C)

The mechanism operating in the intermediate-temperature regime is likely acidic fluxing, alloy-induced acidic fluxing, or potentially a solid-state attack if a high P_{SO_3} is obtained. The results shown indicate the same trend as the low-temperature regime; i.e. the extent of attack increases as the SO_2 content increases. As in the low-temperature regime, Na_2SO_4-$NiSO_4$ eutectic is not stable in any of the environments. In the intermediate-temperature regime, Na_2SO_4-$CoSO_4$ eutectic is stable at 700°C in O_2-10 ppm SO_2 and from 700°C to 800°C in O_2-100 ppm SO_2. The environments where the Na_2SO_4-$CoSO_4$ eutectic is stable show uniform attack, suggesting the traditional Type II hot-corrosion mechanism is operating in the intermediate-temperature regime.

At 850°C for all environments localized attack occurs with distinct pit formation. Pit formation that occurs at 850°C was found to initiate due to the presence of carbides and the

chemical variation from dendritic-structure formation. Heat-treated PWA 1484 alloys showed a decrease in pit fraction with an increase in heat-treatment time. Surface SEM images of the dendritic structure along with EDS-point measurements along the cross-section showed a more uniform elemental distribution as the heat-treatment time increased. Considering protection against hot corrosion, selective oxidation of Al or Cr to form a protective Al_2O_3 or Cr_2O_3 scale is known to mitigate against sodium sulfate attack [126]. The selective oxidation process is affected by many variables, one of which is the local composition of the alloy and the extent to which that is affected by segregation. The heat-treated alloys were oxidized for a short time to determine the uniformity of the oxide scale that develops. The exposure was at 850°C for 5 min in air. Prior to the exposure a thermocouple was spot-welded onto a sample to allow measurement of the heating profile, as shown in the plot in Fig. 5-65. The last data point on the plot corresponds to the sample reaching 850°C.

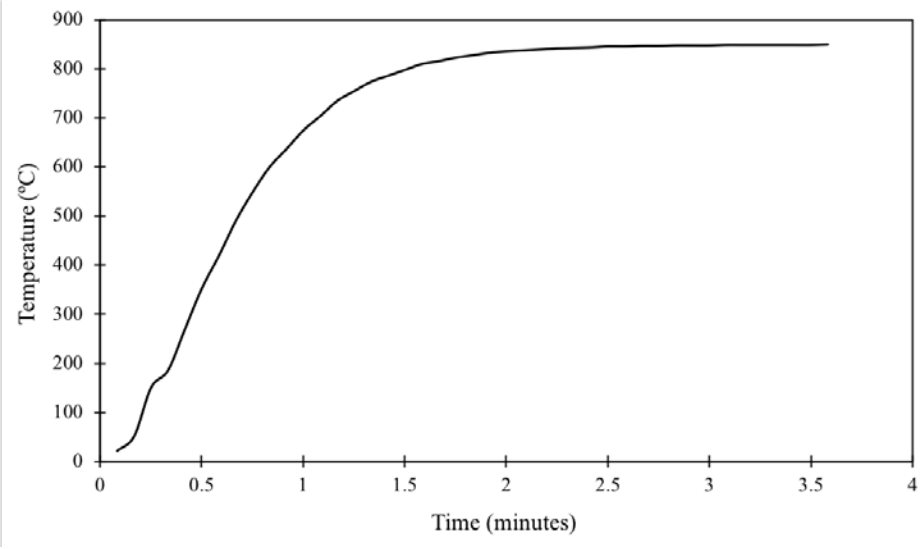

Figure 5-65. Heating profile of the time to reach 850°C.

The resulting surface SEM images after the oxidation exposure for 5 min at 850°C are shown in Fig. 5-66 for the heat-treated alloys as well as PWA 1484. The images clearly show more uniform scale development as the heat-treatment time increases. The scale reveals the dendritic structure of the alloy. PWA 1484 and the HT-short alloy show areas of coarse-grained oxide formation and areas of fine-grained oxide formation. The HT-medium and HT-long alloys show primarily coarse-grained oxide formation across the entire surface. In addition, carbides present on the surface were observed to oxidize, as confirmed by EDS. Correlating the scale development to hot corrosion resistance, the uniform establishment of an Al_2O_3 scale would protect the alloy. Initiation points for hot corrosion are postulated to occur in regions where protective scale formation has not occurred and where carbides are present. Thus, the HT-short alloy with a non-uniform scale would show a higher pit fraction, which is in agreement with the current and a past study. With regard to the latter, for an exposure to an air-SO_2 environment, Jalowicka et al. [127] showed that CMSX-4 has superior corrosion resistance over CM247 because of the quick establishment of a pure and dense alumina scale on CMSX-4. The scale formed on CM247 was non-uniform, with an initial Cr_2O_3 scale formed in regions of lower Al content. The chromia scale is a more defective structure than Al_2O_3, allowing for transport of sulfur in some form through the Cr_2O_3 scale. The result is the formation of chromium sulfides, setting up the alloy for more accelerated attack. A similar mechanism is envisioned to occur for the hot-corrosion exposures presented here. Figure 5-67 shows cross-sectional SEM images taken to illustrate the dendritic structure and pit formation. Pit formation was found in dendritic and interdendritic regions. To rationalize, the formation in interdendritic regions may primarily be due to the presence of carbides. In the dendritic regions, initially due to the lower Al content, a pure Al_2O_3 scale does not

establish, alloying sulfur access to the alloy, resulting in chromium sulfide formation. Resulting alloy/sulfate interaction follows. Regardless of where the pits form, the key aspect is that a more homogenous composition decreases the extent of corrosion at 850°C.

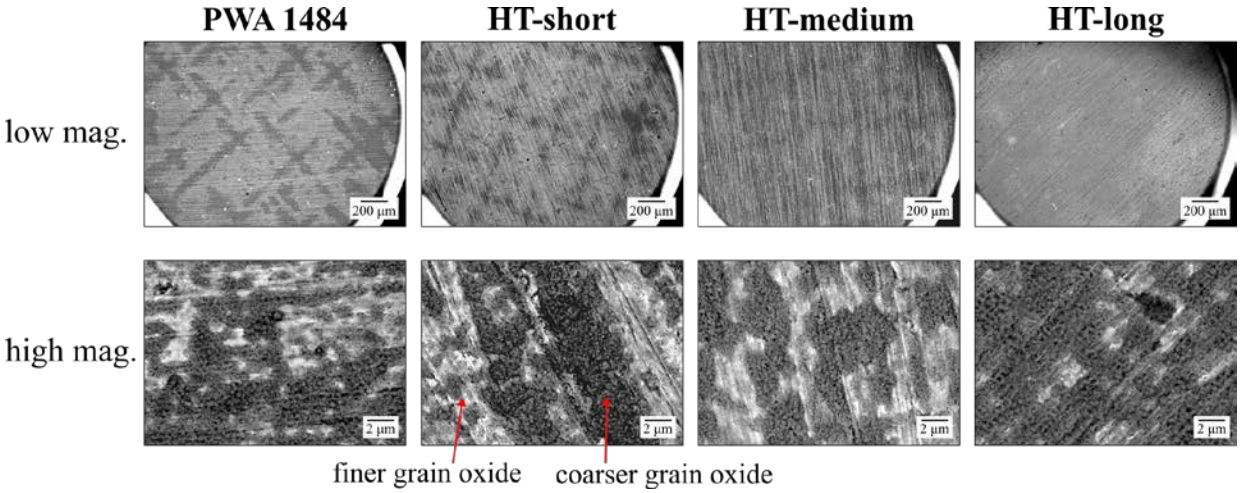

Figure 5-66. Surface SEM images of PWA 1484 and three heat treated (HT) PWA 1484 alloys after a 5 min. oxidation exposure at 850°C in air. A high magnifcation and low magnification image is shown.

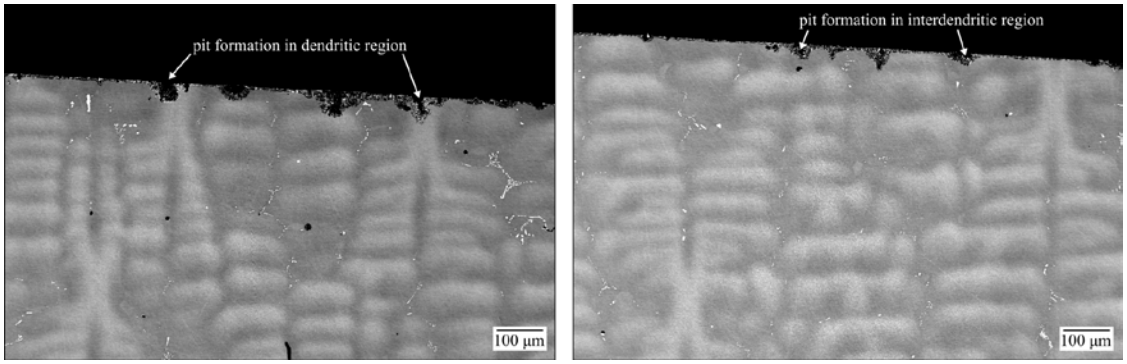

Figure 5-67. Cross-sectional SEM image of the short heat-treated PWA 1484 alloy after exposure at 850°C in O_2-10 ppm SO_2 for 20 h with 2.5 mg/cm^2 Na_2SO_4. The images show pit formation initiation at dendritie and interdendritic regions.

Exposure of PWA 1484 at 850°C with 2.5 mg/cm^2 Na_2SO_4 led to the development of deep pits filled with mixed oxide and sulfide particles in the alloy. The structure of PWA 1484 was shown to have chemical variation and the short-term oxidation exposure discussed previously indicated the scale that developed had areas of coarse-grain and fine-grain oxide. The initiation of pits was correlated to the development of a non-uniform oxide scale at 850°C. A 100 h oxidation exposure of PWA 1484 was completed in dry air and O_2-10 ppm SO_2 to determine if the alloy establishes an Al_2O_3 scale after a long term exposure in the absence of a deposit. The resulting cross-sectional SEM images are shown in Fig. 5-68. In dry-air environment localized pits formed with internal mixed oxide and an external (Ni, Co)O. In the O_2-10 ppm SO_2 environment, no protective areas were observed. The oxide consisted of a mixed internal oxide with external NiO, and sulfide present in the alloy. Thus, in an SO_2 containing environment the alloy is intrinsically not protective. Adding a sulfate deposit further exacerbated the attack.

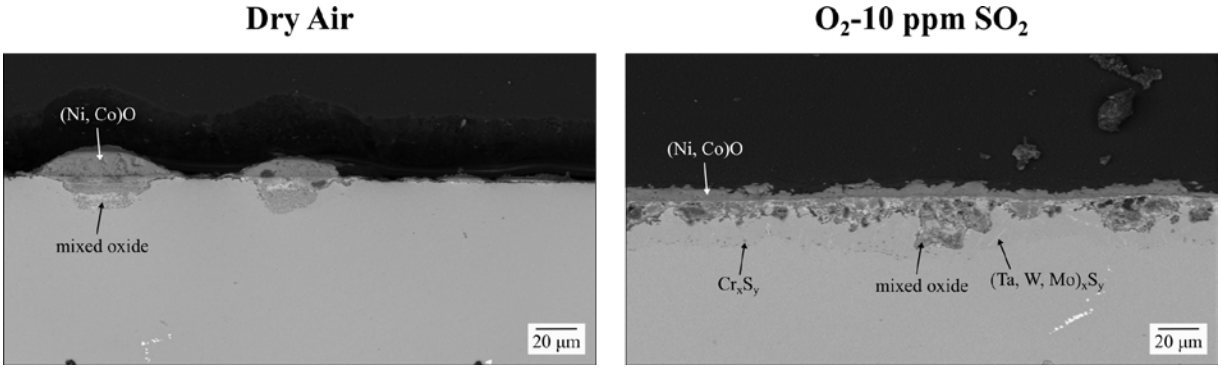

Figure 5-68. Cross-sectional SEM images after oxidation of PWA 1484 at 850°Cin dry air and O_2-10 ppm SO_2 for 100 h.

Localized attack was also observed in dry air and O_2-(2.5 and 10) ppm SO_2 at 750°C and 800°C. Under these conditions, the Na_2SO_4-$CoSO_4$ eutectic is not stable. Considering other mechanisms that can occur, alloy-induced acidic fluxing is possible for initiating the attack. The reaction for alloy-induced acidic fluxing of molybdenum is,

$$MoO_3 + Na_2SO_4 = Na_2MoO_4 + SO_3 \qquad (5-8)$$

If MoO_3 reacted with Na_2SO_4, SO_3 is released. The local increase in SO_3 could potentially allow for the traditional Type II hot corrosion mechanism to locally occur. A similar reaction can be written for W as well. The localized attack may also relate to the nature of the oxide scale that develops on PWA 1484. To test the importance of refractory-metal content on the initiation of attack, a Ni-5Cr-6Al (weight %) alloy was hot-corrosion tested at 750°C and 800°C for 20 h in O_2-10 ppm SO_2. The Cr and Al contents of this model alloy are similar to PWA 1484. The resulting cross-sectional SEM image is shown in Fig. 5-69. Without the refractory additions, minimal interaction occurs. Only minor sulfidation is observed in the alloy and the deposit is un-reacted. Additionally, ICP-OES was completed after exposure of PWA 1484 for 1.5 h and 5 h at 800°C in O_2-10 ppm SO_2. The results are shown in Table 5-4. After 1.5 h, W and Mo are detected as well as Ni, Cr, and Co. After 5 h, the W, Mo, and Cr contents decrease. The Ni content detected remains and Co content increases. Therefore, it is deduced that the formation of Na_2MoO_4 (T_m=687°C) or Na_2WO_4 (T_m=698°C) initiates hot corrosion under these conditions, with the refractory constituents interacting with the deposit due the non-uniform sale that develops. Additional SEM was completed on the scale that forms beneath the deposit in areas that are protective at 750°C in

O_2-2.5 ppm SO_2 for 20 h. Figure 5-70 shows the resulting image with EDS analysis. An Al-rich scale was identified, which prevented interaction with the sulfate deposit.

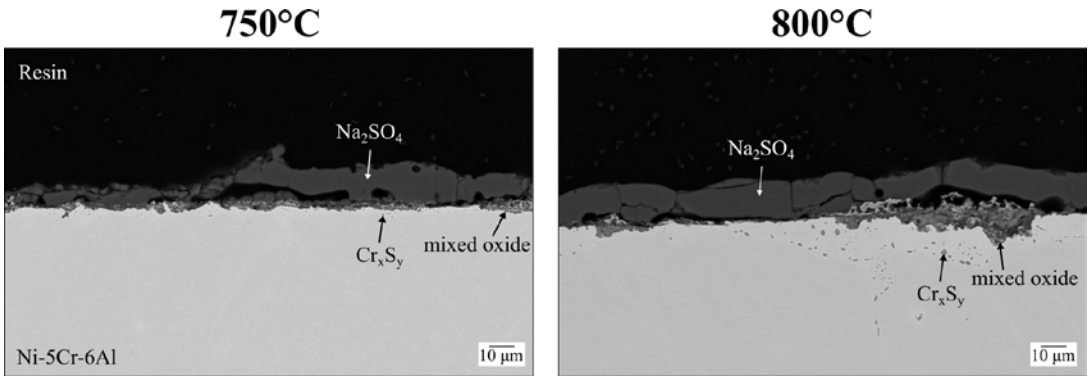

Figure 5-69. Cross-sectional SEM image of Ni-5Cr-9Al after exposure at 750°C and 800°C for 20 h in O_2-10 ppm SO_2 with 2.5 mg/cm^2 Na_2SO_4.

Table 5-4. ICP-OES results after exposure of PWA 1484 at 800°C for 1.5 h and 5 h with 2.5 mg/cm^2 Na_2SO_4. The concentration is in mmol*10^3/cm^2.

	W	**Mo**	**Cr**	**Al**	**Ni**	**Co**
1.5 h	0.09	0.12	0.27	0.00	1.54	0.09
5 h	0.05	0.07	0.06	0.00	1.53	0.11

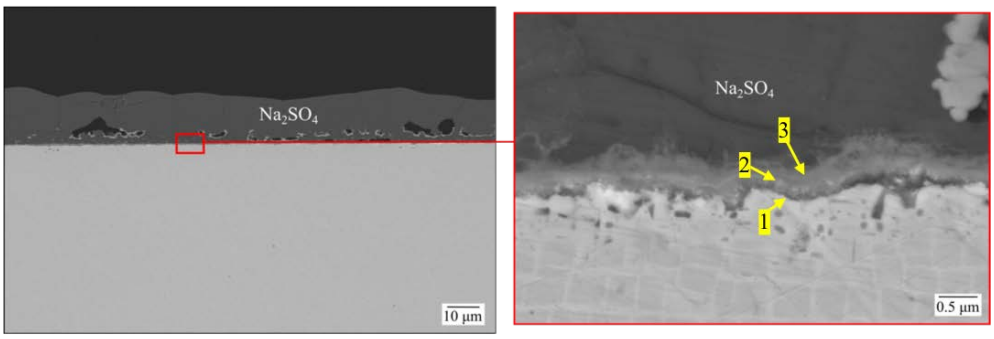

Spectrum	O	Al	Cr	Ni	Co	Ta	W	Na	S
1	61	18	10	2	2	2	2	1	2
2	59	18	2	7	3	3	1	4	2
3	53	13	5	7	5	1	0	12	4

Figure 5-70. Cross-sectional SEM image of PWA 1484 after exposure at 750°C for 20 h in O_2-2.5 ppm SO_2, along with EDS analysis of oxide formed in area unreacted with deposit.

Another aspect to discuss is the change in the corrosion-product morphology in the intermediate temperature regime. The cross-sectional SEM images, Fig. 5-48, show from 700°C-800°C a double-layer oxide forms, which is similar to the low-temperature corrosion morphology that was observed (Fig. 5-3). The product consists of an outer porous (Ni, Co) O and an internal mixed oxide/sulfide with sulfur enrichment at the alloy/scale interface. At 850°C, distinct sulfide particles are identified in the base alloy. The extent of sulfur diffusion into the alloy increases as the temperature increases [128]; which in turn enables internal sulfidation, provided the solubility product for a given sulfide is exceeded [129]. The discrete sulfide particles that formed in the base alloy were identified to be Cr_xS_y and $(Ta, W, Mo)_xS_y$. The sulfide formation can be understood by considering the free energy of formation of the various sulfides, as shown by the Ellingham diagram in Fig. 5-71. The diagram indicates the most stable sulfide is Al_2S_3.

However, P_{O_2} must be very low to stabilize aluminum sulfide [85]. Instead, chromium sulfide particles are formed, as detected by EDS analysis. The next stable sulfide is TaS_2. Chang et al. [85] reported formation of needle-like TaS_2 after hot corrosion of a nickel-based superalloy at 900°C. The sulfide composition was determined using an elemental map; corresponding maps for W and Mo were not shown. In this study, as indicated in the WDS map, refractory sulfides are detected to consist of Ta, Mo, and W. While TaS_2 is the most stable refractory sulfide, the stoichiometry is unable to be determined without TEM analysis. The formation of the refractory sulfides are predicted to occur because of Cr-depletion in the denuded zone. Without available Cr for sulfide formation, refractory sulfides are able to form.

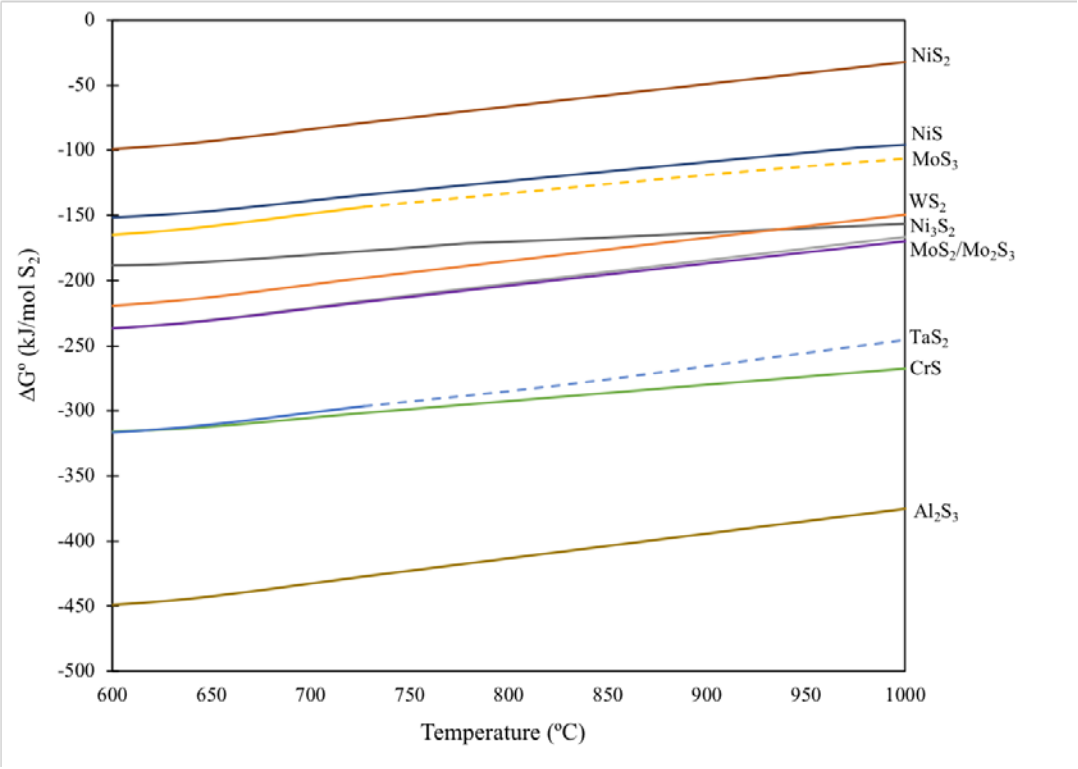

Figure 5-71. Free energy of formation per mole of S_2, data obtained from [130]. Dashed lines indicate the data was extrapolated to higher temperatures.

5.3.4.3 High Temperature (≥ 900°C)

Determining a definite mechanism to explain the trend observed in the high-temperature regime is challenging. Many different dynamic processes are involved in the degradation process, including scale establishment, sulfide formation, alloy/deposit interaction, and changing composition of the denuded zone. All these factors make interpreting the results of the multi-component alloy difficult. A definitive mechanism for the high temperature exposures would require further research. However, some deductions will be made after analyzing the current results.

First considering the corrosion rate, the reaction products shown in the high-temperature regime (Fig. 5-54) are significantly influenced by the various competing kinetic processes. Considering the dry-air environment, minimal attack was observed at 900°C. At 950°C, localized attack was observed after 20 h that leads to breakaway corrosion between 20 h and 100 h. At 1000°C, the corrosion rate was very rapid after the 20 h exposure. The variation in corrosion rate from 900°C-1000°C is deemed to be the result of the kinetics of alloy-deposit interaction and the kinetics of scale establishment. At 900°C in the dry-air environment a protective scale must have been able to establish which precluded further alloy/deposit interaction. At 1000°C, although the rate constant of Al_2O_3 increases, the alloy/deposit reactions must increase at a faster rate, leading to breakaway corrosion after the 20 h exposure.

The mechanism occurring will be discussed initially by considering the 950°C exposures. The question to answer is: Why does the dry-air and O_2-2.5 ppm SO_2 environments show rapid internal oxidation while the O_2-(10 and 100) ppm SO_2 environments do not? The weight change vs. time plot shown in Fig. 5-57 indicate that in the O_2-(10 and 100) ppm SO_2 environments a

diffusion-controlled process is occurring (i.e. the kinetics are parabolic). Figure 5-58 identifies a mixed-oxide scale at the gas/alloy interface. The measured kinetics are deemed to be dominated by the growth of that scale product. A key aspect is in the O_2-(10 and 100) ppm SO_2 environments, the establishment of a semi-protective scale was able to prevent further alloy/deposit interaction. The WDS map shown in Fig. 5-59 for the O_2-10 ppm SO_2 environment revealed the oxide product consists of Cr, Al, Ta, and W. Al is enriched at the oxide/alloy interface.

In the dry-air and O_2-2.5 ppm SO_2 environments the kinetics indicate breakaway corrosion. The WDS map after the 20 h exposure in dry air in Fig. 5-60 showed an internal-oxide product containing Al, Cr, Ta, W, Ni, and Mo. Additional EDS elements maps were collected after the 100 h exposure to compare the extensive reaction product formed in the dry-air environment to the highest SO_2-containing environment. Figure 5-72 shows EDS maps of Ni, Cr, Al, and O from the reaction products formed after 100 h exposure in dry air and O_2-100 ppm SO_2. The key aspect is the relatively high nickel content in the scale. In O_2-100 ppm SO_2, the oxide scale consists of Cr and Al, with Al enrichment at the scale/alloy interface. Ta and W oxides are also present, but not shown in the figure; the Ta and W oxide formation is speculated to be similar to the 20 h exposure in the O_2-10 ppm SO_2 environment in Fig. 5-59. In the dry-air environment, the internal oxide product consists of Ni, Cr, and Al. Ta, W, and Mo are also present but not shown in the figure; the distribution of these elements is similar to a WDS map of a 65 h exposure in dry-air to be shown later (Fig. 5-73). The co-existence of Ni- containing oxides with Cr- and Al-containing oxides does not follow an expected sequence based on a gradient of O_2 potential and relative stability of the oxides [29]. Therefore, a well-defined steady-state situation does not exist. The likely reason is that the deposit is playing a significant role, allowing for rapid nickel oxidation. Another relevant

aspect to mention is that the WDS maps in Figs. 5-59 and 5-60 show refractory oxides. Tantalum is known to be beneficial in hot corrosion protection because of the formation of $NaTaO_3$, which is a solid compound and was identified in the EDS (Fig. 6-62) and XRD (5-63) analysis [85, 129, 130]. However, refractory oxides were found after all exposures and the extent of formation did not correlate with an increase in SO_2 content. Therefore, the presence of Ta does not explain the difference in morphology between the environments.

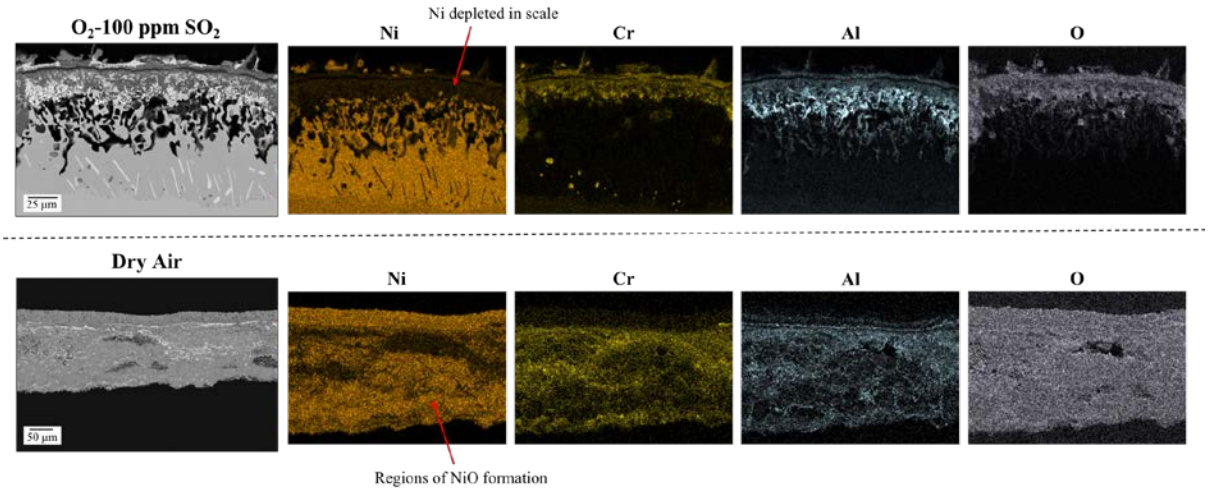

Figure 5-72. EDS elemental maps with corresponding cross-sectional SEM image after 100 h exposure of PWA 1484 in dry air and O_2-100 ppm SO_2 with 2.5 mg/cm^2 Na_2SO_4.

Two known mechanisms of high-temperature hot corrosion are alloy-induced acidic fluxing and basic fluxing [4]. The ICP-OES results showed significant Cr dissolution in the oxide, likely by basic fluxing. As the SO_2 content increases, the Cr concentration decreases, which can be rationalized in terms of Cr solubility in Na_2SO_4 and the stability of Na_2CrO_4. Figure 2-11 shows solubility plots of various oxides as a function of melt basicity at 1200 K. Assuming basic fluxing

of Cr, an increase in SO_2 content (decrease in activity of Na_2O) will decrease the solubility of Cr in Na_2SO_4. As mentioned previously, Cr is known to be beneficial for formation of a protective Al_2O_3 scale [36, 131]. Increased dissolution in the sulfate deposit would likely impact protective scale formation. Exposure to the dry-air environment for 20 h showed less Cr concentration compared to O_2-(2.5 and 10) ppm SO_2. However, the dry-air environment also showed localized attack whereas the other environments showed uniform attack. Therefore, it is difficult to interpret the dry-air environment ICP-OES results in which localized attack occurred.

Considering the formation of Na_2CrO_4, Fig. 5-73 shows an equilibrium stability diagram for Cr-Na-O-S, assuming unit activity of all species. In the O_2-100 ppm SO_2 environment, Cr_2O_3 is stable. In the O_2-10 ppm SO_2 environment, the composition is on the border of Na_2CrO_4 stability. In the O_2-2.5 ppm SO_2, where breakaway corrosion occurred, Na_2CrO_4 is stable. Dry air is not indicated in the diagram, but Na_2CrO_4 would also be stable for such an exposure. In the initial stages, there is a local increase in the basicity of the melt in accordance with the mechanism proposed by Goebel and Pettit studying pure nickel [12]. An increase in basicity would cause Cr dissolution in all environments. Additionally, Fig. 5-74 shows a schematic of the measured Cr_2O_3 solubility. In all environments, initially basic fluxing of the Cr_2O_3 occurs at the sulfate/alloy interface. Since SO_3 can dissolve in the Na_2SO_4 melt [14], at that interface the melt basicity decreases as SO_2 content increases. Hypothetical locations of the melt basicity in dry air and O_2-100 ppm SO_2 are indicated on the diagram. As the basicity of the melt decreases, the Cr_2O_3 (i.e., CrO_4^{2-}) solubility decreases. Therefore, in the higher SO_2-containing environment less Cr_2O_3 dissolution occurs, which was supported by the ICP-OES analysis. With evaporation of the deposit there would be a point reached in which equilibrium with the environment in the O_2-(10 and 100)

ppm SO_2 would cause Cr_2O_3 precipitation out of the melt in a manner described by Otsuka and Rapp [82, 84]. The ICP-OES results also support this conclusion, since after 100 h little Cr was detected in the products formed in the O_2-(10 and 100) ppm SO_2 environments, while in the dry-air and O_2-2.5 ppm SO_2 environments significant Cr was still present, indicating Na_2CrO_4 formation. To summarize, the higher CrO_4^{2-} solubility in dry air and O_2-2.5 ppm SO_2 and the stability of Na_2CrO_4 would likely negatively impact the ability of the alloy to form a protective scale.

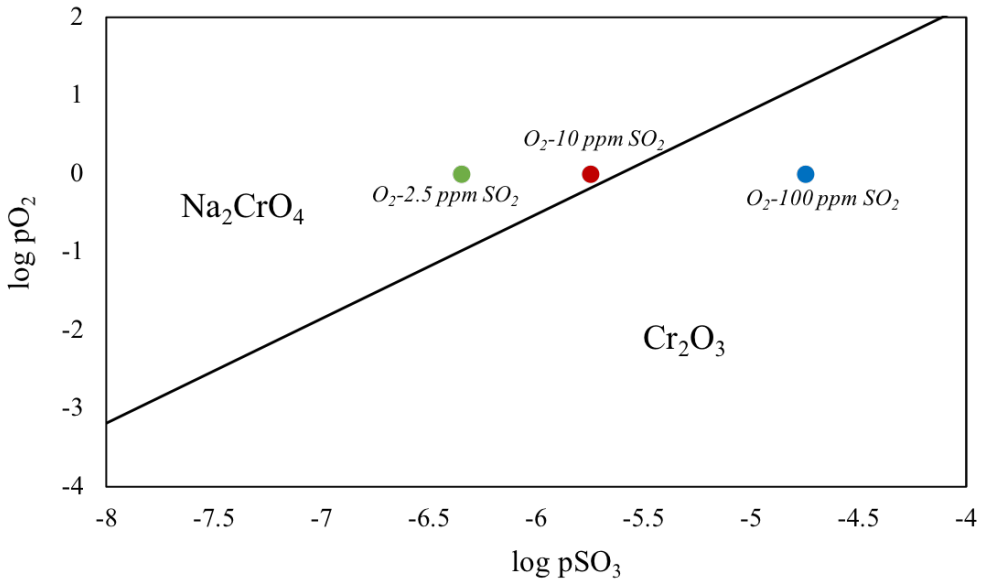

Figure 5-73. Na-Cr-O-S stability diagram at 950°C, with P_{SO_3} in O_2-(2.5, 10, and 100) ppm SO_2 envrionments indicated. Data for diagram was taken from [130].

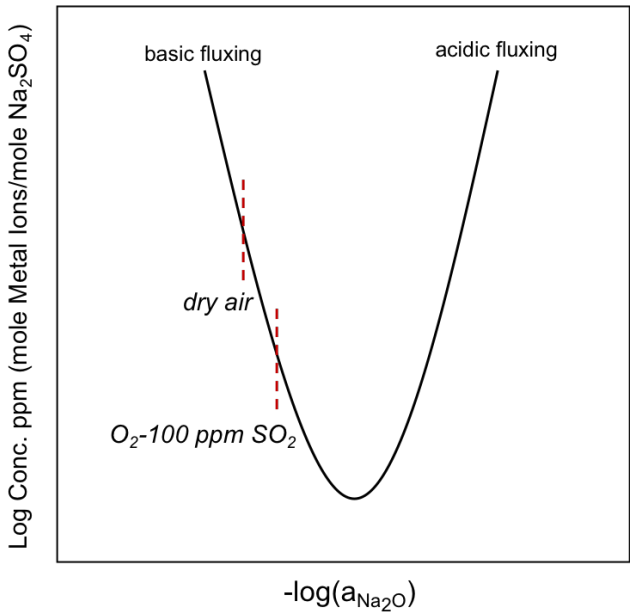

Figure 5-74. Schematic of solubility of Cr_2O_3 in Na_2SO_4 as a function of melt basicity, with hypothetical location for a dry air and O_2-100 ppm SO_2 enviornment.

Considering the alloy-deposit interaction, a well-studied mechanism at high temperatures is alloy-induced acidic fluxing, which involves Mo or W. Previous studies were conducted by Misra [56, 74] on Mo-containing nickel-based superalloys and Fryburg [76, 78] on Mo- and W-containing nickel-based superalloys. Analysis of water-soluble species revealed that at the onset of breakaway corrosion there was a significant decrease in Cr concentration and an increase in Mo concentration. The initiation time ranged from 20 h to 70 h in those studies. In addition, Misra [74] studied environments of O_2, O_2-105 ppm SO_2, and O_2-(0.108%-2%) SO_2 and reported the same trend as found in this thesis, which was a decrease in corrosion rate with increasing SO_2 content. The reasoning was determined to be due to the decrease in the incorporation of MoO_3 in the melt [57]. A melt of Na_2MoO_4-MoO_3 is necessary for accelerated attack, as explained in Section 2.3.3. With the absence of MoO_3 incorporated in the sulfate deposit in the high-SO_2 environments, the

mechanism is oxidation-sulfidation, which has a lower rate of corrosion than alloy-induced acidic fluxing, but still much higher than basic oxidation.

While the alloy-induced acidic fluxing mechanism is reasonable, there is not a direct connection to the results in this thesis. The ICP-OES analysis shows Mo and W presence, but only in a minor amounts. The dry-air and O_2-2.5 ppm SO_2 environments gave the highest W concentration after 100 h, and showed an increase in Mo concentration, but the increase with time was not as significant as the previous studies. However, at 1000°C the morphology of the corrosion product in dry air after the 20 h exposure was very similar to that reported for alloy-induced acidic fluxing, where a highly porous oxide formed [59]. In addition, the WDS map after the 20 h exposure in dry air indicated molybdenum-oxide formation at the sulfate/oxide interface. No molybdenum was detected in the oxide formed in 10 ppm SO_2. Tungsten oxide was observed in both the dry-air and O_2-10 ppm SO_2 environments. An additional WDS map was collected after a 65 h exposure in dry air to determine if Mo is present after a longer time. The results are shown in Fig. 5-75 for the majority of the elements in the alloy and the Mo map shows a layer of molybdenum oxide at the scale/alloy interface. Also, the Na is incorporated in the oxide product. While the ICP-OES results do not support alloy-induced acidic fluxing, the similar morphology at 1000°C, the presence of MoO_3 in the dry-air environment and not in the O_2-10 ppm SO_2 environment, and the breakaway corrosion observed do strongly indicate that Mo is playing a role. As mentioned previously, W can also initiate alloy-induced acidic fluxing, but W was observed in the oxide product of both the dry-air and O_2-10 ppm SO_2 environments. However, the dry-air environments showed the highest W concentration from the ICP-OES analysis. In addition, the XRD results (Fig. 5-63) identified $NiWO_4$ which could have formed from reaction of NiO with

Na_2WO_4 or WO_3 [76]. Additional experiments would need to be carried out to determine if W is playing a role.

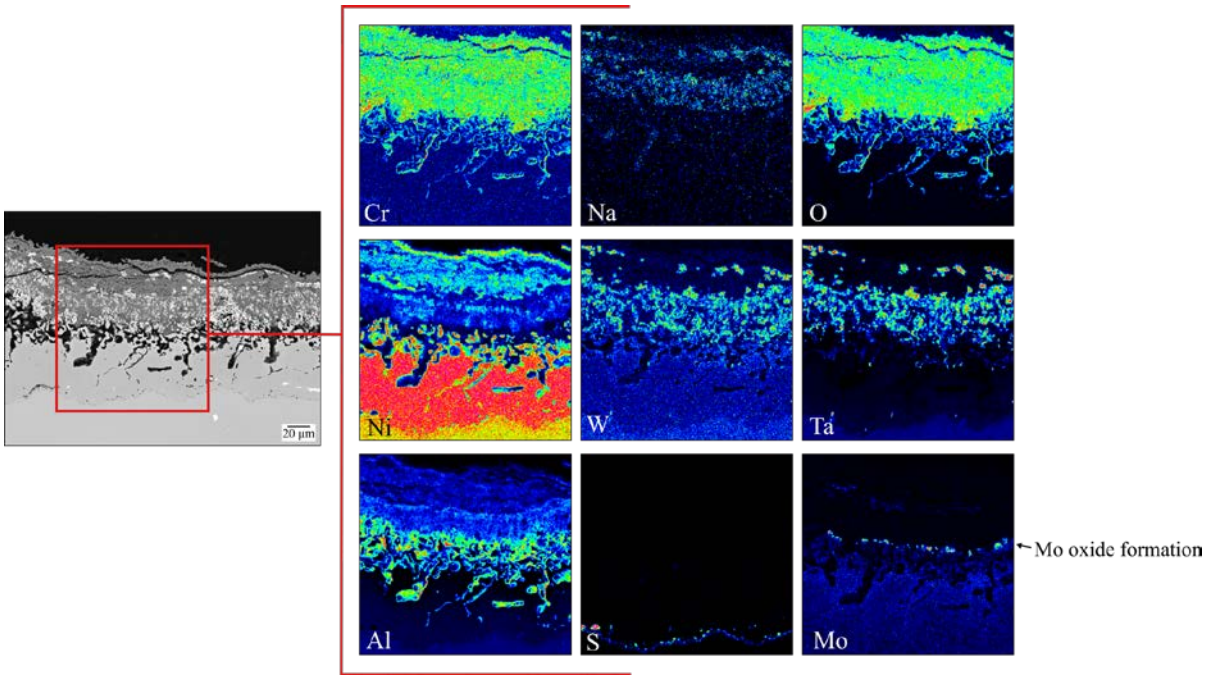

Figure 5-75. Cross-sectional SEM image of PWA 1484 after 65 h exposure in dry air with 2.5 mg/cm^2 Na_2SO_4, along with WDS elemental maps.

If alloy-induced acidic fluxing is the mechanism occurring, a possible explanation for the trend of increasing SO_2 content resulting in decreased attack is that the SO_2 content may be impacting the solubility at the gas interface. Considering the Rapp-Goto criterion [51], a negative-solubility gradient must exist for the sequence of oxide dissolution followed by precipitation. For alloy-induced acidic-fluxing to occur, a melt of MoO_3-Na_2MoO_3 (or equivalent for W) forms resulting in acidic fluxing of the oxides. Figure 5-76 a) shows a schematic of SO_3 gradients that may develop in the dry air vs. O_2-100 ppm SO_2 environment and Fig. 5-76 b) shows the resulting

solubility plots. The schematic shows that the SO_2-containing environment increases the solubility at the gas interface. The result may be decreased reprecipitation and thus less attack.

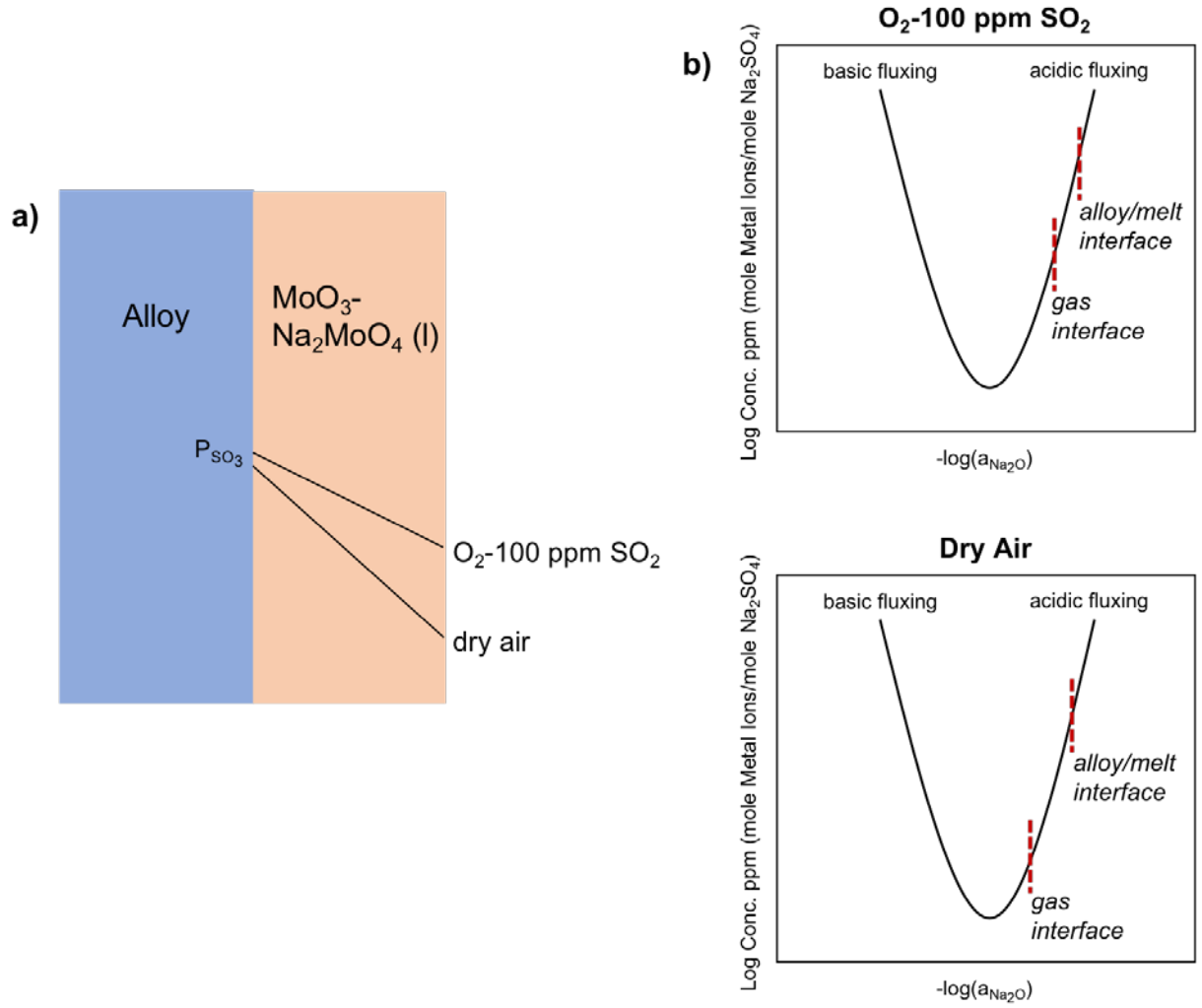

Figure 5-76. a) Schematic of P_{SO_3} gradient that can develop for alloy-induced acdic fluxing in dry air and O-100 ppm SO_2, along with solubility diagrams for each environment.

One aspect to mention with regard to the SO_2-containing environments is that, as the SO_2 content increased, chromium sulfide formation also increased. As explained by Grabke *et al.* [134], an increase in SO_2 increases sulfur uptake resulting in a higher amount of internal sulfide formation. Chromium sulfide formation will also deplete the alloy matrix of Cr necessary for establishing an Al_2O_3 scale. However, after the 1.5 h exposure, in all environments there was Al-rich scale formation. The fraction of sulfides after 1.5 h was minimal and consistent for all environments, indicating initial sulfide formation is due to the sulfate deposit. After the 5 h exposure a larger fraction of sulfide formation was observed in the SO_2-containing environments. The 100 h exposure showed that the scale formed in dry air and O_2-2.5 ppm SO_2 after 1.5 h eventually broke down and was unable to re-establish, resulting in breakaway corrosion. In O_2-(10 and 100) ppm SO_2 the scale remained, as no NiO formation was detected after 100 h. The composition of the denuded zone after 5 and 100 h of exposure was determined to better understand the Cr and Al depletion in each environment, which impacts the scale formation. The measurement was taken in the center of the denuded zone. The results are shown in Table 5-5. After the 5 h exposure, the O_2-2.5 ppm SO_2 environment shows the highest depletion of Cr due to dissolution in the sulfate deposit as well as internal sulfide formation. Dry air and O_2-(10 and 100) ppm SO_2 are also depleted in Cr but to a slightly lesser extent. Comparing Al, the subsurface content is higher for dry air and O_2-2.5 ppm SO_2 than O_2-(10 and 100) ppm SO_2. It is reasonable to assume that Al depletion is due to Al_2O_3 formation because detection of Al from the ICP-OES analysis was negligible. Further supporting this hypothesis is the enrichment of Al in the denuded zone after 100 h exposure. Al_2O_3 is a slow-growing oxide and, once established its slow growth rate would allow for Al enrichment in the alloy subsurface. The complete depletion of Cr from the

alloy matrix is due to sulfide formation, and the Cr-detection in the scale shown in Fig. 5-59 may be due to oxidation of the sulfide particles, releasing sulfur to diffuse further into the alloy. In the dry-air and O_2-2.5 ppm SO_2 environments, after 100 h the denuded zone was depleted of all elements due to the accelerated deposit/alloy interaction that is occurring as a result of the alloy being unable to establish or maintain a protective scale. In addition, doubling the deposit mass, shown in Fig. 5-63, in the dry-air significantly accelerated corrosion rate after the 20 h exposure, while in O_2-10 ppm SO_2 environment corrosion rate was unaffected. These results further validate the deduction that a semi-protective scale formed in O_2-10 ppm SO_2 which prevented further deposit/alloy interaction.

Table 5-5. EDS results of composition in center of dendued zone after exposure of PWA 1484 at 950°C for 5 h and 100 h with 2.5 mg/cm^2 Na_2SO_4.

5 hours

	Cr	Al	Ni	Co
Dry Air	1.2	3.0	75.0	12.3
2.5 ppm	0.5	3.9	78.4	10.7
10 ppm	1.2	2.8	77.1	11.4
100 ppm	1.4	2.8	75.0	12.4

100 hours

	Cr	Al	Ni	Co
Dry Air	0.6	0.7	89.8	4.5
2.5 ppm	1.3	2.3	86.0	7.5
10 ppm	0.6	5.2	78.3	11.0
100 ppm	0	7.92	78.6	11.2

5.4 Influence of Chromium Content on the Low-temperature Hot Corrosion Behavior of Model Ni-Cr-Al Based Alloys

At low-temperatures, the base composition of PWA 1484 does not establish a protective Al_2O_3 scale, making the alloy suspectable to hot corrosion. Therefore, as discussed in Section 2.4, a diffusion coating is often used, where the surface of the alloy is enriched in an element that aids in passivation. Past literature found that chromized diffusion coatings out-perform Aluminide diffusion coatings in Type II hot corrosion exposures [86, 133], which can be understood in terms of the formation of a protective oxide. Kinetically, the formation of Cr_2O_3 is faster than that of Al_2O_3 [91]. Therefore, chromized coatings are able to establish a protective oxide at a low temperature, which is essential for protecting against hot corrosion.

In engine application, Pratt & Whitney's chromized coating is referred to as PWA 70 [86]. Figure 5-77 shows the cross-section of a PWA 70 coating. As mentioned in Section 2.4, it is well known within industry that producing a uniform coating is challenging. The Cr content can significantly vary. From the standpoint of quality control, it is therefore highly useful to understand the dependence between Cr content in the chromide coating and resistance to hot corrosion. This chapter addresses the Cr content needed to provide protection against hot corrosion at 600°C-700°C, model Ni-Cr-Al alloys shall be used, with composition chosen to represent PWA 70. The compositions of the alloys in atomic % are: Ni-16Cr-4Al, Ni-19Cr-4Al, Ni-23Cr-4Al, and Ni-26Cr-4Al. Notable differences between the model alloys and the PWA 70 coating are: (1) presence of aluminum nitrides in PWA 70; (2) presence of tantalum carbides in PWA 70; (3) a concentration gradient of Cr exists on PWA 70; and (4) the PWA 70 coating contains various alloying elements. The environment for all of the following exposures was O_2-10 ppm SO_2.

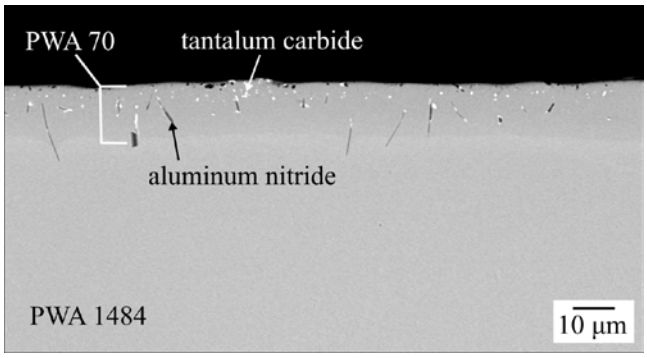

Figure 5-77. Cross-sectional SEM image of PWA 70.

5.4.1 Short-term Oxidation Behavior

5.4.1.1 Exposures Without a Deposit

Initially the short-term oxidation behavior of the Ni-Cr-Al alloys (alloy 1-4) in O_2-10 ppm SO_2 of was assessed. No deposit was applied in oxidation exposures. The goal was to determine if a Cr_2O_3 scale forms in the initial stage at temperatures of 600°C, 650°C and 700°C. Figures 5-78, 5-79, and 5-80 show the Raman results at the three temperatures after a 2 h exposure in O_2-10ppm SO_2 for each Ni-Cr-Al model alloy. Raman peaks were identified using literature values [133–135] and standard samples of Cr_2O_3 and NiO. For all alloys, at 600°C, only Cr_2O_3 was detected. However, the intensity was low indicating that a very thin scale formed. At 650°C and 700°C, Cr_2O_3 and $NiCr_2O_4$ were detected. No NiO formation was detected, which is known to be deleterious to hot-corrosion resistance. NiO may have formed in the transient oxidation stage, but subsequently reacted to form $NiCr_2O_4$. The important takeaway is that, in the absence of a sulfate deposit, all alloys formed a chromia scale at the temperatures studied. As to be discussed in the following sections, maintaining the scale will be a key criterion in protecting the alloy against hot corrosion.

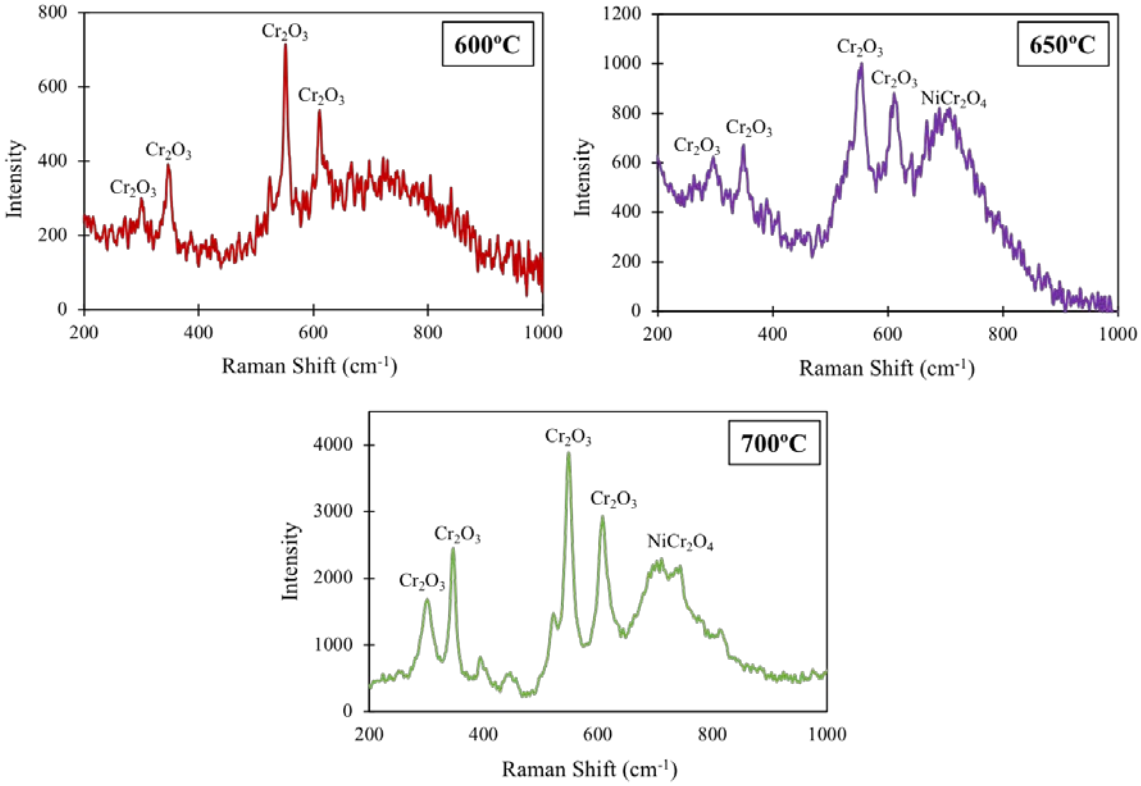

Figure 5-78. Raman spectrum from surface of Ni-16Cr-4Al after 2 h oxidation exposure in O_2-10 ppm SO_2 at 600°C-700°C.

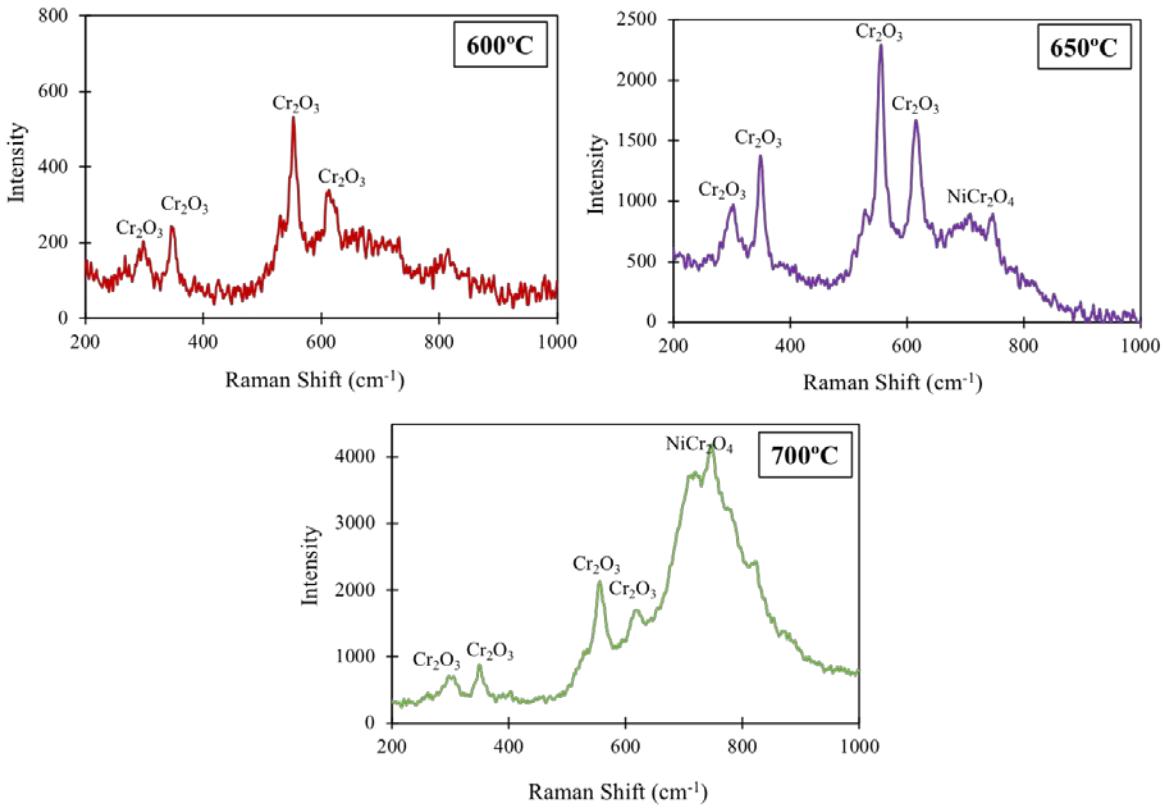

Figure 5-79. Raman spectrum from surface of Ni-19Cr-4Al after 2 h oxidation exposure in O_2-10 ppm SO_2 at 600°C-700°C.

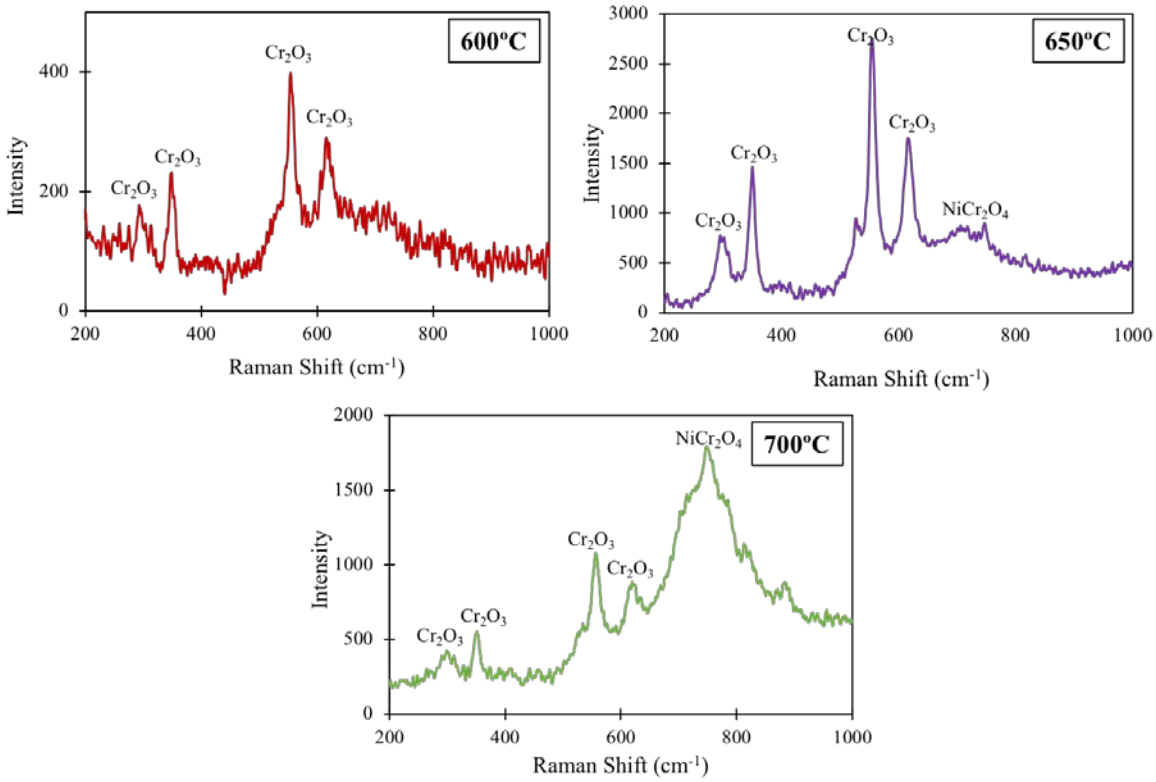

Figure 5-80. Raman spectrum from surface of Ni-23Cr-4Al after 2 h oxidation exposure in O_2-10 ppm SO_2 at 600°C-700°C.

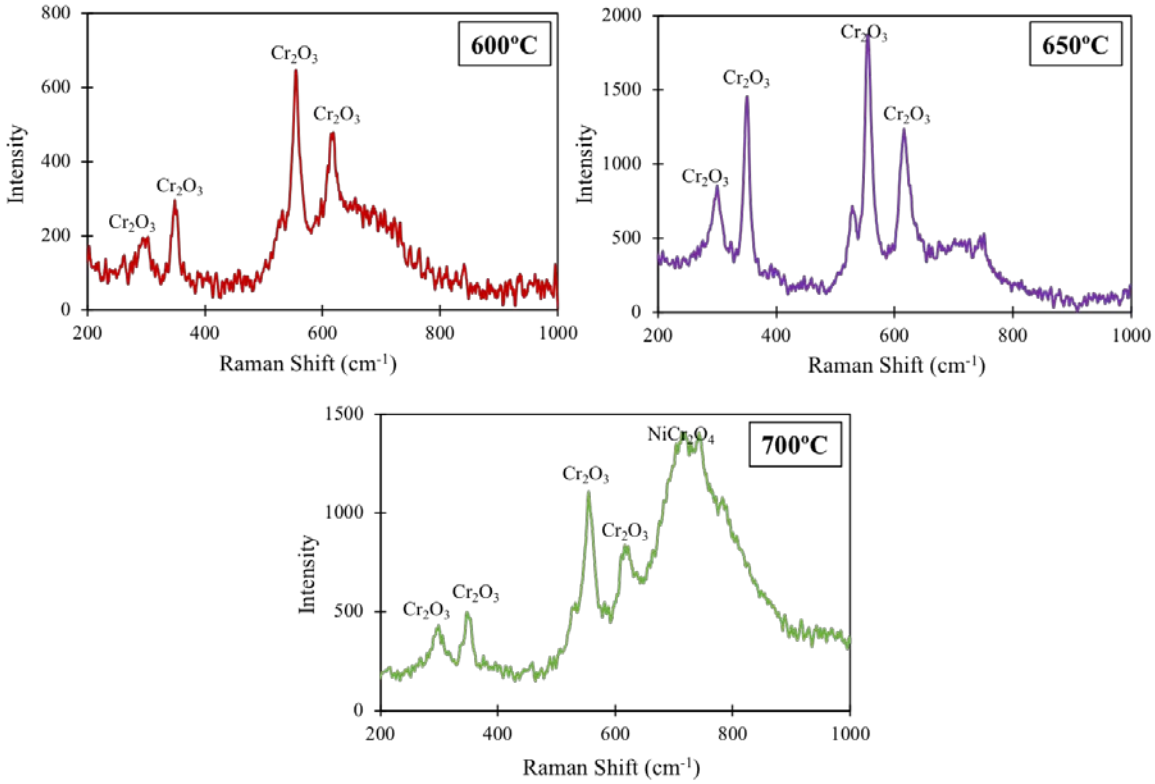

Figure 5-81. Raman spectrum from surface of Ni-26Cr-4Al after 2 h oxidation in O_2-10 ppm SO_2 at 600°C-700°C.

5.4.1.2 Exposure with an Na_2SO_4 Deposit

To analyze if the alloys are still able to form a protective scale in the presence of a deposit, the NiCrAl alloys were exposed at 650°C for 2 h in O_2-10 ppm SO_2 with 2.5 mg/cm^2 Na_2SO_4 deposit. Following the experiment, the deposit was washed off and the resulting oxide analyzed using Raman. Figure 5-82 shows the resulting Raman spectrum along with SEM surface images. Raman results shown for the Ni-16Cr-4Al alloy apply to the Ni-19Cr-4Al alloy as well, and Raman results shown for the Ni-26Cr-4Al alloy apply to the Ni-23Cr-4Al alloy. Ni-16Cr-4Al and Ni-19Cr-4Al showed islands of NiO formation, while Ni-23Cr-4Al and Ni-26Cr-4Al showed only

Cr_2O_3 and $NiCr_2O_4$. Another relevant observation is that the color difference on the surface images of all alloys indicate a non-uniform scale develops in the presence of a deposit.

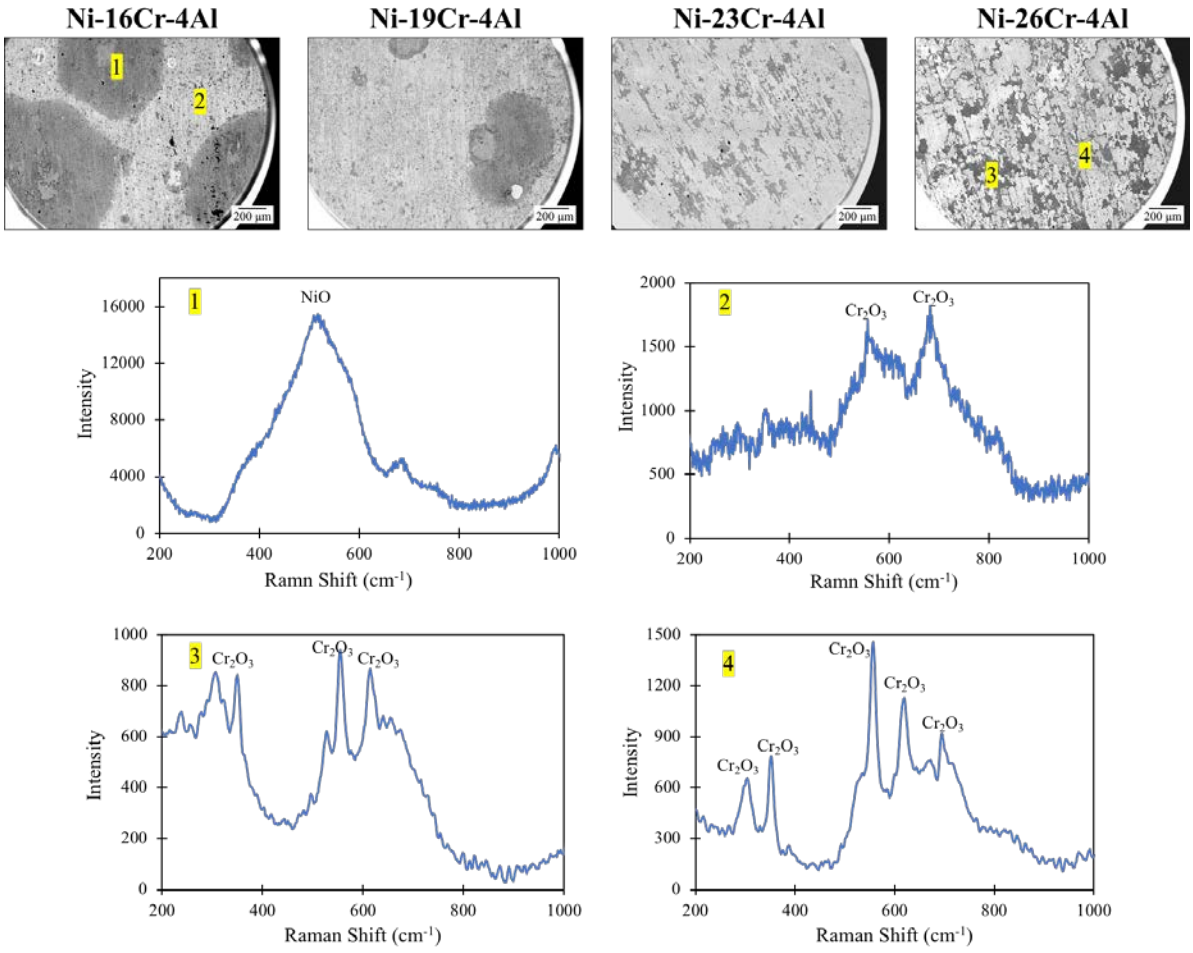

Figure 5-82. Surface SEM images of NiCrAl alloys following removal of Na_2SO_4 deposit after exposure at 650°C in O_2-10 ppm SO_2 for 2 h with 2.5 mg/cm^2 Na_2SO_4 deposit. Numbers in surface SEM images correspond to number Raman spectrum below the images.

5.4.2 Low-temperature Hot Corrosion Exposures

100 h hot-corrosion exposures with 2.5 mg/cm^2 Na_2SO_4 were completed at 600°C-700°C. Figure 5-83 shows the resulting graph of weight change vs. temperature after this 100 h exposure. It is seen that the weight change is similar for all alloys at 600°C. At 650°C and 700°C, the low-Cr containing alloys (Ni-16Cr-4Al and Ni-19Cr-4Al) show higher weight gain than the alloys with higher Cr content (Ni-23Cr-4Al and Ni-26Cr-4Al). The difference in weight gain becomes most apparent at 700°C.

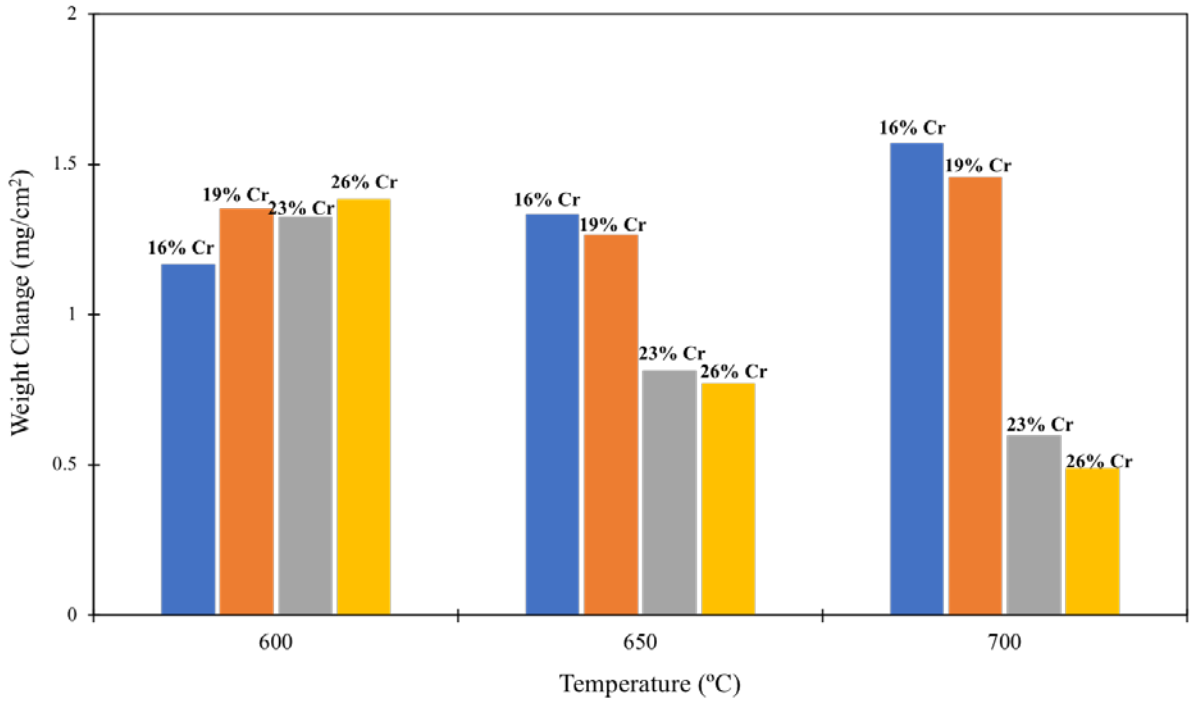

Figure 5-83. Weight change vs. tempertature of Ni-(16, 19, 23, and 26) Cr-4Al alloys after 100 h exposure at 600°C-700°C in O_2-10 ppm SO_2 with 2.5 mg/cm^2 Na_2SO_4 deposit.

Cross-sectional SEM images were collected to characterize the reaction products. Figure 5-84 shows the result for all alloys after the 100 h exposure. At 600°C the morphology looks similar for all alloys, with significant corrosion occurring. The products consist of a porous $NiO+Na_2SO_4$ at the gas interface, an inner Cr-rich oxide, and chromium-sulfide particles in the alloy. At 650°C and 700°C, the Ni-23Cr-4Al and Ni-26Cr-4Al alloys have only minor internal sulfide formation with evidence of a thin Cr-rich scale at the deposit/alloy interface, and no porous $NiO+Na_2SO_4$ formed. The Ni-16Cr-4Al and Ni-18Cr-4Al alloys were significantly attacked at 650°C and 700°C. The resulting products consist of a porous NiO at the gas interface with entrapped Na_2SO_4, an internal Cr-rich oxide, and significant internal sulfide formation.

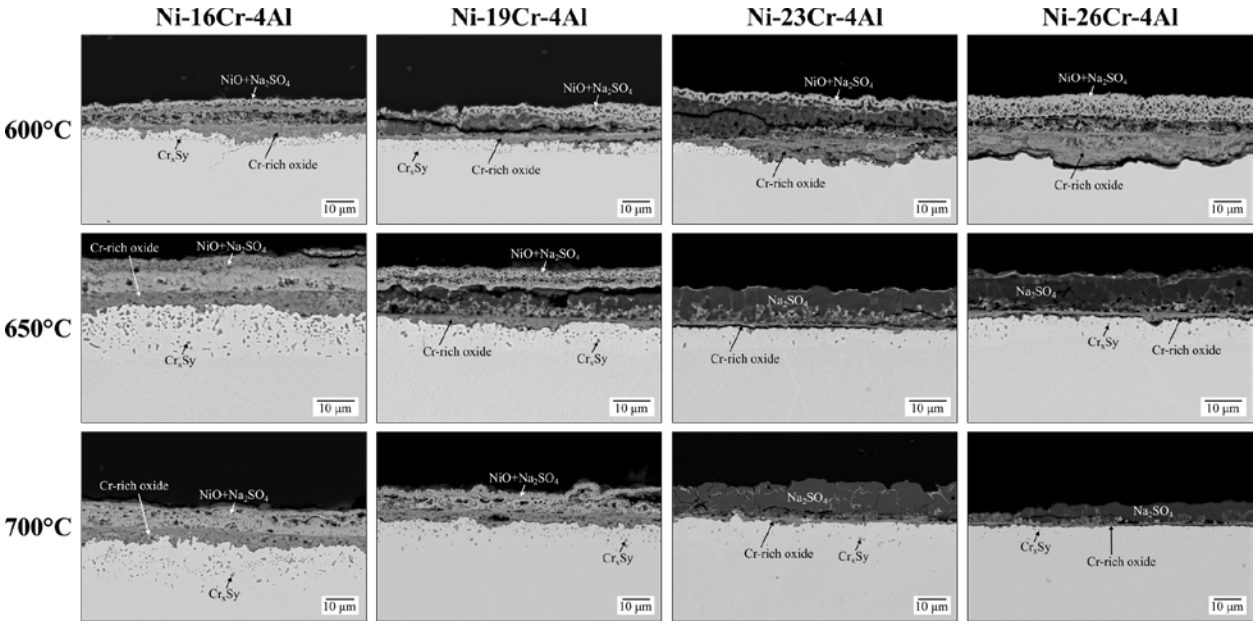

Figure 5-84. Cross-sectional SEM images of Ni-(16, 19, 23, and 26)Cr-4Al after 100 h exposure in O_2-10 ppm SO_2 with 2.5 mg/cm^2 Na_2SO_4 deposit.

20 h exposures were also completed to determine the time dependence of the reaction. Figure 5-85 shows plots of weight change vs. time for each temperature and alloy studied. At 600°C, all alloys showed increased weight gain from 20 h to 100 h. It is clear from the cross-sectional SEM images shown in Fig. 5-84 that after the 100 h exposure at 600°C all alloys exhibited hot-corrosion attack. Thus, the increase in weight gain is a result of deposit/alloy interaction. Cross-sectional SEM images of each alloy after the 20 h exposure at 600°C are shown in Fig. 5-86. Minor interaction between the base alloy and deposit occurred with minimal internal sulfide formation, and there was a presence of a thin Cr-rich scale. The images indicate that there is a long initiation period before the onset of hot corrosion at this temperature.

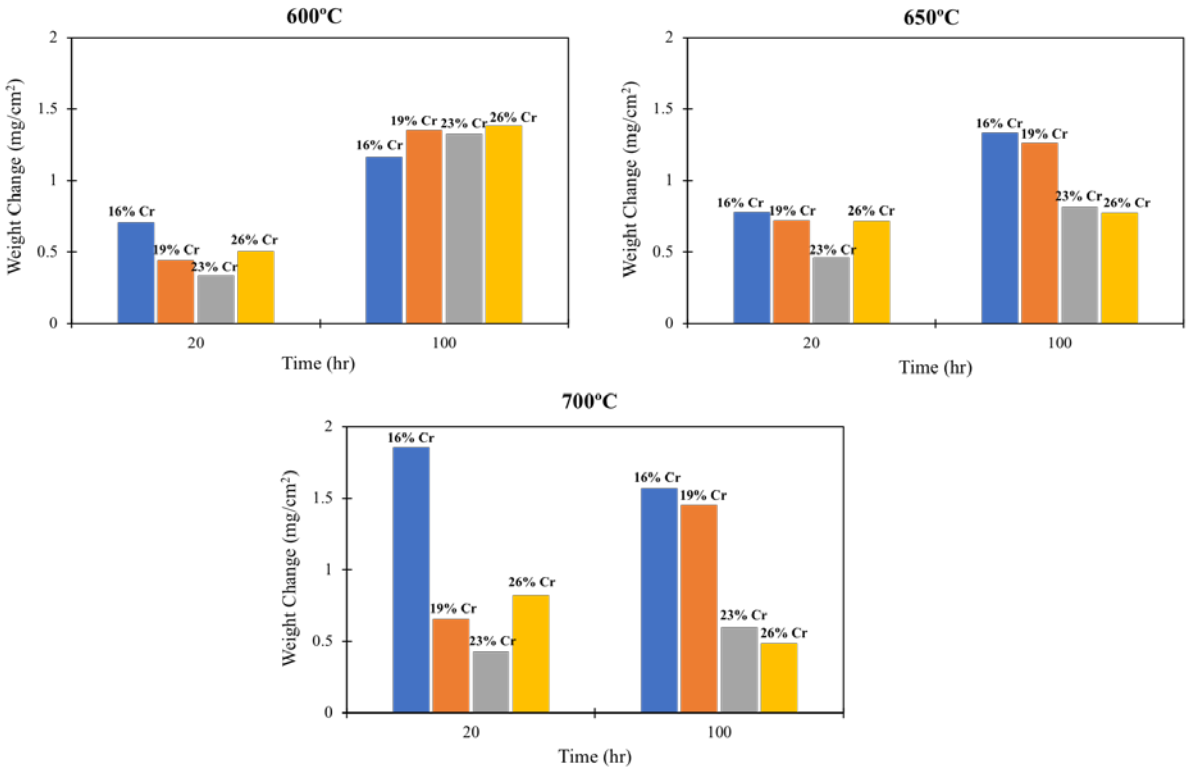

Figure 5-85. Weight change vs. time graphs after hot corrosion exposure of Ni-(16, 19, 23, and 26)Cr-4Al at 600°C, 650°C, and 700°C in O_2-10 ppm SO_2 with 2.5 mg/cm^2 Na_2SO_4 deposit.

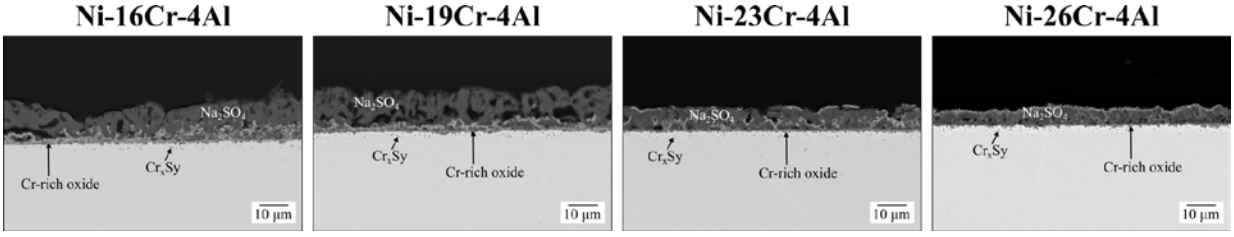

Figure 5-86. Cross-sectional SEM images of Ni-(16, 19, 23, and 26)Cr-4Al after 20 h exposure at 600°C in O_2-10 ppm SO_2 with 2.5 mg/cm^2 Na_2SO_4 deposit.

At 650°C, Ni-23Cr-4Al and Ni-26Cr-4Al had a minor increase in weight gain from 20 h to 100 h. After the 100 h exposure, these alloys were able to protect against hot corrosion, as evidence by the cross-sectional images shown in Fig. 5-84. Alloys Ni-16Cr-Al and Ni-19Cr-4Al showed a more significant increase in weight from 20 to 100 h. Figure 5-87 shows cross-sectional SEM images of the lower-Cr-content alloys after the 20 h exposure at 650°C. The results show that significant attack occurred after this shorter exposure time. Thus, compared to 600°C the initiation period is inferred to be shorter at 650°C. Parts of the samples had relatively minimal attack, but are not shown in Fig. 5-87. Another aspect to note is that pits are evident after the 20 h exposure at 650°C. However, after 100 h the attack appears to be uniform. Additional EDS analysis was done to determine the denuded-zone composition and the oxide composition for all alloys exposed for 20 h at 650°C, Fig. 5-88. The denuded zone measurements were taken ~1 μm below the Cr-rich scale. The Ni-16Cr-4Al and Ni-19Cr-4Al areas with apparent corrosion had significant subsurface Cr depletion and the oxide contained a higher content of Ni compared to the protective alloys.

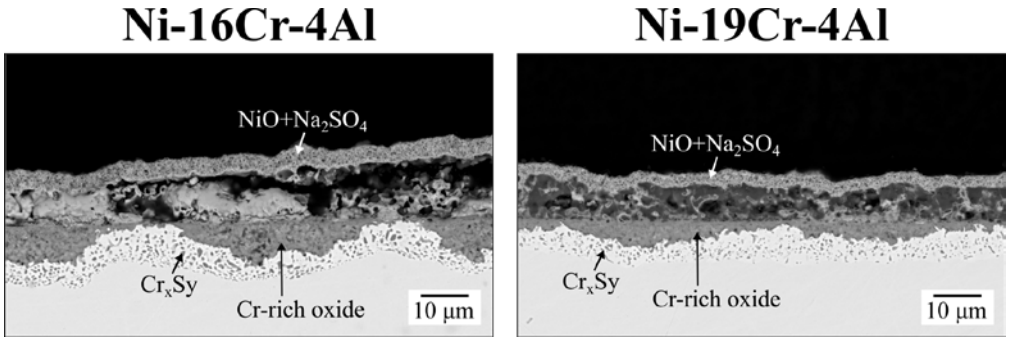

Figure 5-87. Cross-sectional SEM image of Ni-(16 and 19)Cr-4Al after 20 h exposure at 650°C in O_2-10 ppm SO_2 with 2.5 mg/cm^2 Na_2SO_4.

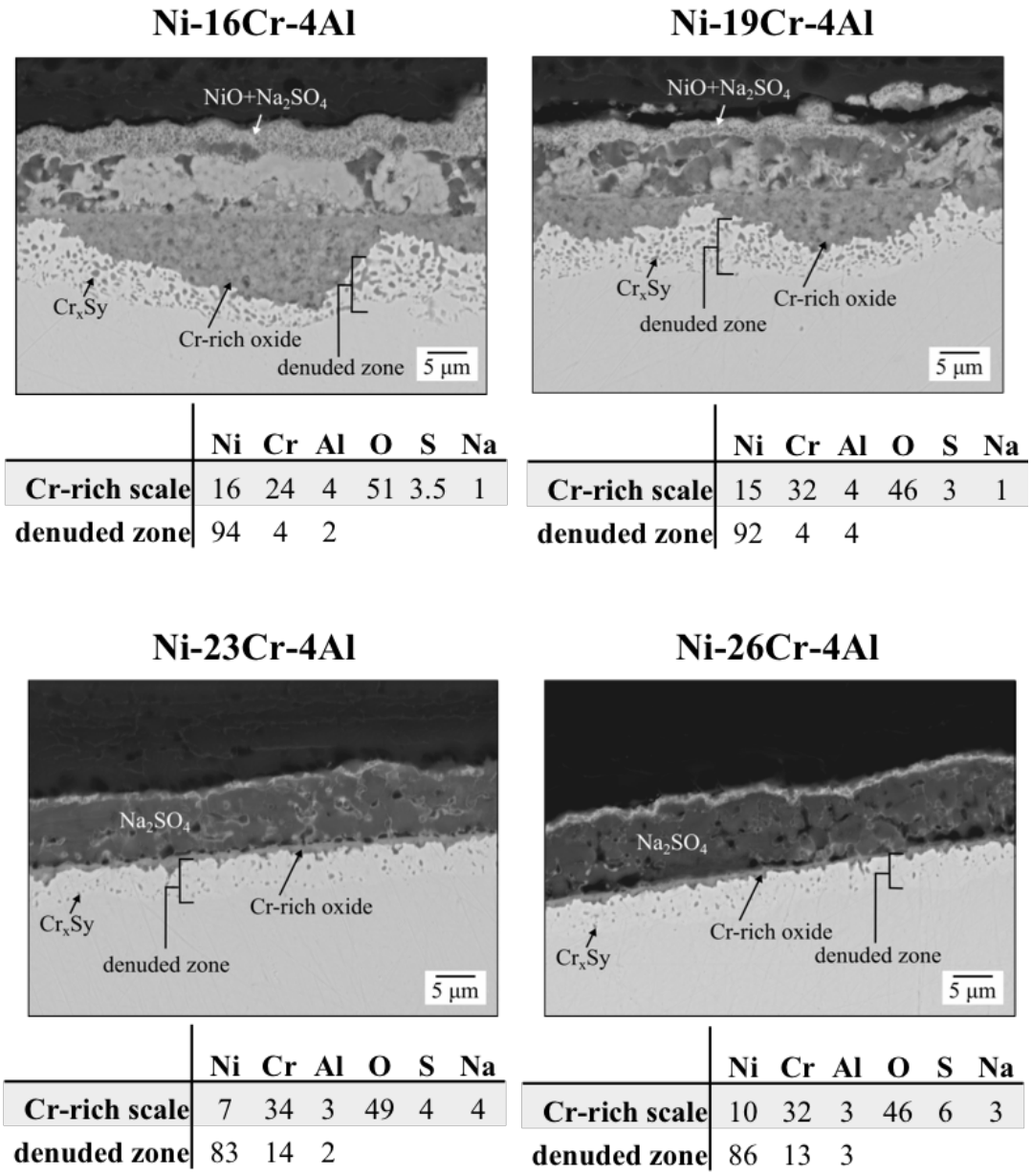

	Ni	Cr	Al	O	S	Na
Cr-rich scale	16	24	4	51	3.5	1
denuded zone	94	4	2			

	Ni	Cr	Al	O	S	Na
Cr-rich scale	15	32	4	46	3	1
denuded zone	92	4	4			

	Ni	Cr	Al	O	S	Na
Cr-rich scale	7	34	3	49	4	4
denuded zone	83	14	2			

	Ni	Cr	Al	O	S	Na
Cr-rich scale	10	32	3	46	6	3
denuded zone	86	13	3			

Figure 5-88. Cross-sectional SEM images of NiCrAl alloys after 20 h exposure at 650°C in O2-10 ppm SO_2 with 2.5 mg/cm2 Na_2SO_4, along with EDS analysis of the Cr-rich scale and denuded zone.

The Ni-16Cr-4Al and Ni-19Cr-4Al alloys had notably more weight gain than Ni-23Cr-4Al and Ni-26Cr-4Al after 100 h exposure at 700°C. The lower-Cr-content alloys showed comparatively significant degradation at this temperature (Fig. 5-82); whereas, the higher-Cr-content alloys are protective. From 20 to 100 h, the plot in Fig. 5-85 shows increased weight gain for Ni-19Cr-4Al. All other alloys had only a minor increase from 20 to 100 h. Figure 5-89 shows the cross-sectional SEM images of the lower-Cr content alloys after 20 h at 700°C. Ni-16Cr-4Al shows significant attack after just 20 h. By this stage most of the deposit is consumed. Looking at the weight-change data in Fig. 5-85, the weight change of Ni-16Cr-4Al after 100 h is lower than that after 20 h. Different samples were used for each data point, so the decrease in weight change is likely a result of sample variation. The important aspect is significant weight gain did not occur between 20 and 100 h because the deposit was consumed. The cross-sectional SEM images for Ni-19Cr-4Al show minimal attack after 20 h of exposure at 700°C. However, after 100 h uniform attack occurs, indicating the Ni-19Cr-4Al alloy had a relatively long initiation period before aggressive attack occurred.

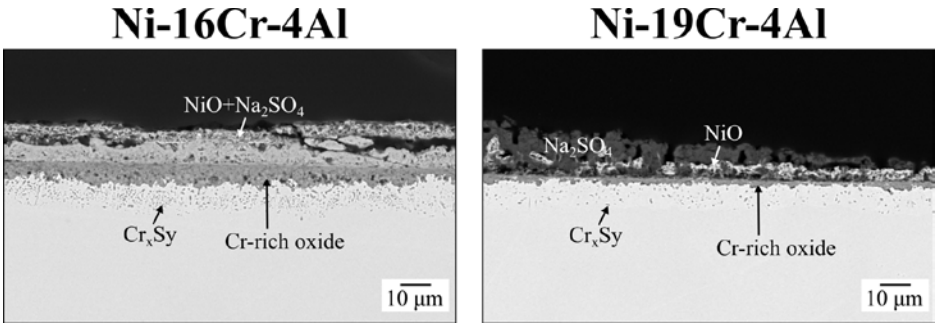

Figure 5-89. Cross-sectional SEM image of Ni-(16 and 19)Cr-4Al after 20 h exposure at 700°C in O_2-10 ppm SO_2 with 2.5 mg/cm^2 Na_2SO_4.

5.4.3 Influence of Cobalt

Cobalt is an alloying element present in PWA 70 coating. Based on the conventional understanding of low-temperature hot corrosion, cobalt is known to be more reaction than nickel in the presence of an Na_2SO_4 deposit [11, 101]. Therefore, it is informative to understand if the previous results hold with a small amount of Co present in the alloy. A fifth model alloy was made based on the high Cr alloy, with the addition of cobalt. The composition was Ni-26Cr-10Co-4Al. Figure 5-90 shows the resulting cross-sectional SEM images after a 100 h exposure at 600°C and 650°C with 2.5 mg/cm^2 Na_2SO_4 deposit. At 600°C, the cobalt-containing alloy clearly underwent degradation; whereas, at 650°C minimal attack occurred. The trend is the same as the Ni-26Cr-4Al alloy without cobalt, indicating cobalt did not play a major role in the degradation process.

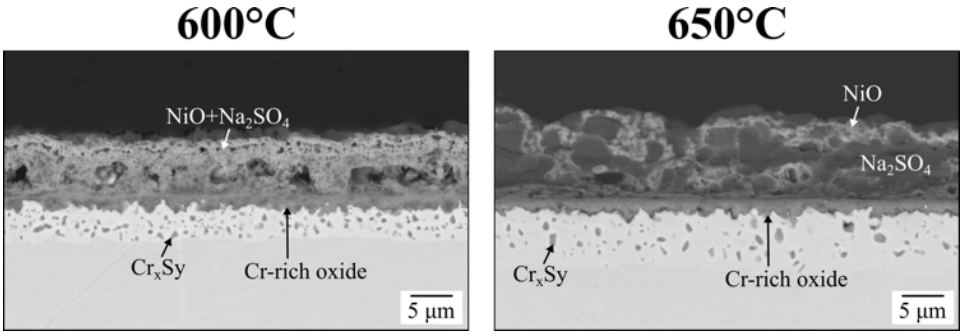

Figure 5-90. Cross-sectional SEM image of Ni-26Cr-10Co-4Al after 100 h exposure at 600°C and 650°C in O_2-10 ppm SO_2 with 2.5 mg/cm^2 Na_2SO_4 deposit.

5.4.4 Influence of Carbides and Nitrides

The PWA 70 coating contains carbides and nitrides from processing that may have an impact on hot corrosion. To assess the influence of nitrides, Ni-26Cr-4Al was exposed to Ar-2%NH_4 at 900°C for 20 h to cause internal aluminum-nitride formation. The nitrided Ni-26Cr-4Al sample was then tested at 650°C in O_2-10 ppm SO_2 with 2.5 mg/cm^2 Na_2SO_4 for 100 h. To assess the influence of carbides, another model alloy was made based on the composition of the high Cr alloy, with the addition of TaC. The composition was Ni-26Cr-4Al-4TaC. The model alloy containing TaC was then also tested under the same conditions as the nitrided alloy. The resulting cross-sectional SEM images with the addition of nitrides and carbides are shown in Fig. 5-91. The result for Ni-26Cr-4Al alloy exposed to the same conditions is also shown in Fig. 5-91 for comparison. Nitrides did not accelerate the hot corrosion attack, but the presence of TaC did promote more extensive corrosion.

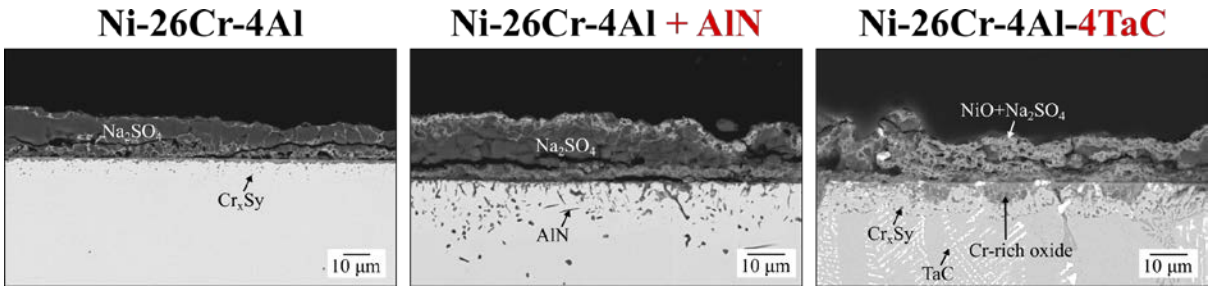

Figure 5-91. Cross-sectional SEM images of Ni-26Cr-4Al,with additions of aluminum nitrides and tantalum carbides, after exposure at 650°C for 100 h in O_2-10 ppm SO_2 with 2.5 mg/cm^2 Na_2SO_4 deposit.

5.4.5 Discussion

5.4.5.1 Corrosion Mechanism

The solid-state corrosion mechanism is inferred to be operating in the 600-700°C temperature range the model Ni-Cr-Al alloys were studied. The mechanism was discussed in Section 5.1 and 5.2 and is operative because $NiSO_4$-Na_2SO_4 is not stable in the low-SO_2 containing environments at the low temperatures studied. Comparing the structure of the corrosion products to the morphology of the product from the low-temperature hot corrosion of PWA 1484, presented in Section 5.1, both consist of a porous NiO+Na_2SO_4 at the gas interface, with an internal mixed oxide product. In the case of PWA 1484, sulfur was present in the internal oxide product, with enrichment at the oxide/alloy interface. In the case of the model Ni-Cr-Al alloys, there was distinct chromium sulfide formation in the base of the alloy, which can be rationalized considering the formation of CrS, as shown in Eq. 5-9 and 5-10. The underline indicates Cr and S are in solid solution. According to Sievert's law, the sulfur concentration is proportional to P_{S_2}, and according to Le Chatelier's principle, increasing the activity of Cr or the P_{S_2} would favor the CrS formation. The NiCrAl model alloys have a higher Cr content, and thus higher Cr activity compared to PWA 1484. Also, PWA 1484 is single crystal whereas the NiCrAl model alloys have a grain size of ~30 μm. Internal sulfide particles were often found around grain boundaries, indicating rapid diffusion along the grain boundaries and thus the establishment of higher sulfur potential to form sulfides.

$$\frac{1}{2}S_2 = \underline{S} \qquad (5-9)$$

$$\underline{Cr} + \underline{S} = CrS \qquad (5-10)$$

5.4.5.2 Concept of "Critical Cr Content" Beneath a Deposit

To prevent hot-corrosion attack it is critical for the alloys to form and maintain a protective Cr_2O_3 scale in the presence of a sulfate deposit, as discussed by various authors [139]–[143]. The Raman results completed on samples oxidized for 2 h show all alloys have the ability to form a Cr_2O_3 scale at the temperatures studied. Therefore, considering Eq. 2.2 shown in Section 2.2, all NiCrAl model alloys should contain a solute concentration (Cr) above that needed to form and maintain a Cr_2O_3 scale. However, in the presence of a deposit some alloys either did not establish an Cr_2O_3 scale or were unable to maintain the scale at a given temperature. Specifically, at 600°C all alloys were non-protective. At 650°C and 700°C, Ni-23Cr-4Al and Ni-26Cr-4Al were protective while Ni-16Cr-4Al and Ni-19Cr-4Al were non-protective.

Figure 5-82 showed Ni-16Cr-4Al and Ni-19Cr-4Al formed NiO islands beneath the sulfate deposit after exposure at 650°C for 2 h in O_2-10 ppm SO_2. Ni-23Cr-4Al and Ni-26Cr-4Al only formed Cr_2O_3 and $NiCr_2O_4$. The alloys that showed NiO formation (Ni-16Cr-4Al and Ni-19Cr-4Al) also showed significant hot-corrosion attack after 20 and 100 h of exposure, as seen in Fig. 5-84 and 5-87. NiO formed at a low temperature is a defective oxide, as shown in Section 5.1, allowing for transport through the scale [109, 110], leading to hot corrosion. The alloys that formed a protective Cr_2O_3 scale (Ni-23Cr-4Al and Ni-26Cr-4Al) were able maintain the scale formation, as very minimal attack occurred after 100 h of exposure. To further illustrate the importance of

scale formation, Ni-16Cr-4Al was pre-oxidized at 900°C for 6 h to establish a Cr_2O_3 scale. The pre-oxidized alloy was then tested at 650°C for 100 h in O_2-10 ppm SO_2 with 2.5 mg/cm^2 Na_2SO_4. The cross-sectional SEM image after exposure is shown in Fig. 5-92. No interaction occurs between the alloy with the lowest Cr content and the deposit when a uniform scale is present. In addition, sulfide formation is not observed in the alloy indicting the scale was not permeable to sulfur species. In Section 5.3, it was discussed that sulfur is able to transport through a Cr_2O_3 scale formed on a nickel-based superalloy. Past literature shows instances of species able to diffuse through a Cr_2O_3 scale and other occurrences where the scale is protective [144]–[146]. Therefore, permeability of species through the chromia scale will be dependent on the alloy, the scale structure, and the environment.

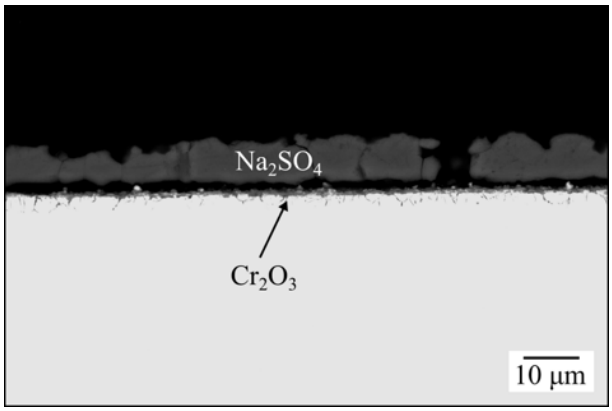

Figure 5-92. Cross-sectional SEM image of Ni-16Cr-4Al pre-oxidized at 900°C for 6 h in air with no deposit followed by exposure at 650°C in O_2-10 ppm SO_2 with 2.5 mg/cm^2 Na_2SO_4.

In service, the protective scale that develops on an alloy is prone to eventually breakdown [147]. The presence of a sulfate deposit leads to the introduction of chromium sulfides, which depletes the alloy of Cr needed for maintaining the scale. The EDS analysis of the denuded zone

and oxide after the 20 h exposure at 650°C (Fig. 5-88) showed significant Cr depletion and a higher content of Ni in the oxide on the Ni-16Cr-4Al and Ni-19Cr-4Al alloys. The importance of this is that a sufficient supply of Cr is needed to maintain the scale once established. If the Cr is tied up in the form of sulfides, the scale is more prone to breakdown and ensuing hot-corrosion attack. The thick internal Cr-rich scale that develops on the corroded samples is predicted to occur due to oxidation of the chromium sulfides. As shown by Choi and Stringer [148], the volume of CrS per unit mass of Cr (20.5 mol/cm^3) is larger than that of Cr_2O_3 per unit mass of Cr (14.6 mol/cm^3), the oxide that forms from oxidation of the sulfide is porous and permeable to sulfur. The released sulfur diffuses further into the alloy forming new sulfide particles [148]. Figure 5-93 presents a schematic of the inferred initial interaction between the sulfate deposit and the Ni-Cr-Al model alloys.

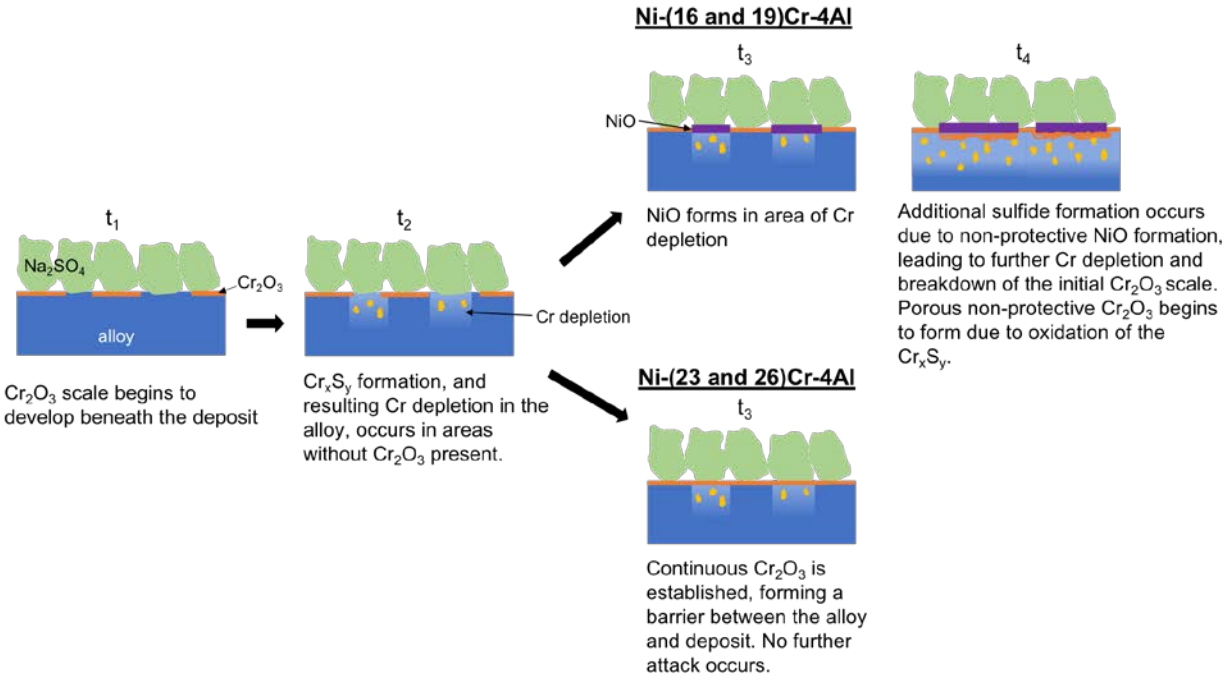

Figure 5-93. Schematic of initial stages of deposit/alloy interaction.

Based on the previous discussion, Fig. 5-94 presents two schematics summarizing the results after 20 and 100 h of exposure. In the following, the critical Cr-content at each temperature will be discussed.

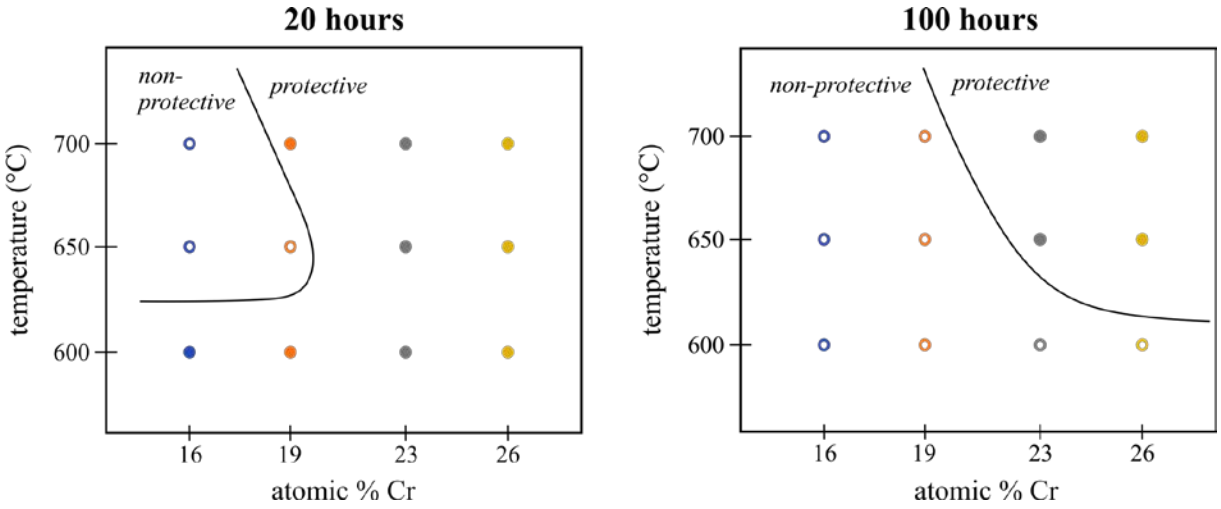

Figure 5-94. Schematic of NiCrAl exposures for 20 and 100 h in O_2-10 ppm SO_2 with 2.5 mg/cm^2 Na_2SO_4, illustrating protective vs. non-protective alloys.

600°C

At 600°C, minimal interaction was shown to occur after 20 h of exposure. After 100 h, all alloys were attacked. ICP-OES analysis was completed on samples after a 2 h exposure at 600°C to understand if any deposit/alloy interaction occurred. Figure 5-95 shows the resulting measured plots of mmol*10^3/cm^2 for each alloy. The plots show Cr and Ni dissolution, indicating interaction of those elements with the sulfate deposit in the initial stages. Therefore, the scale that appears to develop on the alloys after 20 h delays significant corrosion from occurring, but is likely non-

uniform and non-protective as significant attack is shown to occur after 100 h exposure. To protect the alloys at 600°C, a higher Cr content would be needed, or pre-oxidation of the alloy.

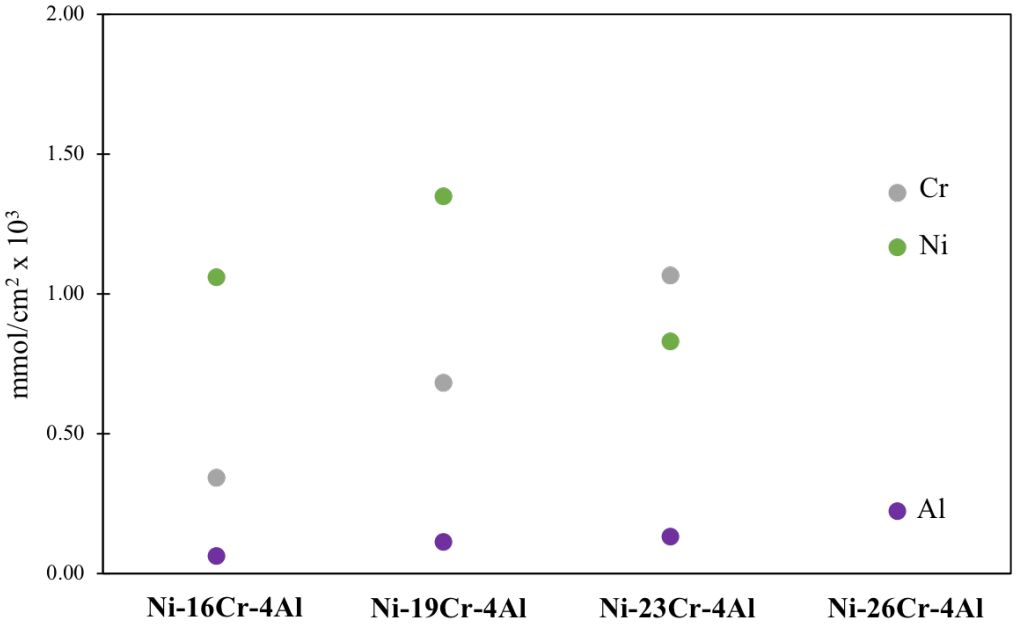

Figure 5-95. Plot of measured concentration of Al, Ni, and Cr from ICP-OES analysis after exposure at 600°C for 2 h in O_2-10 ppm SO_2 with 2.5 mg/cm^2 Na_2SO_4 deposit.

650°C

At 650°C, Ni-16Cr-4Al and Ni-19Cr-4Al were non-protective and Ni-23Cr-4Al and Ni-26Cr-4Al were protective. As temperature increases both the growth rate of the scale and the corrosion rate will increase. Therefore, the higher-Cr-containing alloys are able to establish and maintain a protective scale. However, the lower-Cr-containing alloys show significant attack after the 20 h exposure and the Raman results revealed the sulfate deposit impacted scale formation on

these alloys. The critical Cr content for protection at this temperature is therefore above 19 atomic %.

700°C

At 700°C, the same trend was observed as 650°C where Ni-16Cr-4Al and Ni-19Cr-4Al were non-protective and Ni-23Cr-4Al and Ni-26Cr-4Al were protective. An interesting observation was Ni-19Cr-4Al showed minimal interaction after 20 h, where Ni-16Cr-4Al was severely attacked and the deposit completely consumed. The reason for this is believed to be the competition between the kinetics of scale growth and that of hot corrosion. At a temperature of 700°C, Ni-19Cr-4Al is able to initially establish a protective oxide. However, there must be areas where the scale either broke down or is non-uniform serving as initiation points for attack. Once sulfides are introduced in the alloy and the subsurface is depleted below the Cr content required for maintaining the scale, the kinetics of hot corrosion takes over and rapid reaction follow. Therefore, at 700°C a 100 h exposure was required to reveal the critical Cr content needed for protection is above 19 atomic %.

5.4.5.3 Effect of Alloying Additions Present in PWA 70

The effect of alloying additions is linked to the impact on scale formation. The addition of cobalt to Ni-26Cr-4Al, an element known to be detrimental to low-temperature hot corrosion [11], did not result in enhanced corrosion at 650°C in O_2-10 ppm SO_2. This is likely due to Co not impacting the Cr_2O_3-scale formation. Once a protective scale is established, interaction between cobalt and the deposit will not occur. Additional ICP-OES analysis was completed at 650°C after a 4 h exposure for the NiCrAl alloys and the alloy with a cobalt addition. The result is shown in

Fig. 5-96. The alloys that showed significant corrosion at 650°C (Ni-(16, 19)Cr-4Al) also reacted to form products with the highest Ni content. The Ni-26Cr-10Co-4Al alloy showed low Ni and Co dissolution, indicating minimal interaction with the deposit and therefore, Co is not impacting the scale formation. By contrast, the Ni-26Cr-10Co-4Al alloy did show corrosion after 100 h at 600°C, consistent with the results of the NiCrAl alloys studied. The reasoning is due to the inability of the alloy to maintain the protective scale.

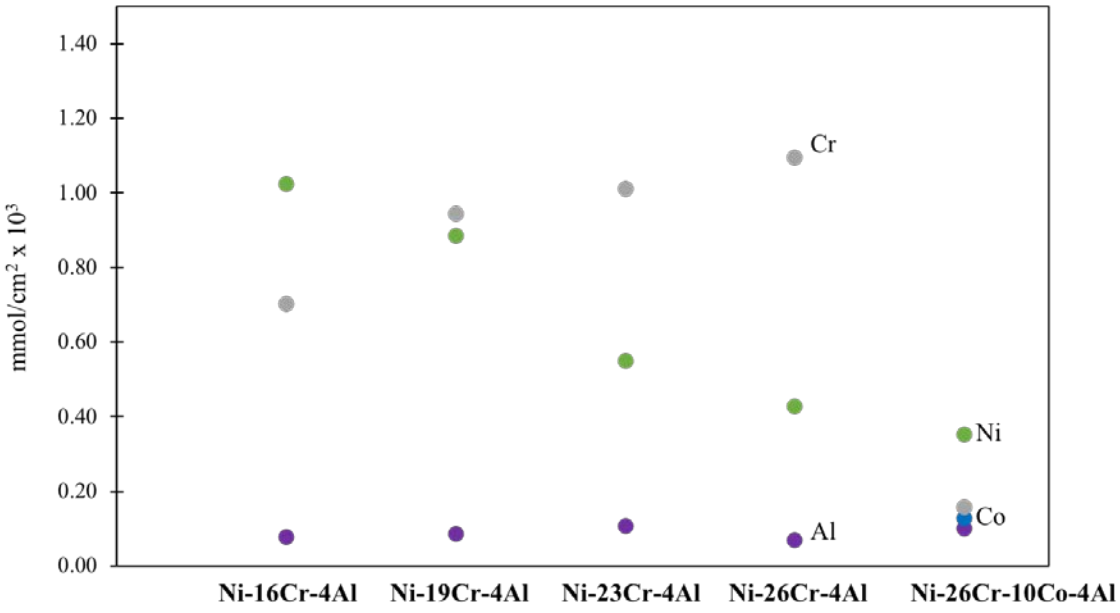

Figure 5-96. Plot of measured concentration of Al, Ni, and Cr from ICP-OES analysis after exposure at 650°C for 4 h in O_2-10 ppm SO_2 with 2.5 mg/cm^2 Na_2SO_4 deposit.

The addition of nitrides to Ni-26Cr-4Al did not result in corrosion. As with the addition of cobalt, the nitrides did not impact the scale formation. However, the addition of TaC to the alloy did show an increase in corrosion. Potter et al. [122] studied nickel and cobalt-based alloys with refractory carbides and concluded that the presence of carbides at the surface disrupts the scale

integrity and the oxidation of the carbides allows for inward transport of species. The same mechanism is inferred to be operating for the Ni-26Cr-4Al alloys containing TaC. The TaC readily oxidizes, disrupting the establishment of a uniform protective scale. The volume of TaC per unit mass of Ta (13.5 cm^3/mol) is less than that of Ta_2O_5 per unit mass of Ta (28.0 cm^3/mol). As the TaC oxidizes, the increased volume will be disruptive to establishing a uniform Cr_2O_3 scale. The volume of AlN per unit mass of Al (12.6 cm^3/mol) is very similar to the volume of Al_2O_3 per unit mass of Al (12.9 cm^3/mol), so oxidizing an AlN did not result in a volume change and hence did not impact protective scale formation.

6.0 Concluding Remarks

6.1 Solid-state Mode of Hot Corrosion Occurring at 700°C and Below

Preliminary experiments completed on PWA 1484 showed hot corrosion at temperatures and P_{SO_3} levels where liquid formation is not stable. Additional experiment were conducted on ME 16 and also found hot corrosion at low-temperatures was similarly found. In-depth analysis was completed on PWA 1484 and pure nickel samples were tested to more clearly determine the mechanism. The following summarizes the findings:

- Analyses using SEM and DSC were completed on ternary mixtures of $NiSO_4$-$CoSO_4$-Na_2SO_4. The lowest melting eutectic was ~600°C. Since hot corrosion occurred as low as 550°C on PWA 1484, the hot-corrosion mechanism was determined to be solid state.
- Based on a diffusion couple experiment and experiments using Na_2SO_4 grains, it was deduced that nickel diffusion was occurring along the surfaces of the sulfate grains.
- TEM analyses on PWA 1484 and a pure nickel sample identified a nanocrystalline $Na_2Ni_2SO_5$ phase present next to NiO filaments, which penetrated into and along the Na_2SO_4. The $Na_2Ni_2SO_5$ was assessed to be metastable, with eventual decomposition resulting in porous NiO plus particles of Na_2SO_4. The nanocrystalline structure of the $Na_2Ni_2SO_5$ allowed for the requisite rapid nickel transport for the accelerated attack.
- Three criteria were deemed necessary for the proposed solid-state mechanism to occur: a significantly high nickel flux; SO_3 in the atmosphere to stabilize $Na_2Ni_2SO_5$ formation; and sufficiently slow Na_2SO_4 deposit sintering to allow for adequate wetting by NiO to occur.

- The proposed solid-state mechanism is applicable to K_2SO_4 deposits as well, based on experiments completed which found similar reaction with a nickel sample.

6.2 Spatial Influence of Na_2SO_4 Deposit on Oxidation and Corrosion

Experiments completed on PWA 1484 and pure nickel with isolated Na_2SO_4 grains revealed the proposed solid-state mechanism has a spatial influence. The following summarizes the findings:

- TEM analysis on pure nickel in an area away from where the sulfate grain was located revealed the presence of a nanocrystalline $Na_2Ni_2SO_5$ phase.
- TEM analysis on the NiO formed in the area where the nanocrystalline $Na_2Ni_2SO_5$ phase was identified measured a fine-grained NiO structure.
- DFT calculations found the presence of S, Na, or Na and S decrease the grain-boundary energy of NiO, favoring nucleation of new NiO grains over growth of existing grains. The calculations support the identification of the fine-grained NiO in areas containing the $Na_2Ni_2SO_5$ phase. However, the fine-grained structure alone does not explain the NiO thickness. It is hypothesized that S and/or Na are increasing the diffusion of Ni through NiO.
- To account for rapid diffusion of Na^+ along the sample surface, an additional reaction was proposed.

6.3 Effect of SO_2 Content on Alloy Hot Corrosion Over the Temperature Range 550-1000°C

The corrosion rate of PWA 1484 was studied from 550-1000°C in dry air and O_2-(2.5, 10, and 100) ppm SO_2 with a Na_2SO_4 deposit. The following summarizes the findings:

- In the low-temperature regime, as SO_2 content increased, corrosion rate increased. ICP-OES analysis showed increased Ni as SO_2 content increased, which is predicted to be due to an increased formation of the nanocrystalline $Na_2Ni_2SO_5$ phase.
- In the intermediate-temperature regime, as SO_2 content increased, corrosion rate increased. Additionally, if the $CoSO_4$-Na_2SO_4 eutectic was stable, a similar corrosion rate existed across the temperature range.
- Pit formation that occurred at 850°C was found to initiate due to the presence of carbides and the dendritic structure of the alloy, as heat-treated alloys tested showed a more homogenous composition had less attack.
- In environments where the $CoSO_4$-Na_2SO_4 eutectic is not stable, initiation is predicted to occur due to alloy-induced acidic fluxing. This was supported by ICP-OES analysis after exposure at 800°C. In addition, Ni-Cr-Al alloys tested with a similar composition to PWA 1484 did not show deposit/alloy interaction.
- In the high-temperature regime, a longer exposure time of 100 h showed a much higher corrosion rate in dry air and O_2-2.5 ppm SO_2 than O_2-(10 and 100) ppm SO_2. The reasoning was determined to relate to the ability of the alloy to form a semi-protective scale. ICP-OES analysis completed showed as the SO_2 content increased Cr dissolution in the sulfate

deposit decreased. Cr is beneficial for oxide formation, so increased Cr depletion would impact the alloys ability to establish a scale, leading to accelerated attack. The mechanism of attack needs further study, but there were some indications alloy-induced acidic fluxing could be playing a role.

6.4 Influence of Chromium Content on the Low-temperature Hot Corrosion Behavior of Model Ni-Cr-Al Based Alloys

The influence of Cr content on hot corrosion was studied in the low-temperature regime. The following summarizes the findings:

- The oxidation behavior of the alloys was shown to be negatively affected by the presence of an Na_2SO_4 deposit.
- If the alloy is able to establish and maintain a protective scale, minimal attack is observed.
- At 600°C, all alloys showed attack. At 650°C and 700°C Ni-16Cr-4Al and Ni-19Cr-4Al showed attack while Ni-23Cr-4Al and Ni-26Cr-4Al were protective.
- The addition of cobalt to the Ni-26Cr-4Al alloy did not accelerate attack because Co did not impact the ability of the alloy to establish a protective scale.
- The addition of AlN to the Ni-26Cr-4Al alloy did not accelerate attack. The addition of TaC did. The reasoning was determined to be the significant volume change from the oxidation of TaC is disruptive to oxide scale establishment.

Appendix A

Average Attack Measurements

A graph of average attack vs. temperature was presented in this thesis after exposure of PWA 1484 in dry air and O_2-(2.5, 10, and 100) ppm SO_2 with 2.5 mg/cm^2 Na_2SO_4. The following will present data used in creating that graph. Fig. A-1 shows an example image of how the measurements were taken. A sectioned line was placed on an SEM image and at each mark, a measurement was made using ImageJ. 10 measurements were taken for each data point. Table A-1 lists the average attack measured and standard deviation at each temperature in dry air and O_2-(2.5, 10, and 100) ppm SO_2.

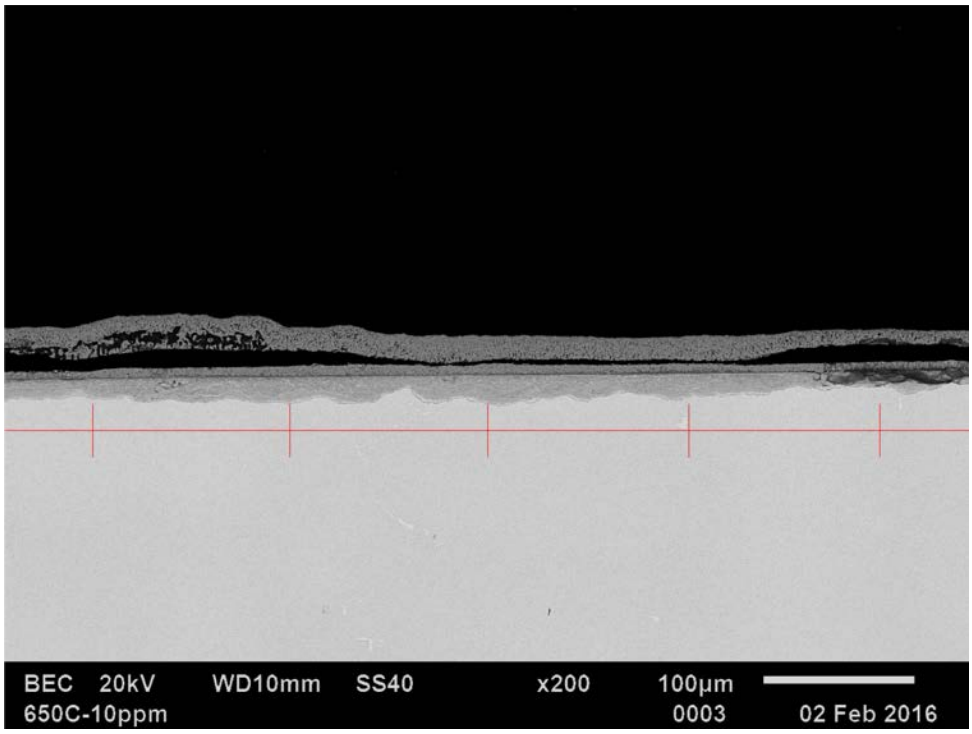

Figure A-1. Example of average attack measurement on cross-sectional SEM image of PWA 1484 after exposure at 650°C in O_2-10 ppm SO_2 after 20 h with 2.5 mg/cm^2 Na_2SO_4.

Table A-1. Data from measurements after exposure of PWA 1484 after 20 h with 2.5 mg/cm^2.

	Dry Air		**O_2-2.5 ppm SO_2**		**O_2-10 ppm SO_2**		**O_2-100 ppm SO_2**	
	Average attack (µm)	St. Dev.	Average attack (µm)	St. Dev.	Average attack (µm)	St. Dev.	Average attack (µm)	St. Dev.
550	1	1	6	2	17	3	13	3
600	1	1	11	2	24	3	36	9
650	2	3	11	1	46	8	54	10
700	4	3	20	7	52	14	75	7
750	4	2	17	8	17	17	76	7
800	9	13	18	16	20	20	78	53
850	4	7	21	23	35	21	72	38
900	5	6	29	12	23	3	30	10
950	21	17	56	5	65	8	60	7
1000	162	44	86	42	77	21	78	7

EDS Measurement for Nanocrystalline phase

Table A-2 lists all measurements of the nanocrystalline phase for determination of the stoichiometry. The average and standard deviation are included. The composition was determined from the average of all measurements. However, as mentioned in Section 5.1, the stoichiometry may not be exact and structural data would be needed to index the diffraction pattern.

Table A-2. EDS measurements of nanocrystalline phase.

Measurement	Na	Ni	S	O
1	21	14	4	60
2	18	10	8	64
3	14	23	9	54
4	16	15	11	58
5	16	20	8	55
6	22	13	6	58
7	15	16	7	59
8	15	15	8	62
9	19	15	2	51
10	14	19	6	61
11	13	21	5	61
12	18	14	8	60
13	20	14	7	58
14	10	25	4	61

Table A-2. (continued).

15	17	18	13	52
16	15	28	8	49
17	17	17	6	60
18	12	34	5	50
19	26	20	8	46
20	19	23	7	51
21	23	18	12	47
Average	17	19	7	56
St. dev	3.1	4.8	2.7	4.3

Bibliography

[1] B. Geddes, H. Leon, and X. Huang, *Superalloys: Alloying and Performance*. Material Park: ASM International, 2010.

[2] J. Stringer, “Hot Corrosion of High-Temperature Alloys,” no. 4, pp. 477–509, 1977.

[3] N. S. Bornstein and W. P. Allen, “The Chemistry of Sulfidation Corrosion-Revisited,” *Mater. Sci. Forum*, vol. 251–254, pp. 127–134, 1997.

[4] N. Birks, G. H. Meier, and F. S. Pettit, *Introduction to the High Temperature Oxidation of Metals*. Cambridge University Press, 2006.

[5] G. J. Gibson, K. M. Perkins, S. Gray, and A. J. Leggett, “Influence of shot peening on high-temperature corrosion and corrosion-fatigue of nickel based superalloy 720Li,” *Mater. High Temp.*, vol. 3409, no. May, pp. 1–9, 2016.

[6] T. Gheno, M. Zahiri Azar, A. H. Heuer, and B. Gleeson, “Reaction morphologies developed by nickel aluminides in type II hot corrosion conditions: The effect of chromium,” *Corros. Sci.*, vol. 101, pp. 32–46, 2015.

[7] T. Gheno and B. Gleeson, “On the Hot Corrosion of Nickel at 700C,” *Oxid. Met.*, vol. 84, no. 5–6, pp. 567–584, 2015.

[8] K. L. Luthra, “Kinetics of the Low Temperature Hot Corrosion of Co-Cr-Al Alloys,” *J. Electrochem. Soc.*, vol. 132, no. 6, p. 1293, 1985.

[9] K. L. Luthra, “Low Temperature Hot Corrosion of Cobalt-Base Alloys: Part I. Morphology of the Reaction Product,” *Metall. Trans. A*, vol. 13A, pp. 1843–1852, 1982.

[10] D. W. McKee, D. A. Shores, and K. L. Luthra, “The Effect of SO2 and NaCl on High Temperature Hot Corrosion,” *J. Electrochem. Soc.*, vol. 125, no. 3, p. 411, 1978.

[11] K. L. Luthra and D. A. Shores, “Mechanism of Na2SO4 Induced Corrosion at 600-900C,” *J. Electrochem. Soc. Solid-State Sci. Technol.*, vol. 127, no. 10, pp. 2202–2210, 1980.

[12] J. a. Goebel and F. S. Pettit, “Na2SO4-induced accelerated oxidation (hot corrosion) of nickel,” *Metall. Trans.*, vol. 1, no. 7, pp. 1943–1954, 1970.

[13] P. Lortrakul, R. W. Trice, K. P. Trumble, and M. a. Dayananda, “Investigation of the mechanisms of Type-II hot corrosion of superalloy CMSX-4,” *Corros. Sci.*, vol. 80, pp. 408–415, 2014.

[14] K. L. Luthra, “Low Temperature Hot Corrosion of Cobalt-Base Alloys: Part II. Morphology of the Reaction Product,” *Metall. Trans. A*, vol. 13A, pp. 1853–1864, 1982.

[15] D. A. Shifler, “The Increasing Complexity of Hot Corrosion,” *J. Eng. Gas Turbines Power*, 2017.

[16] M. Rezazadeh Reyhani, M. Alizadeh, A. Fathi, and H. Khaledi, “Turbine blade temperature calculation and life estimation - a sensitivity analysis,” *Propuls. Power Res.*, vol. 2, no. 2, pp. 148–161, 2013.

[17] Y. Taamneh, “Thermal analysis of gas turbine disk integrated with rotating heat pipes,” *Case Stud. Therm. Eng.*, vol. 10, pp. 335–342, 2017.

[18] G. W. Goward, “Progress in coating for gas turbine airfoils,” *Surf. Coatings Technol.*, vol. 108–109, pp. 73–79, 1998.

[19] T. M. Pollock and S. Tin, “Nickel-Based Superalloys for Advanced Turbine Engines: Chemistry, Microstructure and Properties,” *J. Propuls. Power*, vol. 22, no. 2, pp. 361–374, 2006.

[20] R. C. Reed, *The Superalloys : Fundamentals and Applications*. Cambridge University Press, 2008.

[21] N. Saunders, “Phase Diagram Calculations for Ni-Based Speralloys,” *Superalloys 1996*, pp. 101–110, 1996.

[22] J. K. Tien and R. N. Jarett, “Effects of Cobalt in Nickel-base Superalloys,” New York, New York, 1983.

[23] M. J. Donachie and S. Donachie, *Superalloys: A Technical Guide*. ASM International, 2002.

[24] T. P. Gabb, J. Telesman, B. Hazel, and D. P. Mourer, “The effects of hot corrosion pits on the fatigue resistance of a disk superalloy,” *J. Mater. Eng. Perform.*, vol. 19, no. 1, pp. 77–89, 2010.

[25] M. P. Jackson and R. C. Reed, “Heat treatment of UDIMET 720Li : the effect of microstructure on properties,” vol. 259, pp. 85–97, 1999.

[26] M. Rezazadeh, M. Alizadeh, and A. Fathi, “Turbine blade temperature calculation and life estimation - a sensitivity analysis,” *Propuls. Power Res.*, vol. 2, no. 2, pp. 148–161, 2013.

[27] J. Sumner, A. Encinas-Oropesa, N. J. Simms, and J. E. Oakey, “High temperature oxidation and corrosion of gas turbine component materials in burner rig exposures,” *Mater. High Temp.*, vol. 28, no. 4, pp. 369–376, 2011.

[28] B. Gleeson, “High-temperature corrosion of metallic alloys and coatings,” in *Materials Science and Technology: A Comprehensive Treatment: Corrosion and Environmental Degradation*, Weinhein, Germany: Wiley-VCH Verlag GmbH, 2000.

[29] D. J. Young, *High Temperature Oxidation and Corrosion of Metals*, vol. 1. Elsevier, 2008.

[30] C. Wagner, “No Title,” *J. Electrochem. Soc.*, vol. 99, p. 369, 1956.

[31] C. Wagner, “Reaktionstypen bei der Oxydation von Legierungen,” *Zeitschrift fuer Elektrochemie*, vol. 63, no. 7, pp. 772–782, 1959.

[32] X. Liu, “Effects of Trace SO2 and Na2SO4 Deposit on the Reaction Behavior of Al2O3-Scale Forming Alloys,” University of Pittsburgh, 2014.

[33] W. Zhao, “Steam Effects on Oxidation Behavior of Alumina-Scale Forming Nickel-Based Alloys and a Kinetics Analysis of Complex Scale Evolution During Isothermal Oxidation,” University of Pittsburgh, 2012.

[34] M. W. Brumm and H. . Grabke, “The Oxidation Behaviour of NiAl-I. Phase Transformations in the Alumina Sclae During Oxidation of NiAl and NiAl-Cr Alloys,” *Corros. Sci.*, vol. 33, pp. 1677–1690, 1992.

[35] G. H. Meier, “A Review of Advances in High-temperature Corrosion,” *Mater. Sci. Eng.*, vol. 120–121, pp. 1–11, 1989.

[36] F. S. Pettit, “Oxidation Mechanism for Nickel-Aluminum Alloys at Temperatures Between 900C and 1300C,” *Trans. Metall. Soc. AIME*, vol. 239, pp. 1296–1306, 1967.

[37] C. S. Giggins and F. S. Pettit, “Oxidation of Ni-Cr-Al Alloys Between 1000° and 1200°C,” *J. Electrochem. Soc.*, vol. 118, no. 11, p. 1782, 1971.

[38] F. Pettit, “Hot corrosion of metals and alloys,” *Oxid. Met.*, vol. 76, no. 1–2, pp. 1–21, 2011.

[39] R. Viswanathan, *Damage Mechanisms and Life Assessment of High-Temperature Components*, 1st ed. Metals Park, Ohio: ASM International, 1989.

[40] E. L. Simons, G. V. Browning, and H. A. Liebhafsky, “Sodium Sulfate in Gas Turbines,” *Corrosion*, vol. 11, p. 505, 1955.

[41] Y. Niu, F. Gesmundo, F. Viani, and W. Wu, “The corrosion of Ni3Al in a combustion gas with and without Na2SO4-NaCl deposits at 600-800°C,” *Oxid. Met.*, vol. 42, no. 3–4, pp. 265–284, 1994.

[42] R. a. Rapp and Y. S. Zhang, “Hot Corrosion of Materials: Fundamental Studies,” *JOM*, vol. 46, no. 12, pp. 47–55, 1994.

[43] R. A. Gupta, D.K., Rapp, “The Solubilities of NiO, Co3O4, and Ternary Oxides in Fused Na2SO4 at 1200°K,” *J. Electrochem. Soc.*, vol. 127, pp. 2194–2202, 1980.

[44] D. K. Gupta and R. A. Rapp, “Erratum,” *J. Electrochem. Soc.*, vol. 127, no. 12, p. 2656, 1980.

[45] Y. S. Zhang and R. A. Rapp, “Solubility of α-Fe2O3 in fused Na2SO4 at 1200 K,” *J. Electrochem. Soc.*, vol. 132, no. 3, pp. 735–737, 1985.

[46] Y. S. Zhang and R. A. Rapp, “Solubilities of CeO2 , HfO_2 and Y_2O_3 in Fused Na_2SO_4-30 mol% $NaVO_3$ and CeO_2 in Pure Na_2SO_4 at 900 C,” pp. 348–352, 1987.

[47] Y. S. Zhang, “Solubilities of Cr2O3 in Fused Na2SO4 at 1200 K.,” *J. Electrochem. Soc.*, vol. 17, no. 29, pp. 655–657, 1986.

[48] P. D. Jose, D. K. Gupta, and R. A. Rapp, “Solubility of α-Al2O3 in Fused Na2SO4 at 1200K,” *J. Electrochem. Soc.*, vol. 132, no. 3, pp. 735–737, 1985.

[49] D. Z. Shi and R. A. Rapp, “The solubility of SiO2 in fused Na2SO4 at 900°C,” *J. Electrochem. Soc.*, vol. 133, no. 4, pp. 849–850, 1986.

[50] R. A. Rapp, “Chemistry and Electrochemistry of Hot Corrosion of Metals,” *Mater. Sci. Eng.*, vol. 87, pp. 319–327, 1987.

[51] R. A. Rapp and K. S. Goto, “The hot corrosion of metals by molten salts,” in *Molten Salts*, 1981, pp. 159–173.

[52] R. a. Rapp, “Hot corrosion of materials: A fluxing mechanism?,” *Corros. Sci.*, vol. 44, no. 2, pp. 209–221, 2002.

[53] N. S. Bornstein and W. P. Allen, “The Chemistry of Sulfidation Corrosion-Revisited,” *Mater. Sci. Forum*, vol. 251–254, pp. 127–134, 1997.

[54] V. E. Fioletov *et al.*, “A global catalogue of large SO2 sources and emissions derived from the Ozone Monitoring Instrument,” *Atmos. Chem. Phys.*, vol. 16, no. 18, pp. 11497–11519, 2016.

[55] “Sulfur Dioxide Trends.” [Online]. Available: https://www.epa.gov/air-trends/sulfur-dioxide-trends%0D%0A.

[56] “China’s Sulfur Dioxide Emissions Drop, India’s Grow Over Last Decade,” 2017.

[57] A. K. Misra, “Mechanism of Na2SO4-Induced Corrosion of Molybdenum Containing Nickel-Base Superalloys at High Temperatures,” *J. Electrochem. Soc. Solid-State Sci. Technol.*, vol. 133, no. 5, pp. 1029–1038, 1986.

[58] K. T. Chiang, F. S. Pettit, and G. H. Meier, “Low Temperature Hot Corrosion,” in *NACE*, 1983, p. 519.

[59] B. S. Lutz, G. H. Meier, J. M. Alvarado-Orozco, and L. Garcia-Fresnillo, “Na2SO4-Deposit-Induced Corrosion of Mo-Containing Alloys,” *Oxid. Met.*, vol. 88, no. 5, pp. 599–620, 2017.

[60] R. F. Reising, “Nickel Oxide Scales and Sodium Sulfate-Induced Hot Corrosion of Nickel,” *Corrosion-NACE*, vol. 33, no. 3, pp. 84–88, 1977.

[61] K. P. Lillerud and P. Kofstad, “Sulfate-induced hot corrosion of nickel,” *Oxid. Met.*, vol. 21, no. 5–6, pp. 233–270, 1984.

[62] D. A. Shores and W. C. Fang, “Transport of Oxidant in Molten Na SO in O2-SO2-SO3 Environments,” *J. Electrochem. Soc.*, vol. 128, no. 2, pp. 127–129, 1981.

[63] W. C. Fang and R. A. Rapp, “Electrochemical Reactions in a Pure Na2SO4 Melt,” *J. Electrochem. Soc.*, vol. 130, no. 12, pp. 2335–2341, 1983.

[64] K. L. Luthra, “Mechanism of Oxidation-Sulfidation Reactions of CoO in the Presence of Na2SO4,” *Metall. Trans. A*, vol. 13A, pp. 1647–1654, 1982.

[65] A. K. Misra and D. P. Whittle, “Effects of SO2 and SO3 on the Na2SO4 induced corrosion of nickel,” *Oxid. Met.*, vol. 22, no. 1–2, pp. 1–33, 1984.

[66] K. L. Luthra and W. L. Worrell, “Simultaneous Sulfidation-Oxidation of Nickel at 603°C in SO2-O2-SO3 Atmospheres,” vol. 10, 1979.

[67] R. L. Jones and S. T. Gadomski, “Reactions of SO2(SO3) with NiO-Na2SO4 in Nickel-Sodium Mixed Sulfate Fomation and Low Tempearture Hot Corrosion,” *J. Electrochem. Soc.*, vol. 129, no. 7, pp. 1613–1618, 1980.

[68] J. Sumner, A. Encinas-Oropesa, N. Simms, and J. R. Nicholls, “Type II hot corrosion: Behaviour of CMSX-4 and IN738LC as a function of corrosion environment,” *Mater. Corros.*, no. 2, pp. 188–196, 2014.

[69] G. S. Mahobia, N. Paulose, and V. Singh, “Hot Corrosion Behavior of Superalloy IN718 at 550 and 650C,” vol. 22, no. August, pp. 2418–2435, 2013.

[70] V. Mannava, A. S. Rao, N. Paulose, M. Kamaraj, and R. S. Kottada, “Hot corrosion studies on Ni-base superalloy at 650C under marine-like environment conditions using three salt mixture (Na2SO4+NaCl+NaVO3),” *Corros. Sci.*, vol. 105, pp. 109–119, 2016.

[71] J. G. Smeggil, “Hot Corrosion of Turbine Materials in the Prescence of Mixed Sulfates,” East Hartford, CT, 2000.

[72] W. J. Zhang and R. Sharghi-Moshtaghin, “Revisit the Type II Corrosion Mechanism,” *Metall. Mater. Trans. A Phys. Metall. Mater. Sci.*, vol. 49, no. 9, pp. 4362–4372, 2018.

[73] J. a. Goebel, F. S. Pettit, and G. W. Goward, “Mechanisms for the hot corrosion of nickel-base alloys,” *Metall. Trans.*, vol. 4, no. 1, pp. 261–278, 1973.

[74] A. K. Misra, “Mechanism of Na2SO4-Induced Corrosion of Molybdenum Containing Nickel-Base Superalloys at High Temperatures,” *J. Electrochem. Soc.*, vol. 133, no. 5, p. 1038, 1986.

[75] A. K. Misra, “Mechanism of Na2SO4-Induced Corrosion of Molybdenum Containing Nickel-Base Superalloys at High Temperatures,” *J. Electrochem. Soc.*, vol. 133, no. 5, pp. 1029–1040, 1986.

[76] G. C. Fryburg, F. J. Kohl, and C. a. Stearns, “Chemical reactions involved in the initiation of hot corrosion of IN-738,” *J. Electrochem. Soc.*, vol. 131, no. 12, pp. 2985–2997, 1984.

[77] K. R. Peters, D. P. Whittle, and J. Stringer, “Oxidation and hot corrosion of nickel-based alloys containing molybdenum,” *Corros. Sci.*, vol. 16, no. 11, pp. 791–796, 1976.

[78] G. C. Fryburg, F. J. Kohl, C. A. Stearns, and W. L. Fielder, “Chemical Reactions Involved in the Initiation of Hot Corrosion of B-1900 and NASA-TRW VIA,” *J. Electrochem. Soc.*, vol. 129, no. 3, p. 571, 1982.

[79] A. U. Seybolt, “Contribution to the Study of Hot Corrosion,” *Trans. Metall. Soc. AIME*, vol. 232, pp. 1955–1961, 1968.

[80] N. S. Bornstein and M. A. DeCrescente, “The Relationship Between Compounds of Sodium and Sulfur and Sulfidation,” *Trans. Metall. Soc. AIME*, vol. 245, pp. 1947–1952, 1969.

[81] P. Knutsson, H. Lai, and K. Stiller, “A method for investigation of hot corrosion by gaseous Na2SO4,” *Corros. Sci.*, vol. 73, pp. 230–236, 2013.

[82] N. Otsuka and R. A. Rapp, “Hot Corrosion of Preoxidized Ni by a Thin Fused Na2S04 Film at 900C,” *J. Electrochem. Soc.*, vol. 137, no. 1, p. 53, 1990.

[83] N. Otsuka and R. a Rapp, “Hot Corrosion of Preoxidized Ni by a Thin Fused Na2S04 Film,” vol. 137, no. 1, pp. 46–52, 1990.

[84] R. A. Rapp and N. Otsuka, “The Role of Chromium in the Hot Corrosion of Metals,” *ECS Trans.*, vol. 16, no. 49, pp. 271–282, 2009.

[85] J. X. Chang, D. Wang, T. Liu, G. Zhang, L. H. Lou, and J. Zhang, “Role of tantalum in the hot corrosion of a Ni-base single crystal superalloy,” *Corros. Sci.*, vol. 98, pp. 585–591, 2015.

[86] J. R. Nicholls, “Advances in Coating Design for High- Performance Gas Turbines,” *MRS Bull.*, vol. 28, no. 9, pp. 659–670, 2003.

[87] G. H. Meier, C. Cheng, R. A. Perkins, and W. Bakker, “Diffusion chromizing of ferrous alloys,” *Surf. Coatings Technol.*, vol. 39–40, no. C, pp. 53–64, 1989.

[88] B. Gleeson and D. J. Young, “Codeposited Chromium-Aluminide Coatings I. Definiton of Codeposition Regimes,” *J. Electrochem. Soc.*, vol. 141, no. 6, pp. 1464–1471, 1994.

[89] M. N. Task, “Method of Chromizing An Article Including Internal Passages of the Article,” 15/207,745, 2018.

[90] M. J. Pomeroy, “Coatings for gas turbine materials and long term stability issues,” *Mater. Des.*, vol. 26, no. 3, pp. 223–231, 2005.

[91] K. L. Luthra and J. H. Wood, “High chromium cobalt-base coatings for low temperature hot corrosion,” *Thin Solid Films*, vol. 119, no. 3, pp. 271–280, 1984.

[92] M. N. Task, B. Gleeson, F. S. Pettit, and G. H. Meier, “Compositional factors affecting protective alumina formation under type ii hot corrosion conditions,” *Oxid. Met.*, vol. 80, no. 5–6, pp. 541–552, 2013.

[93] M. N. Task, B. Gleeson, F. S. Pettit, and G. H. Meier, “The effect of microstructure on the type II hot corrosion of Ni-base MCrAlY alloys,” *Oxid. Met.*, vol. 80, no. 1–2, pp. 125–146, 2013.

[94] G. W. Goward, “Recent Developments in High Temperature Coatings for Gas Turbine Airfoils,” in *NACE International*.

[95] B. Grégoire, X. Montero, M. C. Galetz, G. Bonnet, and F. Pedraza, “Mechanisms of hot corrosion of pure nickel at 700C: Influence of testing conditions,” *Corros. Sci.*, vol. 141, pp. 211–220, 2018.

[96] J. Sumner, A. Encinas-Oropesa, N. J. Simms, and J. R. Nicholls, “Type II hot corrosion: Kinetics studies of CMSX-4,” *Oxid. Met.*, vol. 80, no. 5–6, pp. 553–563, 2013.

[97] G. A. El-Awadi, S. Abdel-Samad, and E. S. Elshazly, “Hot corrosion behavior of Ni based Inconel 617 and Inconel 738 superalloys,” *Appl. Surf. Sci.*, vol. 378, pp. 224–230, 2016.

[98] a. D. Cetel and D. N. Duhl, “Second-Generation Nickel-Base Single Crystal Superalloy,” *Superalloys 1988 (Sixth Int. Symp.*, pp. 235–244, 1988.

[99] Y. F. Gu *et al.*, “Development of Ni-Co base alloys for high-temperature disk applications,” *Proc. Int. Symp. Superalloys*, pp. 53–61, 2008.

[100] “HSC Chemistry.” Outotec.

[101] E. Kistler, W. T. Chen, G. H. Meier, and B. Gleeson, “A new solid-state mode of hot corrosion at temperatures below 700°C,” *Mater. Corros.*, vol. 70, no. December 2018, pp. 1346–1359, 2019.

[102] A. K. Misra, D. P. Whittle, and W. L. Worrell, “Thermodynamics of Molten Sulfate Mixtures,” *J. Electrochmeical Soc.*, vol. 129, no. 8, pp. 1840–1845, 1982.

[103] R. H. Barkalow and G. W. Goward, “Microstructural Features of Low Temperature Hot Corrosion in Nickel and Cobalt Base MCrAlY Coating Alloys,” *NACE*, vol. 6, pp. 502–606, 1981.

[104] K. A. Bol’shakov and P. I. Feorov, “I.,” *J. Inorg. Chem.*, vol. 26, p. 348, 1956.

[105] M. Kovalchuk, “Unpublished reserach,” 2017.

[106] F. Zhou, “Unpublished research in collaboration with Matthew Kovalchuk.”

[107] K. A. Bol’shakov and P. I. Feorov, “II. The ternary system of sodium, cobalt, and nickel sulfates,” *J. Inorg. Chem.*, vol. III, no. 8, pp. 1896–1900, 1958.

[108] H. Mehrer, “Diffusion in Solids.”

[109] D.-I. Kim, “Unpublished research,” 2018.

[110] R. Peraldi, D. Monceau, and B. Pieraggi, “Correlations between growth kinetics and microstructure for scales formed by high-temperature oxidation of pure nickel. I.morphologies and microstructures,” *Oxid. Met.*, vol. 58, no. 3–4, pp. 249–27, 2002.

[111] R. Peraldi, D. Monceau, and B. Pieraggi, “Correlations between growth kinetics and microstructure for scales formed by high-temperature oxidation of pure nickel. II. Growth kinetics,” *Oxid. Met.*, vol. 58, no. 3–4, pp. 275–295, 2002.

[112] A. Atkinson, “Transport processes during the growth of oxide films at elevated temperature,” *Rev. Mod. Phys.*, vol. 57, no. 2, pp. 437–470, 1985.

[113] A. Atkinson, R. I. Taylor, and A. E. Hughes, “A quantitative demonstration of the grain boundary diffusion mechanism for the oxidation of metals,” *Philos. Mag. A*, vol. 45, no. 5, pp. 823–833, 1982.

[114] W. Eysel, H. H. Höfer, K. L. Keester, and T. Hahn, “Crystal chemistry and structure of Na2SO4(I) and its solid solutions,” *Acta Crystallogr. Sect. B*, vol. 41, no. 1, pp. 5–11, 1985.

[115] S. E. Rasmussen, J. E. Jørgensen, and B. Lundtoft, “Structures and Phase Transitions of Na2SO4,” *J. Appl. Crystallogr.*, vol. 29, no. PART 1, pp. 42–47, 1996.

[116] “The materials project.” [Online]. Available: https://materialsproject.org/.

[117] Z. Liu and G. Wang, “Unpublished research,” 2020.

[118] D. M. Duffy and P. W. Tasker, “Computer simulation of grain boundaries in ionic crystals,” *Phys. B+C*, vol. 131, no. 1–3, pp. 46–52, 1985.

[119] T. E. Karakasidis, “Vibrational properties of a Σ5(3 1 0)[0 0 1] NiO grain boundary: A local analysis by molecular dynamics simulation,” *Surf. Sci.*, vol. 515, no. 1, pp. 1–12, 2002.

[120] L. Brooking, S. Gray, J. Sumner, J. R. Nicholls, and N. J. Simms, “Interaction of hot corrosion fatigue and load dwell periods on a nickel-base single crystal superalloy,” *Int. J. Fatigue*, vol. 117, no. June, pp. 13–20, 2018.

[121] N. S. Bornstein, “Reviewing sulfidation corrosion—Yesterday and today,” *Jom*, vol. 48, no. 11, pp. 37–39, 1996.

[122] A. Potter, J. Sumner, and N. J. Simms, “The role of superalloy precipitates on the early stages of oxidation and type II hot corrosion,” *Mater. High Temp.*, vol. 35, pp. 1–7, 2017.

[123] R. M. Kearsey, J. C. Beddoes, P. Jones, and P. Au, “Compositional design considerations for microsegregation in single crystal superalloy systems,” *Intermetallics*, vol. 12, pp. 903–910, 2004.

[124] M. Ganesan, D. Dye, and P. D. Lee, “A technique for characterizing microsegregation in multicomponent alloys and its application to single-crystal superalloy castings,” *Metall. Mater. Trans. A Phys. Metall. Mater. Sci.*, vol. 36, no. 8, pp. 2191–2204, 2005.

[125] G. E. Fuchs and B. A. Boutwell, “Modeling of the partitioning and phase transformation temperatures of an as-cast third generation single crystal Ni-base superalloy,” *Mater. Sci. Eng. A*, vol. 333, no. 1–2, pp. 72–79, 2002.

[126] F. S. Pettit and G. H. Meier, “Oxidation and Hot Corrosion of Superalloys,” *Superalloys 1984 (Fifth Int. Symp.*, pp. 651–687, 1984.

[127] A. Jalowicka, W. J. Nowak, D. Naumenko, and W. J. Quadakkers, “Effect of SO2 Addition on Air Oxidation Behavior of CM247 and CMSX-4 at 1050°C,” *Jom*, vol. 68, no. 11, pp. 2776–2785, 2016.

[128] L. Rivoaland, V. Maurice, P. Josso, M. P. Bacos, and P. Marcus, “The effect of sulfur segregation on the adherence of the thermally-grown oxide on NiAl-I: Sulfur segregation on the metallic surface of NiAl(001) single-crystals and at NiAl(001)/Al2O3 interfaces,” *Oxid. Met.*, vol. 60, no. 1–2, pp. 137–157, 2003.

[129] J. L. Meijering, *Internal oxidation in alloys*. John Wiley & Sons, Inc., 1971.

[130] I. Barin, *Thermochemical data of pure substances*, Third. Weinheim, Germany: Wiley-VCH Verlag GmbH, 1995.

[131] J. X. Chang, D. Wang, G. Zhang, L. H. Lou, and J. Zhang, “Interaction of Ta and Cr on Type-I hot corrosion resistance of single crystal Ni-base superalloys,” *Corros. Sci.*, vol. 117, pp. 35–42, 2017.

[132] G. C. Fryburg, C. A. Stearns, and F. J. Kohl, “Mechanism of beneficial effect of tantalum in hot corrosion of nickel-base superalloys,” vol. 205, no. I, pp. 1147–1148, 1977.

[133] B. H. Kear, F. S. Pettit, D. E. Fornwalt, and L. P. Lemaire, “On the transient oxidation of a Ni-15Cr-6Al alloy,” *Oxid. Met.*, vol. 3, no. 6, pp. 557–569, 1971.

[134] H. J. Grabke, R. Lobnig, and P. Papaiacovou, *Selected topics in high temperature chemistry: defect chemistry of solids*. New York: Elsevier, 1989.

[135] J. E. Restall, M. Malik, and L. Singheiser, “Metallic diffusion and overlay coatings,” in *High Temperature Alloys for Gas Turbines and Other Applications Part I*, 1986, p. 356.

[136] J. J. Truhan and R. E. Benner, “Use of Laser Raman Spectroscopy to Study Hot Corrosion of Ni-Cr Alloys,” in *Symposium on High Temperature Materials Chemistry-II*, 1983, pp. 190–198.

[137] R. L. Farrow and A. S. Nagelberg, “Raman spectrocopy of surface oxides at elevated temperatures,” *Appl. Phys. Lett.*, vol. 36, no. 12, pp. 945–947, 1980.

[138] Z. Wang, S. K. Saxena, P. Lazor, and H. S. C. O’Neill, “An in situ Raman spectroscopic study of pressure induced dissociation of spinel NiCr2O4,” *J. Phys. Chem. Solids*, vol. 64, no. 3, pp. 425–431, 2003.

[139] C. Zhang, X. Peng, J. Zhao, and F. Wang, “Hot corrosion of an electrodeposited Ni-11 wt % Cr nanocomposite under molten Na 2 so 4 -K 2 so 4 -NaCl,” *J. Electrochem. Soc.*, vol. 152, no. 9, pp. 321–326, 2005.

[140] D. M. Johnson, D. P. Whittle, and J. Stringer, “Oxidation of Na2SO4-Coated Cobalt Base Alloys,” *Corros. Sci.*, vol. 15, pp. 649–661, 1975.

[141] D. M. Johnson, D. P. Whittle, and J. Stringer, “Mechanisms of Na2SO4-induced accelerated oxidation,” *Corros. Sci.*, vol. 15, no. 6–12, pp. 721–739, 1975.

[142] G. W. Goward, “Low-Temperature Hot Corrosion in Gas Turbines: a Review of Causes and Coatings Therefor,” *J. Eng. Gas Turbines Power*, vol. 108, pp. 421–425, 1986.

[143] P. L. Norman and J. D. Hartson, “An evaluation of the hot corrosion resistance of commercial high chromium nickel-base alloys for use in gas turbines,” in *Deposition and corrosion in gas turbines*, A. B. Hart and A. J. B. Cutler, Eds. New York, New York, 1973, p. 260.

[144] X. G. Zheng and D. J. Young, “Formation After Pre-Oxidation,” *Corros. Scinece*, vol. 38, no. 11, pp. 1877–1897, 1996.

[145] R. E. Lobnig, H. J. Grabke, H. P. Schmidt, and K. Hennessen, “Sulfur in chromia,” *Oxid. Met.*, vol. 39, no. 5–6, pp. 353–370, 1993.

[146] A. G. Andersen and P. Kofstad, “Reactions of chromium in SO2-containing atmospheres,” *Oxid. Met.*, vol. 43, no. 3–4, pp. 301–315, 1995.

[147] B. Gleeson and B. Li, “Cyclic oxidation of chromia-scale forming alloys: Lifetime prediction and accounting for the effects of major and minor alloying additions,” *Mater. Sci. Forum*, vol. 461–464, no. I, pp. 427–438, 2004.

[148] S. H. Choi and J. Stringer, “The breakaway corrosion of FeCr alloys in atmospheres containing sulfur and oxygen,” *Mater. Sci. Eng.*, vol. 87, no. C, pp. 237–242, 1987.